Advances in Materials Science and Engineering

Advanced Cementitious Materials: Mechanical Behavior, Durability, and Volume Stability

Guest Editors: Doo-Yeol Yoo, Nemkumar Banthia, Kazunori Fujikake, Paulo H. R. Borges, and Rishi Gupta

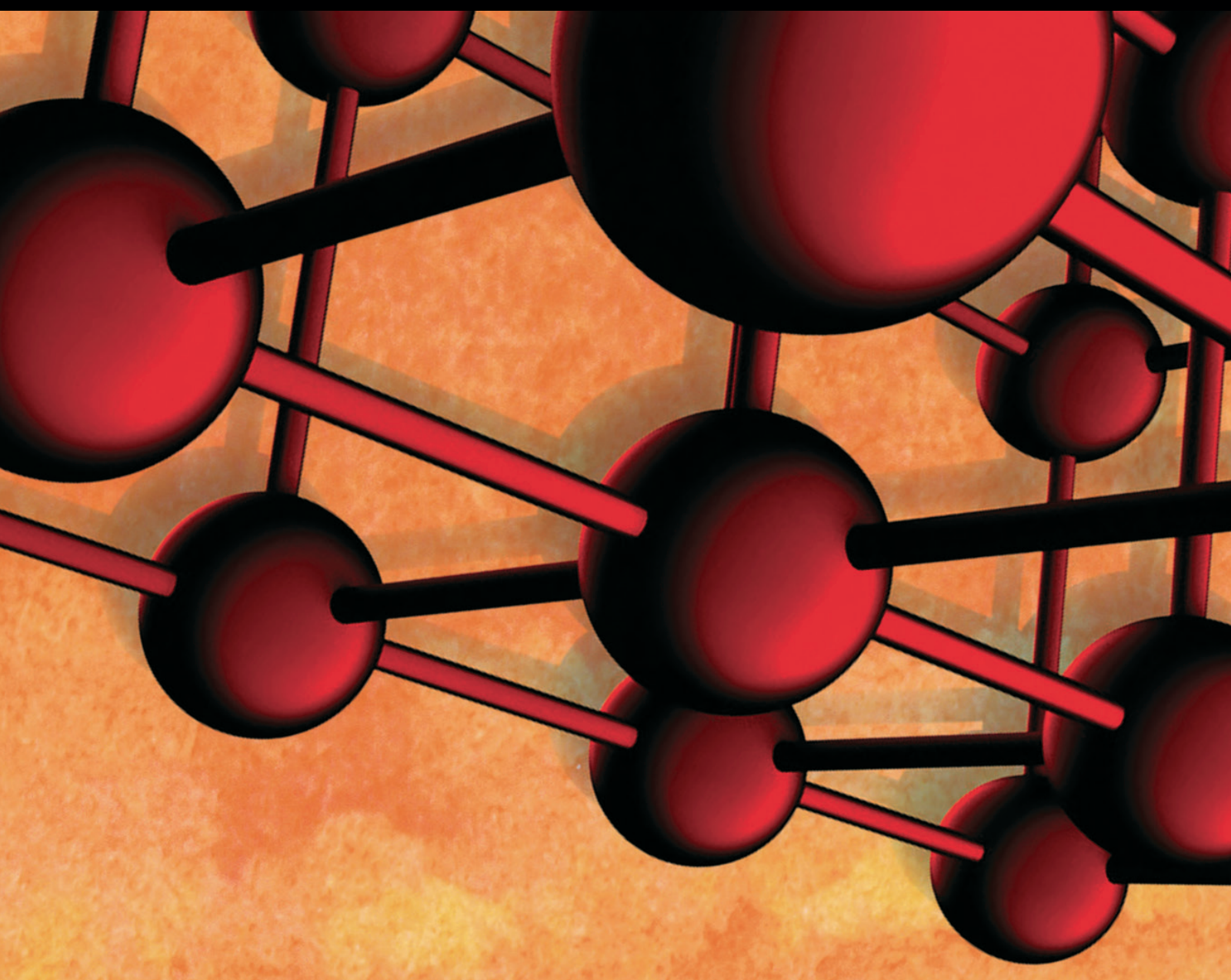

Advanced Cementitious Materials: Mechanical Behavior, Durability, and Volume Stability

Advances in Materials Science and Engineering

Advanced Cementitious Materials: Mechanical Behavior, Durability, and Volume Stability

Guest Editors: Kazuo Toda, Jorge L. Zeredo, Sae Uchida, and Vitaly Napadow

Editorial Board

Contents

Hindawi
Advances in Materials Science and Engineering
Volume 2017, Article ID 5862531, 2 pages
https://doi.org/10.1155/2017/5862531

Editorial

Advanced Cementitious Materials: Mechanical Behavior, Durability, and Volume Stability

Doo-Yeol Yoo,[1] Nemkumar Banthia,[2] Kazunori Fujikake,[3] Paulo H. R. Borges,[4] and Rishi Gupta[5]

[1]*Department of Architectural Engineering, Hanyang University, 222 Wangsimni-ro, Seongdong-gu, Seoul 04763, Republic of Korea*
[2]*Department of Civil Engineering, The University of British Columbia, 6250 Applied Science Lane, Vancouver, BC, Canada V6T 1Z4*
[3]*Department of Civil and Environmental Engineering, National Defense Academy, Yokosuka 239 8686, Japan*
[4]*Department of Civil Engineering, Federal Centre for Technological Education of Minas Gerais (CEFET-MG), Av. Amazonas 7675, 30510-000 Belo Horizonte, MG, Brazil*
[5]*Department of Civil Engineering, University of Victoria, 3800 Finnerty Road, Victoria, BC, Canada V8W 2Y2*

Correspondence should be addressed to Doo-Yeol Yoo; dyyoo@hanyang.ac.kr

Received 6 June 2017; Accepted 6 June 2017; Published 30 August 2017

Several types of advanced cementitious materials, including fiber-reinforced cement composite, eco-friendly concrete including supplementary cementitious materials (i.e., fly ash, ground granulated blast furnace slag, and silica fume), geopolymer concrete, (ultra)high-performance concrete, and self-consolidating concrete, have been developed worldwide since the 1960s. Fiber-reinforced cement composite is suited for structures under flexure or tension due to its inhibition of crack propagation and widening through fiber bridging. Eco-friendly/geopolymer concrete became very important in construction technology after the UN Climate Change Conference held in 2015, since it can reduce carbon dioxide emissions from cement production. (Ultra)high-performance concrete may improve several shortcomings of ordinary concrete in terms of strength-to-weight ratio, ductility, durability, workability, and so forth, and also self-consolidating concrete is an example of high-performance concrete improving workability.

This special issue aimed to provide a comprehensive overview on cementitious materials, including aspects related to mechanical behavior, durability, and time-dependent volume changes, such as shrinkage and creep. Authoritative review articles and original research papers describing recent findings in the field of advanced cementitious materials successfully covered the above topics. This special issue was also very competitive. In total, 58 scientific papers were submitted, and among them, only 14 papers were finally accepted for publication. Acceptance rate was approximately 24%.

Several experimental and numerical papers addressed new research findings with regard to durability properties of concrete. K. Y. Ann et al. examined the effect of frost damage on the rate of chloride transport in ordinary concrete subjected to a rapid freeze-thaw cyclic environment. In their study, the chloride transport was accelerated by frost damage and it was more obvious at a lower cement content. The freezing condition also increased the volume of large capillary pores in ordinary concrete. K.-B. Park et al. numerically simulated the time-dependent chloride diffusion coefficients of concrete including ground granulated blast furnace slag. With an addition of the slag, the changes of total porosity, pore refinement on macro- and microscales due to filling effect, latent-hydraulic properties, and pozzolanic reaction were also analyzed. By comparing the numerical and experimental data, it was concluded that the proposed model is valid for concrete with different water-to-binder ratios, slag replacement ratios, and curing ages. H. J. Yang et al. evaluated the chloride transport in various types of high alumina cement mortar. An increase of Al_2O_3 content in the high alumina cement clinker led to an increase of diffusion

coefficient and concentration of surface chloride due to the increase of chloride binding. But the pore distribution in the cement matrix was not influenced by the types of high alumina cement, except for macropores. An extensive literature review was also conducted by P. Azarsa and R. Gupta for a connection between the electrical resistivity of concrete and the deterioration processes like increase in permeability and corrosion of embedded steel.

The volume stability of cement paste and concrete was investigated by several researchers. B. Kucharczyková et al. introduced an advanced measurement equipment and procedure for simultaneous measurement of length changes, mass losses, acoustic responses, and temperature development. The cement composite's setting and hardening characteristics were evaluated by the continuous measurements of the relative length changes and mass losses. In addition, the formation of microcracks during the setting and hardening of the composites, substantially affecting the final mechanical properties, was possible to be determined using acoustic emission method. Y. Chen et al. examined the effects of amorphous nano-SiO_2 on the early-age properties, such as consistency, setting time, strength, and chemical/autogenous shrinkages. The addition of nano-SiO2 resulted in higher consistency, significant reductions in setting times, higher early-age strength, and higher chemical/autogenous shrinkages. The implications of concrete age and creep on the ultimate load carrying capacity of concrete-filed steel tube columns were also reported by H. Y. Wang et al. based on both experimental tests and numerical analyses. H. Xiong et al. investigated the strain behavior of external thermal insulation cladding systems with Glazed Hollow Beads thermal insulation mortar under hygrothermal cycles. Their test results indicated that the finishing coat shrank at early stage, while the finishing coat tended to expand and became damaged at later stage. The crack length and width on the finishing coat increased with age, but the cracks stopped growing around 70 cycles.

Some other properties, including mechanical property, rheological property, hydration activity, and pore structure, of cement paste and concrete were also reported. R. Chakravarthy et al. tried to develop ductile high volume fly ash concrete including steel, polypropylene (PP), and basalt fibers. In their study, a significant improvement of mechanical properties of high volume fly ash concrete was obtained by including hybrid fibers (i.e., 1% steel fiber, 0.75% PP fiber, and 0.75% basalt fiber). A limiting combination of 3% overall fibers was determined based on the workability of concrete. K.-K. Yun et al. mainly evaluated the pumpability of wet-mix shotcrete including various admixtures, that is, silica fume, fly ash, ground granulated blast furnace slag, metakaolin, and steel fibers based on rheological properties. The addition of silica fume and metakaolin led to satisfactory pumpability, whereas those of fly ash and steel fibers failed to meet the pumping criteria at normal pump pressure. On the other hand, the use of ground granulated blast furnace slag had no significant effect on the pumpability. J. H. Kim et al. introduced the alpha test to examine the performance of polycarboxylate-based high-range water-reducing admixture. To overcome some drawbacks of the mini-slump flow test, the channel flow test was proposed. The final spread and the time to get the stoppage of the spread were measured, and a model converting them into rheological properties was developed. Y. Gao et al. modeled a pore structure in cement paste by means of the recently proposed solid mass fractal model and an enhanced Maxwell homogenization method to determine the associated ionic diffusivity. They verified the developed model by comparing it with experimental results, that is, mercury intrusion porosimetry and rapid chloride migration. S. K. Kim et al. suggested a method for sustainable development of cement industry as well as waste recycling on a national scale that was replacing a portion of cement with a high quality liquid crystal display (LCD) processing waste glass (LPWG) powder. For this, they investigated both fresh and hardened properties of concrete with various amounts of the LPWG powder. Lastly, the reasons why f-CaO in basic oxygen furnace slag is expanded and shows slow hydration activity were studied by R. Jia and J. Liu based on simulated experiments.

The guest editors hope that readers of this special issue can obtain useful experimental and numerical results and discover recent research trends regarding advanced cementitious materials. Furthermore, we wish that their academic curiosities and difficulties can be solved by investigating the valuable research results in this special issue containing both experimental and numerical developments. This publication considers a wide range of disciplines, including civil, architectural, and chemical engineering, and may appeal to the scientists and engineers.

Doo-Yeol Yoo
Nemkumar Banthia
Kazunori Fujikake
Paulo H. R. Borges
Rishi Gupta

Hindawi
Advances in Materials Science and Engineering
Volume 2017, Article ID 8453095, 30 pages
https://doi.org/10.1155/2017/8453095

Review Article

Electrical Resistivity of Concrete for Durability Evaluation: A Review

Pejman Azarsa and Rishi Gupta

Department of Civil Engineering, University of Victoria, Victoria, BC, Canada

Correspondence should be addressed to Rishi Gupta; guptar@uvic.ca

Received 17 October 2016; Revised 30 March 2017; Accepted 2 May 2017; Published 31 May 2017

Academic Editor: Gianfranco Palumbo

Degradation processes in reinforced concrete structures that affect durability are partially controlled by transport of aggressive ions through the concrete microstructure. Ions are charged and the ability of concrete to hold out against transfer of ions greatly relies on its electrical resistivity. Hence, a connection could be expected between electrical resistivity of concrete and the deterioration processes such as increase in permeability and corrosion of embedded steel. Through this paper, an extensive literature review has been done to address relationship between concrete electrical resistivity and its certain durability characteristics. These durability characteristics include chloride diffusivity and corrosion of reinforcement as these have major influence on concrete degradation process. Overall, there exists an inverse or direct proportional correlation between these parameters. Evaluated results, from measuring the concrete electrical resistivity, can also be used as a great indicator to identify early age characteristics of fresh concrete and for evaluation of its properties, determination of moisture content, connectivity of the micropores, and even condition assessment of in-service structures. This paper also reviews and assesses research concerning the influential parameters such as environmental conditions and presence of steel rebar and cracks on measuring electrical resistivity of concrete. Moreover, concrete resistivity concept, application, and its various measurement techniques are introduced.

1. Introduction

The durability of concrete is defined as its ability to resist weathering action, chemical attack, abrasion, or any other deterioration process to retain its original form, quality, and serviceability when exposed to harsh environment [1]. To a large extent, it is commonly accepted that concrete durability is governed by concrete's resistance to the penetration of aggressive media. This media may be present in a liquid or gaseous state and that may be transported by various mechanisms such as permeation, diffusion, absorption, capillary suction, and combinations of the items just mentioned. Hence, for concrete in service, a combined action of various media may prevail and mixed modes of transport processes occur. Moreover, there are correlations between transport parameters of concrete and the following durability characteristics: carbonation, sulphate attack, alkali-aggregate reaction, frost resistance, leaching, soft water attack, acid attack, abrasion, chloride ingress, and reinforcement corrosion. Consequently, the transport of ions through microstructure of concrete plays an important role in the control of concrete durability. When ions are charged, then it is the concrete's ability to withstand transfer of charged ions which is highly dependent upon its electrical resistivity. In this study, since chloride ingress and reinforcement corrosion are reported as major concrete deterioration processes, one of the main concentration areas is on these durability characteristics and their relationship with concrete electrical resistivity.

Over the last few decades, a great deal of attention has been paid to research and development of electrical resistivity measurement techniques as a nondestructive technique (NDT) to evaluate the durability of concrete structures. This method is becoming more popular especially for field evaluations due to its simplicity, rapidness, and cost during test conduction. However, the inclusion of these methods into the standards and guidelines is quite slow. Electrical resistivity has been standardized in 2012 by ASTM C1760 [2] to measure the concrete bulk resistivity and also by AASHTO

TP 95-11 [3] to quantify the surface resistivity of concrete. However, there is a gap that still exists between the current knowledge and industry practice.

Electrical resistivity is a material property that can be used for various purposes, one of which is to identify early age characteristics of fresh concrete. When the fresh concrete sets and hardens, depercolation (discontinuity) of the capillary pore space leads to an increase in its electrical resistivity. Since electrical current is conveyed by dissolved charged ions flowing into the concrete pore solution, it is a good indicator of concrete pore structures [4]. This pore structure formation at early-ages can define the long-term durability of concrete. In addition, the tensile strength of cementitious materials at early-ages is low and the material is prone to cracking. This initial cracking also serves as a pathway for deleterious materials to ingress into the matrix. This cracking can also be captured by resistivity measurements and thus helps predict the long-term durability of concrete. In addition, electrical resistivity can be used as an index to determine the moisture content and the connectivity of the micropores in the concrete [5].

Several researchers attempted to characterize the effects of various parameters on electrical resistivity measurements. One of the important factors affecting the measurements is environmental conditions such as temperature, rainfall, and relative humidity. During testing, good electrical connection between concrete and electrodes as well as specimen geometry plays a key role in having a reliable measurement. The electrical resistivity measurements are highly influenced by the moisture content of concrete. For instance, when the moisture content is reduced, the resistivity is increased significantly. Therefore, considering all these influencing parameters for on-site resistivity measurements and to make meaningful conclusions is not a simple task.

In this paper, the correlation between electrical resistivity and certain durability characteristics of concrete is discussed. These concrete characteristics include chloride permeability, corrosion rate, and compressive strength. Also, different approaches in the measurement of concrete resistivity including bulk and surface resistivity measurements are presented. This paper reviews the effect of several influencing parameters such as external environment (e.g., temperature) and concrete mixture on the electrical resistivity. In addition, some of bulk and surface resistivity test setups (both of laboratory and field tests) conducted by authors are also presented.

2. Theoretical Background

2.1. Concept. Electrical resistivity (ρ) of a material is defined as its capability to withstand the transfer of ions subjected to an electrical field. It is largely dependent on the microstructure properties of concrete such as pore size and shape of the interconnections (i.e., tortuosity) [6]. Specimens with similar degree of water saturation and temperature should be used as both of these factors affect resistivity. Lower permeability results from a finer pore network with less connectivity and eventually leads to higher electrical resistivity. The range spanned by resistivity is one of the greatest of any material property [12]. For concrete, it varies from 10^6 Ω·m for oven dried samples to 10 Ω·m for saturated concrete [13]. Electrical resistivity is the ratio between applied voltage (V) and resulting current (I) multiplied by a cell constant and the electrical current is carried by ions dissolved in the pore liquid [7, 14]. Thus, it is a geometry independent property and an inherent characteristic of a material, as described in the following [6, 14]:

$$\rho = k \cdot R = k \cdot \left(\frac{V}{I}\right), \tag{1}$$

where R is the resistance of concrete; k is a geometrical factor which depends on the size and shape of the sample as well as the distance between the probes on the testing device [6]. There are several factors that may affect electrical resistivity of concrete, and they can be divided into two groups: (1) intrinsic factors affecting the electrical resistivity of concrete, such as w/c ratio, aging, and pore structure; (2) factors affecting the resistivity measurements, including specimen geometry, moisture content, temperature, electrode spacing, and presence of rebar. For instance, more pore water as well as wider pores results in lower concrete resistivity and environmental factors such as higher temperature decreases the resistivity values [7]. Furthermore, adding reactive supplementary cementitious materials such as blast furnace slag and fly ash leads to lower permeability and higher electrical resistivity due to reduction in capillary porosity and hydroxyl ions (OH^-). Both carbonation and chloride penetration also individually cause an increase in concrete resistivity in particular in Portland cement concrete but penetrated chloride impact is relatively small [7]. The effects of the above-mentioned parameters will be discussed in detail later in this paper.

2.2. Measurement Techniques. Electrical resistivity measurements can be performed in several ways nondestructively: using electrodes positioned on a specimen surface, or placing an electrode-disc or linear array or a four-probe square array on the concrete's surface. Types of device techniques that can be used typically to measure resistivity physically include (1) bulk electrical resistivity test, (2) surface disc test, (3) Wenner four-point line array test, and (4) four-probe square array test.

2.2.1. Bulk Electrical Resistivity Test. In the bulk resistivity method (or uniaxial method), two electrodes are placed on the concrete surface (usually two parallel metal plates) with moist sponge in between (Figure 1(a)). Generally, only standard cylinders/prismatic specimens or cores taken from existing structures are used in this method. The geometrical factor in this method can be obtained by the following equation:

$$k = \frac{A}{L}, \tag{2}$$

where A is the cross-sectional area perpendicular to the current and L is the height of sample. Although this nondestructive test takes only a few seconds, its application is limited for field evaluation because electrodes access to

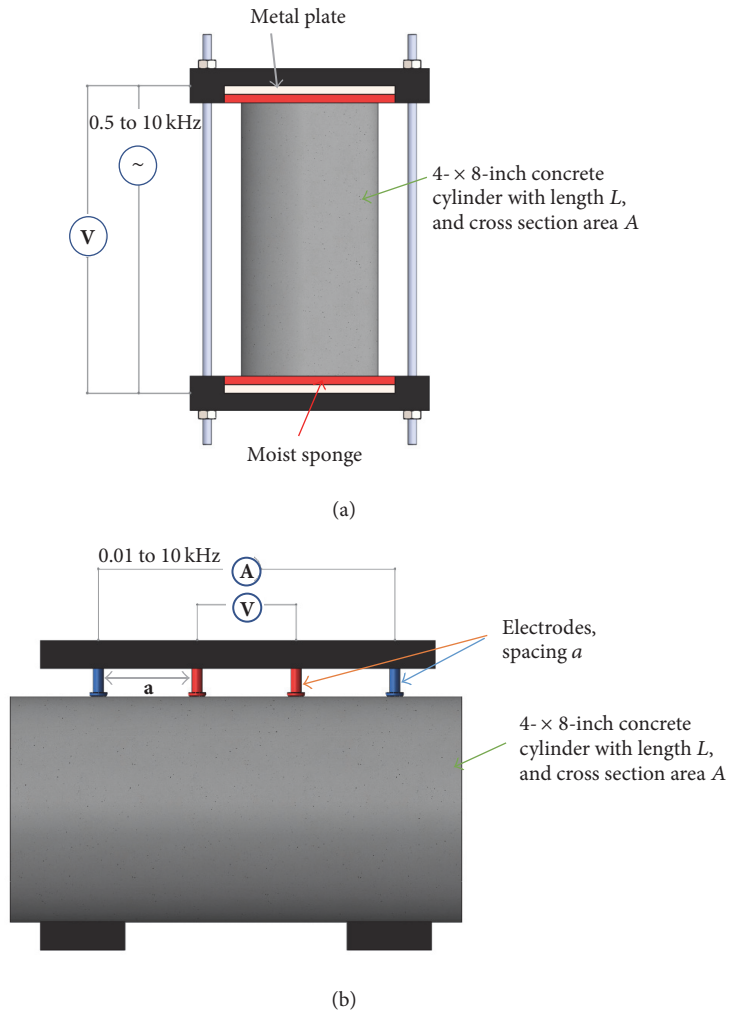

Figure 1: Electrical resistivity measuring techniques: (a) two-point uniaxial method and (b) four-point (Wenner probe) method (reproduced from [6]).

opposite sides of the concrete element is not possible all the time; while other above-mentioned resistivity measurement (surface disc test, Wenner four-point line array test, and four-probe square array test) methods may use probes placed on only one side surface of specimen.

2.2.2. Surface Disc Test. The electrode-disc test method includes an electrode (disc) placed over a rebar and measuring the resistance between the disc and the rebar, as shown in Figure 2 [7]. One disadvantage of this method is a connection requirement to the steel reinforcement and full rebar continuity. In this technique, a cell constant is dependent on cover depth (which varies over the surface) and the rebar diameter whose precise measurements are impossible due to lack of exact current flow prediction [7]. For cover depth, disc and bar diameters being 10–50 mm, the cell constant is approximately 0.1 m. Hence, the resistivity can be derived using

$$\rho\,(\text{disc}) = 0.1 \times R\,(\text{disc} - \text{bar})\,. \tag{3}$$

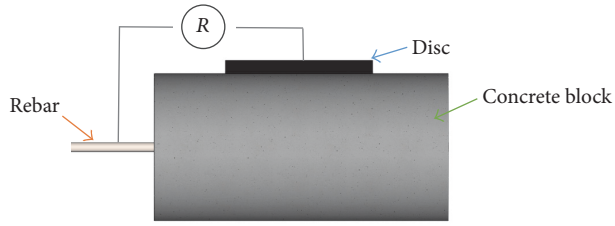

Figure 2: Setup of one electrode-disc: measurement of concrete resistivity (reproduced from [7]).

2.2.3. Wenner Four-Point Line Array Test. The Wenner probe technique was first introduced for the geologist's field in order to determine soil strata by Wenner at the National Bureau of Standards in the 1910s and then modified through time for concrete application [15]. In this technique, four equally spaced linear electrodes are used to measure the surface electrical resistivity of concrete (Figure 1(b)). The two exterior electrodes apply an AC current to the concrete surface while

the electrical potential is measured from the interior probes. It should be noted that DC current is not desirable as it may result in inaccurate readings because of polarization effect. The effect of current frequencies on measurements is discussed in Section 5.2.6 (studies on electrical signal shape and frequency). The constant cell is defined as (4) for semi-infinite homogenous material [6]:

$$k = \gamma \cdot a, \tag{4}$$

where a is the distance between the equally spaced electrodes and γ is the dimensionless geometry factor which is equal to 2π for semi-infinite concrete elements such as concrete slabs [6]. However, the geometry factor is different for tests conducted in a laboratory condition on small cylinders or cubic specimens. To measure the surface electrical resistivity, AASTHO TP 95-11 is the only specified standard which requires an electrode spacing of 1.5 inch (or 38 mm) with an AC frequency of 13 Hz [3]. Due to its configuration, this method is reliable for on-site measurement; however many factors that will be discussed in Section 5 can affect the results such as rebar and cracks presence, surface conditions, concrete mixture, and environmental conditions.

2.2.4. Four-Probe Square Array Test. The four-probe square array consists of the four probes that are arranged in square position with spacing of 50 to 100 mm [10].

2.3. Applications. Electrical resistivity can be related to certain performance characteristics of concrete and can be used as a promising quality assurance tool for fresh or hardened concrete [6]. Some of these correlations will be discussed in the following sections. It can be used as a measure of concrete resistance to chloride ingress as well as corrosion initiation and rate measurements. The concrete diffusion coefficient as an important factor in the service life estimation of structures also can be obtained by electrical resistivity technique. In addition, it is a reliable test method to detect and monitor the initiation and propagation of cracks in concrete since they change the connectivity of concrete pore structure, and thus its electrical conductivity [16]. Cement mortars and concrete setting time can be determined through the concept of electrical resistivity. However, the correlation between setting time and concrete durability is not fully understood. Another potential application of the electrical resistivity method is to compute the moisture content of concrete, although reliability of this method is still under question [5]. However, electrical resistivity method is a simple and reliable nondestructive test method; the application and reliability of this method in determining certain characteristics of concrete has yet to be widely evaluated. This is more due to the limited knowledge in this area especially for on-site evaluation.

3. Objective and Methodology

The primary objective of this paper is to review the existing state of practice on the electrical resistivity measurements technique. This paper also identifies the applicability and limitation of electrical resistivity method and reviews the correlation between resistivity and certain durability properties of concrete. Correlation between surface and bulk electrical resistivity and their applications is also discussed. Finally, key parameters affecting the electrical resistivity readings are identified for future research in the area.

An extensive literature search was undertaken from most relevant publications in the area. A comparison was made of the experimental setup (Section 4), and the way in which the correlated data was obtained between resistivity and durability properties of concrete (Sections 6–8). Several parameters influencing the concrete resistivity were identified and compared (Section 5). The information observed from the literatures was based on experimental and numerical studies. The reviewed data was compiled in tables and later compared. Detailed information on the experimental setups is presented in Abbreviations section and Tables 1–4. The literature search covered both laboratory and field investigation.

4. Comparison of the Experimental Investigations

In this section, experimental setups developed by other researchers have been summarized in Tables 1–4. These tables consist of specimens' configuration, materials type, resistivity measurement techniques, and specimen curing/exposure conditions. The data in the tables is arranged in the order in which the citations appear in Sections 5–8. An additional row that contains authors' data on measuring electrical resistivity of simulated field circular hollow-section columns is also included. The extent to which differences in the setups can influence electrical resistivity measurements are discussed later in Sections 5–8 using data presented in this section. A comparison of the experimental setups is given in Sections 4.1–4.3. Abbreviations and symbols are defined in Abbreviations section.

4.1. Specimen Geometry and Setup. Frequently, in the electrical resistivity studies, samples with dimensions between 100 and 400 mm were used (Table 1). Specimens with dimensions over 1000 mm to simulate real-world condition were more seldom used. According to Table 2, the steel rebar diameter varied from 4 to 25 mm. In most cases, no detailed information was provided about the type of steel embedded; both smooth and ribbed steel was used. Cover depth ranging from 10 to 80 mm was considered for steel reinforcement bars in the majority of the experimental investigations. For those studies investigating the relationship between steel reinforcement corrosion and concrete resistivity, chloride ingress was the major cause of corrosion. However, no information was provided on the size of the anode and the ratio between anode and cathode in the reviewed articles. Only one study concentrated solely on carbonation-induced corrosion.

4.2. Materials and Exposure Conditions. According to data in Table 1, concrete or mortar samples were casted with a w/b ratio between 0.4 and 0.65 by mass in most reviewed

Table 1: Details of the specimen geometry (in terms of specimen size), material type, and number of specimens.

Refs	Specimen configuration			Materials type							w/b ratio	Rebar presence
	Type	Size (mm)	TNVM	Mix type	OPC	SLG	FA	MK	SF	Others		
[4]	Disk	Φ100 × 50	44	CON/CEM	×	×	×	—	× (5% & 10%)	NP (30% and 50%)	0.35, 0.4, 0.45	N
[16]	Slab	254 × 76 × 12.7	18	CON	× Type I	—	×	—	—	—	0.26	N
[22]	Cylinder	Φ47 × 95	30	CEM	× Type I	—	× (classes C & F)	—	—	$CaCO_3$ (10% & 15%)	0.35	N
[23]	Slab	250 × 200 × 120	1	CON	×	—	—	—	—	—	0.5	Y
[8]	Slab, cube, cylinder	300 × 300 × 135, 300 × 300 × 200, 100 × 100 × 100, Φ100 × 200	6	CON	× (blended)	—	× (20% blended)	—	—	—	0.4	Y
[24]	Prism	300 × 300 × 150	7	CON	× Type I	—	×	—	—	—	0.42	Y
[25]	Cylinder, prism	Φ100 × 200, Φ150 × 300, 200 × 200 × 175, 160 × 160 × 140, 120 × 120 × 110	NR	CON	× Type I	—	—	—	—	—	0.4, 0.6	Y
[26]	Cylinder, prism	Φ150 × 300, 40 × 40 × 160	NR	MOR	×	—	—	—	—	—	0.5	Y
[27]	Prism	400 × 400 × 100	6	MOR	×	—	—	—	—	—	0.6	Y
[28]	Cylinder	Φ150 × 220	4	CON	×	—	—	—	—	—	0.4, 0.6	Y
[29]	Slab, cube	650 × 650 × 100, 150 × 150 × 150	1	CON	×	—	—	—	—	—	0.5	N
[30]	Slab	600 × 600 × 120	9	CON	×	—	—	—	—	—	0.36, 0.48, 0.61	Y
[11]	Beam	1500 × 200 × 100	2	CON	×	—	—	—	—	×	0.7	N
[31]	Cylinder	Φ100 × 200	21	CON	× Type I/II	× (grades 100 & 120, 50%)	× (classes C & F, 20%)	—	× (5% & 10%)	—	0.35, 0.5, 0.65	N
[32]	Cylinder	Φ100 × 200	33	CON	× Type I/II	—	×	—	×	—	0.41	N
[33]	Cube	150 × 150 × 150	47	CON	×	×	—	—	—	—	0.4–0.55	N
[34]	Prism	100 × 100 × 170	12	CON	×	× (50% and 70%)	—	—	—	WPC	0.3, 0.42, 0.55	N
[35]	Cylinder	Φ150 × 300	3	CON	× Type I	—	—	—	—	—	0.45, 0.55, 0.65	N
[36]	Cylinder	Φ75 × 150	NR	CON	× Type V	—	—	—	—	—	0.45	N
[37]	Cube, cylinder, block	100 × 100 × 100, Φ100 × 200, Φ150 × 300, 300 × 300 × 200	NR	CON	× (blended)	—	× (18% blended)	—	—	—	0.4	N
[38]	Cube	150 × 150 × 150	NR	CON	×	×	—	—	×	PFA	0.59–0.7	N
[39]	Cylinder	Φ100 × 200	12	CON	×	×	×	×	×	Micro-FA	0.3–0.4	N
[40]	Cube	150 × 150 × 150	33	CON	× Type I & Type V	×	—	—	—	—	NR	N
[41]	Cylinder	Φ100 × 200	19	CON	×	×	×	—	×	—	0.41	N
[42]	Slab, cylinder	280 × 280 × 102, Φ102 × 204	NR	CON	×	×	×	×	—	MS	0.35–0.45	N
[43]	NR	NR	NR	MOR/CEM	× Type I	—	—	—	—	—	0.42	N
[44]	Cylinder	Φ100 × 200	12	CON	×	×	×	—	—	—	0.41	N

Table 1: Continued.

Refs	Specimen configuration				Materials type						w/b ratio	Rebar presence
	Type	Size (mm)	TNVM	Mix type	OPC	SLG	FA	MK	SF	Others		
[45]	Block	300 × 300 × 200	3	CON	×	×	—	—	—	PFA	0.39, 0.4, 0.44	Y
[46]	Slab, cylinder	610 × 610 × 152, Φ100 × 200, Φ150 × 300	10	CON	×	×	× (class F)	—	—	MS	0.43	Y
[47]	Prism	1000 × 1000 × 300, 150 × 270 × 150	NR	CON	×	—	×	—	—	—	0.35–0.65	Y
[48]	Cylinder	Φ100 × 200	NR	CON	× Type I/II	—	× (20%)	—	× (8%)	—	0.4	N
[49]	Cylinder	Φ100 × 200	10	CON	×	× (SC)	—	—	—	—	0.45, 0.65	Y
[50]	Prism	100 × 100 × 300	12	CON	×	×	×	—	—	—	0.4, 0.45, 0.5	Y
[51]	Cylinder, cube	Φ100 × 200, 100 × 100 × 100	12	CON	×	×	—	—	×	—	0.25, 0.28, 0.35	N
[52]	Cylinder	Φ100 × 200	12	CON	×	×	×	×	×	(Super fine fly ash)	0.28–0.49	N
[53]	Cylinder	Φ100 × 200	11	CON	×	×	×	—	—	—	0.37–0.45	N
[54]	Cylinder	Φ100 × 200	343	CON	× Type I/II	—	× (class C, 25%)	—	—	—	0.42	N
[55]	Cylinder	Φ100 × 200	514	CON	×	×	× (class F)	—	—	—	0.41	N
[56]	Cylinder	Φ100 × 200	57	CON	× Type I	—	—	×	×	RHA, NP	0.4–0.6	N
[57]	Cube, slab	100 × 100 × 100, 250 × 250 × 100	10	CON	×	×	—	(5%, 10%, 20%)	—	MS (5% and 10%) & PFA (30%)	0.52	N
[58]	Disk	Φ100 × 50	6	CON	×	× (30%)	—	—	× (10%)	—	0.25, 0.28, 0.35	N
[59]	Cylinder	Φ150 × 300	24	CON	×	× (50%)	—	—	8%	NP (12%, 25%)	0.28–0.6	N
[60]	Cylinder	Φ150 × 200	4	CON	×	—	—	—	—	—	0.4, 0.6	Y
[21]	Cylinder, prism	Φ102 × 178, 406 × 76 × 102	NR	MOR	×	—	—	—	—	WPC	0.42	N
[61]	Cylinder	Φ100 × 200	33	CON	× Type II–V	(grades 100 & 120)	(classes C & F)	×	×	—	0.44	N
[62]	Cylinder	Φ100 × 200, Φ150 × 300	23	CON	× Type II–V	× (grade 120)	(class F, 20%)	×	×	—	0.44	N
Authors	Hollow section, cylinder	Inner dia. 152 and external dia. 304, Φ100 × 200	18	CON	×	×	—	×	—	CA (2%), PLC	0.5	Y

Table 2: Details of the reinforcements and measurement methods used to record corrosion rate.

Refs	Reinforcement			Cause of corrosion	Corrosion rate		Correction for ohmic drop
	Φ (mm)	Length (mm)	Cover depth (mm)		Technique	Details	
[23]	10	200	1, 10, 20	Carbonation	—	—	—
[8]	10	300	50 & 75	Not studied (NS) (only effect of rebar presence on resistivity measurement was considered)	—	—	—
[24]	16	300	50	Cyclic ponding with sea water	—	—	—
[25]	4	110, 160, 200	Various (53.5–100)	NS	—	—	—
[26]	8	40	80	NS	—	—	—
[27]	13, 19, 25	410	20, 30, 40	NS	—	—	—
[28]	10	250	150	NaCl solution/marine exposure	LPR	Embedded steel rebar	N
[30]	10	—	25	NS	—	—	—
[45]	16	200	50	NaCl solution/marine exposure	—	—	—
[46]	NR	NR	NR	NaCl solution	LPR	NR	NR
[47]	NR	NR	70	NaCl solution	—	—	—
[49]	16	NR	42	NaCl solution	NR	Embedded steel rebar	NR
[50]	8	150	10 or 30	NaCl solution	LPR	Embedded CE & RE on the surface	N
[60]	10	200	15	NaCl solution	—	—	—
Authors	10	914	19–38	NaCl solution	LPR	Embedded steel rebar	Y

experimental programs. The mixture proportions and cement content varied and blended cements such as fly ash or slag cements were used in parts of studies. In a couple of studies, no detailed information was provided about the cement type. However, ASTM Type I and CEM I/II cements were used in most of the articles. Only one reported study used White Portland Cement (WPC) [34]. Also, Rice Husk Ash (RHA) as a cementitious supplementary material was only studied by Gastaldini et al. [63]. Work done by authors of this paper seems to be the only one that considered crystalline admixture as a healing agent to investigate its effect on electrical resistivity of concrete.

The specimens were cured and exposed to various and/or changing conditions over the testing period (Table 3). In most studies, samples were cured in the lime-saturated water tank with controlled temperature to eliminate the temperature effect on resistivity measurements. The temperature was kept constant between 20°C and 25°C in most experiments. To achieve a wide range of concrete resistivity, drier climates were considered occasionally. In most experiments, specimens were kept in a water tank during resistivity measurements or exposed to a high relative humidity (RH). For those studies focused on accelerating corrosion process, RH between 90% and 95% was chosen as an exposure regime. In parts of studies, samples were exposed to outside climates, in particular marine conditions (similar to authors' experimental setup). In general, laboratory experiments were undertaken over a period between 28 and 365 days. Only a few studies measured electrical resistivity for a period over one year [42, 50, 64, 65].

4.3. Measurement Methods. Either two-electrode or four-point electrode (Wenner probe setup) techniques were employed to record concrete electrical resistance, which is then converted into resistivity by multiplying it with an appropriate geometrical factor. The limitations of 2-electrode method resulted in using Wenner probe configurations in most studies specially for field investigations. In experimental studies that attempted to find correlation between concrete electrical resistivity and its durability parameters, other destructive and nondestructive testing techniques from standardized measuring protocol including Rapid Chloride Permeability (RCP) test, Rapid Chloride Migration (RCM) test, Bulk Diffusion (BD) test, and Ultrasonic Pulse Velocity (UPV) were employed. Authors ongoing work also employs

Table 3: Details of the curing conditions, exposure conditions, and measurement period.

Refs	Curing conditions	Temperature (°C)	Exposure conditions	Measurement period (days)
[4]	Lime-saturated water tank	20 (except one type mixture kept in water having 5, 20, 35 temperature)	Lime-saturated water tank/lab condition and oven dry state (only one type mixture)	90 (except ten of the mixtures tested at age of 365 days)
[16]	Lime-saturated water tank	23 ± 1	Lime-saturated water tank	28
[22]	NR	15, 26, 40	Plastic wrapped	1
[23]	NR	20	Laboratory (air dry)	1000
[8]	Water tank	20	Water tank (except two slabs were kept in air after 7 days)	30
[24]	NR	NR	Various	120
[25]	Lime-saturated water tank	23	Various	28
[26]	100% relative humidity in a chamber	20 ± 2	100% relative humidity in a chamber	28
[27]	Water tank	20	Water tank	45
[28]	NR	NR	Seashore Exposure/immersed in saline solution	1000
[29]	Plastic wrap	20	Room temperature	90
[30]	NR	NR	NR	28
[11]	Room temperature	25 ± 2	Room temperature	28
[31]	Lime-saturated water tank	Laboratory	Lime-saturated water tank	56
[32]	NR	10–45	Room condition with RH > 95%	2,190
[33]	Water tank	20	Water tank	181
[34]	Wet chamber with RH > 95%	23 ± 2	Wet chamber with RH > 95%	91
[35]	Water tank	23 ± 0.5, 105 ± 2	Various	28
[36]	Wet burlap	20	Oven dried and then water bath	31
[37]	Water tank	20 & 5	Water tank (after 7 days, some cylinders subjected to air condition)	30
[38]	Water tank	20 ± 2	Water bath	720
[39]	Lime-saturated water tank	23 ± 2	Lime-saturated water tank	91
[40]	Water tank	NR	Water tank	365
[41]	Various	21–45	Various	1,100–2,200
[42]	Lime-saturated water tank/wet burlap	NR	Lime-saturated water tank/wet burlap for 3 or 7 days	91
[43]	Lime-saturated water tank	Various (10–45)	Various	65
[44]	Various	Various	Various	500
[45]	Wrapped in damp Hessian and stored under polythene tentage	15–20	Maine exposure	140
[46]	Various	18–32	Salt ponding	90
[47]	Water tank and laboratory air	20 ± 2	Actual tidal zone, wet and dry cycle	NR
[48]	Five various curing regimes (tap water, NaCl solution, rog room)	Room	Various	1500
[49]	Various	20 ± 2/uncontrolled	Various	90

Table 3: Continued.

Refs	Curing conditions	Temperature (°C)	Exposure conditions	Measurement period (days)
[50]	Six days in fog room/three weeks in room condition	20	26 weekly cycles of 24 h 3% NaCl solution penetration and drying for 6 days/after 30 weeks, various conditions	52
[51]	Water tank	25	Water tank	90
[52]	Moist room with a sustained 100% humidity	23	NaCl solution	1,092
[53]	Lime-saturated water tank	22	Lime-saturated water tank	56
[54]	Changing exposure	23 ± 2	Changing exposure	90
[55]	Lime-saturated water tank	21 or 36	Various	1000
[56]	Lime-saturated water tank	23 ± 2	Lime-saturated water tank	28
[57]	Water tank for 14 days/14 days in drying cabinet at 40°C	20 ± 1 & 40 ± 1	Salt ponding (wet & dry cycle)	270
[58]	Lime-saturated water tank	25	Lime-saturated water tank	90
[59]	Chamber with RH > 95%	21	Chamber with RH > 95%	28
[60]	Laboratory environment (kept in plastic bag)	14–27, 3–13	Seashore condition	1,000
[21]	Water tank	21 ± 3	Water tank	7
[61]	Lime-saturated water tank	NR	Lime-saturated water tank	1
[62]	Lime-saturated water tank	NR	Lime-saturated water tank	730
Authors	14 days wet burlap and 14 days air dry	Uncontrolled	Natural environment and simulated seashore condition	720

use of both 2-electrode and 4-electrode techniques as well as UPV technique.

In summary, the experimental setup can have a significant effect on the electrical resistivity measurements. Specifically, the measurement methods and environmental conditions comprise a variety of parameters affecting the obtained data. The geometry of specimen and the general setup have a minor influence on the recorded resistivity values. To investigate electrical resistivity, the material, curing condition, and exposure condition should be carefully selected. Simulating the real-world conditions is in any case desirable since the recorded data can be used later as input in prediction models. As field survey data is rarely reported in the reviewed studies, it seems critical to identify possible deviations between laboratory investigations and field conditions. Also, authors' focus currently is to find these deviations to fill this knowledge gap by measuring concrete resistivity on both laboratory-size and field-size specimens.

5. Influencing Parameters on Electrical Resistivity Measurements

In the following sections, investigated parameters in published literature that influences the electrical resistivity readings have been discussed. For simplicity, they have been divided into two subgroups: (1) factors affecting the intrinsic electrical resistivity of concrete and (2) factors affecting the electrical resistivity measurements.

5.1. Intrinsic Factors Affecting Electrical Resistivity of Concrete

5.1.1. Effect of Water to Cement (w/c) Ratio. Generally, water to cement (w/c) ratio is one of the main factors contributing in permeability of concrete and its properties. Higher w/c ratio results in a high percentage of porosity (more voids) and leads to a lower electrical resistivity value indicating a more permeable concrete [31]. However, concrete containing supplementary cementitious materials such as slag showed an irregular behaviour for various w/c ratios [31]. For instance, an increase in w/c ratio from 0.35 to 0.65 caused an increase in electrical resistivity values, which means a less permeable concrete. Additionally, the electrical resistivity measurements are affected by the degree of hydration as further hydration typically reduces the concrete porosity and how these pores are interconnected [32]. The results from experimental study conducted by Van Noort et al. [33] on different concrete compositions with various w/c ratio ranges also indicated that concrete's electrical conductivity increased as w/c ratio increased. Within a hardened concrete matrix, electrical conduction flows through the fluid contained in the pores; therefore the relative volume of interconnected pores controls the concrete's electrical resistivity. Increasing the w/c ratio (at fixed cement content) leads to a higher volume fraction of hydrated cement paste in the concrete mix and results in higher concrete electrical conductivity. Similar tendency has been observed [34] even for concrete containing White Portland Cement. When w/c ratio was reduced, conductivity

Table 4: Details of the different measurement methods used in the literature.

Refs	Measurement technique			
	Concrete resistivity		Rapid chloride permeability test	Others
	Two-electrode	Four-point method		
[4]	×	—	—	Rapid chloride migration test (NT Build 492) & ASTM C1760
[16]	×	—	—	—
[22]	×	—	—	—
[23]	×	×	—	Multiring electrodes
[8]	×	×	—	NT Build 492
[24]	—	×	—	—
[25]	—	×	—	—
[26]	×	×	—	—
[27]	—	×	—	—
[28]	—	×	—	Steel potential
[29]	×	×	—	—
[30]	—	×	—	Ultrasonic Pulse Velocity
[11]	—	×	—	Electric imaging
[31]	—	×	×	—
[32]	—	×	—	—
[33]	×	—	—	NT Build 492
[34]	—	×	—	—
[35]	—	×	—	—
[36]	×	—	—	—
[37]	×	×	—	NT Build 492
[38]	×	—	—	—
[39]	×	×	—	—
[40]	×	×	—	—
[41]	—	×	—	—
[42]	×	×	× (ASTM C1202)	—
[43]	×	×	—	—
[44]	—	×	—	—
[45]	×	—	—	—
[46]	×	×	× (AASHTO T227)	Half-cell potential
[47]	×	×	—	—
[48]	—	×	—	—
[49]	—	×	—	—
[50]	×	—	—	Steel corrosion potential
[51]	×	—	—	NT BUILD 492
[52]	—	×	—	ASTM C1556-04
[53]	×	×	× (ASTM C1202)	—
[54]	—	×	×	KDOT Boil Testing
[55]	—	×	—	Bulk diffusion test (NT Build 443), NT Build 492
[56]	—	×	×	Water Penetration Depth
[57]	—	—	—	Resistivity using disc method (one external electrode)
[58]	×	×	—	NT Build 492
[59]	—	×	—	Natural diffusion test (90 days)
[60]	—	×	—	Half-cell potential method

Table 4: Continued.

Refs	Measurement technique			
	Concrete resistivity		Rapid chloride permeability test	Others
	Two-electrode	Four-point method		
[21]	×	×	—	—
[61]	×	×	—	—
[62]	×	×	—	—
Authors	×	×	×	UPV, half-cell potential, infrared camera

of pore solution was increased due to the greater ionic concentration of the solution. Su et al. [35] studied the effect of moisture content on concrete resistivity measurements. It was found that the electrical resistivity difference for mixes with 0.55 and 0.65 w/c ratios was not noticeable, although it became significant for specimens with a w/c ratio of 0.45. It seems that both the capillary pore size effect and interconnectivity effect improve resistivity for saturated concrete with a higher w/c ratio. Long-term experimental study also showed the reduction in concrete resistivity with the increase of w/c ratio until approximately 500 days. However, after 500 days, the resistivity results revealed a contrary behaviour because the concrete specimens kept in unsaturated condition (in a laboratory environment) with higher w/c ratio favored the carbonation process that led to larger resistivity values for more advanced ages. Saleem et al. [36] also found similar trend for concrete samples contaminated with sulphate/chloride. About 15–20% reduction in electrical resistivity values was reported when the water/cement ratio increased from 0.4 to 0.6 [25].

5.1.2. Effect of Aggregate Size and Type. In general, aggregates depending on their location and size have a higher electrical resistivity compared to hardened cementitious paste because they have less porosity; thus electrical current can easily flow through the pore system of the paste. Hence, a number of researchers attempted to investigate aggregates' effect on electrical resistivity measurements. The experimental study performed by Sengul [4] indicated that increasing aggregate content resulted in higher electrical resistivity. He also observed that the resistivity of the mixture containing 60% aggregate with the size of 16–32 mm was approximately 3 times higher than that of the hardened cement paste [4]. Increase in aggregate content and reduction in cement paste for a given volume resulted in higher resistivity values because of replacing the porous hardened cement paste with denser aggregates. The investigation on comparing effect of two different aggregate sizes (0–4 mm and 16–32 mm) on electrical resistivity showed that larger aggregate size resulted in higher electrical resistivity values. Morris et al. [18] also reported that the variability was greater on the specimens with larger maximum aggregate size. Two possible causes of this variability originate from the tortuosity effect and formation of more interfacial transition zone (ITZ) (more porous structure compared to bulk cement paste) for smaller aggregate/particle size. Therefore, variation in aggregate content and size should be taken into account when comparing the resistivity values of different concretes.

As reported in the Sengul study [4], aggregate type also affected the electrical resistivity of concrete. For electrical resistivity measurements, comparison between the crushed limestone aggregate and gravel showed higher values when crushed limestone was used [4]. Gravel was rounded shaped aggregates with smooth surface whereas the limestone aggregates have rough surface texture. Therefore, using rounded aggregates such as gravel results in poor bonding between gravel and cement paste which may also be a reason behind the variations in resistivity readings. In addition, tortuosity can be higher for crushed stone aggregates due to the rough surface texture and irregular particle shape, which, in turn, may reduce the rate of electrical flow and affect resistivity [4]. Comparable standard deviation values were also observed when different aggregate type was used with the same maximum aggregate size [18]. Furthermore, using granite as coarse aggregate with fly ash also resulted in higher resistivity measurements than the mixture containing limestone aggregate type [44]. Hence, the effects of aggregate type should not be ignored during resistivity measurements.

5.1.3. Effect of Curing Conditions. The resistivity evolution of concrete is affected by the curing regimes [48]. Two key elements influence this variation in resistivity: the degree of hydration of the cementitious material and the degree of saturation of the specimen. The numerical study performed by Weiss et al. [70] attempted to simulate a mortar with a water to cement ratio of 0.42 with three curing conditions: (a) sealed during curing and testing, (b) sealed during curing and saturated during testing, and (c) saturated during curing and testing. It was concluded that the specimen that was sealed during both curing and testing had the highest resistivity whereas the sample that was sealed during curing and saturated at the time of testing had the lower most resistivity [70]. This difference can be explained by the saturation degree of the sample. The results recommend that storing a sample underwater in the lab may cause a remarkably different degree of hydration than what may occur in a field structure. The sample that was continually saturated and the sample that was sealed and saturated at the time of testing had a similar resistivity for the same degree of hydration; however, the continually saturated sample had a higher degree of hydration at the same age [70]. For specimens cured under saturated lime water, it has also been hypothesized that

the volume of solution in which samples are stored can affect resistivity measurements due to possible pore solution concentration or dilution via leaching [43, 70]. According to AASHTO TP 95-11 [3], for the samples cured in a lime-water tank, the average resistivity value needs to be multiplied by 1.1 while this coefficient is 1 for the specimens stored in a 100% relative humidity moist room. For a given water-cement ratio, it was observed that better curing procedure yielded higher electrical resistivity [49]. For both wet and dry curing conditions experimented in the study [8], the resistivity distinctly increased with increasing age. Sample storage and curing conditions are important, as they can influence the degree of hydration, the degree of saturation, and the pore structure and solution through leaching [43]. Differences in resistivity can develop as a result of sample storage conditions and wetting the specimens prior to the resistivity measurements is recommended.

5.2. Factors Affecting the Electrical Resistivity Measurements

5.2.1. Presence of Rebar. A number of researchers have been exploring the effect of embedded rebar presence on concrete electrical resistivity through experimental and numerical investigation. Theoretically, electrical current fluxes take pathways having the least amount of resistivity and when there is embedded rebar in concrete, the current field is distorted. However, the alternation in current field is dependent on many factors such as orientation of rebar with respect to the probe, rebar diameter and spacing, and depth at which it is located [17, 23, 71].

Millard [71] and Gowers and Millard [17] utilized an experimental setup with steel rebar in the tanks filled with conductive medium solution and its finite element modeling in order to study the effects of concrete cover thickness as well as rebar diameter and spacing on concrete resistivity using four-point Wenner probe. According to this study, distance between the probe and embedded rebar was found to be the main influential parameter when measurements were taken on top of the bar. It was also reported that rebar diameter is not impactful in its disturbance. Moreover, it was found that measurement errors were increased by reducing rebar spacing while measurements are taken between two parallel rebars. However, it should be noted that results were obtained from measurements on the conductive solution tank and not from real concrete block. Similar study of resistivity measurements utilizing Wenner probe on concrete block with embedded steel reinforcement showed that orienting the probe perpendicular to reinforcements significantly reduced their influence on resistivity measurements [23]. It is more common in reinforced concrete structures that rebars are available in both directions and electrically linked together but, in the tested concrete block, no lateral rebars were present which then may have different effects on measured resistivity.

Practical general guidelines were developed by Polder's work [7] from summarizing literature for the RILEM TC 154 [14] technical recommendation for taking resistivity measurement on concrete. It was identified that placing all four electrodes over an embedded rebar at 10 or 20 mm depth can result in errors by a magnitude of two to six times that

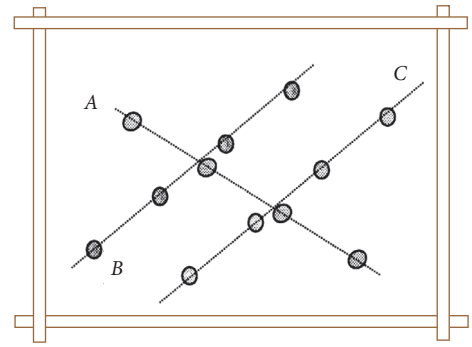

Figure 3: Resistivity using four electrodes at various spots in the same area to minimize influence of rebars [7].

of true resistivity and even if one of the four electrodes was near a rebar, results will lead to errors. Because of lack of research on resistivity measurements over rebar meshes, it was recommended that resistivity measurement with Wenner probe are taken in diagonal alignments on the concrete surface (Figure 3). Five measurements, each a few millimetres in distance from one another, and taking the median of them, are also suggested for collecting the resistivity value of the interested area. However, no recommendations were made for the case where it is not possible to fit all four electrodes inside the mesh unit created by the rebars. In addition, the recommended scheme in this study was not supported by any experimental and numerical works.

Another similar experimental investigation, done by Sengul and Gjorv [8], studied the effects of different parameters on concrete resistivity measurement using Wenner probe setup due to rebar presence. The study included the effective parameters: cover thickness, probe measurement directions relative to embedded rebar, electrode spacing, and probe measurement distance away from the embedded rebar. In total, five different probe positions with respect to the location of embedded steel reinforcement were considered, where four of these configurations were parallel to the rebar and the last one was perpendicular (Figure 4). Similar to Weydert and Gehlen's study [23], only a single rebar was positioned in the slab and two different thicknesses of 50 mm and 70 mm were studied. Their findings similar to the previous works stated that placing the probe orthogonally to the rebar did not influence the resistivity measurements, although significant errors were obtained once measurements were taken directly above and parallel to the rebar. It was also suggested that all measurements should be captured as far away as possible from embedded steel to reduce errors and if it is not possible due to dense reinforcement configuration, then space between electrodes should be kept relatively small. As only one rebar was placed in the tested concrete block as well as a small slab size was being used, this possibly contributed to errors due to edge effect. Hence, it may be difficult to extrapolate these conclusions to real cases.

Presuel-Moreno et al. [24, 72] have recently attempted to numerically and experimentally understand the influences of the number and configuration of embedded steel reinforcement along with the location and angle of the Wenner

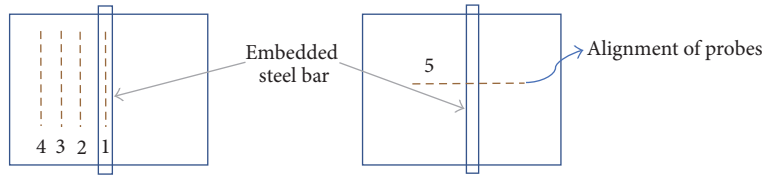

Figure 4: Five Wenner probe configurations with respect to embedded rebar tested by Sengul and Gjorv [8].

probe with respect to rebar alignment on concrete resistivity measurements. One of the few studies considered the effect of rebar mesh as well as orientation of the Wenner probe and demonstrated the difference between data achieved once there is a rebar mesh rather than a single rebar. Overall, six and five different orientations were investigated for the presence of a single rebar and rebar mesh, respectively. Like previous studies, it is also recommended to take the measurements perpendicular to the rebar location. However, the performance of Wenner probe due to variation in rebar spacing, cover thickness, or location and orientation of the probe with respect to the rebar mesh was not considered in this study.

Salehi et al. [9, 73] numerically characterized the effects of different concrete and slab thicknesses, rebar diameter, and probe arrangements with respect to the rebar mesh and rebar mesh densities on concrete electrical resistivity measurements with rebar presence using the four-point Wenner probe technique. It was concluded that the smallest error will result while setting up the probe parallel to the top rebar within the rebar mesh and perpendicular to bottommost rebar during measurements taken, as illustrated in Figure 5. It was also found that the observed resistivity decreased once the rebar mesh densities increased and the rebar diameter effect on concrete resistivity measurements can be neglected, although the numerical study results were not validated by experimental investigation.

For cylindrical concrete specimens with a single embedded steel rebar, study conducted by Chen et al. [25] suggests a correction factor to be applied to resistivity measurements corresponding to the ratio of specimen length to electrode spacing as well as the ratio of specimen diameter to electrode spacing. It was stated that no correction factor for prismatic specimens was necessary with the possibility that the applied current did not pass through the reinforcement. This research also lacked a discussion on the use of a multiple rebar and consideration of larger concrete specimens.

The effect of rebar presence on mortar electrical resistivity conducted by the four-point Wenner method was also investigated numerically and experimentally by Garzon et al. [26] and Lim et al. [27]. In Garzon et al.'s experimental study, small scaled cylindrical and prismatic specimens were casted. As polarization will happen due to double layer at the steel and concrete interface acting as a resistance-capacitor, resistivity measurements taken directly above rebar will result in errors. Hence, a rebar factor was suggested to be applied to the obtained resistivity results. In addition, modified Wenner equations are recommended for various geometric parameters [26]. Only reinforced cylindrical and

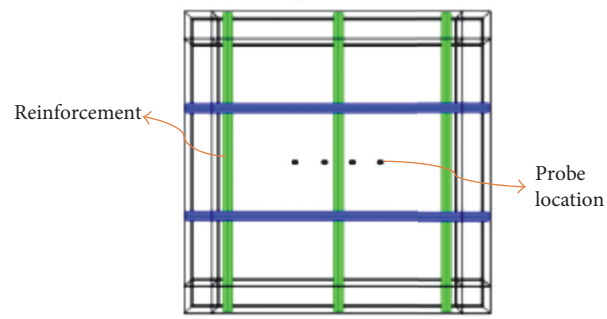

Figure 5: Probe configuration with respect to rebar mesh suggested to reduce electrical resistivity measurement error [9].

prismatic specimens were included in the experimental setup without considering a reinforced slab. However, in a numerical study, a slab with embedded rebar was considered [26]. The experimental investigation lacked in using concrete mixture instead of a mortar mixture which is not exactly representative of real-world cases and may lead to more errors. Furthermore, the proposed rebar factor may not be applicable to a large concrete slab with multiple rebar because their experimental conclusions are based on laboratory testing. Lim et al. [27] also studied the effects of cover depth, electrode spacing, rebar diameter, and the resistivity of concrete and reinforcement in the numerical model. However, only one probe configuration taken right above and parallel to rebar was considered. It was suggested to apply a geometric effect rate that ranges from 0 to 1 in order to estimate the reinforcement geometry impact and this rate is derived utilizing a resistivity estimation model. The geometric effect rate was also validated through the experimental investigation for on-site measurements. Based on experimental findings, it was stated that the geometric effect rate decreased with increasing concrete cover thickness and increased with increasing rebar diameter and increasing electrode spacing. Again, using mortar mixture, only one single rebar, and a single probe configuration with respect to rebar is not completely representative of real-world conditions. An error to resistivity measurements may also be introduced while the epoxy coating on the mortar specimens was used in this study due to a barrier between the electrodes and mortar surface.

The last and recent study in this category belongs to Sanchez et al. [74] who numerically proposed a modified 4-point Wenner method based on the experimental data, deployed on a bridge over the River Danube in Romania.

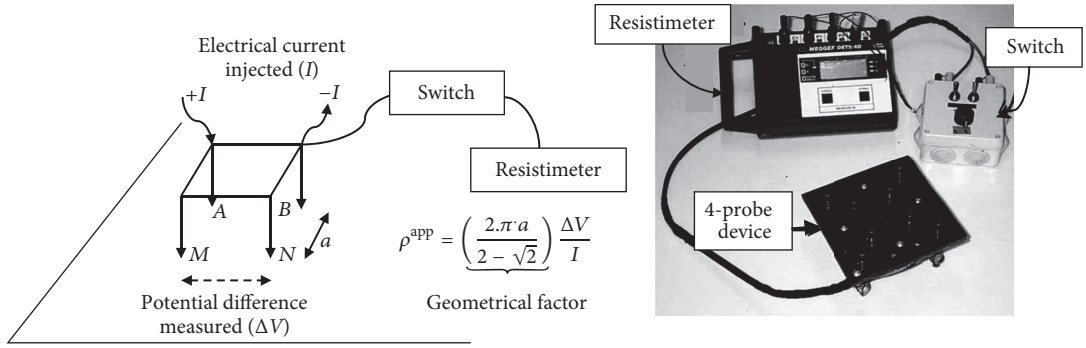

Figure 6: Four-probe square array principle [10].

In this study, a "rebar factor," f_b, was introduced through the modified version of Wenner method to measure the resistivity in reinforced concrete structures with thin concrete covers. Effect of rebar presence on concrete electrical resistivity measurements also can be found in detail in similar studies by [17, 28, 29, 65, 75].

5.2.2. Presence of Cracks in the Concrete Cover. Due to the presence of cracks, apart from embedded rebar, the electrical resistivity measurements may vary using Wenner probe technique because it is initially assumed that concrete is homogeneous and isotropic with semi-infinite geometry. In this section, some researchers' investigations in order to characterize cracks in concrete conducted by electrical resistivity measurements are summarized.

Lataste et al. [10] attempt to identify and locate cracks and spalling in concrete by means of electrical resistivity. For this a utilized instrument was built to measure the electrical resistivity through the use of four electrodes in a square configuration, rather than linearly conventional Wenner probe arrangement (Figure 6). The specified built probe allows taking the measurements in two orthogonal directions without having to rotate the probe between measurements. To change the function of electrodes from current imposing to potential measurement, the use of an electrical switch was considered. Both on-site measurements on a reinforced concrete slab and laboratory measurements on a cracked reinforced concrete beam were experimentally studied. To observe the effects of crack characteristics, such as crack opening and bridging degree between crack lips and depth of crack, a numerical model was developed as well and validated experimentally. It was reported that when a conductive crack was present, depending on the direction of imposed electrical current, resistivity readings could overestimate or underestimate the true resistivity. Once current was orthogonally imposed to the crack, no impact was detected; however, reduction in electrical resistivity measurements was observed while the crack was parallel to the imposed electrical current. For an insulated crack, perpendicular readings overestimated resistivity, and parallel measurements underestimated it. It was also concluded that crack depth has a direct relation to the electrical resistivity measurements (increase in crack depth leads to increase in the resistivity measurements).

A couple of assumptions and conclusions in Lataste et al.'s work [10] may not be adaptable with reality. First, it was assumed that the rebar effect on the resistivity measurements is independent of crack depth or type which might not be true for the cases that rebar mesh or conductive crack present. Second, simulations on limited size concrete block can possibly exaggerate the crack impact. Finally, the four-electrode square configuration, which is a less common electrode setup compared to the Wenner probe array, may generate different measurement errors.

Goueygou et al. [30] used the same square probe configuration proposed in Lataste et al.'s work [10] to compare electrical resistivity measurements with transmission of ultrasonic waves for characterizing, detecting, and localizing the surface cracks. For taking measurements in both directions (parallel and perpendicular), concrete beam specimens bent via three-point loading to induce one main crack were constructed. Both nondestructive techniques were capable of identifying the main simple crack inside the concrete specimens; however, complexity rose when the number of cracks increased and in most cases became impossible to detect cracks depth and patterns. Similarly, experimental and numerical investigations in detecting and characterizing cracks using electrical resistivity measurements with a square probe were done by Shah and Ribakov [76]. In their study, two experimental setups including a set of five cubic laboratory concrete specimens and a small area on a 40-year-old reinforced concrete slab as well as numerical model to identify the crack depth and differentiating insulated and conductive cracks were involved. Overall, it was observed that higher resistivity values were obtained from insulative cracks while lower values resulted from conductive ones. From field data and numerical work, variations on electrical resistivity measurements were observed for different crack depth and opening [76].

Experimental study conducted by Wiwattanachang and Giao [11] also investigated the capability of concrete electrical resistivity measurements with Wenner probe method in detecting a crack development in the concrete beams. Artificial cracks made up of plastic sheet inside a concrete beam to simulate insulated cracks as well as cracks being induced in a beam by a four-step loading test on its tension face were studied in this work. After correcting resistivity

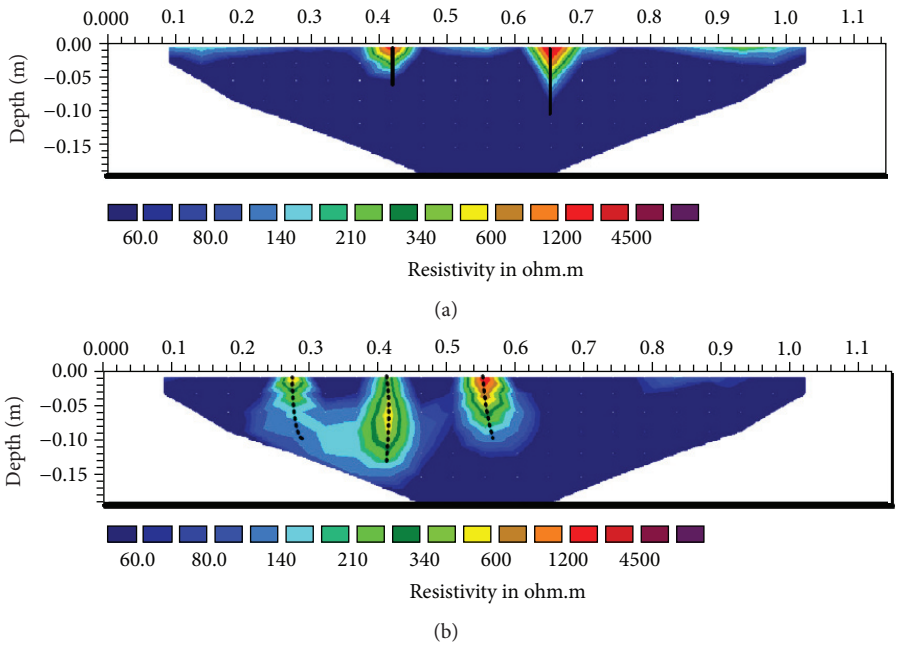

Figure 7: Electrical resistivity image of a concrete beam with cracks [11]: (a) concrete beam with artificial plastic sheets as crack; (b) concrete with cracks being developed from a four-point loading.

readings for the specimens' geometry, it was concluded that obtained data were increased for both crack types; although only insulated cracks were examined, conductive cracks were not. Simulated images of electrical resistivity were plotted from obtained results, as demonstrated in Figure 7. Although using electrical resistivity measurements for detecting cracks inside concrete was explored in the study, investigations on different type of cracks and their orientations toward the probe were ignored.

It was also numerically found that when cracking and delamination were present in reinforced concrete structures, electrical resistivity measurements were different from when they were not present [77]. Similar to previous studies, this finding gave rise to the conclusion that delamination at early stages can be detected using resistivity measurements with 21 linearly aligned electrodes instead of four-point Wenner method. However, proposed model in Chouteau and Beaulieu [77] only identified the effect on resistivity measurements as being different when cracking was present. In addition, to evaluate and detect cracks and discontinuities, such as joints, in massive concrete structures within preexisting boreholes, electrical resistivity measurements with a DC current was stated to be a good quality assessment indicator [78]; however, using a DC current rather than AC current may result in unfavorable results due to polarization effect which was not considered in Taillet et al. [78].

A comprehensive numerical study by Salehi et al. [79] on the effect of different cracks types, depths, and widths incorporating both the presence of cracks and rebar mesh indicated that measurements on conductive cracks result in lower electrical resistivity values. For conductive cracks, numerical results showed that decreasing crack depth did not significantly disturb the electrical resistivity measurements. Furthermore, for an insulated crack between two inner electrodes, electrical resistivity readings led to a maximum error of about 200% higher than actual concrete resistivity. Conductive crack in here represents as a crack filled with water and insulated one denotes a crack without bridging and filled with air. It was also concluded that once the crack depth decreased, lower errors were observed. Also, the rebar and crack were found to act independently of one another while rebar mesh was present. Salehi et al.'s work lacked validating numerical investigation with an experimental study. Following this study, Morales [75] experimentally investigated the effect of rebar, chloride ingress, corrosion, and various crack types on concrete electrical resistivity measurements. For all moisture conditions, it was suggested that discrete cracks of all depth and conductivity properties should be avoided in order to minimize potential errors when performing resistivity measurements. Although it was observed that electrical resistivity measurements were not significantly affected by surficial microcracking, it may be able to identify delamination as the difference observed between measured resistivity of in-tact and delaminated concrete covers. Still, investigations on the effects of cracking induced by corrosion and insulated and conductive cracks with bridging conducting electrical resistivity measurements lacked in this study.

5.2.3. Probe Spacing. Concrete is considered to be a heterogenous material and this is one of the assumptions behind the Wenner probe method. However, this assumption appears to be a likely source of error since aggregates inside concrete typically have greater resistivity and they propagated widely in different locations with various sizes. Hence, this inconsistency in the initial assumption of concrete homogeneity may

affect resistivity measurements. To mitigate this issue, some researchers recommended considering enough wide space between electrodes (usually between 20 mm and 70 mm) in order to reduce the influence of nonhomogeneity due to the aggregates presence [8, 18, 71]. It was suggested to take several readings at various locations and then these measurements should be averaged. Many commercial instruments are also equipped with a variable probe spacing as well to allow the device to measure concrete resistivity involving larger aggregate size.

One recommendation to help reduce variance in resistivity measurements is to consider probe spacing 1.5 times higher than the maximum aggregate size [17]. It was observed that when probe spacing became smaller than the maximum aggregate size, standard deviation in the measurements increased to around 10% (Figure 8) [17]. For various probe spacing (16 mm, 25 mm, and 50 mm), Millard [71] experimentally found that as the maximum aggregate size became closer to the probe spacing, the scattering in the observed results increased. Therefore, to compensate for the local effect of aggregates, larger electrode spacing should be considered for practical purposes. For concrete cubes (100 × 100 × 100 mm), while the electrode spacing was changed in different steps from 20 to 35 mm, the relative resistivity measurements increased by approximately 70% [37]. Increasing electrode spacing also resulted in increasing resistivity values to even a greater extent than that in the cubes for concrete cylinders [37]. Increase in resistivity observed due to wider spacing is in part also due to finite geometry and not just the aggregate size. The results of the resistivity measurements preformed on 28-day water-cured concrete slabs with and without embedded steel rebar indicated only a small difference for probe spacing less than 30 mm [8]. For larger electrode spacing, however, both the steel rebar and the probe spacing showed significant impact on the electrical resistivity measurements, and the larger the electrode spacing, the larger the effect of the steel rebar. For instance, increase in electrode spacing from 20 to 70 mm led to increase in resistivity by approximately 26% for the slab without any steel reinforcement whereas the resistivity values either increased by 33% or decreased by 25% depending on the orientation of taken measurements (perpendicular or parallel) for the slab with rebar [8].

According to Polder [7], the electrical current may travel through the concrete volume with approximately the same depth as that of the electrode spacing. Hence, as the probe spacing increases, the current flows deeper inside the concrete volume and when the electrical current reaches the surface of the rebar, the current is transported through the reinforcement and, thus, results in lower resistivity observation [8]. For prismatic specimens, it was also suggested by Chen et al. [25] that the effects by the probe spacing can be ignored when the spacing is larger than 40 mm; however, the resistivity values increased with less electrode spacing. For application of Wenner probe method, the important role of electrode spacing should be definitely considered during electrical resistivity measurements as it will affect the obtained results.

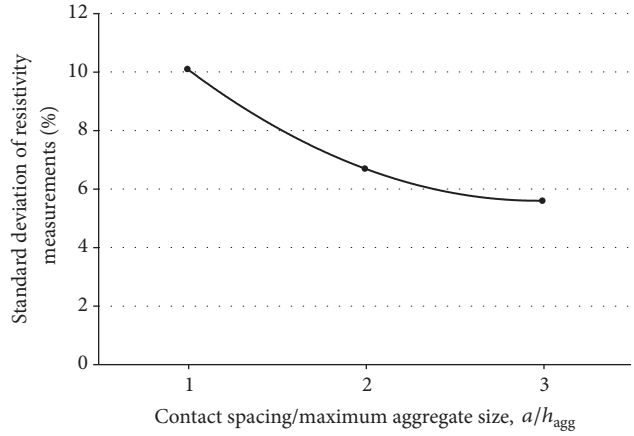

Figure 8: Effect of contact spacing on resistivity measurement [17].

5.2.4. Electrode Contact. The contact area between the electrodes and concrete surface may alter the electrical resistivity measurements using four-point Wenner probe. The experimental investigation in electrolytic tanks and finite element modeling resulted in the fact that the contact between the concrete surface and the probes has no significant influence on Wenner probe resistivity measurements [17, 71]. It was also reported a maximum error of 6% in resistivity (without stating lower or higher readings) when the diameter of electrode contact area varied from 1 mm to 40 mm [71]. According to Gowers and Millard work [17], misleading values can be lessened by use of a fairly low frequency and alternating current (AC). Practically, electrode contact area becomes vital for both external current imposing and internal potential measurement electrodes. It was observed by Ewins [80] that contact resistance between electrodes and concrete surface can lead to significant increase in electrical resistivity values. Both symmetry of the system and the probe performance as it was also confirmed in Gowers and Millard's work [17] may be affected by the contact resistance [80].

In two-electrode method (bulk resistivity measurements), poor contact between the plate electrode and the test cylinder surface is mainly responsible for electrode resistance. One solution to minimize the contact resistance effect is to use flexible electrodes [18]. Also, to mitigate this issue in laboratory testing, using an aid that allows for a good electrical contact such as an electrically conductive jelly was recommended [81, 82]. Other alternative solutions included the use of soft conductive medium, saturated sponges, chamois cloth, and paper towels [38, 83]. By using a saturated sponge, only an average of 2% difference in resistance was reported for contact resistance between the sponge and concrete surface [39]. The sponge resistance is largely dependent on the moisture content of the sponges and the conductivity of the solution in which they are saturated. It was shown that, in the two-point measurement procedure, a sponge contacting system can give a higher resistivity than those obtained using four-point techniques, and careful consideration must be given to the electrode-sample contacting system when trying to evaluate concrete resistivity [40]. According to McCarter et al.'s work [40], the sponge contacting method introduced

a misleading resistance originating from the sponge-sample interface that was in series with the bulk resistance of the sample. Therefore, an operator using an electrical resistivity device needs to ensure proper contact between the electrodes and concrete surface as poor contact may affect the electrical resistivity readings. The influence of electrode contact is less governing in the Wenner probe method than in the uniaxial method and, hence, measurements can be performed in a wider frequency range (10 Hz to 10 kHz) [6].

5.2.5. Specimen Geometry. In the four-point Wenner method, the electrical resistivity measurements are initially presumed to be performed on the domain of semi-infinite medium which is not a practically accurate assumption. This assumption leads to deviation from the ideal condition of having infinitely large geometry which can possibly occur in different electrode orientations. For relatively small size concrete elements (e.g., cylinder or prism specimens), constriction of current to flow into a different field pattern is one of the major reasons for this deviation. Even though several researchers have realized the effect of specimens' geometry, only very limited information is available on this topic.

To account for interference between current flow and coarse aggregates in a small size sample, a suggested correction coefficient factor (or geometry correction factor) has been established in Spragg et al.'s work [84], using the simulations developed by Morris et al. [18]. The correction coefficient factor proposed formula is outlined below (see (5)) and only needs to be used when $d/a \leq 6$ or $L/a \leq 6$ (where a and d are parameters related to electrode spacing and specimen diameter, resp.) [84]:

$$k = 1.10 - \frac{0.730}{d/a} + \frac{7.34}{(d/a)^2}. \quad (5)$$

For a standard cylinder size (φ100 mm × 200 mm), the correction coefficient value ranges from 1.8 to 1.9 while using the probe spacing of 38 mm [41, 84]. Also, for the correction factor (k), Morris et al. [18] plotted a graph based on the finite element modeling data to study a wide range of geometrical variations in concrete cylinders (Figure 9). However, this study provides wide-ranging values for correction factor; different electrode spacing and configuration as well as various geometrical concrete element types were not investigated (only 25.4 mm electrode spacing for concrete cylinders was considered).

According to Millard [71] and Gowers and Millard [17] through experimental findings, electrode spacing should be 1/4 times smaller than concrete section dimensions and half the distance of the contact area from any element edge due to the three-dimensional current flow restriction closer to the edge. It was also observed that when the domain of the medium becomes smaller than the ideal semi-infinite condition, overestimated resistivity values resulted. Study performed by Bryant et al. [42] found an average of 24% higher electrical resistivity values for cylindrical samples in comparison with concrete slab specimens for various ages even when the geometry correction factor was used; however, Shahroodi [85] reported an average 25.8% lower resistivity

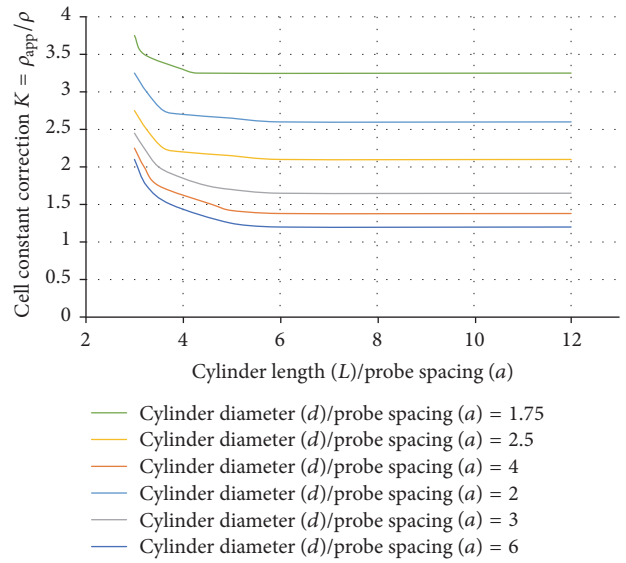

Figure 9: Cell constant correction to determine the concrete resistivity [18].

value. The differences in the mentioned values could possibly originate from variation in geometry correction coefficient, surface texture, device, operator, material, production, and curing process [86]. Measured resistivity values can also change by the geometry of the measuring plane. The variation in resistivity values observed experimentally by Chen et al. [25] on the curved surface and the cutting flat surface showed an increase with the volume of cutting portion. Therefore, correction factor should be applied accordingly, especially for large size specimen. They also confirmed that the resistivity of the cylindrical samples varied with the specimens' size even though the electrode spacing remains the same [25]. Furthermore, for the two-electrode method, since electrical current passes through the entire specimen volume, this measurement method is independent of specimen geometry while, for the four-point method, the depth of the electrical current passing through the concrete volume is related to both the geometry of the sample and the distance between the electrodes. This independency was also reported in Sengul and Gjorv's work [37] when the electrical resistivity values using both two- and four-electrode methods for concrete block of size 300 mm × 300 mm × 200 mm (semi-infinite geometry) and standard cylinder samples were almost the same.

5.2.6. Electrical Signal Shape and Frequency. Due to resistor-capacitor circuits' behaviour in saturated cementitious system, it introduces a phase difference between electrical current imposing and the measured potential (impedance) [43]. At different frequencies, there is a significant difference in impedance and it follows that the real component of the impedance at zero phase angle is the true uniaxial resistance. Since the phase is almost never zero, the meters record the total impedance: the real and imaginary components added in quadrature. The impedance spectrum consisting of

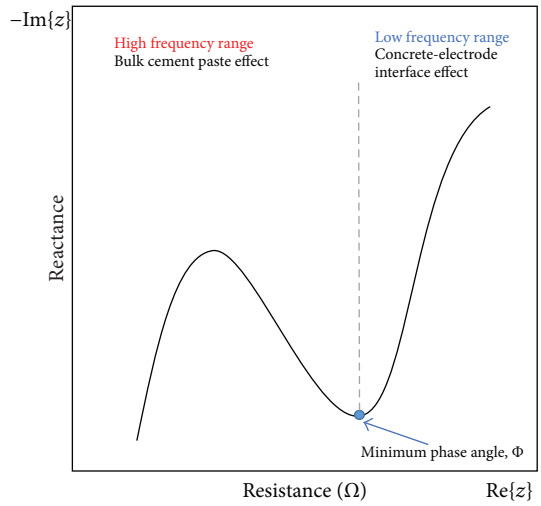

FIGURE 10: Schematic representation of the AC Impedance response of concrete [6].

two arcs in high and low frequency ranges is illustrated in Figure 10 [6]. At higher frequencies, the impedance spectrum characteristics are featured by the concrete microstructure but these characteristics are mainly attributed to the conditions at the electrode-concrete interface for low frequency domain. Generally, the frequency range in between 0.5 and 10 kHz is used for uniaxial electrical resistivity measurements method; however, no general statement can be found on the optimum frequency since it varies with moisture contents and mixture proportions. At lower frequencies (below 500 Hz), it was stated that electrical resistivity measurement can result in overestimated data because of electrode-concrete contact interface impact [6]. As it is described in Section 5.2.4, this effect is less dominant in the four-point probe method, and a wide-ranging frequency (10 Hz to 10 kHz) can be conducted [6].

Two signal shapes used usually for electrical resistivity measurements are sine-wave and square-wave AC current. Ewins [80] reported 800% error in results when high frequency (600 Hz) sinusoidal signals with poor contact were used for taking the resistivity measurements. Presence of parasitic capacitors and uneven contact resistance were the two major error sources that affected the accuracy of the measurements. However, impact from parasitic capacitors was larger. To avoid unwanted effects, using low frequency square-wave signal, instead of sine-wave, was recommended in Ewins work [80]. Similarly, it was found that sine-wave Wenner probe with 300 Hz frequency was adversely affected by the addition of external resistors compared to the case for which square-wave Wenner probe was used or frequency of the sine-wave signal was reduced [71]. The external resistors were used to mimic the unbalanced contact area resistance. Having unbalanced contact resistor in the voltage measurement circuit has the most significant effect on the accuracy of four-point probe method while high frequency sinusoidal AC signal is being used.

5.2.7. Effect of Temperature. Temperature variation has been reported to have a significant influence on electrical resistivity of concrete, and an increase in temperature results in a decrease in resistivity. Electrical current generally flows through the ions dissolved in the pore solution and can be affected by temperature which causes changing the ion (Na^+, K^+, Ca^{2+}, $SO_4{}^{2-}$, and OH^-) mobility and ion-ion and ion-solid interactions, as well as the ion concentration in porous media [7, 87, 88]. It was reported that the effect of temperature on bulk pore solution resistivity was noticeably different from that of cement paste or mortar with the same ion concentration, which was most likely because of strong ion-solid interactions in cement paste or mortar and less internal ionic frictions [17]. Increase in temperature has an impact on concrete isotherm curves and also tends to reduce the moisture content of concrete which indirectly affects the resistivity readings [89]. So, temperature plays an important role in concrete electrical resistivity and a number of researchers attempted to correlate its effect with true concrete resistivity values. It should be noted that not all studies performed the resistivity measurements for the different temperatures at the same moisture content. If not saturated (i.e., immersed), the concrete needs to be left for a long enough time at a given temperature and moisture. Castellote et al. [87] as well as Liu and Presuel-Moreno [41] have attempted to produce equations to convert from one temperature to a normalized temperature.

Studies conducted by Millard et al. [90] and Gowers and Millard [17] found that decrease in ambient temperature led to increase in resistivity values and suggested a correction factor of 0.33 KΩ-cm/°C in order to compensate for the variation in temperature; however, the range of temperatures used in their studies was limited. For simplicity, a change of 3% to 5% on resistivity measurements per °C has been recommended for temperature range of 0°C to 40°C [7, 67]. A linear relationship has been developed on temperature dependency of resistivity [45, 88, 91]:

$$\rho = \rho_0 \left(1 + \alpha \cdot \Delta T\right), \tag{6}$$

where ρ is resistivity at temperature T (°C), ρ_0 is resistivity at reference temperature T_0, ΔT is temperature difference between T and T_0 and α is temperature coefficient (between 0.022 and 0.035/°C).

It was found that the above equation is only applicable over a limited interval of ±5°C to the reference temperature [45, 88, 91]. A model developed in DuraCrete [92] also describes the correlation between ρ_T at temperature T (°C) and resistivity ρ_{20} at 20°C:

$$\rho_T = K_T \cdot \rho_{20}, \tag{7}$$

where K_T is characteristic value of the temperature factor for resistivity and K_T is defined as

$$K_T = \frac{1}{1 + K\left(T - 20\right)}, \tag{8}$$

where $K = 0.025$ when $T < 20$°C and $K = 0.073$ when $T > 20$°C.

Several researchers also defined a wide agreement for this correlation using Arrhenius law [41, 45, 87, 88, 91, 93]:

$$\rho_T = \rho_0 \cdot \exp\left[\frac{E_{a,\rho}}{R}\left(\frac{1}{T} - \frac{1}{T_0}\right)\right], \quad (9)$$

where ρ is resistivity at temperature T (K), ρ_0 is resistivity at reference temperature T_0 (K), R is gas constant ($8.314\,\mathrm{kJ^{-1}mol^{-1}}$), and $E_{a,\rho}$ is activation energy for resistivity (J/mol) (ranges from 16.9 J/mol to 42.77 J/mol).

The activation energy of conduction ($E_{a,\rho}$) can be determined using the slope of a plot of the natural logarithm of resistivity and the inverse of temperature [43]. The slope of the best-fit line is multiplied by the negative of the universal gas constant [$8.314\,\mathrm{kJ^{-1}mol^{-1}}$] to determine the activation energy of conduction. The above-mentioned correlation is published using only standard cylinder samples ($\varphi 100 \times 200$ mm) and additional work is still needed for real-world resistivity measurements and also to consider the influence generated by moisture content as an additional factor. For standard curing conditions in water at 20°C, it was suggested that the effect of temperature can be eliminated [4]. Spragg et al. [43] stated that the resistivity measured using the same mature sample can differ by as much as 80% when the temperature of the sample fluctuates between 10°C and 45°C. Additionally, several other studies showed in detail a prominent effect on resistivity results due to temperature variation [46, 47, 51, 52]. In summary, when the temperature increases, electrons move faster causing higher electrical conductivity, thus lowering resistivity.

5.2.8. Effect of Moisture Content. Moisture content is one of the influencing factors that can inversely affect the concrete electrical resistivity measurements. Essentially, electrical conductivity increases with an increase in moisture content due to change in the ion mobility [41, 94]; however, there could be a difference in resistivity between immersed samples (either water or lime water) and those in high humidity. Larsen et al. [94] found that when moisture degree decreases from 88% to 77%, the resistivity increases by an average of two times and from 88% to 66% it increases by an average of 6 times. In the air-dry state, it was also reported that concrete had approximately 50% higher resistivity than that in saturated condition [4]. As the electrical current is carried by ion flowing through the pore solution in concrete, higher moisture content leads to easier electrical flow and thus the electrical resistivity reduced. However, at low resistivity values, moisture content has less effect on the accuracy of the resistivity measurements [46]. For quality control purposes, it is essential to ensure that the same moisture degree in different mixtures and also the resistivity measurements of the specimens with low moisture content are inappropriate [25]. Furthermore, it was experimentally found that poor surface saturation using pressurized water and static ponding can lead to misinterpretation of resistivity of over 30% compared to full laboratory saturation [86]. So, additional research is still required to simulate the on-site saturation by different systems and to understand how much time is required for water to penetrate through concrete surface in order to obtain constant moisture level through the bulk specimen.

6. Correlation between Concrete Resistivity and Its Durability Characteristics

Through following sections, relationship between electrical resistivity and the two main concrete durability characteristics including chloride ingress and corrosion of embedded reinforcements will be presented.

6.1. Correlation between Electrical Resistivity and Chloride Diffusivity. Diffusivity is the controlling parameter which determines the time it takes for chloride ions to diffuse into concrete and reach the critical chloride threshold for corrosion initiation. Typically, this can be measured through Rapid Chloride Migration (RCM) test, Rapid Chloride Permeability Test (RCPT), or Bulk Diffusion (BD) method [95]. However, such test methods are either time-consuming or expensive for evaluating the concrete permeability properties. Hence, electrical resistivity was found experimentally and theoretically to be an efficient method that can be applied indirectly to determine concrete chloride permeability.

In theory, the relationship between diffusivity of ion species i and its partial conductivity can be described by Nernst-Einstein equation [96]:

$$D_i = \frac{RT\sigma_i}{Z_i^2 F^2 C_i}, \quad (10)$$

where D_i is the diffusivity of ion i ($\mathrm{m^2/s}$); σ_i is the partial conductivity of ion i (s/m); R is the gas constant (8,314 J/mol); T is absolute temperature (K); Z_i is the charge of ion i; F is Faraday's constant (96500 Coulombs/mole); and C_i is the concentration of ion i ($\mathrm{mol/m^2}$). By applying Archie's law, the correlation between the bulk resistivity, pore solution resistivity, and porosity can be expressed by the following [37, 97]:

$$F = \frac{\rho}{\rho_0} = \frac{\sigma_0}{\sigma} = a \cdot \varphi^{-m}, \quad (11)$$

where F is formation factor; a and m are constants; and φ is porosity of concrete. m is dependent on tortuosity of concrete and has been found to be 1.5 to 3.2 [37, 97]. Combining the above equations gives the formation factor as a function of effective chloride diffusion coefficient of concrete (D_{eff}) and chloride ion diffusion coefficient in the pore solution (D_0):

$$F = \frac{D_0}{D_{\mathrm{eff}}}. \quad (12)$$

Several researchers have also conducted various experiments to investigate the relationship between concrete resistivity and chloride diffusivity. A strong correlation between these two parameters has been reported for various concrete mixtures at different ages [4, 42, 47, 50–52]. Due to presence of chloride, experimental results showed that the electrical resistivity of mortar was reduced [17]. The concrete resistivity was inversely related to chloride ingress, where lower

Table 5: Classification of concrete permeability to surface resistivity values.

Chloride ion permeability	RCP test versus surface resistivity				
		Surface Resistivity Test			
	RCP test charged passed (Coulombs)	4 × 8 cylinder (kΩ-cm) $a = 1.5$ $k = 1.8$ (measured)	6 × 12 cylinder (kΩ-cm) $a = 1.5$ $k = 1.8$ (measured)	Semi-infinite slab (real)	KDOT 4 × 8 cylinder (kΩ-cm) $a = 1.5$ $k = 1.8$ (measured)
High	>4000	<12	<9.5	<6.7	<7.0
Moderate	2000–4000	12–21	9.5–16.5	6.7–11.7	7.0–13.0
Low	1000–2000	21–37	16.5–29	11.7–20.6	13.0–24.3
Very low	100–1000	37–254	29–199	20.6–141.1	24.3–191
Negligible	<100	>254	>199	>141.1	>191

resistivity indicated the area where chloride penetration will be faster [7]; however, its effect on electrical resistivity readings is relatively small compared to carbonation process [7, 50]. Recent field experience indicated that the relationship between surface resistivity at 28 days and 56 days with RCP data was moderate [53]. Experimental investigation by Florida Department of Transportation (FDOT) on wet cured concrete specimens in a controlled environment or cured samples in lime water, using RCP test and 4-point Wenner method in conjunction, confirmed the inverse correlation of chloride resistivity [98, 99]. The summary of FDOT proposed relationship between resistivity and chloride can be found in Table 5. The table also shows an indication of the risk of chloride penetrability with regard to charge passed based on ASTM C1202 standard [100]. In RCP test, a 60 V potential is applied across the sample of 95 mm diameter and 50 mm thickness for 6 hours. Current readings are taken every 30 minutes, at minimum, and then the total charge passed in Coulombs is calculated by integrating the Current versus Time graph developed from the readings taken.

Similar experimental investigation conducted by the Louisiana Transportation Research Center (LTRC) also found a good correlation between resistivity and RCP test while the classified concrete permeability to surface resistivity values are equal to those proposed by FDOT as shown in Table 5 [31]. Following these experimental investigations, AASHTO published a provisional method TP 95-11 for indicating the concrete's ability to resist chloride ion penetration using surface resistivity measurement method [3]. However, Kansas Department of Transportation (KDOT) reported different value range for surface resistivity [54]. For instance, it is considered that chloride penetration is high when surface resistivity value is less than 7.0 kΩ-cm for 4 × 8 cylinder with 1.5-inch probe spacing which is a relatively small value compared to two other experimental results (Table 5) [54].

In addition to the experimental study on laboratory specimens, the correlation between electrical resistivity and apparent diffusivity coefficients (D_{app}) is reported by researchers for field specimens [53, 55]. Due to complexity of the exposure environments such as humidity difference, temperature, and the elevation from water level, results are scattered. However, a recent investigation on Florida bridges showed a better correlation between resistivity and apparent diffusivity once resistivity was measured under saturated condition [65]. The authors of this paper are currently involved in a study where the effect of full or partial saturation is being studied. To predict chloride threshold (Cl_{TH}) values, the electrical resistivity method was used periodically during 1000-day monitoring of reinforced concrete element exposure to marine environment [28]. After applying the geometrical factor, the relationship between chloride content, in terms of chlorides relative to the weight of cement, and resistivity (ρ) can be expressed as shown in the following [28]:

$$Cl_{TH}\,(\%) = 0.019\rho + 0.401. \tag{13}$$

A good correlation between RCM coefficients and electrical resistivity measured by two-electrode method was reported in European Union-Brite EuRam III experimental investigation [92]. Similarly, this correlation for resistivity measured by Wenner method is reported in Dhir et al.'s work [101]. Although resistivity measurements can be possibly a good alternative or replacement for the RCM test, more experiments need to be conducted to validate this correlation. The electrical resistivity test was suggested to be used as a quality control predictor of the chloride ingress resistance, but not as a predictor of diffusion behaviour of all kinds of concretes or as replacement of the long-term diffusion tests [56]. FDOT long-term monitoring of various concretes concluded that correlation between the RCM and the long-term tests was equal to or slightly better than those obtained by the RCP and surface resistivity due to less sensitivity of RCM test to presence of supplementary cementitious materials [102]. A linear trend exists between chloride diffusion coefficient (D_{RCM}) derived by RCM test and concrete electrical conductivity using two-electrode resistivity measurements [33, 46, 57, 58]. Additionally, to account for the retardation of chloride penetration due to the chloride reaction or binding with the cement phases, a factor needs to be applied to electrical resistivity measurements [59]. A reaction factor (r_{cl}) is defined as the ratio between the diffusion coefficients D_{app} and D_{eff} assuming lineal chloride binding

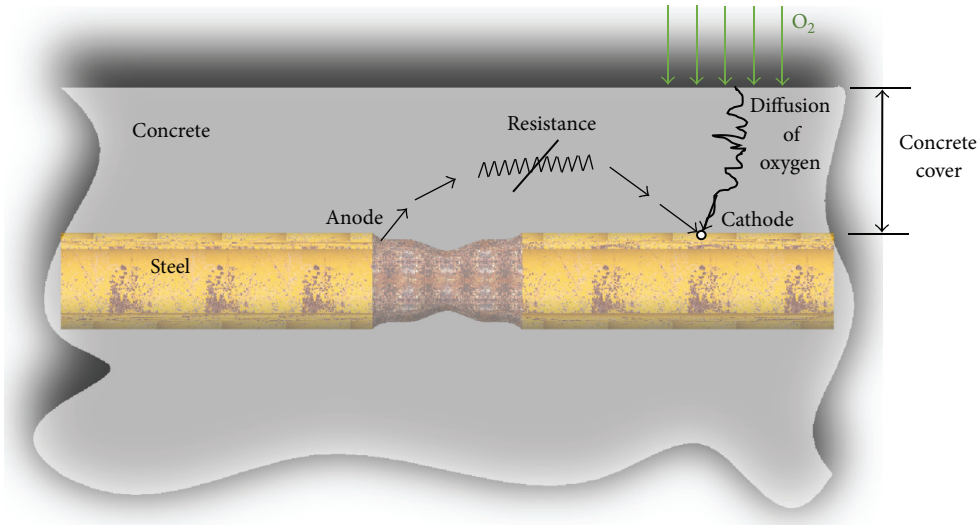

Figure 11: Schematic descriptions of factors which may affect corrosion rate of steel in concrete: (i) O_2 availability and (ii) electrical resistance of concrete (reproduced from [19]).

as shown in (14) where ρ_{app} and ρ_{eff} are apparent and effective electrical resistivity [59]:

$$r_{cl} = \frac{D_{eff}}{D_{app} \cdot \varphi} = \frac{\rho_{app}}{\rho_{eff}}. \quad (14)$$

6.2. Correlation between Electrical Resistivity and Reinforcement Corrosion. Once rebar is depassivated and corrosion is initiated by chloride ions or carbonation, corrosion rate will be the most influential parameter that determines how fast the reinforced concrete structure is deteriorating. It is dependent on many parameters including oxygen availability, ratio of anodic/cathodic area, relative humidity (RH), and concrete electrical resistivity (Figure 11) [19]. When enough oxygen is available to supply the anodic current especially under aerated state (such as the splashing area zone), cathodic control no longer exists. In this condition, the corrosion rate can be limited by controlling the flow of ionic current through concrete which is directly related to electrical resistivity of concrete [19]. Therefore, several researchers have attempted to correlate the corrosion probability and corrosion rate to concrete electrical resistivity [60, 103–108].

Among all the studies conducted so far, there is an agreement that corrosive environment in reinforced concrete and electrical resistivity of concrete have an inverse relationship. As the electrical resistivity of concrete decreases, the rate of steel reinforcement corrosion increases. A theory by Glass et al. [103] stated that the corrosion rate of reinforced concrete is under anodic control with the anodic reaction being limited by the mortar resistivity. Glass's anodic resistance theory is also supported by studies conducted by Morris et al. [60] and Bertolini and Polder [104]. In their investigations, it has been found that concrete resistivity affected not only corrosion rate, but also the corrosion potential [60, 104]. The only standardized test method for corrosion monitoring is the ASTM C876 half-cell potential mapping technique [105]. Hence, electrical resistivity measurements can be an effective standard indicator of steel reinforcement corrosion potential and rate.

Combining both half-cell potential and electrical resistivity measurements techniques makes it possible to examine corrosion probability and corrosion rate once it is initiated [106]. For high resistivity values, Carino [106] stated that even if the embedded rebar in concrete is actively corroding, detected by half-cell potential technique, the corrosion rate may be slow when steel rebar depassivates; thus the concrete electrical resistivity has better correlation with corrosion rate than half-cell potential. Experimental investigation on reinforced concrete specimens immersed in saline solution came to the conclusion that steel rebar is likely to reach a corrosion state while resistivity readings are lower than 10 kΩ·cm and reach a passive state when resistivity measurements are higher than 30 kΩ·cm [60]. The results also showed that the risk for chloride-induced corrosion and the chloride threshold value that will initiate the corrosion process can be estimated via a straightforward and nondestructive technique like concrete resistivity [28]. For various concrete mixture types, Polder and Peelen [50] indicated the corrosion initiation with respect to electrical resistivity under simulated deicing salt, but no relationship or effect was established. Similarly, Basheer et al. [57] and Smith et al. [46] used both electrical resistivity measurements and half-cell potential to evaluate the probability of corrosion in embedded steel rebar but, then again, no correlation was developed. It was also confirmed that corrosion potential can be detected by means of electrical resistivity but it was not specifically indicated how this can be done [107]. In addition, using the electrical resistivity or half-cell potential measurements was suggested to evaluate the deterioration caused by corrosion in the experimental study preformed on a concrete bridge deck [108]. In this study, it was stated that having no need of electrical connection to embedded rebar is the main advantage of electrical resistivity over half-cell potential technique. The effect of concrete cover as an influential parameter on

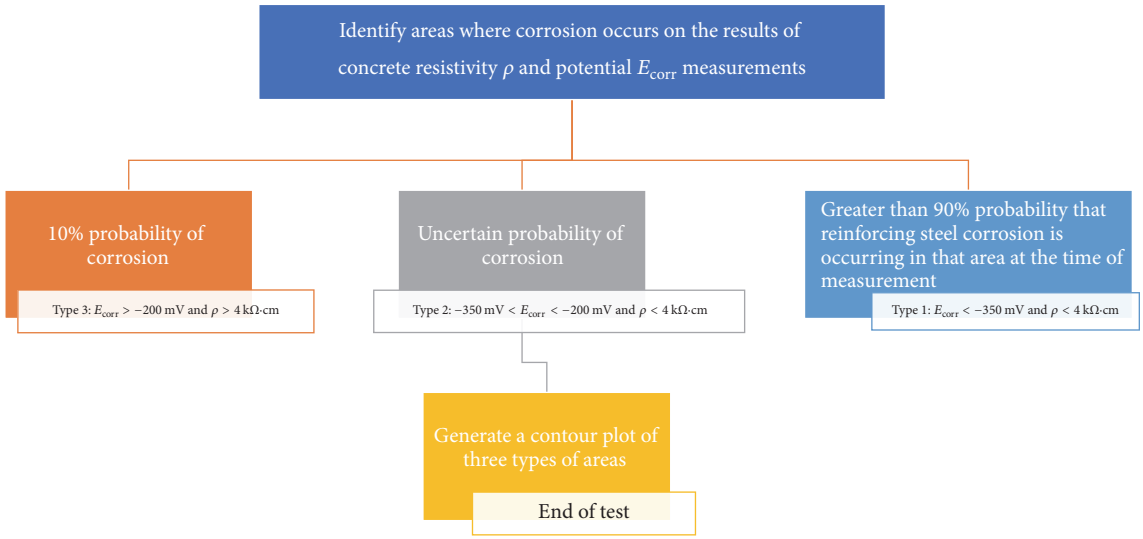

Figure 12: Assessment of corrosion probability in concrete slabs through half-cell potential and resistivity measurements [20].

Table 6: Concrete resistivity and risk of corrosion of steel reinforcement.

Corrosion risk	Resistivity values (kΩ·cm)		
	Polder [7]	Song and Saraswathy [66], Elkey and Sellevold [67]	Commercial Wenner probe instrument manuals [68, 69]
High	<10	<5	≤10
Moderate	10–50	5–10	10–50
Low	50–100	10–20	50–100
Negligible	>100	>20	≥100

corrosion detection using both electrical resistivity and half-cell potential measurements has been studied experimentally [75]. For small concrete cover thickness, it was observed that both measurements corresponded well together, but more discrepancy in measurements values was obtained when concrete cover became thicker [75]. From few published papers in this area that examined the possibility of corrosion by applying both electrical resistivity and half-cell potential technique, it was difficult to find a systematic methodology. As a rule of thumb, methodology proposed in Figure 12 by Sadowski [20] can be used when possible corrosion areas are identified by both half-cell potential and a four-point Wenner probe. Only identifying the probability of corrosion was suggested when conducting a corrosion assessment [20].

A number of researchers as well as commercial Wenner probe instrument manuals (Proceq and Giatec Scientific Inc. [68, 69]) provided a general guideline in terms of corrosion risk when interpreting electrical resistivity measurements, as seen in Table 6. The difference between provided resistivity values originates in the various experimental setup, concrete quality, concrete composition, and initial chloride concentration. For example, the corrosion state resistivity for passivation value reported in Polder's [7] review is higher than the one recorded in Morris et al.'s work [60] due to different experimental setup and test conditions.

A linear relationship between concrete electrical conductivity and corrosion rate has been found in several articles [104, 106, 109–111]. Experimental study on carbonated mortars also confirmed this linear trend and showed a different slope in case of chloride presence as the corrosion rate was affected by Cl^-/OH^- ratio [110]. Variation in concrete cover depth as well as concrete composition also showed an effect on the slope of linear trend between resistivity and corrosion rate [104]. Andrade and Alonso [112] proposed an empirical equation describing relationship between resistivity and corrosion rate:

$$I_{corr} \cong \frac{3 \times 10^3}{\rho}. \quad (15)$$

Two other similar models have been proposed by DuraCrete R17 [92] and LIFECON [113], as illustrated below:

$$I_{corr} = \frac{k_0}{\rho(t)} \times F_{cl} \times F_{Galv} \times F_{O_2}, \quad (16)$$

where I_{corr} is corrosion rate in $\mu A/cm^2$, k_0 is constant regression parameter in $\mu m \cdot \Omega m/a$, $\rho(t)$ is actual resistivity at time t in Ωm, F_{cl} accounts for the influence of the chloride content, F_{Galv} is influence of galvanic effect, and F_{O_2} is availability of oxygen.

In most cases, F_{cl} is dependent on the chloride concentration at the location that corrosion occurs and F_{Galv} and F_{O_2} equal 1. Due to microcell geometric arrangements of anodic and cathodic sites, concrete electrical resistivity plays an important role in controlling corrosion rates [111]. Similar to Glass et al.'s study [103], it was stated by Gulikers [111] that overall corrosion cell resistance is not inherently controlled by concrete electrical resistivity, but rather cathodic activation controls mostly. It should always be considered that the interpretation of electrical resistivity measurements is

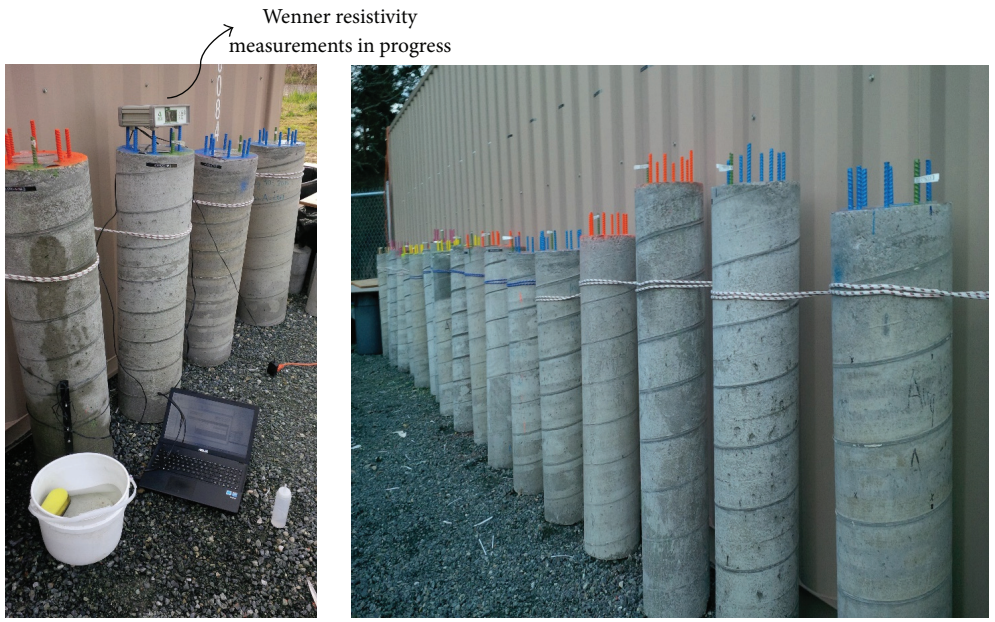

Figure 13: Instrumented circular hollow columns being studied by authors to establish the relationship between electrical resistivity and durability characteristics.

a challenging task due to many variables affecting the results like moisture condition, salt content, and so forth.

In summary, it can be concluded that still large range and scatter exist for correlation between corrosion rate and concrete resistivity. Also, effect of moisture state and temperature as well as corrections to corrosion rate measurements should be considered during an investigation on finding correlation between resistivity and corrosion rate. Knowledge is still lacking in the literature to understand which mechanism dominates the corrosion process and how resistivity measurements are impacted. To practically determine the corrosion and resistivity relationship, more field data should be collected and analyzed. In order to address some of these issues, authors of this paper initiated a project with field specimens as shown in Figure 13. In this study, influence of various parameters (noted below) on resistivity is being studied (parameters: cover thickness, crystalline water-proofing admixtures effect, and cement type). In addition, authors are also studying the effect of self-sealing on resistivity of concrete. Previous work done in this area (self-sealing) is reported elsewhere [114, 115].

7. Correlation between Electrical Resistivity and Compressive Strength

One of the most important mechanical properties of concrete is compressive strength. It can be simply measured by compression testing machine, as load at the failure divided by area of specimen gives the compressive strength of concrete [56]. Thus, a number of researchers performed different experiments to understand the relation between compressive strength and electrical responses in cementitious materials. In the compressive strength, one of the key factors is the strength of interfacial transition zone (ITZ) that has no remarkable impact on concrete electrical resistivity. It was observed when different cementitious materials were used in concrete mixture that there was no sensible relationship between concrete resistivity and compressive strength ($R^2 = 0.413$) [56]. This is mainly linked to the fact that chemical compound of pore solution does not have a great impact on compressive strength while affecting the concrete resistivity significantly. On the other hand, for the case of similar cementitious materials, better correlations can be achieved between compressive strength and concrete resistivity due to relationship between permeability and compressive strength [56]. As the strength increases, the electrical resistivity increases correspondingly for the same concrete mixture design. The study on the electrical properties of concrete with White Portland Cement also found an approximately linear trend between these two properties as both directly depend on the porosity of the matrix at early age. As concrete matured, this relationship was affected by other properties such as the conductivity of the pore solution and the degree of concrete saturation [34]. Also, as the density and compactness of the concrete structure increase, its compressive strength and the electrical resistivity will both increase. It was reported that, at the same w/c ratio, the changes of the specimens' resistivities with different sizes (φ100 mm × 200 mm and φ150 mm × 300 mm) were close to those changes of the compressive strengths. For example, the differences between the resistivities or compressive strengths of the specimens were both around 93% at w/c of 0.6 and 95% at w/c of 0.4 [25]. No direct relationship between 56-day concrete electrical resistivity and 28-day compressive strength was found in Gudimettla and Crawford's work [53] due to variety of samples taken from different field projects. In terms of activation energy, the investigation done

by Liu and Presuel-Moreno [44] showed that resistivity is noticeably higher than the reported activation energy for compressive strength. In conclusion, there is no practical correlation between electrical resistivity and compressive strength for various cementitious materials; however, for the same mixture design, electrical resistivity is linearly related to compressive strength. Generally, as concrete permeability decreases, both electrical resistivity and compressive strength increase.

8. Correlation between Surface and Bulk Electrical Resistivity

As it is discussed in previous sections, every electrical resistivity (ρ) measurement is composed of a resistance (R) and a geometry correction factor (k) that convert the resistance to resistivity which is a geometry independent intrinsic material property [21]. The correction factor (k) depends on the geometry and size of the sample and the electrodes location. Hence, for the same concrete material, variation in electrode geometries and sample size may result in different resistance values but eventually will yield the same resistivity using (17). Four common measurement electrode geometries that have been employed in several studies to conduct electrical test on cementitious cylinders are included: (1) uniaxial resistance (or bulk resistance), (2) surface resistance, (3) embedded sensors, and (4) disc method (one external electrode). In this section, researchers' review on correlation between the first two common (bulk and surface) resistivity measurement methods is summarized.

$$\rho = R \cdot k. \tag{17}$$

Theoretically, the ratio of surface and bulk resistance for standard size cylinder specimen (100 mm × 200 mm) and probe spacing of $a = 50$ mm can be computed in the following equation [18]:

$$\frac{R_1}{R_2} = \left(\frac{\rho_1}{\rho_2}\right)\left(\frac{1}{8}\right), \tag{18}$$

where R_1 is resistance measured by 4-point Wenner method (surface resistance), R_2 is resistance measured by uniaxial method (bulk resistance), ρ_1 is resistivity measured by 4-point Wenner method (surface resistivity), and ρ_2 is resistivity measured by uniaxial method (bulk resistivity).

The ratio of two different resistivity types (ρ_1 and ρ_2) is equal to 2.63 [18]. Therefore, the theoretical ratio of surface and bulk resistance can be computed as

$$\frac{R_1}{R_2} = \frac{2.63}{8} = 0.33. \tag{19}$$

Also, a number of researchers experimentally attempted to study this correlation between bulk and surface resistivity data. Studies performed by Ghosh and Tran [61, 62] showed the correlation between bulk and surface resistivity for different groups of binary and ternary mixtures. It was observed that for most groups of mixtures, the coefficient of determination (R^2) values for linear trend line was higher than 0.8 and sometimes close to 1 except some silica fume mixtures at early-ages where the coefficient became less than 0.80. The linear trend line varied from 0.29 to 0.47 at different concrete ages of 7, 14, 28, 56, 91, and 161 days. For probe spacing $a = 38.1$ mm, Spragg et al. [39] also reported a strong linear correlation with an $R^2 = 0.9986$, with surface resistivity measurements tending to be 1.86 times higher than bulk resistivity which supports previous work done by Morris et al. [18]. Several Department of Transportation (DOT) and other agencies participated in a round robin program (summarized by Indiana DOT). A recent study on specimens casted during actual concrete production in the field through different US states proved that the surface and bulk measurements correlate extremely well with each other at 28- and 56-day age [53]. It was observed that the surface resistivity results were typically 1.9 times higher than the bulk resistivity obtained data. Authors have found a similar correlation between bulk and surface resistivity ($R^2 = 0.979$).

Both surface and bulk resistivity measurement methods have been used to determine the presence of a heterogeneity problem [21]. To investigate the heterogeneous systems, the surface and uniaxial resistivity tests were performed on the cylindrical specimen with a 10-mm thick white cement paste on outer layer and the prismatic specimens with two separate layers of white and grey cement pastes setup in parallel and series configurations, as illustrated in Figure 14 [21]. For the uniaxial case, the total resistivity (ρ_c) can be calculated through the proposed equations (20a) and (20b) for parallel and series configurations. A correction factor (Γ) has been developed for heterogeneity which depends on the material of interest and an approach was proposed to compare the resistivities measured from a surface test and a bulk test. In this approach, if there is heterogeneity, the values from the two tests will be different. This difference can give an indication as to whether the surface layer is more or less resistive [21]. Similarly, correlation between surface and bulk resistivity found in other studies indicated a strong relationship between the resistivity values when the appropriate geometry factor was applied [8, 37]:

$$\frac{1}{\rho_c} = \sum_{i=1}^{n} \frac{A_i}{\rho_i} \quad \text{(Parallel configuration)}, \tag{20a}$$

$$\rho_c = \sum_{i=1}^{n} \rho_i \cdot L_i \quad \text{(Series configuration)}. \tag{20b}$$

In summary, the coefficient of determination value (R^2) for linear trend between bulk and surface resistivity in different literatures for various ages is shown in Table 7. Based on the reported data, it can be concluded that a strong relationship exists between resistivity measured by surface and bulk tests. However, in practical cases, caution is needed for multilayered cementitious composite systems as electrical current flows differently in these two techniques and for the types of layered electrical properties that can occur due to moisture gradients, chemical changes, and ionic gradients [21]. More complicated situations for resistivity measurement that arise during field measurements where seasonal and wet/drying might take place at the tidal section on partially

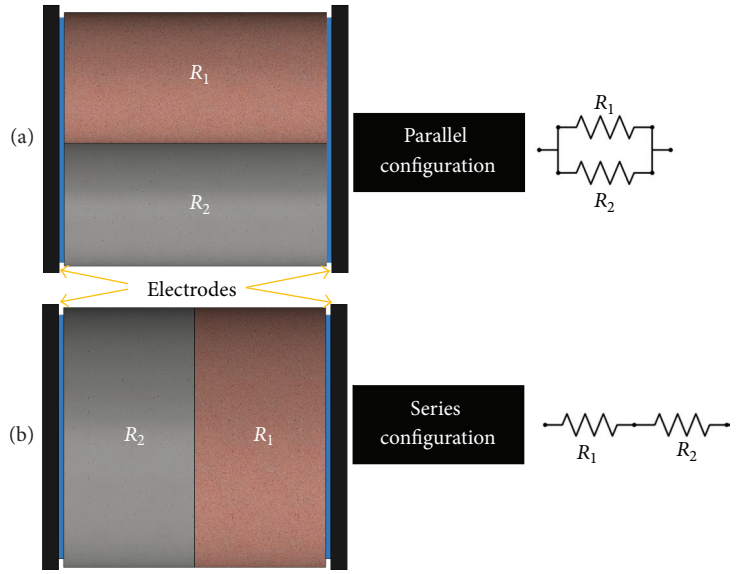

Figure 14: Schematic of the (a) parallel and (b) series models of heterogeneous systems (reproduced from [21]).

Table 7: Coefficient of determination (COD) value for linear trend between bulk and surface resistivity in the literatures.

Reference	Coefficient of determination value (R^2)
Sengul and Gjorv [37] (2008)	0.99
Sengul and Gjorv [8] (2009)	0.99
Spratt et al. [39] (2011)	0.9986
Ghosh and Tran [61] (2015)	0.82–0.95
Gudimettla and Crawford [53] (2016)	0.98
Authors' work (2016)	0.979

immersed structures have been studied by Presuel-Moreno et al. [65].

9. Summary and Conclusions

Through an extensive literature review, this paper identifies several factors which might have potential influence on the electrical resistivity of concrete. Effect of each parameter is briefly summarized below.

(i) In agreement with most studies, when there is an embedded rebar in the concrete, the electrical current field is distorted, and thus errors can result in the electrical resistivity measurements. To minimize this effect, it is suggested to place all electrodes perpendicular to the embedded rebar on the concrete surface and take at least five measurements, each a few millimetres in distance from one another. Also, a correction factor should be applied to resistivity measurements once rebar is present in concrete. However, effect of rebar presence on the resistivity measurements is well-understood; just a few studies could be found to identify the rebar presence effect and more field investigations are still needed in this area.

(ii) Presence of cracks in concrete was also identified as an influential parameter on electrical resistivity since it is initially presumed that concrete is homogenous, isotropic, and uncracked. Depth of crack, orientation of probes on crack, and type of crack (conductive or isolated) can individually affect the resistivity readings. As suggested for embedded rebar in the concrete, all electrodes should be placed in perpendicular direction to cracks. It was reported that higher resistivity readings were obtained from conductive cracks whereas lower resistivity values were gained for insulated cracks. However, no information is provided to show how much cracking induced by corrosion influences concrete resistivity. In addition when both insulated and conductive cracks are bridged together, their integrated influence on electrical resistivity is not well-understood.

(iii) The moisture state and temperature of concrete during resistivity measurements were also found to be of major influence on recorded data. As temperature increases, the ions mobility becomes faster; consequently, electrical conductivity of concrete also increases. To lessen the temperature effect on resistivity results, no practical correlation is still published for real-world conditions. Essentially, electrical resistivity reduces with an increase in moisture content as a result of changing in the ion movement. It is strongly recommended to take resistivity measurements when concrete is in Saturated Surface Dry (SSD) condition. Yet, more investigations are required to understand how much time is needed for water to infiltrate the concrete to obtain constant moisture level through the bulk sample.

(iv) The studies related to resistivity measurement test device confirmed that electrical signal shape and frequency, electrode contact with concrete surface, and probe spacing of surface resistivity measurement device can affect the resistivity results. To minimize the effect of signal shape and frequency, using low frequency range square-wave signal for surface resistivity and high frequency range for bulk resistivity is recommended. Proper contact should also be provided to not mislead resistivity readings. Using a saturated sponge between electrodes and concrete surface can reduce this effect. In 4-point Wenner probe method, as it is assumed that concrete is homogenous material, aggregates inside concrete also affect its homogeneity due to their higher resistivity. Therefore, providing enough wide spaces between electrodes is essential to diminish aggregates effect. As a rule of thumb, probe spacing 1.5 times higher than the maximum aggregate size should be considered.

(v) Aggregate content and type were identified to have an influence on concrete resistivity. Increase in aggregate content results in higher resistivity values due to their less porosity and lower electrical conductivity. Also, aggregates with rough surface texture were found to have higher resistivity as their tortuosity is higher. Therefore, the effect of aggregates content and type should be accounted for in resistivity measurements.

(vi) Carbonation process in aged concrete forms a multilayered system that results in various resistivity values through the concrete depth. So, its effect should be mitigated during resistivity measurements. Lower resistivity is also generated when w/b ratio is high due to higher percentage of porosity.

Correlation between concrete electrical resistivity and its certain durability characteristics such as chloride diffusivity, compressive strength, and corrosion potential/rate was discussed in this paper and is summarized below.

(i) Concrete resistivity is inversely related to chloride ingress, where lower resistivity indicated the area where chloride diffusion will be faster. A retardation of chloride can be taken into account through the introduced reaction factor (r_{cl}). More research is still required to better simulate sea site conditions.

(ii) Furthermore, a strong correlation can be found between increasing electrical resistivity of concrete and the corrosion rate. The relationship can be seen when corrosion has initiated (active conditions). It will not be valid in the case of saturated concrete, where although the resistivity is low, the corrosion rate will be small because of lack of oxygen. Field data was considered in just a few investigations and, thus, it is of high interest to gather more field experience.

(iii) In addition, concrete compressive strength and its electrical resistivity have a direct relationship with each other as both directly depend on the porosity of the matrix at early age. However, at a later age, the conductivity of the pore solution and the degree of concrete saturation both influence this relationship. No practical relationship was identified in the literatures between compressive strength and electrical resistivity.

(iv) Four common measurement electrode geometries that have been employed in several studies to conduct electrical test on cementitious cylinders were introduced in this article. Among them, a strong direct linear correlation between two common methods of resistivity measurements (concrete surface and bulk resistivity) was presented. However, more attention should be paid to multilayered cementitious composite systems in the field as electrical current flows differently in these two techniques and for the types of layered electrical properties that can happen because of moisture gradients, chemical changes, and ionic gradients.

Abbreviations

CON: Concrete
CEM: Cement paste
MOR: Mortar
MK: Metakaolin
SF: Silica fume
RHA: Rice Husk Ash
OPC: Ordinary Portland Cement
SLG: Slag
FA: Fly ash
NP: Natural pozzolan
UPV: Ultrasonic Pulse Velocity
WPC: White Portland Cement
PFA: Pulverized-Fuel Ash
MS: Microsilica
LPR: Linear Polarization Resistance technique
TNVM: Total Number of Various Mixtures
w/b: Water/binder ratio
NR: Not reported
CR: Counter electrode
RE: Reference electrode
SC: Slag cement
CA: Crystalline admixtures
PLC: Portland Limestone Cement.

Conflicts of Interest

The authors declare that there are no conflicts of interest regarding the publication of this paper.

References

[1] P. K. Mehta and P. J. M. Monteiro, *Concrete: microstructure, properties, and materials*, McGraw-Hill, New York, NY, USA, 3rd edition, 2006.

[2] ASTM, "Standard test method for bulk electrical conductivity of hardened concrete," ASTM C1760-12, ASTM International, 2012.

[3] AASHTO, "Method of test for surface resistivity indication of concrete's ability to resist chloride ion penetration," AASHTO TP 95, Am. Assoc. State Highw. Transp. Off., 2011.

[4] O. Sengul, "Use of electrical resistivity as an indicator for durability," *Construction and Building Materials*, vol. 73, pp. 434–441, 2014.

[5] F. Rajabipour, J. Weiss, and D. M. Abraham, "Insitu electrical conductivity measurements to assess moisture and ionic transport in concrete (A discussion of critical features that influence the measurements)," in *Proceedings of the International RILEM Symposium on Concrete Science and Engineering: A Tribute to Arnon Bentur*, 2004.

[6] H. Layssi, P. Ghods, A. R. Alizadeh, and M. Salehi, "Electrical resistivity of concrete," *Concrete International*, pp. 41–46, 2015.

[7] R. B. Polder, "Test methods for on site measurement of resistivity of concrete—a RILEM TC-154 technical recommendation," *Construction and Building Materials*, vol. 15, no. 2-3, pp. 125–131, 2001.

[8] O. Sengul and O. E. Gjorv, "Effect of embedded steel on electrical resistivity measurements on concrete structures," *ACI Materials Journal*, vol. 106, no. 1, 2009.

[9] M. Salehi, P. Ghods, and O. Burkan Isgor, "Numerical investigation of the role of embedded reinforcement mesh on electrical resistivity measurements of concrete using the Wenner probe technique," *Materials and Structures*, vol. 49, no. 1-2, pp. 301–316, 2016.

[10] J. F. Lataste, C. Sirieix, D. Breysse, and M. Frappa, "Electrical resistivity measurement applied to cracking assessment on reinforced concrete structures in civil engineering," *NDT & E International*, vol. 36, no. 6, pp. 383–394, 2003.

[11] N. Wiwattanachang and P. H. Giao, "Monitoring crack development in fiber concrete beam by using electrical resistivity imaging," *Journal of Applied Geophysics*, vol. 75, no. 2, pp. 294–304, 2011.

[12] K. Hornbostel, C. K. Larsen, and M. R. Geiker, "Relationship between concrete resistivity and corrosion rate—a literature review," *Cement and Concrete Composites*, vol. 39, pp. 60–72, 2013.

[13] D. A. Whitting and M. A. Nagi, *Electrical Resistivity of Concrete*, Portland Cement Association, Skokie, Ill, USA, 2003.

[14] RILEM TC 154-EMC, "Recommendations of RILEM TC 154-EMC: electrochemical techniques for measuring metallic corrosion half-cell potential measurements—potential mapping on reinforced concrete structures," *Materials and Structures*, vol. 36, no. 261, pp. 461–471, 2003.

[15] F. Wenner, "A method of measuring earth resistivity," *Bulletin of the Bureau of Standards*, vol. 12, no. 4, pp. 469–478, 1916.

[16] R. Ranade, J. Zhang, J. P. Lynch, and V. C. Li, "Influence of micro-cracking on the composite resistivity of Engineered Cementitious Composites," *Cement and Concrete Research*, vol. 58, pp. 1–12, 2014.

[17] K. R. Gowers and S. G. Millard, "Measurement of concrete resistivity for assessment of corrosion severity of steel using wenner technique," *ACI Materials Journal*, vol. 96, no. 5, 1999.

[18] W. Morris, E. I. Moreno, and A. A. Sagüés, "Practical evaluation of resistivity of concrete in test cylinders using a Wenner array probe," *Cement and Concrete Research*, vol. 26, no. 12, pp. 1779–1787, 1996.

[19] A. Bentur, S. Diamond, and B. N. Steven, *Steel Corrosion in Concrete: Fundamentals and Civil Engineering Practice*, EFN Spon, London, UK, 1st edition, 1997.

[20] L. Sadowski, "Methodology for assessing the probability of corrosion in concrete structures on the basis of half-cell potential and concrete resistivity measurements," *The Scientific World Journal*, vol. 2013, Article ID 714501, 8 pages, 2013.

[21] R. Spragg, C. Villani, J. Weiss et al., "Surface and uniaxial electrical measurements on layered cementitious composites having cylindrical and prismatic geometries," in *Proceedings of the International Conference on the Durability of Concrete Structures*, West Lafayette, Ind, USA, 2014.

[22] D. P. Bentz, K. A. Snyder, and A. Ahmed, "Anticipating the setting time of high-volume fly ash concretes using electrical measurements: feasibility studies using pastes," *Journal of Materials in Civil Engineering*, vol. 27, no. 3, Article ID 4014129, 2015.

[23] R. Weydert and C. Gehlen, "Electrolytic resistivity of cover concrete: relevance, measurement and interpretation," in *Proceedings of CIB W078 Workshop on Information Technology in Construction*, Rotterdam, Netherlands, 1999.

[24] F. Presuel-Moreno, Y. Liu, and M. Paredes, *Understanding the Effect of Rebar Presence and/or Multilayered Concrete Resistivity on the Apparent Surface Resistivity Measured via the Four Point Wenner Method*, NACE International, 2009.

[25] C.-T. Chen, J.-J. Chang, and W.-C. Yeih, "The effects of specimen parameters on the resistivity of concrete," *Construction and Building Materials*, vol. 71, pp. 35–43, 2014.

[26] A. J. Garzon, J. Sanchez, C. Andrade, N. Rebolledo, E. Menéndez, and J. Fullea, "Modification of four point method to measure the concrete electrical resistivity in presence of reinforcing bars," *Cement and Concrete Composites*, vol. 53, pp. 249–257, 2014.

[27] Y.-C. Lim, T. Noguchi, and C.-G. Cho, "A quantitative analysis of the geometric effects of reinforcement in concrete resistivity measurement above reinforcement," *Construction and Building Materials*, vol. 83, pp. 189–193, 2015.

[28] W. Morris, A. Vico, and M. Vázquez, "Chloride induced corrosion of reinforcing steel evaluated by concrete resistivity measurements," *Electrochimica Acta*, vol. 49, no. 25, pp. 4447–4453, 2004.

[29] U. M. Angst and B. Elsener, "On the applicability of the wenner method for resistivity measurements of concrete," *ACI Materials Journal*, vol. 111, no. 6, pp. 661–672, 2014.

[30] M. Goueygou, O. Abraham, and J.-F. Lataste, "A comparative study of two non-destructive testing methods to assess near-surface mechanical damage in concrete structures," *NDT and E International*, vol. 41, no. 6, pp. 448–456, 2008.

[31] T. Rupnow and P. Icenogle, "Evaluation of surface resistivity measurements as an alternative to the rapid chloride permeability test for quality assurance and acceptance," Tech. Rep. 2290, Performing Organization Name and Address Louisiana Transportation Research Center, Baton Rouge, La, USA, 2012.

[32] F. Presuel-Moreno and Y. Liu, "Temperature effect on electrical resistivity measurements on mature saturated concrete," in *Proceedings of the NACE—International Corrosion Conference Series 7*, Salt Lake City, Utah, USA, 2012.

[33] R. Van Noort, M. Hunger, and P. Spiesz, "Long-term chloride migration coefficient in slag cement-based concrete and resistivity as an alternative test method," *Construction and Building Materials*, vol. 115, pp. 746–759, 2016.

[34] A. Lübeck, A. L. G. Gastaldini, D. S. Barin, and H. C. Siqueira, "Compressive strength and electrical properties of concrete with white Portland cement and blast-furnace slag," *Cement and Concrete Composites*, vol. 34, no. 3, pp. 392–399, 2012.

[35] J. Su, C. Yang, W. Wu, and R. Huang, "Effect of moisture content on concrete resistivity measurement," *Journal of the Chinese Institute of Engineers*, vol. 25, no. 1, pp. 117–122, 2002.

[36] M. Saleem, M. Shameem, S. E. Hussain, and M. Maslehuddin, "Effect of moisture, chloride and sulphate contamination on the electrical resistivity of Portland cement concrete," *Construction and Building Materials*, vol. 10, no. 3, pp. 209–214, 1996.

[37] O. Sengul and O. E. Gjorv, "Electrical resistivity measurements for quality control during concrete construction," *ACI Materials Journal*, vol. 105, no. 6, 2008.

[38] M. D. Newlands, M. R. Jones, S. Kandasami, and T. A. Harrison, "Sensitivity of electrode contact solutions and contact pressure in assessing electrical resistivity of concrete," *Materials and Structures*, vol. 41, no. 4, pp. 621–632, 2008.

[39] R. Spratt, J. Castro, T. Nantung, E. Paredes, and W. J. Weiss, "Variability Analysis of the Bulk Resistivity Measured Using Concrete Cylinders," Tech. Rep., Purdue University Press, West Lafayette, Ind, USA, 2011.

[40] J. W. McCarter, G. Starrs, S. Kandasami, M. R. Jones, and M. Chrisp, "Electrode configurations for resistivity measurements on concrete," *ACI Materials Journal*, vol. 106, no. 3, 2009.

[41] Y. Liu and F. J. Presuel-Moreno, "Normalization of temperature effect on concrete resistivity by method using Arrhenius law," *ACI Materials Journal*, vol. 111, no. 4, pp. 433–442, 2014.

[42] J. W. Bryant Jr., R. E. Weyers, and J. M. Garza, "In-place resistivity of bridge deck concrete mixtures," *ACI Materials Journal*, vol. 106, no. 2, 2009.

[43] R. Spragg, C. Villani, K. Snyder, D. Bentz, J. Bullard, and J. Weiss, "Factors that influence electrical resistivity measurements in cementitious systems," *Journal of the Transportation Research Board*, vol. 2342, pp. 90–98, 2013.

[44] Y. Liu and F. Presuel-Moreno, "Effect of elevated temperature curing on compressive strength and electrical resistivity of concrete with fly ash and GGBS," *ACI Materials Journal*, vol. 111, no. 5, 2014.

[45] W. J. McCarter, T. M. Chrisp, G. Starrs, P. A. M. Basheer, and J. Blewett, "Field monitoring of electrical conductivity of cover-zone concrete," *Cement and Concrete Composites*, vol. 27, no. 7-8, pp. 809–817, 2005.

[46] K. M. Smith, A. J. Schokker, and P. J. Tikalsky, "Performance of supplementary cementitious materials in concrete resistivity and corrosion monitoring evaluations," *ACI Materials Journal*, vol. 101, no. 5, 2004.

[47] H. Minagawa and M. Hisada, "Consideration about chloride ion diffusion coefficient estimated by electric resistivity of concrete exposed in tidal zone," in *Proceedings of the 3rd International Conference on Sustainable Construction Materials and Technologies*, Kyoto, Japan, 2013.

[48] F. Presuel-Moreno, Y.-Y. Wu, and Y. Liu, "Effect of curing regime on concrete resistivity and aging factor over time," *Construction and Building Materials*, vol. 48, pp. 874–882, 2013.

[49] E. Güneyisi, T. Özturan, and M. Gesoğlu, "A study on reinforcement corrosion and related properties of plain and blended cement concretes under different curing conditions," *Cement and Concrete Composites*, vol. 27, no. 4, pp. 449–461, 2005.

[50] R. B. Polder and W. H. A. Peelen, "Characterisation of chloride transport and reinforcement corrosion in concrete under cyclic wetting and drying by electrical resistivity," *Cement and Concrete Composites*, vol. 24, no. 5, pp. 427–435, 2002.

[51] T. Y. D. Lim, S. Teng, S. D. Bahador, and O. E. Gjørv, "Durability of very-high-strength concrete with supplementary cementitious materials for marine environments," *ACI Materials Journal*, vol. 113, no. 1, pp. 95–103, 2016.

[52] R. J. Kessler, R. G. Powers, E. Vivas, M. A. Paredes, and Y. P. Virmani, "Surface resistivity as an indicator of concrete chloride penetration resistance," in *Proceedings of the Concrete Bridge Conference*, p. 18, 2008.

[53] J. Gudimettla and G. Crawford, "Resistivity tests for concrete—recent field experience," *ACI Materials Journal*, vol. 113, no. 4, 2016.

[54] A. Jenkins, "Surface resistivity as an alternative for rapid chloride permeability test of hardened concrete," Tech. Rep. FHWA-KS-14-15, Kansas Department of Transportation Bureau of Research, Topeka, Kan, USA, 2015.

[55] Y. Liu, F. J. Presuel-Moreno, and M. A. Paredes, "Determination of chloride diffusion coefficients in concrete by electrical resistivity method," *ACI Materials Journal*, vol. 112, no. 5, pp. 631–640, 2015.

[56] A. A. Ramezanianpour, A. Pilvar, M. Mahdikhani, and F. Moodi, "Practical evaluation of relationship between concrete resistivity, water penetration, rapid chloride penetration and compressive strength," *Construction and Building Materials*, vol. 25, no. 5, pp. 2472–2479, 2011.

[57] P. A. M. Basheer, P. R. V. Gilleece, A. E. Long, and W. J. Mc Carter, "Monitoring electrical resistance of concretes containing alternative cementitious materials to assess their resistance to chloride penetration," *Cement and Concrete Composites*, vol. 24, no. 5, pp. 437–449, 2002.

[58] D. T. Y. Lim, B. Sabet Divsholi, D. Xu, and S. Teng, "Evaluation of high performance concrete using electrical resistivity technique," in *Proceedings of the Our World in Concrete and Structures*, Singapore, 2011.

[59] C. Andrade, R. d'Andrea, and N. Rebolledo, "Chloride ion penetration in concrete: the reaction factor in the electrical resistivity model," *Cement and Concrete Composites*, vol. 47, pp. 41–46, 2014.

[60] W. Morris, A. Vico, M. Vazquez, and S. R. de Sanchez, "Corrosion of reinforcing steel evaluated by means of concrete resistivity measurements," *Corrosion Science*, vol. 44, no. 1, pp. 81–99, 2002.

[61] P. Ghosh and Q. Tran, "Correlation between bulk and surface resistivity of concrete," *International Journal of Concrete Structures and Materials*, vol. 9, no. 1, pp. 119–132, 2015.

[62] P. Ghosh and Q. Tran, "Influence of parameters on surface resistivity of concrete," *Cement and Concrete Composites*, vol. 62, pp. 134–145, 2015.

[63] A. L. G. Gastaldini, G. C. Isaia, T. F. Hoppe, F. Missau, and A. P. Saciloto, "Influence of the use of rice husk ash on the electrical resistivity of concrete: a technical and economic feasibility study," *Construction and Building Materials*, vol. 23, no. 11, pp. 3411–3419, 2009.

[64] C. Andrade, M. Castellote, and R. D'Andrea, "Measurement of ageing effect on chloride diffusion coefficients in cementitious matrices," *Journal of Nuclear Materials*, vol. 412, no. 1, pp. 209–216, 2011.

[65] F. Presuel-Moreno, A. Suares, and Y. Liu, *Characterization of New and Old Concrete Structures Using Surface Resistivity Measurements*, Florida Department of Transportation, Dania Beach, Fla, USA, 2010.

[66] H.-W. Song and V. Saraswathy, "Corrosion monitoring of reinforced concrete structures-a review," *International Journal of Electrochemical Science*, vol. 2, pp. 1–28, 2007.

[67] W. Elkey and E. J. Sellevold, *Electrical Resistivity of Concrete*, supplement 80, Norwegian Road Research Laboratory, Oslo, Norway, 1995.

[68] "Operating Instructions Resipod Family Manual." Proceq.

[69] SURF™, *Surface Electrical Resistivity of Concrete Manual*, Giatec Scientific Inc., https://www.giatecscientific.com/concrete-resistivity/surf/.

[70] J. Weiss, K. Snyder, J. Bullard, and D. Bentz, "Using a saturation function to interpret the electrical properties of partially saturated concrete," *Journal of Materials in Civil Engineering*, vol. 25, no. 8, pp. 1097–1106, 2013.

[71] S. G. Millard, "Reinforced concrete resistivity measurement techniques," *Institution of Civil Engineers*, vol. 91, pp. 71–88, 1991.

[72] F. Presuel-Moreno, Y. Liu, and Y.-Y. Wu, "Numerical modeling of the effects of rebar presence and/or multilayered concrete resistivity on the apparent resistivity measured via the Wenner method," *Construction and Building Materials*, vol. 48, pp. 16–25, 2013.

[73] M. Salehi, *Numerical investigation of the role of embedded reinforcement mesh on electrical resistivity measurements of concrete using the Wenner probe technique [M.S. thesis]*, Carleton University, Ottawa, Canada, 2013.

[74] J. Sanchez, C. Andrade, J. Torres, N. Rebolledo, and J. Fullea, "Determination of reinforced concrete durability with on-site resistivity measurements," *Materials and Structures*, vol. 50, no. 1, 2017.

[75] M. Morales, "Experimental investigation of the effects of embedded rebar, cracks, chloride ingress and corrosion on electrical resistivity measurements of reinforced concrete," *Master, Oregon State University*, 2015.

[76] A. A. Shah and Y. Ribakov, "Non-destructive measurements of crack assessment and defect detection in concrete structures," *Materials and Design*, vol. 29, no. 1, pp. 61–69, 2008.

[77] M. Chouteau and S. Beaulieu, "An investigation on application of the electrical resistivity tomography method to concrete structures," in *Proceedings of the Geophysics 2002. The 2nd Annual Conference on the Application of Geophysical and NDT Methodologies to Transportation Facilities and Infrastructure*, Washington DC, USA, 2002.

[78] E. Taillet, J. F. Lataste, P. Rivard, and A. Denis, "Non-destructive evaluation of cracks in massive concrete using normal dc resistivity logging," *NDT and E International*, vol. 63, pp. 11–20, 2014.

[79] M. Salehi, P. Ghods, and O. B. Isgor, "Numerical study on the effect of cracking on surface resistivity of plain and reinforced concrete elements," *Journal of Materials in Civil Engineering*, vol. 27, no. 12, Article ID 04015053, 2015.

[80] A. J. Ewins, "Resistivity Measurements in Concrete," *British Journal of NDT*, vol. 32, no. 3, pp. 120–126, 1990.

[81] R. Henkensiefken, J. Castro, D. Bentz, T. Nantung, and J. Weiss, "Water absorption in internally cured mortar made with water-filled lightweight aggregate," *Cement and Concrete Research*, vol. 39, no. 10, pp. 883–892, 2009.

[82] M. D. A. Thomas, "The use of conductive gel," 2008.

[83] J. D. Shane, *Electrical conductivity and transport properties of cement-based material measured by impedance spectroscopy [ph.D. thesis]*, Nothwestern University, Evanston, Ill, USA, 2000.

[84] R. Spragg, Y. Bu, K. Snyder, D. Bentz, and J. Weiss, "Electrical testing of cement-based materials: role of testing techniques, sample conditioning," Tech. Rep. FHWA/IN/JTRP-2013/28, Purdue University, 2013.

[85] A. Shahroodi, *Development of test methods for assessment of concrete durability for use in performance-based specifications [M.S. thesis]*, University of Toronto, Toronto, Canada, 2010.

[86] J. M. S. Marquez, *Influence of saturation and geometry on surface electrical resistivity measurements [M.S. thesis]*, Concorida University, Montreal, Canada, 2015.

[87] M. Castellote, C. Andrade, and M. C. Alonso, "Standardization, to a reference of 25°C, of electrical resistivity for mortars and concretes in saturated or isolated conditions," *ACI Materials Journal*, vol. 99, no. 2, 2002.

[88] Y. A. Villagrán Zaccardi, J. F. García, P. Huélamo, and Á. A. Di Maio, "Influence of temperature and humidity on Portland cement mortar resistivity monitored with inner sensors," *Materials and Corrosion*, vol. 60, no. 4, pp. 294–299, 2009.

[89] S. Poyet, "Experimental investigation of the effect of temperature on the first desorption isotherm of concrete," *Cement and Concrete Research*, vol. 39, no. 11, pp. 1052–1059, 2009.

[90] S. G. Millard, J. A. Harrison, and K. R. Gowers, "Practical measurement of concrete resistivity," *British Journal Non-Destructive Testing*, vol. 33, pp. 59–63, 1991.

[91] T. M. Chrisp, G. Starrs, W. J. McCarter, E. Rouchotas, and J. Blewett, "Temperature-conductivity relationships for concrete: an activation energy approach," *Journal of Materials Science Letters*, vol. 20, no. 12, pp. 1085–1087, 2001.

[92] DuraCrete R17, "Probabilistic performance based durability design of concrete structures, includes general guidelines for durability design and redesign," Tech. Rep. BE95-1347/R17, The European Union – Brite EuRam III, CUR, Gouda.

[93] M. Pour-Ghaz, O. B. Isgor, and P. Ghods, "The effect of temperature on the corrosion of steel in concrete. Part 1: Simulated polarization resistance tests and model development," *Corrosion Science*, vol. 51, no. 2, pp. 415–425, 2009.

[94] C. K. Larsen, E. J. Sellevold, J.-M. Østvik, and Ø. Vennesland, "Electrical resistivity of concrete—Part II: influence of moisture content and temperature," in *Proceedings of the 2nd International RILEM Symposium on Advances in Concrete through Science and Engineering*, 2006.

[95] Y. Liu, *Accelerated curing of concrete with high volume pozzolans -resistivity, diffusivity and compressive strength [ph.D. thesis]*, Florida Atlantic University, Boca Raton, Fla, USA, 2012.

[96] X. Lu, "Application of the Nernst-Einstein equation to concrete," *Cement and Concrete Research*, vol. 27, no. 2, pp. 293–302, 1997.

[97] K. R. Backe, O. B. Lile, and S. K. Lyomov, "Characterizing curing cement slurries by electrical conductivity," *SPE Drilling and Completion*, vol. 16, no. 4, pp. 201–207, 2001.

[98] FDOT, "Florida Method of Test For Concrete Resistivity as an Electrical Indicator of its Permeability," FM 5-578, 2004.

[99] R. J. Kessler, R. G. Powers, and M. A. Paredes, "Resistivity measurements of water saturated concrete as an indicator of permeability," in *Proceedings of the Corrosion*, Houston, Tex, USA.

[100] ASTM, "Standard test method for electrical indication of concrete's ability to resist chloride ion penetration," ASTM International C1202-12, 2012.

[101] R. K. Dhir, M. J. McCarthy, and M. D. Newlands, Eds., *Challenges of Concrete Construction: Concrete for Extreme Conditions: Proceedings of the International Conference held at the University of Dundee, on 9–11 September 2002*, vol. 6, Thomas Telford Publishing, Scotland, UK.

[102] E. Vivas, A. Boyd, and H. R. Hamilton III, "Permeability of concrete-comparison of conductivity and diffusion methods,"

Tech. Rep. 4910 45 04 992-12 (0026899), Florida Department of Transportation, Tallahassee, Fla, USA, 2007.

[103] G. K. Glass, C. L. Page, and N. R. Short, "Factors affecting the corrosion rate of steel in carbonated mortars," *Corrosion Science*, vol. 32, no. 12, pp. 1283–1294, 1991.

[104] L. Bertolini and R. Polder, Concrete resistivity and reinforcement corrosion rate as a function of temperature and humidity of the environment TNO 97-NaN-R0574, Netherlands Organisation for Applied Scientific Research, Delft, The Netherlands, 1997.

[105] ASTM, "Test Method for Corrosion Potentials of Uncoated Reinforcing Steel in Concrete," ASTM International C876, 2015.

[106] N. J. Carino, "Nondestructive techniques to investigate corrosion status in concrete structures," *Journal of Performance of Constructed Facilities*, vol. 13, no. 3, pp. 96–106, 1999.

[107] N. Gucunski, F. Romero, S. Kruschwitz, R. Feldmann, A. Abu-Hawash, and M. Dunn, "Multiple complementary nondestructive evaluation technologies for condition assessment of concrete bridge decks," *Transportation Research Record: Journal of the Transportation Research Board*, no. 2201, pp. 34–44, 2010.

[108] N. Gucunski, A. Imani, F. Romero et al., *Nondestructive testing to identify concrete bridge deck deterioration*, Transportation Research Board, Washington DC, USA, 2012.

[109] C. Alonso, C. Andrade, and J. A. González, "Relation between resistivity and corrosion rate of reinforcements in carbonated mortar made with several cement types," *Cement and Concrete Research*, vol. 18, no. 5, pp. 687–698, 1988.

[110] C. Andrade and C. Alonso, "Corrosion rate monitoring in the laboratory and on-site," *Construction and Building Materials*, vol. 10, no. 5, pp. 315–328, 1996.

[111] J. Gulikers, "Theoretical considerations on the supposed linear relationship between concrete resistivity and corrosion rate of steel reinforcement," *Materials and Corrosion*, vol. 56, no. 6, pp. 393–403, 2005.

[112] C. Andrade and C. Alonso, "Test methods for on-site corrosion rate measurement of steel reinforcement in concrete by means of the polarization resistance method," *RILEM*, vol. 37, pp. 623–643, 2004.

[113] E. Vesikari and M.-K. Soderqvist, "Life cycle management of concrete infrastructures for improved sustainability," in *Proceedings of the 9th International Bridge Management Conference*, pp. 15–28, 2003.

[114] R. Gupta and A. Biparva, "Innovative test technique to evaluate 'self-sealing' of concrete," *Journal of Testing and Evaluation*, vol. 43, no. 5, pp. 1091–1098, 2015.

[115] R. Gupta and A. Biparva, "Do crystalline water proofing admixtures affect restrained plastic shrinkage behavior of concrete?" *Revista ALCONPAT*, vol. 7, no. 1, p. 15, 2017.

Hindawi
Advances in Materials Science and Engineering
Volume 2017, Article ID 8212856, 7 pages
https://doi.org/10.1155/2017/8212856

Research Article

Chloride Transport in OPC Concrete Subjected to the Freeze and Thaw Damage

Ki Yong Ann,[1] Min Jae Kim,[1] Jun Pil Hwang,[1] Chang-geun Cho,[2] and Ki Hwan Kim[1]

[1]*Department of Civil and Environmental Engineering, Hanyang University, Ansan 15588, Republic of Korea*
[2]*School of Architecture, Chosun University, Gwangju 61452, Republic of Korea*

Correspondence should be addressed to Ki Yong Ann; kann@hanyang.ac.kr

Received 7 October 2016; Revised 21 December 2016; Accepted 26 January 2017; Published 16 February 2017

Academic Editor: Rishi Gupta

To predict the durability of a concrete structure under the coupling degradation consisting of the frosting and chloride attack, microstructural analysis of the concrete pore structure should be accompanied. In this study, the correlation between the pore structure and chloride migration for OPC concrete was evaluated at the different cement content in the concrete mix accounting for 300, 350, and 400 kg/m^3 at 0.45 of a free water cement ratio. The influence of frosting damage on the rate of chloride transport was assessed by testing with concrete specimens subjected to a rapid freezing and thawing cyclic environment. As a result, it was found that chloride transport was accelerated by frost damage, which was more influential at the lower cement content. The microscopic examination of the pore structure showed that the freezing environment increased the volume of the large capillary pore in the concrete matrix.

1. Introduction

Concrete structures such as concrete pavements and concrete bridge decks in the cold climate often experience the deicer to mitigate the slipperiness of the pavement surface arising from snowing. Sodium chloride (NaCl) salt and calcium chloride ($CaCl_2$) are the representative deicers, which however imposes a potential risk of chloride-induced corrosion of steel in the concrete structure. Steel embedment in concrete is usually protected from the risk of corrosion by a thin oxide layered film, the so-called "γ-Fe_2O_3 passive film" generated in the alkaline concrete pore solution [1]. Notwithstanding, chloride ions present in the concrete, pore solution may activate the electrochemical reaction then to corrode steel [2]. Once corrosion starts on the steel surface, the volume of the steel rebar expands about 3–8 times of the original volume [3], leading to a loss of the tensile capacity of steel and spalling of cover concrete, which substantially could bring a devastating failure of the structure. Despite the risk of steel corrosion, the deicing salt is an unavoidable manner to secure the traffic condition against snowing.

Moreover, the concrete pore structure may be damaged by freezing and thawing in the cold climate. Water confined in the pore system of cement matrix, when freezing, exposes the pore walls to stresses, which might cause intense damage to the structure. In particular, in the presence of the deicing salt, the destruction of the pore structure can be accelerated. Ice bodies, which have already been formed in coarser pores, are able to attract unfrozen water from finer capillary pores and gel pores, due to the difference in free energy between ice and water [4]. Then, there would be a water transfer to the freezing site, thereby a growth of the ice body in the pores and a breakdown of cement paste surrounding the pore system (i.e., a generation of microcracking). Substantially, the frost damage may provide a better path for chloride ions to reach at the depth of the steel in concrete, as being associated with further corrosion process and thus the severer deterioration of the concrete structure may occur. However, the combined deterioration, especially about a degradation of physical property and accelerated chloride penetration induced by frost damage, has not been fully clarified.

Table 1: Oxide composition of use material.

Binder type	Oxide compositions (%)							
	CaO	SiO_2	Al_2O_3	Fe_2O_3	MgO	Na_2O	K_2O	SO_3
OPC	64.7	20.7	4.6	3.0	1.0	0.13	0.65	3.0

In this reason, the present study is concerned about the combined effect of the two deteriorations (i.e., chloride attack and frost damage) by measuring relative dynamic modulus of elasticity and the degree of chloride transport. Moreover, microstructure analysis was also conducted to verify the change of pore system during repetitive freezing and thawing condition.

2. Experimental Work

Concrete specimens were fabricated in a cylindrical (Ø100 mm × 200 mm) and cuboidal (100 × 100 × 400 mm) mould for chloride migration test and relative dynamic modulus of elasticity test, respectively. The specific gravity of the fine aggregate was 2.60 and coarse aggregate was 2.65. The maximum size of the coarse aggregate used in a concrete mix was always 10 mm to minimize the disruption of ionic transport. The ratio of the fine aggregate to total was 0.4 for all mixes. Ordinary Portland cement (OPC) was used for a binder and its oxide composition is given in Table 1.

The binder content was ranged from 300, 350 and 400 kg/m^3. The freezing and thawing test specimens generally manufactured by less than 0.35 of water-cement ratio. However, since the purpose of this study is to observe the combined deterioration induced by frost damage and chloride attack, the water-cement ratio was kept at 0.45 for all cases. Moreover, no chemical admixture such as air entrainer was used to avoid unexpected chemical reaction which can influence the test result. All concrete specimens were demoulded 24 hours after casting and cured in a chamber with 95% RH at 20 ± 2°C for 500 days of which hydration effect become negligible during the test. After curing, the concrete specimens were directly subjected to the freeze-thaw condition, followed by tests for chloride migration and microscopic investigation. For all tests, the replications were always five to cover the variation in the values. The details of each test procedure are given in the following.

2.1. Testing for Frost Damage. To emulate the frost damage on concrete, the concrete specimens were exposed to a cyclic freeze and thaw environment. The concrete specimens after 500 days of curing were allowed to rapidly freeze in the atmospheric condition and then to thaw in water in an insulting chamber. The temperature variation in the chamber ranged from 5 to −18°C. For the freezing period, the temperature of the chamber was kept at −18°C for 1.5 hours and then still water was supplied to thaw the specimens by increasing the temperature back to 5°C within 5.0 h. The freezing and thawing rate were kept at 10°C/h. The cyclic freeze and thaw were repeated up to 60, 120, and 180 cycles. The details of testing procedure are given elsewhere [5].

The relative dynamic modulus of elasticity of concrete specimens was measured to detect internal degradation by applying ultrasonic pulse. The test was conducted at 60, 120, and 180 cycles of freeze and thaw, accompanied with chloride migration test and MIP.

2.2. Testing for Chloride Migration. Cylindrical concrete specimens sawed off to produce a disc sample with 50 mm in the thickness, after the completion of curing for 500 days. The specimen was connected to two chambers filled with 10.0% NaCl and with 0.3 M sodium hydroxide (NaOH) solutions, respectively, to form an electric cell. A direct current at 30 V was applied to the cell for 30 hours.

After applying the current, the specimens were axially split into two pieces and 0.1 M silver nitrate ($AgNO_3$) solution was sprayed on the surface of the split section to form the visible precipitation of silver chloride (AgCl). The depth of the precipitation of silver chloride was measured by a ruler four times and then the average value was chosen as the chloride penetration depth. Then, the migration coefficient was calculated by (1), derived by the Nernst-Plank equation. The detailed procedure for measuring the chloride migration coefficient is given elsewhere [6].

$$D_{\text{mig}} = \frac{0.0239\,(273 + T)\,L}{(U - 2)\,t} \left\{ X_d - 0.0238 \sqrt{\frac{(273 + T)\,L X_d}{U - 2}} \right\}, \tag{1}$$

where D_{mig} is migration coefficient, $\times 10^{-12}$ m^2/s; U is applied voltage, V; T is temperature of the cell, °C; L is thickness of the specimen, mm; X_d is chloride penetration depth, mm; t is test duration, hour.

2.3. Testing for Microscopic Examination. Deformation of pore structure after severe freeze-thaw environment was examined using mortar sample, not to reflect the distortion effect of coarse aggregate. The mortar samples, after 500 days of curing, were crushed to obtain the middle of specimen, which may form a homogeneous pore matrix. Then, the sample was dried out in an oven at 50°C for 7 days to liberate water content inside of the material that might otherwise give undesired test result. The sample was initially evacuated to about 50 μm mercury (Hg) and the low pressure was generated up to 0.21 MPa by nitrogen gas, and then the pressure was gradually increased to 117.21 × 10^3 MPa at the rate of 9.1 × 10^3 kPa/s. The pressure was converted to the

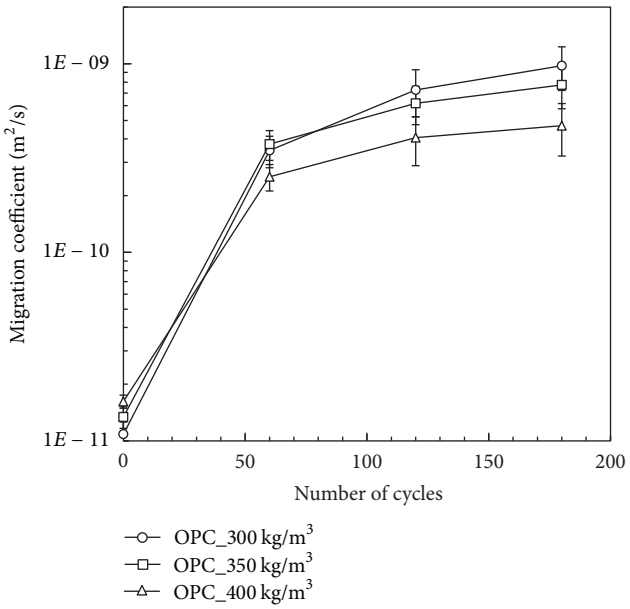

Figure 1: Migration coefficient for concrete after frosting depending on binder content.

equivalent pore diameter using the Washburn equation as given in (2). Then the pore volume distribution at a given pore diameter was obtained. The pore volume was adjusted to the percentage of the volume of each sample.

$$d = \frac{-4\gamma \cos\theta}{P}, \tag{2}$$

where d is pore diameter, m; γ is surface tension, N; θ is contact angle, °; P is pressure, MPa.

3. Result and Discussion

3.1. Frost Damage. After an exposure of concrete specimens to different cyclic durations for freeze and thaw (i.e., 0, 60, 120 and 180 cycles), the migration coefficient of chloride ions of the specimens was calculated by (1), as given in Figure 1. The initial migration coefficient for 300, 350, and 400 kg of cement content was 0.109×10^{-10}, 0.134×10^{-10}, and 0.162×10^{-10} m^2/s, respectively, before being subjected to a freeze and thaw cyclic environment. The migration coefficients increased with the number of cycles, irrespective of cement content. This implies that the pore structure was presumed to turn more porous in the process of freeze and thaw, due to the internal pressure generated by ice formation in the pore solution, which could, in fact, enhance the connectivity between capillary pores including even isolated pores. Thus, continuous pore fractions can be used for chloride ions to increase the mobility through the pores. Furthermore, a reduction of the concrete surface in the process of freeze and thaw could produce further porosities, in terms of cracking of cover concrete, which provides additional paths for chloride transport. It is notable that, at a high number of freeze and thaw cycles, the rate of chloride penetration was less increased. At the initial cycles, up to 60, the migration coefficient was more rapidly increased, compared to longer exposure period, from 60 to 180. For example, the migration coefficient for 300 kg of cement content was 3.47×10^{-10} m^2/s at 60 cycles and reached 9.77×10^{-10} m^2/s after 180 cycles. This may be attributed to limited deterioration of cover concrete arising from freeze and thaw cyclic conditions. An increase in the pore connectivity and cracking-originated pores may result from frost damage more or less, and however, after a certain level of deterioration, the pore structure may be stably sustained with no increase in the capillary pores. Then, ionic transport would be less influenced by the number of freeze and thaw cycles in a long term.

It is evident that increased cement content in the concrete mix was more resistant to chloride migration under frost damage. It was observed that an increase in the cement content resulted in a lower migration coefficient with cycles of freeze and thaw. In fact, there was a marginal variation in the migration coefficient with cement content at no exposure to freeze and thaw condition. Then, with increasing the cycles of freeze and thaw, the higher cement content in mix produced the lower migration coefficient. For example, at 180 cycles, the migration coefficient for 300, 350, and 400 kg/m^3 of cement accounted for 9.77×10^{-10}, 7.73×10^{-10}, and 4.70×10^{-10} m^2/s, respectively. It may reflect that the higher cement content may resist the frost damage. As a given free water cement ratio (0.45) was used in concrete mixes, no possibility of the variation in the pore structure could be achieved, as long as the pores are assumed to be produced in the cement matrix. However, the higher cement content, in turn, implies the lower aggregate content and thus lowers interfacial porosity between cement paste and aggregate, which is usually vulnerable to frost damage. Thus, the higher cement content in the concrete mix may be more resistant to frost damage in terms of increased porosities, in particular, connectivity between capillary pores.

This phenomenon can be confirmed by measuring the relative dynamic modulus of elasticity of concrete subjected to freeze and thaw cycles, as given in Figure 2. An increase in the cycle numbers of freeze and thaw resulted in a decrease in the relative dynamic modulus of elasticity, irrespective of cement content. However, concrete at the lower cement content produced a more rapid reduction of the relative dynamic modulus of elasticity at a given number of the freeze and thaw cycles. For example, for 300 kg/m^3 of cement content, the relative dynamic modulus of elasticity accounted for 88.29, 72.32, and 49.39% of elasticity at 60, 120, and 180 cycles, whilst 400 kg/m^3 produced 87.55, 75.28, and 58.59% at the equivalent cycles. Thus it can be said that the higher cement content may benefit in raising the resistance to frost damage at a given free water cement ratio, except for the use of air-entraining agents. Notwithstanding, all specimens did not maintain the minimum level for the relative dynamic modulus of elasticity to secure the safety of the structure, accounting for 60% at 300 cycles; in fact the relative dynamic modulus of elasticity was lower than 60% at 180 cycles due to the absence of air entraining agent and the higher water-cement ratio rather than guided values.

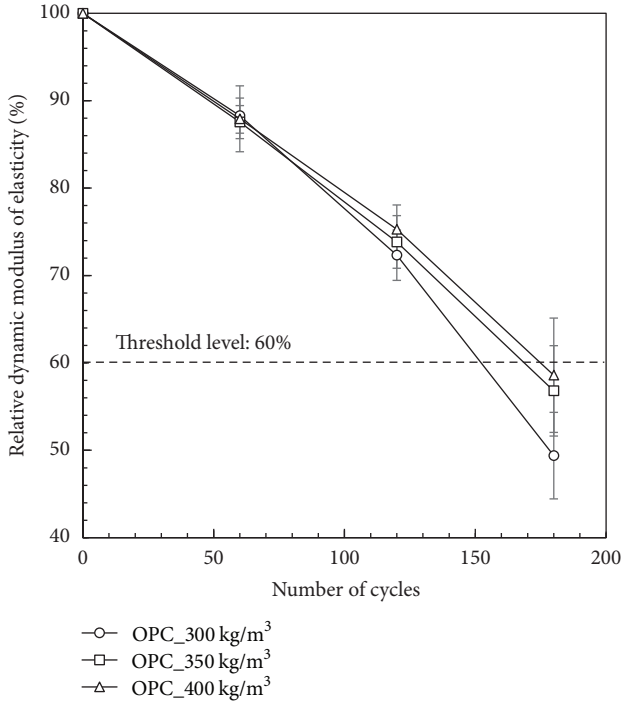

Figure 2: The relative dynamic modulus of elasticity under freeze-thaw condition.

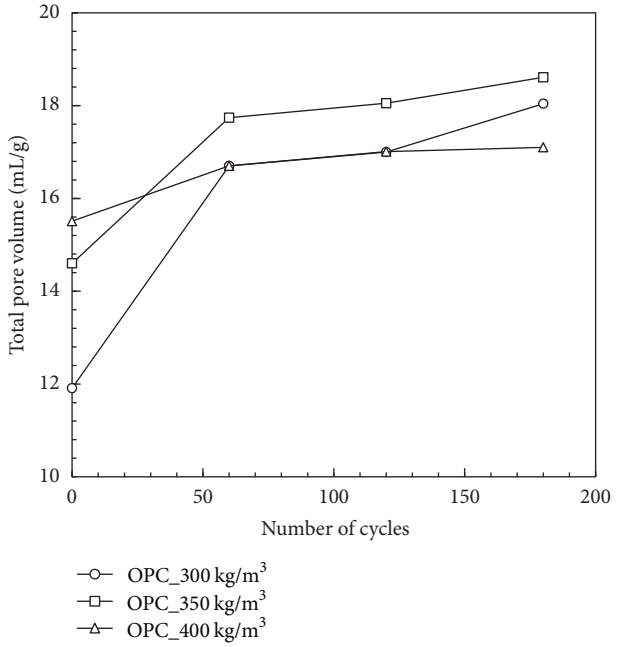

Figure 3: Total pore volume for 300, 350, and 400 kg/m^3 of cement content at 0, 60, 120, and 180 cycles.

3.2. Pore Structure Analysis. To ensure a modification of the porosity under freeze and thaw damage, the pore structure was examined by the mercury intrusion porosimetry (MIP). The total pore volume was obtained at each cycle and cement content as given in Figure 3. It is evident that cement content was crucial in increasing the total pore volume; the initial porosity was 11.91, 14.60, and 15.51 mL/g for 300, 350, and 400 kg/m^3 of cement content, respectively. However, after 180 cycles of freezing and thawing, the total pore volume was changed to 18.04, 18.61, and 17.10 for 300, 350, and 400 kg/m^3 of cement content, respectively. This may be attributed to the resistance of porosity or/and air bubble to frost damage. In fact, increased porosity may buffer internal stress arising from freezing the pore solution in the pores and thus frost damage could be mitigated. The higher porosity may benefit in lowering breakage of pore network, resulting from freeze and thaw cycles. Additionally, it was observed that an increase in the porosity was observed at 60 cycles rather than subsequent cycles, at which there was no significant change in the total pore volume for 350 and 400 kg/m^3 of cement content and only marginal increase was observed for 300 kg/m^3 of cement content. It implies that the crack-induced porosity would be formed at an early stage of freeze and thaw cycles, which would buffer subsequent internal stress from freezing the pore solution and thus no further formation of cracking was formed.

The pore size distribution was used to determine modification of pore structure change after frost damage, as given Figure 4. The pore diameter of pore at the highest peak (i.e., critical diameter) was determined, and simultaneously, pores were classified by the size as small capillary ($d < 0.1\,\mu$m), large capillary ($0.1 < d < 10\,\mu$m), and macropores ($d > 10\,\mu$m). At 0 cycle, the peak of porosity was observed at about 0.5–0.7 μm in the diameter. It was seen that the pore volume was strongly dependent on large capillary pore, of which the volume accounted for 4.32, 5.12, and 6.95 mL/g, respectively, and 300, 350, and 400 kg/m^3 of cement with no exposure to freeze and thaw cycles. With increasing cycles of freeze and thaw, the volume of large capillary pore was significantly increased, compared to other sizes of pores. This may be due to the fact that crack formed in the process of freeze and thaw would be equated to the large capillary pores in size. The other pores were also modified by the freeze and thaw. For example, the breakage of small capillary pore was reduced by suspended pressure in the pore network, which in turn gave relatively lower expansive force [7]. It is notable that freeze and thaw cycles were influencing critical pore diameter, which was, for example, 0.045, 0.072, 0.088, and 0.095 μm at 0, 60, 120, and 180 cycles of freeze and thaw, respectively, for 300 kg/m^3 of cement. The shift of peak diameter was commonly observed in all cement contents. Thus, small capillary pore has only marginal impact from freeze and thaw in the total volume. The macropore may reflect the resistance to frost damage in terms of spacing factor [8], which can be defined as average length of connected small pores with voids. Thus, ice formation may largely affect the macro pore wall but the degree of degradation become reduced as capillary pore fraction increases.

3.3. Combined Degradation. As a parametric value of frost damage, the volume of large capillary pore at each cycle was used to relate the migration coefficient as given in Figure 5.

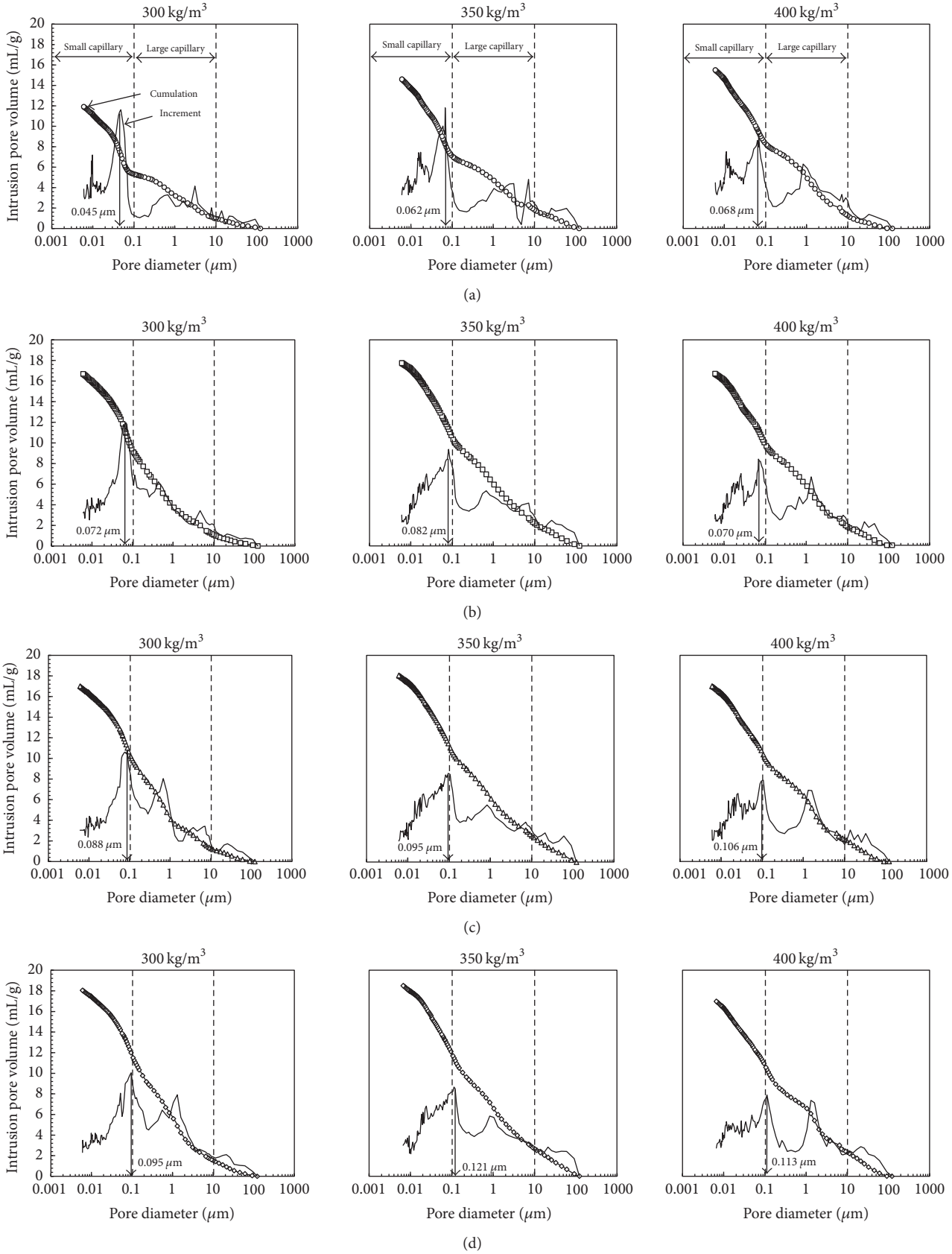

Figure 4: Pore-size distribution for 300, 350, and 400 kg/m^3 of cement content at (a) 0, (b) 60, (c) 120, and (d) 180 cycles.

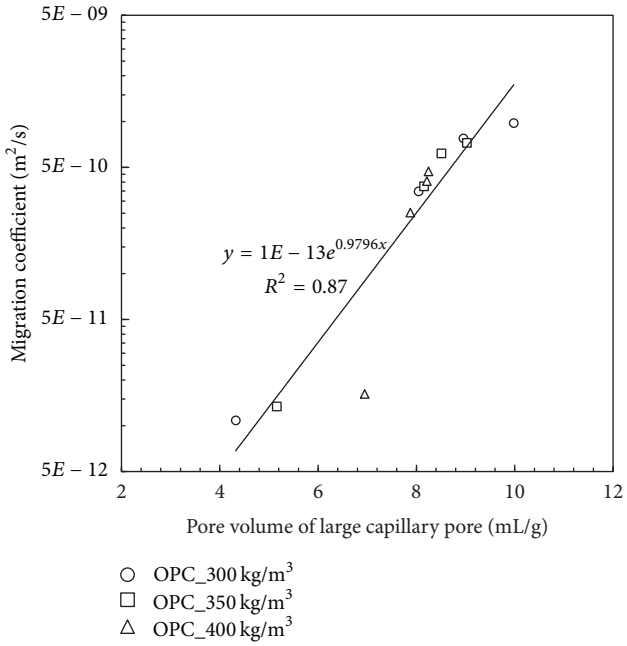

Figure 5: The relation between chloride migration coefficient and pore volume of large capillary pores for three different cement content in the concrete mix at freeze-thaw environment.

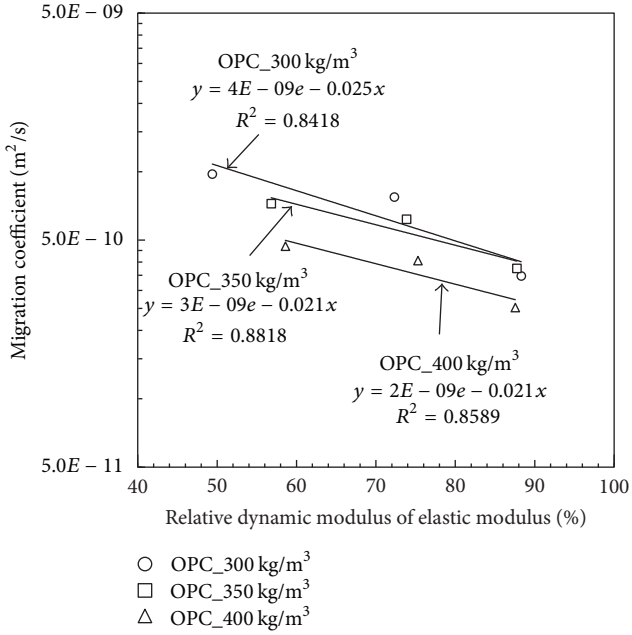

Figure 6: The relation between chloride migration coefficient and relative dynamic modulus of elasticity.

It is seen that there was a linear relation between the large capillary pore volume and migration coefficient. It has an important implication in predicting the corrosion risk of concrete under coupling degradation of frost damage and chloride attack. The pore distribution is usually influenced by a free water cement ratio and binder type (i.e., highly grained pozzolanic materials). However, in this study, the pore volume, in particular, large capillary pores, were further generated by the freeze and thaw cyclic condition. Substantially, an increase in the large capillary pores resulted in an increase in the chloride migration. Once a certain level of capillary pores was generated/produced by the freeze and thaw condition, the cement content had a marginal influence on chloride migration. The critical pore is regarded as the smallest pore that can complete the connection of pores to form pore network. Thus, a further formation and generation of pores in terms of increased critical pore diameter during freeze and thaw cycles may increase the penetration of chloride ion. Additionally, the critical pore diameter is crucial on concrete permeability [9, 10].

The relation between the chloride migration coefficient and relative dynamic modulus of elasticity was depicted in Figure 6. The relative dynamic modulus of elasticity was strongly influenced by the cement content; an increase in the cement content resulted in an increase in the relative dynamic modulus of elasticity at a given cycle of freeze and thaw. Substantially, a reduction of the relative dynamic modulus of elasticity was accompanied by increased migration of chloride ions. It is evident that the higher cement content concrete imposed the low increasing rate of chloride migration coefficient. Thus, to protect steel from corrosion in concrete, the relative dynamic modulus of elasticity also must be kept high against freezing climate, for example, the concrete pavements or bridge deck exposed to the deicing salts in the cold climate. It suggests that the higher cement content could benefit in lowering frost damage and thus mitigating the rate of chloride transport after the frost damage.

4. Conclusion

In this study, the coupling degradation of concrete, when exposed to a chloride and frost environment, was assessed by experimental works using OPC. Concrete and mortar specimens were exposed to a cyclic freeze-thaw environment to induce the frost damage, and then the chloride migration and pore structure were examined. The freeze and thaw was repeated up to 180 cycles to meet the quality of concrete specimens for chloride transport. The conclusion obtained from experiments is given as follows:

(1) With no frost damage, the rate of chloride transport in terms of migration was increased by cement content at a given free water cement ratio, which could increase the porosity of the concrete matrix, arising from an increase in the amount of cement paste.

(2) When concrete is subjected to chloride permeation and frost damage, the rate of chloride transport was increased by the number of cycles of freeze and thaw; especially a rapid increase was sighted up to 60 cycles, presumably due to increased large capillary pores produced by microcracking in the cement matrix.

(3) Furthermore, the higher cement content lowered the rate of chloride transport at a given number of cycles of freeze and thaw, since the cement contents increase

the porosity to resist against frost damage. Substantially, higher cement contents in concrete benefits against the freeze and thaw environment and thus chloride permeation.

Competing Interests

The authors declare that they have no competing interests.

Acknowledgments

This research was supported by Basic Science Research Program through the National Research Foundation of Korea (NRF) funded by Ministry of Science, ICT & Future Planning (no. 2015R1A5A1037548) and a grant (16RDRP-B076268-03) from R&D program funded by Ministry of Land Infrastructure and Transport of Korea government.

References

[1] C. L. Page, "Mechanism of corrosion protection in reinforced concrete marine structures," *Nature*, vol. 258, no. 5535, pp. 514–515, 1975.

[2] K. Y. Ann and H.-W. Song, "Chloride threshold level for corrosion of steel in concrete," *Corrosion Science*, vol. 49, no. 11, pp. 4113–4133, 2007.

[3] A. M. Neville, *Properties of Concrete*, Longman Group Ltd, Harlow, UK, 4th edition, 1997.

[4] G. Fagerlund, "On the service life of concrete exposed to frost action," in *Freeze-Thaw Durability of Concrete*, J. Marchand, M. Pigeon, and M. Setzer, Eds., pp. 23–41, E & FN Spon, London, UK, 1997.

[5] ASTM C 666, "Standard test method for resistance of concrete to rapid freezing and thawing," ASTM International, 2003.

[6] NT Build 492, "Concrete mortar and cement-based repair materials," Nordtest method, Nordtest, Espoo, Finland, 1999.

[7] B. Zuber and J. Marchand, "Modeling the deterioration of hydrated cement systems exposed to frost action—Part 1: description of the mathematical model," *Cement and Concrete Research*, vol. 30, no. 12, pp. 1929–1939, 2000.

[8] K. A. Kalliopi, *Pore Structure of Cement Based Materials Testing, Interpretation and Requirement*, Taylor & Francis, Oxfordshire, UK, 1st edition, 2006.

[9] L. Cui and J. H. Cahyadi, "Permeability and pore structure of OPC paste," *Cement and Concrete Research*, vol. 31, no. 2, pp. 277–282, 2001.

[10] P. Halamickova, R. J. Detwiler, D. P. Bentz, and E. J. Garboczi, "Water permeability and chloride ion diffusion in portland cement mortars: relationship to sand content and critical pore diameter," *Cement and Concrete Research*, vol. 25, no. 4, pp. 790–802, 1995.

Hindawi
Advances in Materials Science and Engineering
Volume 2017, Article ID 3928047, 12 pages
https://doi.org/10.1155/2017/3928047

Research Article

Effects of Particle Size and Cement Replacement of LCD Glass Powder in Concrete

Seong Kyum Kim,[1] Su Tae Kang,[2] Jin Kwang Kim,[3] and Il Young Jang[4]

[1]*Department of Civil and Environmental Engineering, Hanyang University, 55 Hanyangdaehak-ro, Sangnok-gu, Ansan, Gyeonggi-do 15588, Republic of Korea*
[2]*Department of Civil Engineering, Daegu University, 201 Daegudae-ro, Jillyang, Gyeongsan, Gyeongbuk-do 38453, Republic of Korea*
[3]*Safety and Disaster Management Division, Korea Expressway Corporation, 77 Hyeoksin 8-ro, Gimcheon, Gyeongbuk-do 39660, Republic of Korea*
[4]*Department of Civil Engineering, Kumoh National Institute of Technology, 61 Daehak-ro, Gumi, Gyeongbuk-do 39177, Republic of Korea*

Correspondence should be addressed to Il Young Jang; jbond@kumoh.ac.kr

Received 7 October 2016; Accepted 28 November 2016; Published 30 January 2017

Academic Editor: Kazunori Fujikake

The high quality liquid crystal display (LCD) processing waste glass (LPWG) generated from the manufacturing process of Korea's LCD industries, having the world's highest technological level and production, was finely ground into particles smaller than cement particles (higher fineness than OPC) to verify their applicability and performance as a replacement for cement. For a concrete mix having a W/B ratio of 0.44, cement was replaced with LPWG glass powder (LGP) at ratios of 5, 10, 15, and 20% (LGP12) and 5 and 10% (LGP5) according to the particle size to prepare test cylinder specimens, which were tested with respect to air contents, slump in fresh concrete, and compressive strength and splitting tensile strength of hardened concrete. The microstructure of the concrete specimens was analyzed through Scanning Electron Microscopy (SEM), Energy Dispersive X-ray (EDX), and a Mercury Intrusion Porosimetry (MIP). Replacement of cement with LGP for cement could effectively decrease the quantity of cement used due to the excellent performance of LGP. It may positively contribute to the sustainable development of the cement industry as well as waste recycling and environment conservation on a national scale.

1. Introduction

The 21st century's concrete and cement technology requires various functions, durability, and quality stability to attain sustainability, environment-friendliness, high performance, high strength, and economic feasibility. In harmony with these requirements, many researchers have made efforts to reduce the utilization of cement and to maximize the performance [1–4]. In particular, liquid crystal display (LCD) waste glass has been produced in a large amount due to the development of the display industry. The international display market share was 39.2% in Korea, 27.4% in Taiwan, 15.5% in China, and 17.9% in other countries in 2015. Korea's investment in the LCD industry is as high as 27 billion USD per year, and the production in Korea is 480,000 panels per month (the 8th generation, 50 inches), which is the highest in the world. On the basis of the production of mobile devices, such as smartphones and tablet PCs, and the future demand, LCD production is predicted to continuously increase. Accordingly, the amount of waste LCD has increased since the early 2000s to reach 2 million panels or more in 2015, and the weight of waste LCD generated each year is about 460,000 tons [5]. As most waste LCD is incinerated or buried, it wastes resources and causes various types of environment pollution on a national scale [6].

LCD waste glass is classified into three categories: (1) LCD cullet, (2) LCD waste glass, (LPWG), and (3) end of life (EOL) LCD waste glass. LPWG, used in this study, is waste glass generated from LCD manufacturers due to defects in processing and cutting or bonding in the LCD

Table 1: Physical properties of cement.

Specific gravity	Blaine (cm^2/g)	Stability (%)	Setting time		Compressive strength (MPa)		
			Initial (min)	Final (min)	3 days	7 days	28 days
3.15	3,450	0.04	205	295	29.5	43.8	58.9

Table 2: Physical properties of sand and aggregate.

	Fineness modulus (FM)	Water absorption (%)	Weight of unit volume (kg/m^3)	Specific Gravity	Others
Fine aggregate	2.92	2.40	1,597	2.60	Pass 2.2% (#200 sieve)
Coarse aggregate	7.27	0.6	1,648	2.65	20 mm (D_{Max})

Table 3: Mix proportions of concrete with WLGP.

W/C (%)	Unit water content (kg/m^3)	S/a (%)	LCD glasses powder content (%)		By the mass of binder (kg/m^3)				
					C	S	G	LGP	SP
44	175.03	43.7	OPC		397.8	705.3	943.1	0	3.9
			12 μm	5	377.9			19.9	3.7
				10	358.0			39.8	3.5
				15	338.1			59.7	3.3
				20	318.2			79.6	3.1
			5 μm	5	377.9			19.9	3.7
				10	358.0			39.8	3.5

manufacturing process. Such elements as Cu, Mn, Mo, and Fe may exist at a ppm level on the glass surface due to chemical processing in the manufacturing process. LCD products including these elements may not be recycled due to product quality degradation that occurs during remelting, and thus they are incinerated or buried. About 40,000 tons of LPWG in 2015, which is unavoidable waste from the LCD manufacturing process, is generated each year, and the amount of generated LPWG is dependent on the LCD market size [7].

Studies on waste glass as a replacement material for cement have been conducted with soda-lime glass, which may cause expansion or cracking through a reaction of alkalis (Na and K), which are contained in considerable amounts in soda-lime glass, with silica (SiO_2) [8]. Considering the alkali-silica reaction is very important when using a material for the replacement of cement. However, the dependency of the reactivity of glass on the type, components, and physical properties of glass should also be taken into account [9]. In particular, ground glass powder, as a Pozzolanic material, has an effect of reducing alkali-aggregate reaction (AAR) and inhibiting alkali-silica reaction (ASR) in the paste [10, 11]. The LCD used in this study may be appropriately used as a replacement material for cement because the LCD is free of alkalis (particularly Na) due to the intended use of the LCD product and has constant material quality [12, 13]. In addition, the LCD contains SiO_2 as the main component, which is similar to silica fume (SF), fly ash (FA), and blast furnace slag (BS) that enable improved Pozzolanic reactivity [14, 15]. Many researchers have recently investigated LCD because of these advantages. In particular, many reports have been published in Taiwan, which has the second highest LCD market share in the world. Most of the research conducted in Taiwan has been focused on methods of replacement LCD as an aggregate. Studies about using LCD as a replacing material for cement have not been conducted sufficiently yet [16–20]. In this study, LPWG generated in the manufacturing process of glass for LCD was investigated experimentally to improve the properties and performance as a replacement material for cement or as a binder for concrete.

2. Materials and Methods

2.1. Materials. The cement complied with KS L 5201 Ordinary Portland Cement. The physical properties of the cement are shown in Table 1. And, the standard sand was used as fine aggregate. Aggregate has a 20 mm nominal maximum size (D_{max}) which was used as coarse aggregate. The physical properties of the aggregates are shown in Table 2. LPWG powder (LGP) was provided by Inno Co. Ltd. in Korea. The pure alkali-free glass is used only, such as 0.4~1.1 mm the average film thickness and the other chemical compositions are not indicated. Also, two different types of LGP, according to the average diameter and fineness, were used in this study. It was ground separately through the ball mill to distinguish the spread of two different diameter; its density is 2.79.

2.2. Specimens and Test Variables. The concrete mixer was used to make cylindrical specimens such as Table 3. After the dry mixing was completed, admixture and water were added to the concrete mix. Two types of LGP were based on the 0.44 W/B ratio. It was replaced every 5% by the mass of OPC up to 20% (LGP12), such as 5%, 10%, 15%, and 20%, for the effective and efficient performance as a replacement of cement [4, 16, 20]. In addition, a total of seven types of the specimens were

Table 4: Test method for concrete with LGP.

Test item for concrete	Test method (KS, Korea Standard)	Reference (ASTM)
Fresh concrete		
Air content	KS F 2421	ASTM C 231
Slump	KS F 2402	ASTM C 143
Hardened concrete		
Compressive strength	KS F 2405	ASTM C 39
Splitting tensile strength	KS F 2423	ASTM C 496
Microstructure		
SEM	—	—
EDX	—	—
MIP	—	—

made, including two different types of specimens that were replaced by high fineness LGP (LGP5) such as 5% and 10%. Water reducing admixture (superplasticizer, SP) based on Polycarboxylate (Dongnam Ltd. Co. FlowMix 3000S, specific gravity: 1.05 ± 0.05, pH: 5.0 ± 1.5) was added at 1% for a high strength and improving the workability of concrete. The specimens were followed by KS F 2403 specification which made 100 × 200 mm cylindrical concrete specimens and it cured for 24 hours in the mold. After that, specimens were cured in moist curing chamber (21 ± 2°C, 100% RH) for the each necessary period, such as 3, 7, 14, and 28 days.

2.3. Analysis Methods. LGP concrete specimens including OPC concrete were performed following test of the fresh and hardened concrete. The tests applied in this study to investigate the properties of concrete containing LGP as cement replacement are shown in Table 4.

(1) Test for Air Content of Fresh Concrete by Pressure Method. The measuring steel vessel had a capacity of 7 L and a minimum diameter equal to 0.75 to 1.25 times height of cylindrical in shape. Working pressures of 7.5 to 30.0 psi (51 to 207 kPa) had been used satisfactorily.

(2) Test for Slump of Concrete. The following form of mold shell was used in this test: the top, 100 mm in diameter; the base, 200 mm in diameter; the height, 300 mm; and the thickness, 1.5 mm. After the mold is removed immediately from the concrete by raising it, we measured its collapsed height.

(3) Test for Compressive Strength of Concrete. The specimens were made by following the KS F 2403 and measured by a consistent load of added force (0.6 ± 0.4 MPa/s) until the specimens were the failure from the compression tester. 7 types of specimens were conducted on 3, 7, 14, and 28 days.

(4) Test for Splitting Tensile Strength of Concrete. The specimens were made by following the KS F 2403 and measured by a consistent load of added force (0.06 ± 0.04 MPa/s) until the specimens were the failure from the UTM tester. 7 types of specimens were conducted on 28 days.

(5) SEM-EDX. Through the scanning electron microscope (SEM), which was able to use EDX (energy dispersive X-ray), we confirmed the microstructure of LGP concrete. The cement paste was observed in the hydration process and we analysed compositions of the specific point in image. The equipment "JSM-6500F" was made by "JEOL" that supported 0.5 kV~20 kV, 1.5 nm (15 kV). It was conducted 7 types of specimens on 3 and 28 days.

(6) MIP. In order to confirm the internal pore size and pore distribution of the concrete specimens on the 7 and 28 days, it was measured by the Mercury Intrusion Porosimetry (MIP) method after using the 24-hour drying oven. The equipment "POROSIMETER" was made by "Micromeritics" that supported 60,000 psi of maximum pressure and 0.003~360 μm range of pore size.

3. Results and Discussion

3.1. Characteristics of LGP. LGP as a replacement for cement was classified into two types depending on particle size. High fineness of the glass power may enable improved Pozzolanic activity, and the particle size is a critical parameter regarding the characteristics of the Pozzolanic reaction [21]. Therefore, the first type of LGP12 was prepared as particles size of 12.651 μm, which is similar to that of cement, and the second type LGP5 with fine particles size of 5.807 μm with particle size about two times smaller than that of cement. Both types of LGP contained fine powder smaller than 1 μm. Figure 1 shows the particle size distribution of the two LGP types.

LGP used in the experiment was prepared by using a Ball mill to obtain an average particle size smaller than that of OPC in order to increase the applicability and performance as a replacement for cement. While the size of the smallest particles of OPC is about 3 to 5 μm, LGP used in test included some particles having a size smaller or slightly greater than 1 μm. In other words, the fine powder of LGP is smaller than OPC, although the pattern of the particle size distribution of the LGP was similar to that of OPC. The smaller particle size of LGP may help to improve the strength and durability of the cement paste in a concrete, either physically or chemically, as LGP contributes the role of filler or participates in the Pozzolanic reaction [21]. Figure 2 shows SEM images of the cement and the two types of LGP. Since the magnification of all the images is 1,000 times, the size of the particles may be compared with each other. As shown in Figure 2, the particle size of the LGP was smaller than that of OPC, and the LCP particles were smooth on the surface but rough at the edges. Table 5 indicates the chemical properties of LGP and compares the compositions with those of OPC. The basic chemical compositions of the LGP were SiO_2 (60.1%) and Al_2O_3 (16.1%). LGP having low alkali content and a rich SiO_2 content may be hydrated with more $Ca(OH)_2$ to enhance the Pozzolanic reaction.

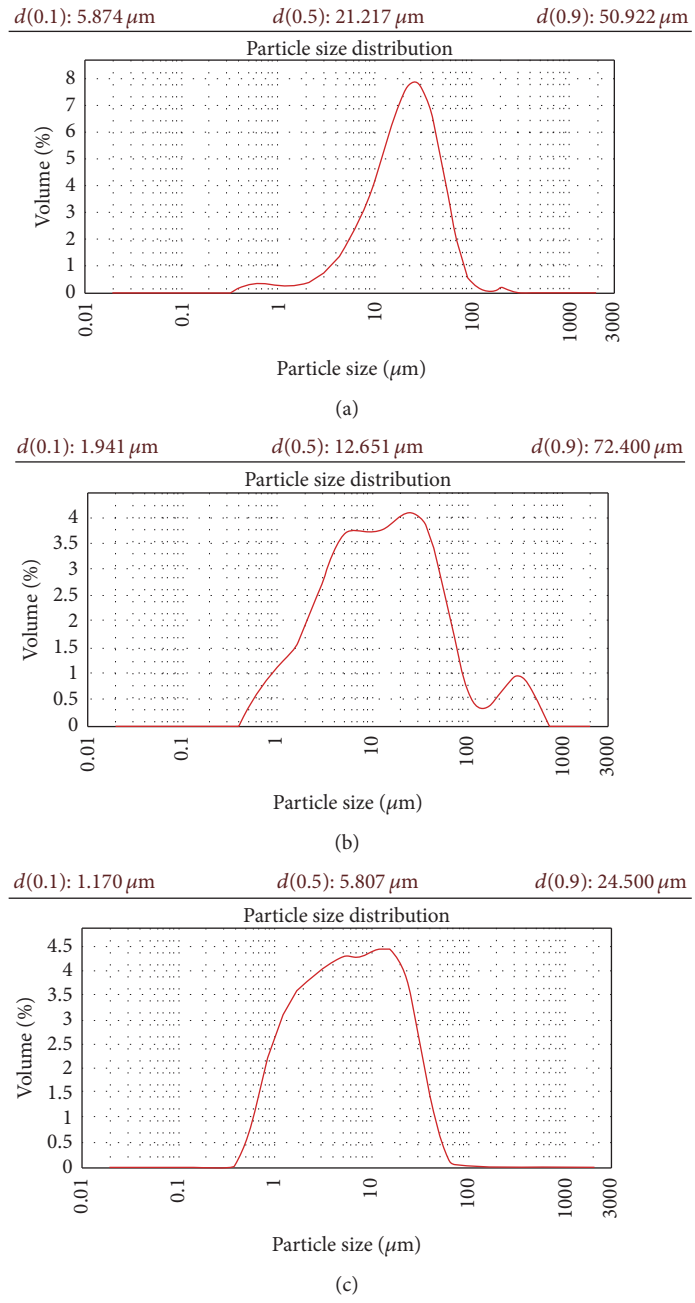

Figure 1: Particle size distributions of OPC (a), LGP12 (b), and LGP5 (c).

3.2. Air Content. Figure 3 shows the air content depending on LGP particle size and replacement. The overall air content was from 1.8% to 2.4%, which was lower than that of OPC. Comparison of the air content between LGP of different sizes showed that the air content was higher in LGP5 than in LGP12. Comparison of the air content of LGP with different replacement ratios showed that the air content was reduction in the LGP having a replacement ratio up to 10%. Soliman and Tagnit-Hamou replaced cement with fine glass powder (with a particle size less than 30 μm) in high-strength concrete (containing PC based SP admixture) at a replacement ratio from 10% to 50%, by increments of 10% and reported that the air content was increased by 0%, 10.52%, 7.89%, 10.53%, and 23.68%, respectively [22]. The high specific surface area, nonabsorbability, and friction depending on particle form of LGP may reduce the workability when LGP replaces cement in concrete. Therefore, adding a proper amount of admixture (SP) may be appropriate to secure workability and durability of high fineness LGP.

3.3. Slump. The slump test with LGP12 having a replacement of 5% and 10% was higher than that of the other substitution amounts and OPC. Figure 4 shows result of slump with

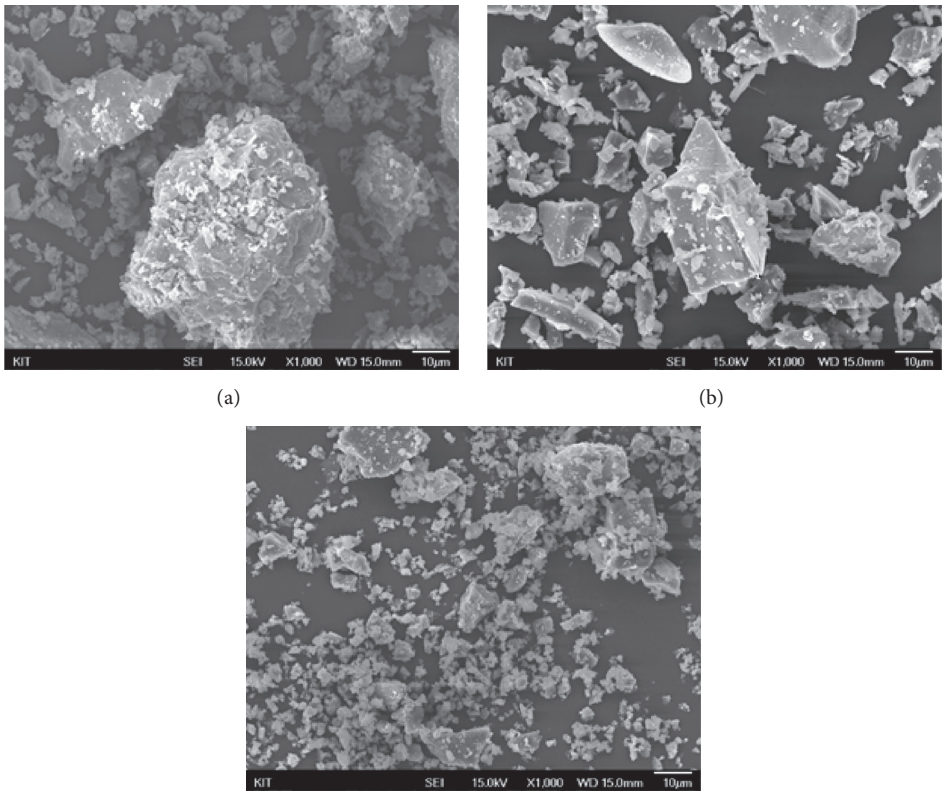

(a) (b)

(c)

Figure 2: SEM images (×1,000) of (a) cement, (b) LGP12, and (c) LGP5.

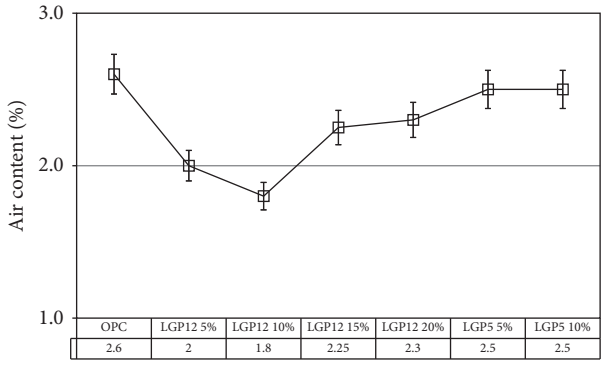

Figure 3: Air content of concrete with LGP amount.

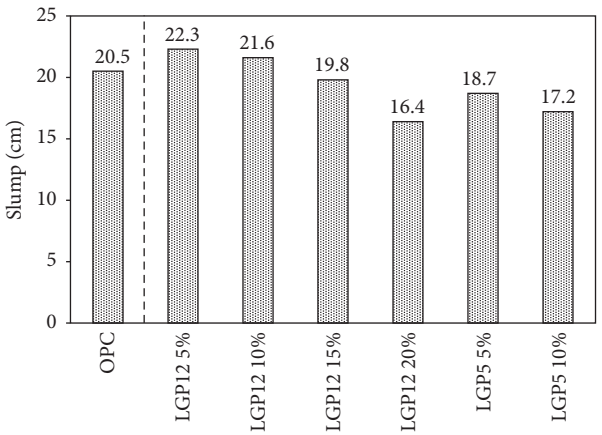

Figure 4: Slump of concrete with LGP amount.

different replacement and LGP particle size. The slump of LGP12 having a replacement of 10% was higher than that of OPC, although it slightly decreased when compared with a replacement ratio of 5%. This result indicates improved slump caused by the lower absorptivity and smooth particle surface of LGP despite the similar particle sizes [18]. However, the slump behavior in LGP12 replacement of 15% and 20% was significantly reduction. The slump of fresh concrete is influenced by the material roughness or shape even when the particle size is similar. As shown in the SEM images of Figure 2(b), the surface and the edges of LGP particle were angled and sharp. The effect of the surface roughness resulted in decrease of the slump at replacement of 15% or more. In the case of LGP5, the slump at a replacement of 5% was lower than that of OPC by 16% and the trend of decreased slump at replacement ratios of 10% or higher was similar to that of LGP12. The decrease of the slump in LGP5 may be attributed to the increase of specific area and aggregation, because LGP5 was added at a higher fineness due to the fact that larger water demand generally results in a decrease in compactness [11].

Table 5: Composition of the ordinary Portland cement and LCD glass powder by XRD.

	OPC	LCD glass powder	
		LGP12	LGP5
Fineness (cm^2/g) KS L 5106	3,450	2,729	4,462
Density (g/cm^3)	3.15	2.79	
SiO_2 (%)	21.7	60.1	
Na_2O (%)	—	0.07	
MgO (%)	3.2	0.85	
K_2O (%)	—	0.01	
Ca (%)	63.1	7.3	
Fe_2O_3 (%)	3.2	0.04	
Al_2O_3 (%)	5.7	16.1	
TiO_2 (%)	—	0.02	
ZrO_2 (%)	—	0.05	
CuO (%)	—	0.02	
BaO (%)	—	0.41	
SrO (%)	—	4.25	
SnO_2 (%)	—	0.25	
B_2O_3 (%)	—	10.1	
SO_3 (%)	2.2	—	
Ig-Loss (%)	0.9	0.43	

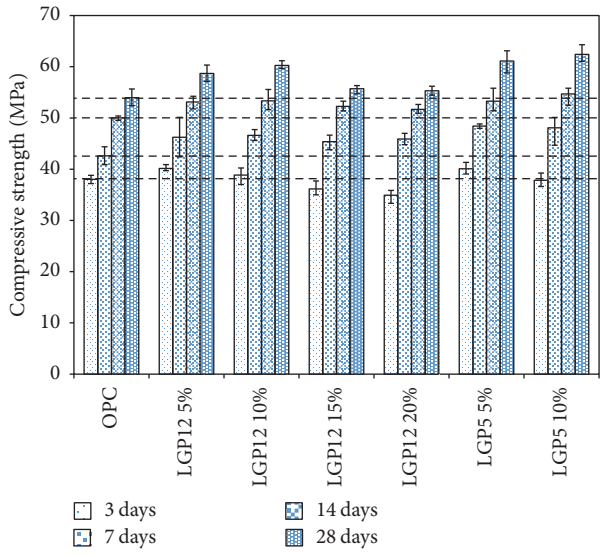

Figure 5: Comparison on each age strength development of LGP concrete cylinders.

3.4. Compressive Strength. Figure 5 shows the compressive strength of concrete at different curing days with the LGP depending on the replacement ratio for OPC. The overall compressive strength of LGP concrete was high, likely because of the water-reducing effect of an added polycarbonate admixture (SP) and the increase of the dispersion and plasticity. The effect of the environmental conditions of the experiment (specifically the curing temperature, where the average air temperature during the experiment was exceeding 38°C) should also be taken into account. Increased curing temperature accelerates the activation of Pozzolanic materials including glass powder, and then the compressive strength indicated that the glass powder had a greater effect on the Pozzolanic material activation than fly ash [23]. The compressive strength of LGP concrete specimens was generally higher than that of OPC, except in the early age (3 days). Figure 6 shows the compressive strength activity in comparison with OPC. On 3 days, the compressive strength of LGP12 replacement of 15% and 20% was lower than OPC by 4.93% and 8.17%, respectively. However, the compressive strength of all the specimens was higher than that of OPC after 7 days. The compressive strength was the highest in LGP replacement of 5%, regardless of the particle size before 14 days. However, the compressive strength was the highest in both LGP12 and LGP5 replacement of 10% after 14 days. In particular, the compressive strength of LGP5 was notably increased. This is because the Pozzolanic materials begin in earnest contribution to the Pozzolanic reaction 3 to 14 days after the hydration has begun. At that time, approximately 70% to 80% of Alite in OPC already proceeded to reaction [24]. Therefore, the Si and Al ions eluted from LGP may have reacted with the Ca ions included in the pore solution to produce C-S-H and C-A-H to make the dense and more compact. Comparison of the compressive strength with different particle sizes (LGP5 and LGP12) showed a higher compressive strength of LGP5 than LGP12 after 7 days. This result clearly showed the effect of LGP replacement on the concrete, and smaller particle size and high fineness as replacement for cement may increase not only the compressive strength but also the durability. Therefore, the Pozzolanic material activation may be enhanced by fine grounding the LGP into smaller particles [15, 25–27].

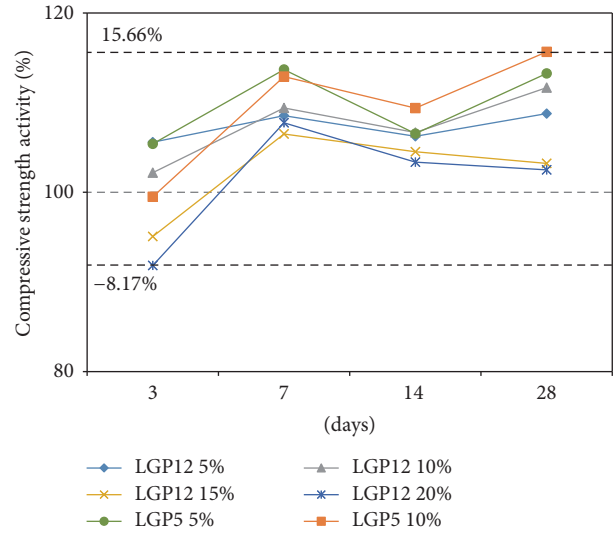

Figure 6: Relationship of compressive strength activity and age.

3.5. Splitting Tensile Strength. The splitting tensile strength of LGP concrete was similar to OPC (see Figure 7). The splitting tensile strength was increased as the compressive strength of LGP was increased. LGP12 5% showed the highest

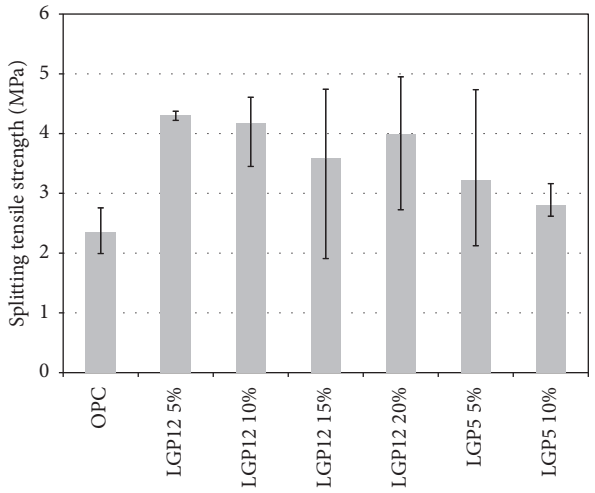

Figure 7: Comparison on splitting tensile strength of LGP concrete cylinders.

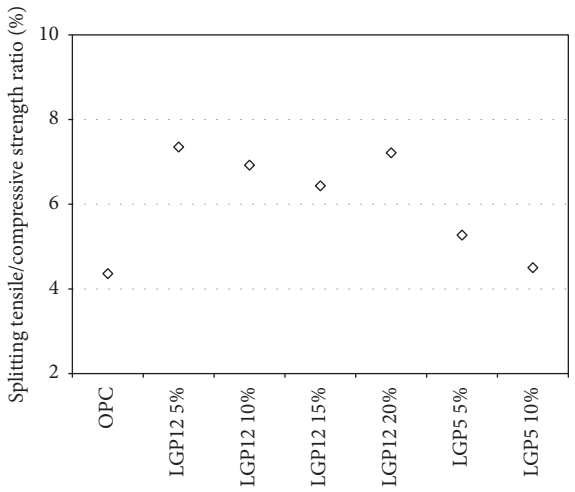

Figure 8: Relationship of splitting tensile by compressive strength ratio and LGP proportion.

splitting tensile strength, 4.31 MPa, which was 83% higher than that of OPC. LGP5 10% specimen showed the lowest splitting tensile strength, 2.81 MPa, which was 19% higher than that of OPC. However, the splitting tensile strength tends to decrease with increasing proportion of LGP replaced. Figure 8 shows relationship of splitting tensile by compressive strength ratio and LGP proportion on 28 days. LGP12 5% specimen showed the highest ratio, 7.35%. The ratio of OPC was 4.36%. Mcdonald reported the splitting tensile by compressive strength ratio in a range from 5.8% to 8.2% in concrete mixed with silica fume, a Pozzolanic material, at same ages [28]. The splitting tensile by compressive strength ratio of hardened concrete is dependent on the properties of added materials. The results showed that LGP had a positive effect on the enhancement of the splitting tensile.

3.6. Interfacial Microstructure SEM of Concrete. The interfacial microstructure of the specimens was analyzed at different

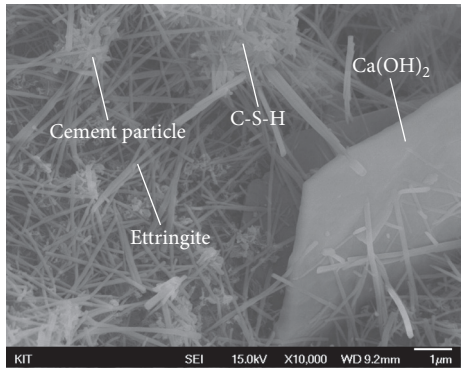

Figure 9: SEM image of OPC (3 days).

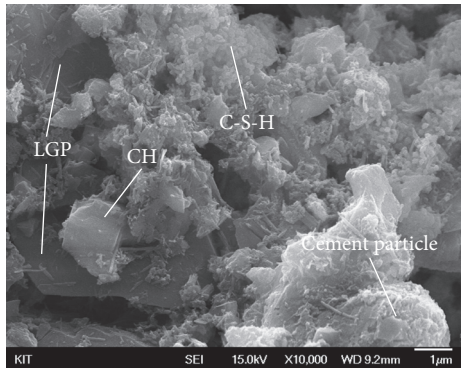

Figure 10: SEM image of composition paste which contained LGP12 10% (3 days).

ages of concrete hydration, on 3 and 28 days, by using SEM images. An EDX analysis was performed to identify the atoms and their weight ratios from the SEM images. The SEM image in Figure 9 shows the microstructure of OPC on 3 days. The OPC was hydrated in a typical manner to produce C-S-H and $Ca(OH)_2$ hydrates, but the darker regions of the image indicate that a considerable amount of water or air was included in the pores.

Figure 10 is a SEM image of LGP12 10%, and Figure 11 shows the EDX analysis results of LGP12 10%. The LGP12 10% specimen shown in Figures 10 and 11 had a cement paste structure where LGP having a material age of 3 days was substituted, as in the case of the specimen shown in Figure 9. Figure 10 verifies that the LGP particles stably existed between the C-S-H (gel) and C-H hydrates (crystals). LGP has a wave pattern on the cutting section due to the high hardness. The image of the LGP particles on 3 days showed that a significant amount of hydrates had already been generated but the LGP particles were not fully involved in the Pozzolanic reaction. This result showed that the LGP particles, unlike cement, did not immediately participate in the hydration reaction with water in early age. This indicates that a high LGP replacement ratio in concrete may have a negative effect on strength at early age. Figure 11 shows the results of the surface component investigation through EDX, indicating that it is rich in Si, O

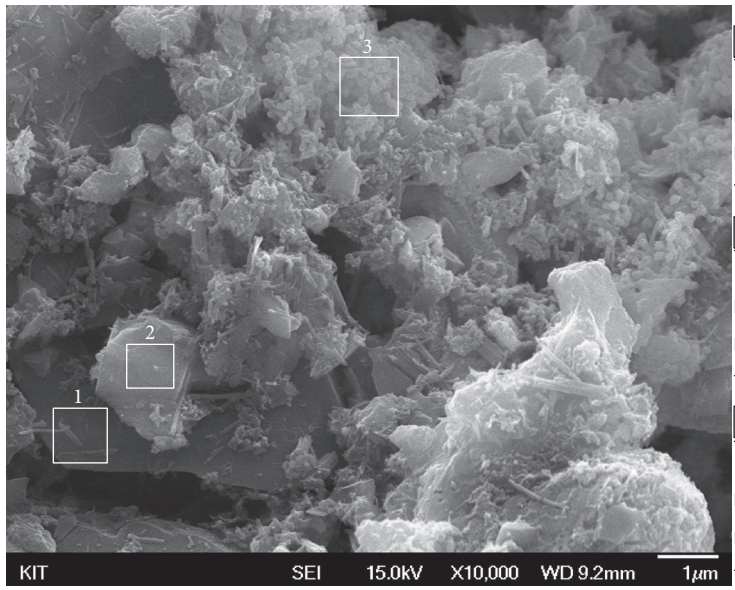

1

Element	Weight%	Atomic%
O	46.90	63.33
Al	7.51	6.01
Si	24.52	18.86
S	—	—
K	8.63	4.77
Ca	11.67	6.29
Total	100.00	

2

Element	Weight%	Atomic%
O	58.80	76.11
Al	2.37	1.82
Si	8.23	6.07
S	1.31	0.85
K	1.32	0.70
Ca	27.96	14.45
Total	100.00	

3

Element	Weight%	Atomic%
O	55.11	73.75
Al	3.32	2.64
Si	8.11	6.18
S	1.33	0.89
K	1.02	0.56
Ca	25.98	13.88
Total	100.00	

Figure 11: SEM view and chemical detected property by EDX of LGP12 10% (3 days).

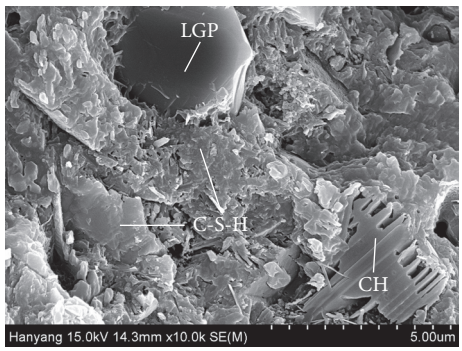

Figure 12: SEM image of composition paste which contained LGP12 10% (28 days).

and has a material composition similar to that of LGP raw material.

Figures 12 and 13 show the microstructure of the LGP cement paste on 28 days. As shown in Figure 12, the structure included well-developed hydrates and was more compact than of OPC, such that independent LGP particles could not be identified. LGP particles were assimilated with cement paste and partially existed inside the hydrates. The dark regions containing pores were significantly reduced, and increase of C-S-H hydrates closely reflected the hydrate composition as a result of the Pozzolanic reaction. The binding of C-S-H hydrates to apparent LGP particles was found in the microstructure, indicating that the Pozzolanic reaction occurred more easily on crushed edge sections than on the relatively smooth and stable surfaces. The EDX analysis on 7 and 28 days showed that the C/S ratio of the C-S-H hydrates was changed with time. The increased calcium content on 28 days might have affected the improvement of the strength of the concrete.

Table 6: Comparison of reduction average pore diameter.

	Average pore diameter (nm)	
	7 days	28 days
OPC	17.7926	14.4250
LGP12 5%	16.3242	13.6883
LGP12 10%	16.9954	13.7393
LGP5 5%	18.3079	13.7930
LGP5 10%	19.2284	13.2687

3.7. MIP. The pore distribution in the cement matrix is generally dependent on the quantity of hydrates, because the pores are distributed by the hydrates contained in the cement matrix. The results shown in Figure 14 indicate that porosity of the high fineness LGP5 on 7 days was 18.31% in LGP5 5% and 19.23% in LGP5 10%, which were higher than that of OPC. However, the entire LGP porosity was reduced, which was lower than 7 days by 2.6% to 6%. The decrease of the porosity is closely related to the strength, consistent with the results described in Section 3.4. The Pozzolanic reaction is generally slower than the cement hydration reaction of OPC. Hence, concrete has been replaced with the Pozzolanic material showing high permeability in early age, but the permeability is decreased as the reactions progress. Since the capillary porosity is related to permeability, the addition of LGP may reduce permeability to contribute to improvement of the material durability.

The hydration reaction and the secondary Pozzolanic reaction reduced the capillary porosity in the entire pore size range, except the capillary pore (medium size) range, and decreased the maximum pore size. Table 6 shows the average pore size of LGP concrete depending on curing ages. The decrease of the pores was significant particularly in the pore size range from 50 to 110 nm. Considering LGP particle

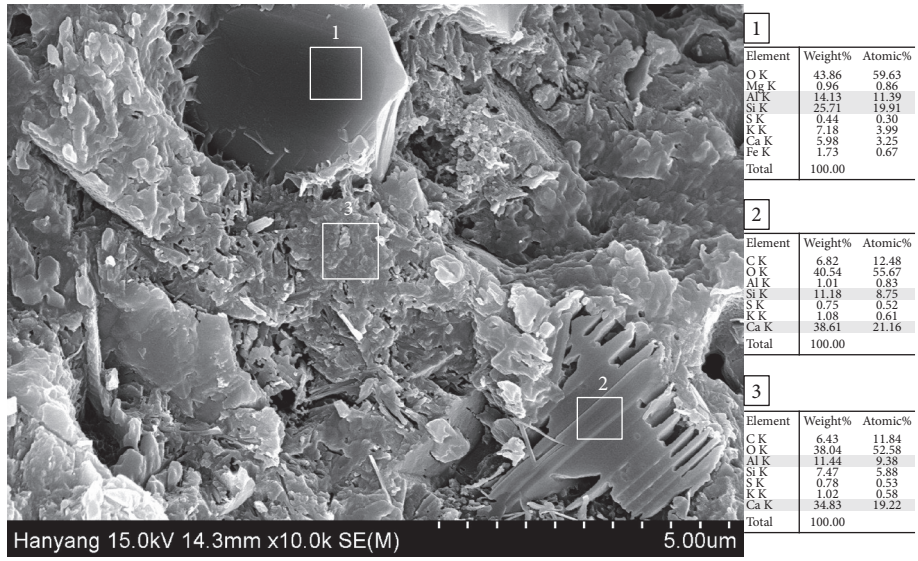

1

Element	Weight%	Atomic%
O K	43.86	59.63
Mg K	0.96	0.86
Al K	14.13	11.39
Si K	25.71	19.91
S K	0.44	0.30
K K	7.18	3.99
Ca K	5.98	3.25
Fe K	1.73	0.67
Total	100.00	

2

Element	Weight%	Atomic%
C K	6.82	12.48
O K	40.54	55.67
Al K	1.01	0.83
Si K	11.18	8.75
S K	0.75	0.52
K K	1.08	0.61
Ca K	38.61	21.16
Total	100.00	

3

Element	Weight%	Atomic%
C K	6.43	11.84
O K	38.04	52.58
Al K	11.44	9.38
Si K	7.47	5.88
S K	0.78	0.53
K K	1.02	0.58
Ca K	34.83	19.22
Total	100.00	

Figure 13: SEM view and chemical detected property by EDX of LGP12 10% (28 days).

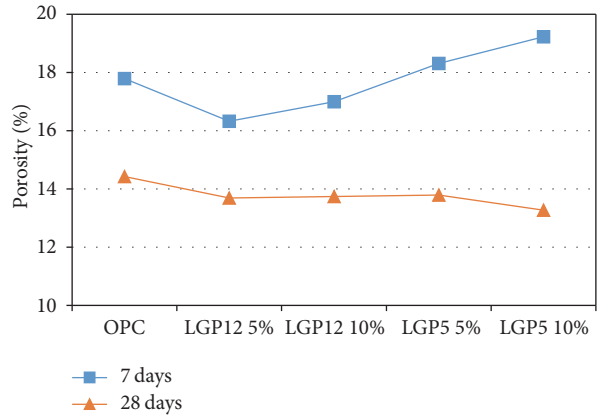

Figure 14: Porosity characteristics of concrete with LGP.

size distribution, the decrease of pores in this range may not be ascribed simply to the pore filling effect of LGP. Rather, as the cement paste was sufficiently hydrated, the produced hydrates developed a compact structure to block and divide the interconnected capillaries, producing pores that are interconnected with only gel pores. This might have considerably contributed to the increase of the strength [29]. In particular, the porosity in the capillary pore (medium size) range including gel pores of 4 to 50 nm was higher in the LGP specimen on 28 days than 7 days. The large pores decreased, but the capillary pores smaller than 50 nm increased when compared with the OPC. This indicates that the filling of LGP particles in the large-sized capillary pore range as well as the production of hydrates through the Pozzolanic reaction might have filled or divided the large-sized capillary pores, converting the interconnected pores into closed pores [30]. As LGP replacement of cement was increased, the interconnected pores were converted into smaller pores regardless of the particle size. In addition, in the pore size range from 50 to 200 μm (Interfacial Transition Zone, ITZ), the porosity of LGP concrete was considerably decreased on 28 days. Figure 15 shows that the porosity decrease of OPC in this pore size range was not significant on 7 and 28 days. On the contrary, as shown in Figure 16, the porosity of all the LGP was significantly decreased in this pore size range. The particle size distribution of LGP5 shown in Figure 1 indicates that the specimen did not include particles of size around 100 μm. However, according to the results shown in Figure 16, the porosity of the LGP specimens in this pore size range decreased to a similar level, regardless of the particle size. This suggests that the hydrates produced during 28 days might have made the pores more compact and dense, thereby increasing the strength. The pore distribution and the pore size decrease in the ITZ were verified through a chloride ion permeability test conducted with concrete specimens produced by mixing Pozzolanic materials, such as SF, BS, and FA [31]. The most significant factors were a compact densification filling of microparticles and a modification of the hydration process [32]. This indicates that the mixing of concrete LGP materials may reduce the porosity of the

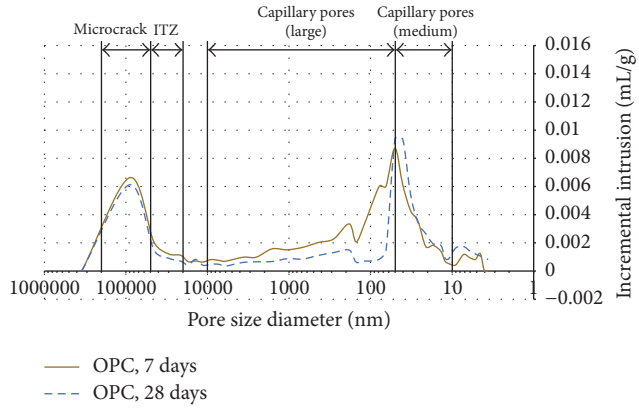

Figure 15: Relationship incremental intrusion and pore size diameter distribution with OPC.

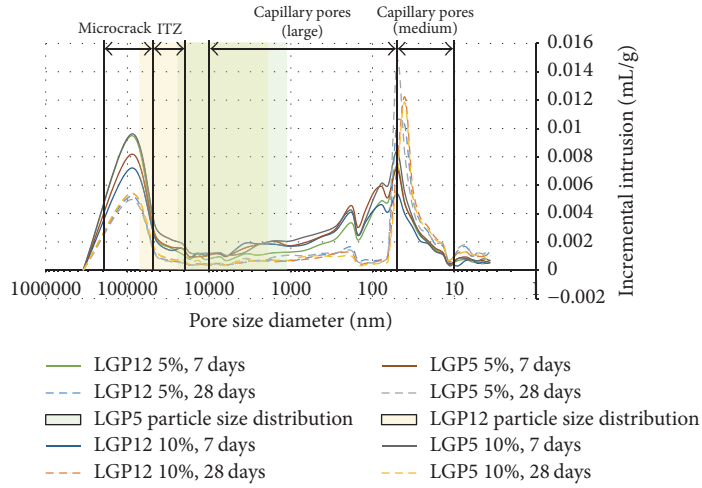

Figure 16: Relationship incremental intrusion and pore size diameter distribution with LGP according to replacement and age.

concrete system, increase the matrix density, and develop the strength.

4. Conclusion

In this study, LGP, which is one of the LPWG and made in Republic of Korea, replaced the cement depending on the ratio. LGP is much smaller than cement. It demonstrated the good performance and utilization possibilities of replacement. Results from the experiment are as follows.

(1) In the case of LGP concrete, it showed lower air content than OPC. In particular, when the LGP12 replaced 10%, it showed the lowest amount of air content. LGP5 concrete showed similar air content with OPC. Considering the replacement dosage of cement and high fineness of LGP, the use of admixture (SP) is considered appropriate for improvement of workability, freeze-thaw resistance, and durability.

(2) LGP12 has 9% higher slump than OPC in 5% replacement, due to the smooth surface and low absorption of the LGP. However, the slump decreases while the replacement is increasing. In the case of LGP5, slump was 16% lower than OPC in 5% replacement. The slump tends to drop with an increasing LGP replacement and high fineness.

(3) Compressive strength of LGP is higher than OPC in 28 days. The highest compressive strength showed in 10% replacement, which is the highest in LGP5. The tendency of strength development showed lower strength than OPC in the replacement of over 15% until 3 days. But after 7 days, entire compressive strength of LGP is higher than OPC. After 14 days, the compressive strength activity was increased due to the pozzolanic reaction.

(4) Entire splitting tensile strength is higher than OPC in 28 days. The maximum development was 83% in LGP5 5%, indicating that increasing LGP replacement would result in a decrease in splitting tensile strength. In case of LGP5 replacement, it showed the lowest level of splitting tensile strength development (19% increased). Relationship of splitting tensile strength by compressive strength ratio indicated 4.5~7.4% level.

(5) SEM results indicate that the dense hydrate was produced at the interface between the LGP and the cement paste, which can verify some of LGP with C-S-H gel. The compressive strength of LGP concrete may have a deleterious effect with increased LGP replacement in early age, because low cement content may deteriorate the hydration reaction.

(6) The porosity of LGP concrete is decreased, which is expected to have a positive effect on improving durability and permeability. Therefore, the result of hydration and pozzolanic reaction showed a tendency to transfer pores to a relatively smaller pore distribution pattern. Furthermore, Capillary porosity of 50~110 nm and ITZ of 50~200 μm indicated porosity reduction which means that an increase in the density and a decrease in the porosity with LGP.

Competing Interests

The authors declare that they have no competing interests.

Acknowledgments

This research was supported by a grant from R&D Program funded by Ministry of Land, Infrastructure and Transport of Korean government (16RDRP-B076268-03).

References

[1] M. Schneider, M. Romer, M. Tschudin, and H. Bolio, "Sustainable cement production—present and future," *Cement and Concrete Research*, vol. 41, no. 7, pp. 642–650, 2011.

[2] M. M. Hossain, M. R. Karim, M. Hasan, M. K. Hossain, and M. F. M. Zain, "Durability of mortar and concrete made up of pozzolans as a partial replacement of cement: a review," *Construction and Building Materials*, vol. 116, pp. 128–140, 2016.

[3] M. Batayneh, I. Marie, and I. Asi, "Use of selected waste materials in concrete mixes," *Waste Management*, vol. 27, no. 12, pp. 1870–1876, 2007.

[4] H.-Y. Wang, "The effect of the proportion of thin film transistor–liquid crystal display (TFT–LCD) optical waste glass as a partial substitute for cement in cement mortar," *Construction and Building Materials*, vol. 25, no. 2, pp. 791–797, 2011.

[5] D. Y. Shin, L. S. Kang, J. L. Park, C. G. Lee, J. H. Yoon, and H. S. Hong, "Current research trend on recycling of waste flat panel display panel glass," *Journal of the Korean Institute of Resources Recycling*, vol. 24, no. 1, pp. 58–65, 2015.

[6] S. Lee, L. Kang, C. G. Lee, M. H. Hong, S. Cho, and H. S. Hong, "Disassembly and compositional analysis of waste LCD displays," *Journal of the Korean Institute of Resources Recycling*, vol. 22, no. 2, pp. 29–36, 2013.

[7] K. Kim, K. Kim, and J. Hwang, "LCD waste glass as a substitute for feldspar in the porcelain sanitary ware production," *Ceramics International*, vol. 41, no. 5, pp. 7097–7102, 2015.

[8] C. Shi, Y. Wu, Y. Shao, and C. Riefler, "Alkali-aggregate reaction of concrete containing ground glass powder," in *Proceedings of the 12th International Conference on AAR in Concrete*, pp. 789–795, 2004.

[9] H. Woods, *Durability of Concrete*, ACI Monograph 4, American Concrete Institute, Detroit, Mich, USA, 1968.

[10] K. Zheng, "Pozzolanic reaction of glass powder and its role in controlling alkali-silica reaction," *Cement and Concrete Composites*, vol. 67, pp. 30–38, 2016.

[11] K. Afshinnia and P. R. Rangaraju, "Influence of fineness of ground recycled glass on mitigation of Alkali–silica reaction in mortars," *Construction and Building Materials*, vol. 81, pp. 257–267, 2015.

[12] C. S. Lam, C. S. Poon, and D. Chan, "Enhancing the performance of pre-cast concrete blocks by incorporating waste glass—ASR consideration," *Cement and Concrete Composites*, vol. 29, no. 8, pp. 616–625, 2007.

[13] A. Saccani and M. C. Bignozzi, "ASR expansion behavior of recycled glass fine aggregates in concrete," *Cement and Concrete Research*, vol. 40, no. 4, pp. 531–536, 2010.

[14] M. E.-S. I. Saraya, "Study physico-chemical properties of blended cements containing fixed amount of silica fume, blast furnace slag, basalt and limestone, a comparative study," *Construction and Building Materials*, vol. 72, pp. 104–112, 2014.

[15] C. Shi and K. Zheng, "A review on the use of waste glasses in the production of cement and concrete," *Resources, Conservation and Recycling*, vol. 52, no. 2, pp. 234–247, 2007.

[16] H.-Y. Wang, "A study of the effects of LCD glass sand on the properties of concrete," *Waste Management*, vol. 29, no. 1, pp. 335–341, 2009.

[17] W. Her-Yung, "A study of the engineering properties of waste LCD glass applied to controlled low strength materials concrete," *Construction and Building Materials*, vol. 23, no. 6, pp. 2127–2131, 2009.

[18] H.-Y. Wang and W.-L. Huang, "Durability of self-consolidating concrete using waste LCD glass," *Construction and Building Materials*, vol. 24, no. 6, pp. 1008–1013, 2010.

[19] H.-Y. Wang, H.-H. Zeng, and J.-Y. Wu, "A study on the macro and micro properties of concrete with LCD glass," *Construction and Building Materials*, vol. 50, pp. 664–670, 2014.

[20] K. L. Lin, W.-J. Huang, J. L. Shie, T. C. Lee, K. S. Wang, and C. H. Lee, "The utilization of thin film transistor liquid crystal display waste glass as a pozzolanic material," *Journal of Hazardous Materials*, vol. 163, no. 2-3, pp. 916–921, 2009.

[21] M. Á. Sanjuán, C. Argiz, J. C. Gálvez, and A. Moragues, "Effect of silica fume fineness on the improvement of Portland cement strength performance," *Construction and Building Materials*, vol. 96, pp. 55–64, 2015.

[22] N. A. Soliman and A. Tagnit-Hamou, "Development of ultra-high-performance concrete using glass powder—towards ecofriendly concrete," *Construction and Building Materials*, vol. 125, pp. 600–612, 2016.

[23] C. Shi, Y. Wu, C. Riefler, and H. Wang, "Characteristics and pozzolanic reactivity of glass powders," *Cement and Concrete Research*, vol. 35, no. 5, pp. 987–993, 2005.

[24] S. Mindess, F. Young, and D. Darwin, *Concrete*, Prentice-Hall, Upper Saddle River, NJ, USA, 2003.

[25] L. M. Federico and S. E. Chidiac, "Waste glass as a supplementary cementitious material in concrete—critical review of treatment methods," *Cement and Concrete Composites*, vol. 31, no. 8, pp. 606–610, 2009.

[26] Y. Shao, T. Lefort, S. Moras, and D. Rodriguez, "Studies on concrete containing ground waste glass," *Cement and Concrete Research*, vol. 30, no. 1, pp. 91–100, 2000.

[27] C. Meyer, S. Baxter, and W. Jin, "Potential of waste glass for concrete masonry blocks," in *Proceedings of the 4th Materials Engineering Conference*, pp. 666–673, Washington, DC, USA, 1996.

[28] J. E. Mcdonald, "Properties of silica fume concrete," Tech. Rep. REMR-CS-32, REMR Research Program, U.S. Army Engineer Waterways Experiment Station, Vicksburg, Miss, USA, 1991.

[29] R. D. Hooton, "Permeability and pore structure of cement pastes containing fly-ash, slag, and silica fume," Blended Cements ASTM STP-897, ASTM, West, 1986.

[30] P. Chindaprasirt, C. Jaturapitakkul, and T. Sinsiri, "Effect of fly ash fineness on compressive strength and pore size of blended cement paste," *Cement and Concrete Composites*, vol. 27, no. 4, pp. 425–428, 2005.

[31] P. Plante and A. Bilodeau, "Rapid chloride ion permeability test: data on concretes incorporating supplementary cementing materials," in *Fly Ash, Silica Fume, Slag, and Natural Pozzolans in Concrete: Proceedings, Third International Conference, Trondheim, Norway, 1989*, American Concrete Institute, 1989.

[32] J. P. Ollivier, J. C. Maso, and B. Bourdette, "Interfacial transition zone in concrete," *Advanced Cement Based Materials*, vol. 2, no. 1, pp. 30–38, 1995.

Hindawi
Advances in Materials Science and Engineering
Volume 2017, Article ID 3832072, 10 pages
https://doi.org/10.1155/2017/3832072

Research Article

Comprehensive Testing Techniques for the Measurement of Shrinkage and Structural Changes of Fine-Grained Cement-Based Composites during Ageing

Barbara Kucharczyková, Libor Topolář, Petr Daněk, Dalibor Kocáb, and Petr Misák

Faculty of Civil Engineering, Brno University of Technology, Veveří 331/95, 602 00 Brno, Czech Republic

Correspondence should be addressed to Barbara Kucharczyková; barbara.kucharczykova@vutbr.cz

Received 6 October 2016; Revised 1 December 2016; Accepted 22 December 2016; Published 15 January 2017

Academic Editor: Rishi Gupta

The paper deals with an experimental analysis focusing on the utilization of a specific measurement technique for determining the development of shrinkage and for monitoring structural changes in fine-grained cement-based composites during their ageing. Advanced measurement equipment and procedure allowing simultaneous measurement of length changes, mass losses, acoustic responses, and temperature development were designed and verified by the experimental investigation. The main scope of the experiments performed was focused on finding the relationships between the characteristics being investigated while maintaining a uniform test setup. For the purpose of the experimental measurement, three fine-grained cement composite mixtures were designed and manufactured. The mixtures differed in the water-to-cement ratio (*w/c*) and in the amount of plasticizer. The measurement outputs are presented in the form of diagrams showing the relations between the studied parameters, such as relative length changes, mass losses, temperature progress, and acoustic emission (AE) activity during solidification of the composites. The measurement results showed close relations between the examined characteristics. The progress of relative length changes together with the progress of mass losses and temperature development is reflected in the AE activity. The advanced measurement procedure and technique provided valuable information about the behaviour of cement-based composites during early setting and long-term hardening.

1. Introduction

The determination of the volume change development and crack formation in cement-based composites is currently receiving attention from civil engineers and concrete producers. Along with the design of new materials, factors influencing volume changes appear throughout the whole period of their setting and hardening [1, 2]. Progress in technology and the composition of building materials require advancements in test procedures for determining the physical and mechanical parameters of new materials. The current testing approach is based on the earliest possible identification of disruptions in the internal structure of structural elements, which facilitates early diagnostics of the problem allowing relevant precautions to be taken in order to prevent later collapse of the structure being designed.

The reason why this area is being focused on is because many problems with cracking of cement composites arise at early ages [3–5]. In civil engineering, crack formation and propagation are closely associated with tensile strength (the value of which is generally only about 10 percent of that of compressive strength) and with fracture parameters. At early ages, there are internal stresses generated by volume changes but the strength of the element is not yet fully developed. Controlling the variables that affect volume change can minimize high stresses and cracking [4, 6, 7]. Recent measurements suggest the necessity of assessing the magnitude of shrinkage in two consecutive stages of a composite's ageing, at an early age and at later ages [7–10]. Early-age measurements reveal differences in the development of volume changes as well as differences in the initiation and propagation of cracks which cannot normally be identified with traditional

measurement made after specimens have been removed from moulds (typically after 24 hours) [11]. Literature offers a number of approaches to determine the value of cement-based composite shrinkage [12–14]. However, these methods mostly determine separate components of shrinkage at an early age, for example, methods for determining plastic or autogenous shrinkage [5, 6, 9, 13, 15–18] and methods for determining the shrinkage due to drying (defined mainly in the standards of various countries). Contemporary approaches to shrinkage measurement are based primarily on the determination of relative length changes. In most cases, measurement begins after removing specimens from moulds, which is typically no sooner than 24 hours of ageing. In important or complicated concrete structures, such as bridges, suspended slabs, or structures with a complex shape, shrinkage can be measured directly on a concrete element using a special type of wire strain gauge designed to be embedded directly in the concrete. Such gauges are typically fixed to the reinforcement cage of the element by means of rebar extensions [19–23]. Guidelines reflecting recent progress in theoretical and experimental research in the field of cement composite creep and shrinkage (especially concrete) have been published under RILEM TC-242-MDC (chair Zdeněk P. Bažant) [24].

In recent years, the method of acoustic emission (AE) has also been widely used as supplemental measurement in the nondestructive monitoring of changes in a specimen's internal structure during static and dynamic loading tests as well as for the monitoring of the behaviour of composite materials during setting and hardening [11, 25, 26]. The AE method is considered to be a "passive" nondestructive technique because it usually identifies defects as they develop during the test [27] and allows the monitoring of changes in the behaviour of materials over a long period of time without moving any of their components. This, together with its ability to detect crack propagation taking place not only on the surface but also deep inside the material, makes the technique quite unique.

A crack developing in a material is accompanied by the release of stored strain energy, which is then consumed by nucleating new external surfaces (cracks) and emitting elastic waves known as AE waves. The elastic waves propagate inside a material and are detected by an AE sensor. With the exception of contactless sensors, AE sensors are directly attached to the surface [28].

In practice, there are situations where attaching a sensor directly onto the surface is not possible, for example, installation onto a part of an element that is inaccessible or onto a surface which reaches very high temperatures. Detection sensitivity can be increased by using a waveguide. A typical case in civil engineering is the placement of a waveguide into a prepared hole in a fresh composite. An acoustic waveguide is a physical structure for guiding sound waves, that is, a sound-propagation duct that behaves like a transmission line. The duct contains some sound-propagation medium [8].

2. Experimental Part

2.1. Materials. Three fine-grained cement composite mixtures were designed and manufactured for the purposes of the experiment. They differed in the water-to-cement ratio (w/c) and in the amount of plasticizer. Compositions of mixtures are based on the standard ČSN EN 196-1 [29]. The fresh composite was made with standardized quartzite sand (maximum nominal grain size of 2 mm pursuant to ČSN EN 196-1 [29]) and CEM I 42.5 R Portland cement and water at a ratio of 3 : 1 : 0.5 (S : C : W), 3 : 1 : 0.47, and 3 : 1 : 0.35 with the addition of SIKA SVC 4035 superplasticizer (polycarboxylate ether-based technology) at an amount of 1% by cement mass. A mixing device with controllable mixing speed was used to prepare the fresh mixtures. Six specimens with the dimensions of 100 × 60 × 1000 were prepared from each mixture. Table 1 shows basic information about the composition, manufacturing, and fresh-state properties. The workability was determined using the flow table with a calibrated scale designed for the testing of fresh mortars pursuant to ČSN EN 1015-3 [30]. Bulk density of the fresh composite was determined in accordance with ČSN EN 1015-6 [31] using a calibrated vessel with the volume of 1 dm^3.

2.2. Test Equipment and Procedures

2.2.1. Determination of Length Changes. The measurement procedure designed to determine the progress of cement composites' shrinkage was designed to simultaneously record relative length changes, mass losses caused by free drying, temperature inside the tested specimens, and AE activity due to structural changes during solidification. The ambient temperature and relative humidity were also monitored. The measurement of shrinkage was performed using measurement equipment standardized pursuant to the Austrian standard OENORM B 3329:2009-06-01 [32]. Special moulds of 1000 mm in length and with a 60 × 100 mm cross section were used for recording the length changes measured along the central axis of the specimens using an inductive sensor leaning against the movable head of the mould. These moulds are primarily designed for cement composite shrinkage measurement in the early stages of setting and hardening. Special markers designed at the Brno University of Technology (BUT) were used to perform subsequent long-term measurement of relative deformation [33]. These markers were embedded into the upper surface of the cement composite placed in the shrinkage moulds. This way, two gauging bases were created for further measurement (see Figure 1). This arrangement enabled the capture of the total relative length change of the composite since the time at which the composite is placed into the mould until its long-term ageing after the specimen has been removed from the shrinkage mould. Details about the marker types and their drawing and arrangement can be found in [33]. A polyethylene foam mat (MIRELON) of 2 mm in thickness was placed on the bottom and along both sides of the shrinkage moulds in order to ensure that the specimen can move freely in the mould. The shrinkage moulds were filled with a fine-grained cement composite and placed onto a special weighing table that enables continuous recording of mass losses caused by free drying of the specimen surfaces. For more details about the weighing table, see [34].

Table 1: Composition and properties of fresh composites.

Components and properties	Units	Composite ID		
		0	III	IV
Sand	kg	45.9	45.9	45.9
Cement I 42.5 R	kg	15.3	15.3	15.3
Water	kg	7.65	7.16	5.35
Superplasticizer SVC 4035	% by cement mass	—	—	1.0
w/*c* ratio	—	0.5	0.47	0.35
Mixing speed	Revolutions/min	20	30	40
Workability	mm	140	128	135
Bulk density	kg/m^3	2200	2210	2280

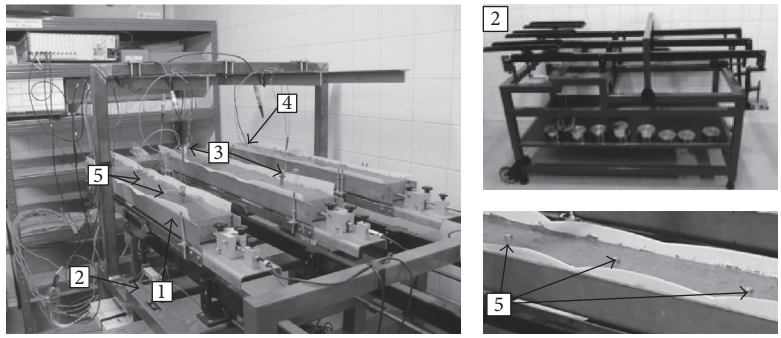

Figure 1: Arrangement of measurement devices (1: shrinkage mould; 2: weighing table; 3: acoustic emission sensor with a waveguide; 4: temperature probe; 5: markers for long-term measurement).

A thermal sensor COMET was embedded at one end of the shrinkage moulds in order to measure the temperature inside the specimens. The ambient temperature and relative humidity were recorded by an automatic gauging station COMET.

This measurement configuration enabled simultaneous measurement of all investigated parameters of the composite placed in a shrinkage mould. The final arrangement of the measurement devices before starting the measurement is shown in Figure 1.

Note that the measurement in shrinkage moulds can only be started after the composite has set a little so that the movable head of the mould is not pushed out under the composite's own weight. Due to the consistency of the fresh composite, measurement was started approximately one hour after the composite was poured into the moulds. The length change was measured on the specimens in the moulds, which were placed on the weighing table standing on hard rubber pads in a climate control chamber at a temperature of 21 ± 2°C and relative humidity of 60 ± 10% until the composite was 3 days old. The top surface of the composite was not protected from drying. During this time, the chamber was locked, which prevented people from entering the chamber so that the measurement could continue undisturbed. Also, the shrinkage moulds and all measurement devices were secured against movement.

Once early measurement was finished, the specimens were extracted from the moulds, placed on the table, and left to dry freely in the climate chamber at a stable temperature of 21 ± 2°C and relative humidity of 60 ± 10%. The following measurements were performed using a strain gauge which was fixed onto the surface of the specimens. The positions of the gauging points were predefined by the markers embedded at spacing of 200 mm. The specimens were left to dry freely throughout the entire time of the measurement and were weighed at regular intervals.

2.2.2. Determination of Structural Changes by Acoustic Emission Method. Changes in the specimens' internal structure during the early stage of setting and hardening were monitored using the nondestructive passive method of AE. Magnetic AE sensors (type IDK09 with 35 dB preamplifier) were placed in positions predefined by the embedded steel probes (waveguides) (see Figure 1). Drawing on experience from previous measurements, the threshold was set to the value of 72 μV. The threshold value of the signals was set with the aim of eliminating background noise and recording only the signals produced by the formation of the material's microstructure and internal cracking. The measurement chain consists of the measurement sensor attached to the waveguide followed by a preamplifier with a gain of 35 dB and finally there is a data recorder with a software preamplifier with a gain of 40 dB. The internal structure changes were monitored with two AE sensors placed in each shrinkage mould: the first one was placed near the movable head (AE2) and the second one was located near the other end of the

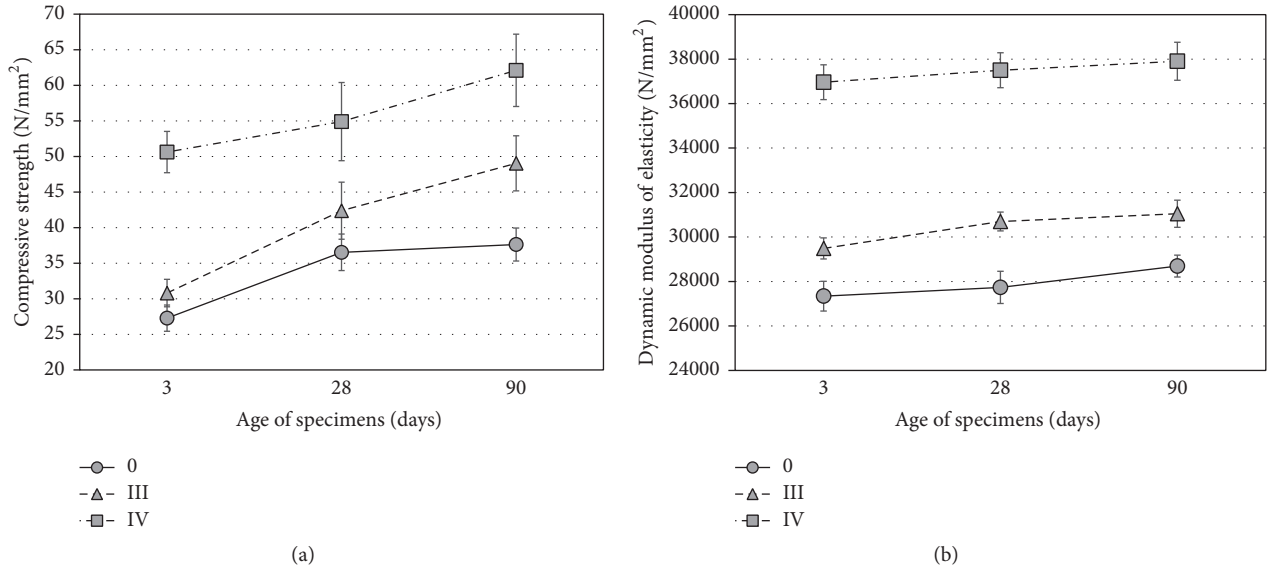

Figure 2: Development of compressive strength (a) and dynamic modulus of elasticity (b) during composite ageing.

mould (AE3). This way, the progress of events occurring during the cement composites' setting and hardening was recorded continuously. AE signals were being detected for 72 hours by the measuring equipment DAKEL XEDO with two channels. The measurement of AE was started together with the measurement of relative length changes, mass losses, and temperature. To eliminate outside noise, guard sensors were placed on the bottom of the frame of the shrinkage moulds. This setup ensured that AE waves coming from the area being measured hit the sensors on the waveguides before hitting any of the guards. Conversely, waves from outside hit at least one of the guards before hitting the sensors on the waveguides.

3. Results and Discussion

The measurement results are presented below. Table 2 and Figure 2 show the development of compressive strength and dynamic modulus of elasticity determined for all the mixtures being examined. The results confirm general presumptions. The highest values of both parameters were found in mixture IV (low *w/c* with the addition of plasticizer).

Concerning shrinkage measurement, the following trends were found. Figure 3 shows the progress of relative deformation and mass losses determined at an early age. The data were obtained from measurements performed on the specimens in shrinkage moulds placed on a weighing table. As shown below, different progress of shrinkage and mass losses were recorded for the mixtures being investigated (see Figure 3). Shortly after the start of the measurement, both mixtures without plasticizer were expanding (length increment), while specimens with plasticizer were shrinking rapidly (see Figure 3(a)).

Also, the progress of mass losses recorded within the first 72 hours of ageing is different in mixtures which contain plasticizer and which do not. The mass losses of both composites without plasticizer are higher than in the case of the composite with plasticizer (see Figure 3(b)). This progression is closely linked with the adjustment of water content. Once plasticizer is added, water content is reduced which influences the progress of volume changes as well as mass losses. Thus, the *w/c* ratio of the composites without plasticizer was rather high (see Table 1). No component segregation in fresh mixture was observed during either the mixing or the manufacturing of the test specimens. On the other hand, a relatively large amount of water rose to the upper surface of the test specimens after their manufacturing and storing. This phenomenon is commonly known as bleeding [35]. Gradually, during the solidification of the composite, a part of the water evaporates from the specimen surface, causing mass losses, while some amount is drawn back into the pore structure of the composite, contributing to the composite's expansion [9].

It is known and has been proven by previous experimental measurements [36] that the addition of plasticizer also has a substantial influence on cement hydration. The addition of superplasticizer retards cement hydration and has a critical influence on its overall progress. The margin of hydration retardation is strongly dependent on the amount and properties of the cement and plasticizer used in the composite mixture [37].

The progress of shrinkage corresponds well with the progress of temperature measured inside the test specimens (see Figure 4). In case of composites without superplasticizer, the highest temperature was recorded approximately 11 hours after the start of measurement. At that same time, a surge of expansion (length increment) can be seen as well. This length increment can be ascribed to the cement composites' thermal expansion. It was proved by earlier measurements that the initial expansion is typical for cement composites with a high *w/c* ratio [4]. The origin of this expansion is not fully understood and is the object of ongoing research. Similar

Table 2: Values of compressive strength and dynamic modulus of elasticity.

Composite ID	Age of specimens [days]					
	3	28	90	3	28	90
	Compressive strength [N/mm^2] (standard deviation)			Dynamic modulus of elasticity [N/mm^2] (standard deviation)		
0	27.28 (1.84)	36.53 (2.57)	37.62 (2.32)	27340 (669)	27735 (724)	28693 (492)
III	30.80 (1.92)	42.38 (4.01)	49.03 (3.87)	29487 (473)	30698 (424)	31047 (610)
IV	50.61 (2.90)	54.90 (5.49)	62.10 (5.08)	36962 (782)	37500 (786)	37903 (854)

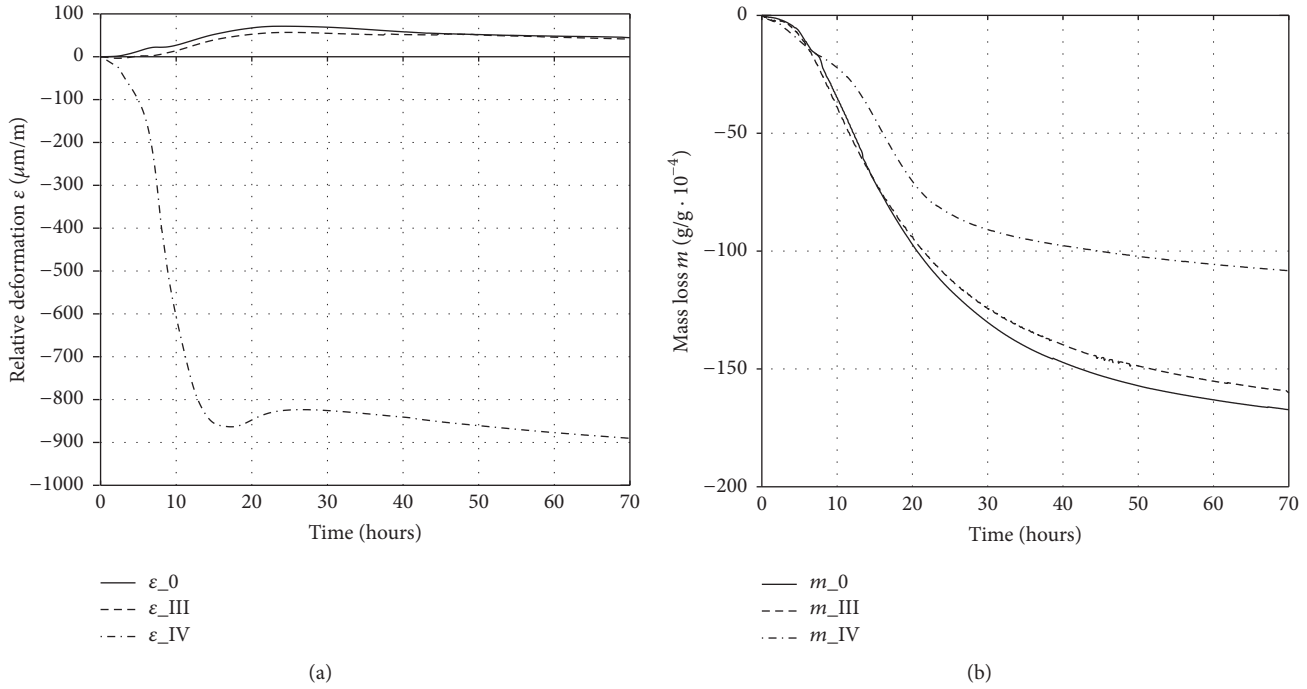

Figure 3: Relative deformations and mass losses measured during the first 72 hours of specimen ageing.

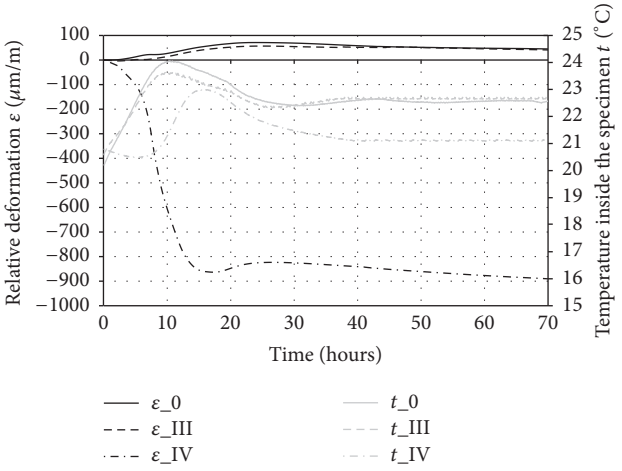

Figure 4: Relative deformations and temperature measured inside the test specimen (during the first 72 hours of specimen ageing).

relationship between temperature and progress of deformation was recorded in the composite with superplasticizer. The presence of the superplasticizer retarded early hydration and delayed temperature growth by approximately 5 hours (in comparison with the composite without the plasticizer). A dormant period accompanied by short expansion during the progress of shrinkage was observed after the maximum temperature was measured.

Next progress of shrinkage in all mixtures is affected by the setup of the experiment. Note that in this stage of measurement the test specimens are placed in the shrinkage moulds and only the specimens' upper surface is not protected from drying. This fact is also reflected in the progress of mass losses whereas the most prominent effect was observed in mixture IV (see Figures 3(b) and 9(b)).

Concerning the AE measurement, different results were again obtained for mixtures with and without superplasticizer. The acoustic waves recorded by the measurement

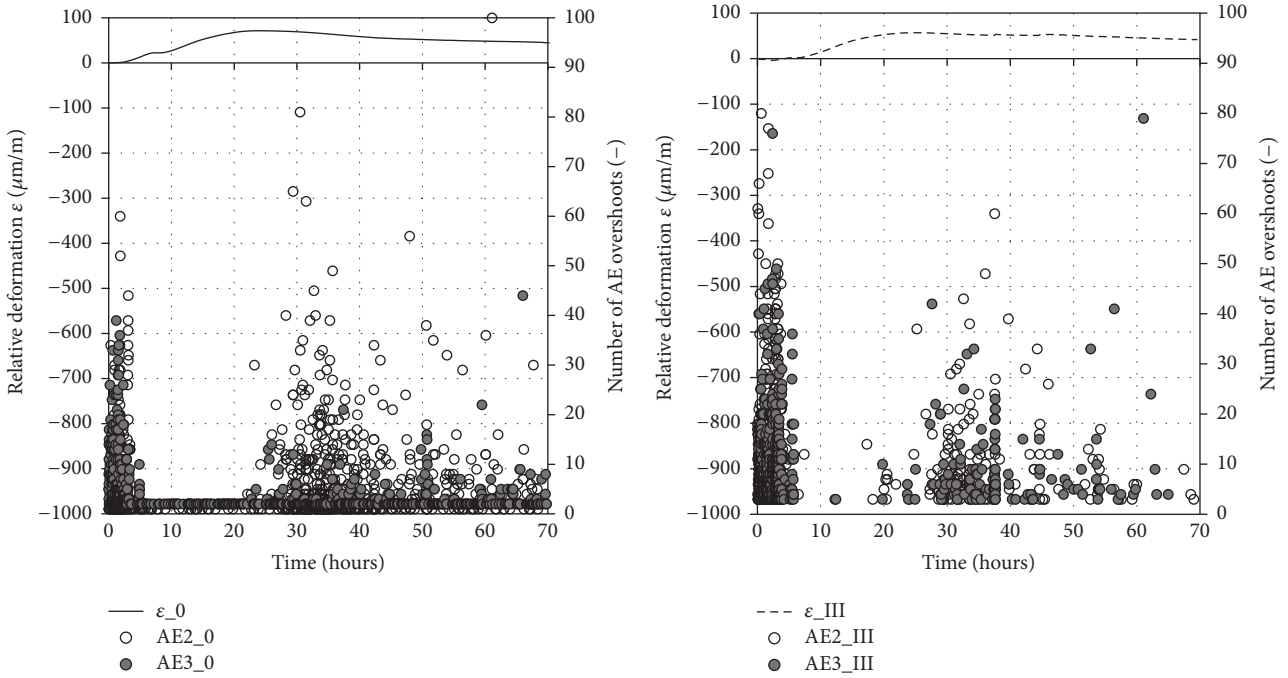

Figure 5: Relative deformations and AE overshoots measured during the first 72 hours of specimen ageing for mixtures without a superplasticizer.

equipment were converted to a number of overshoots for the purposes of result interpretation. This number of overshoots indicates the number and size of structural changes taking place within a certain period. Note that there is not a strict relationship between a particular structural change and the number of overshoots. This number can be defined as a relative value relating to the setting of the measurement sensitivity that must always be the same for all measurements performed as part of comparative tests. At the start of measurement, a high number of AE signals' overshoots exceed the adjusted threshold value (see Figure 5). The high number of AE overshoots is due to the physical and chemical changes which take place in this early setting phase. During the first hours of composite solidification, plastic shrinkage is taking place. The movement of particles and the formation of new hydration products are the primary sources of the acoustic waves' formation. The data show that, in this early setting phase, the mixture with plasticizer (composite IV, Figure 6) exhibited a lower number of AE overshoots than both mixtures without plasticizer, composites 0 and III (Figure 5). This is closely connected with the *w/c* ratio and initial bleeding observed in composites without superplasticizer. After the initial setting was finished, no notable structural changes were recorded for the mixtures without plasticizer until 20 hours of age (see Figure 5). The mixture with superplasticizer behaved rather differently; after the initial activity, another acoustic response was recorded at the time of initial temperature growth. Within the same period, a surge of shrinkage was recorded too (see Figures 4 and 6). This behaviour is associated with the low *w/c* ratio (of mixture IV), retardation of early hydration, and temperature growth due to the presence of plasticizer (as mentioned above). After 20 hours of ageing, more acoustic activity was recorded again in all the mixtures. Taking into account the fact that all of the composites had hardened by this stage, it is possible that the increased AE activity originated from the creation of microcracks (the highest AE activity recorded in mixture 0 with the highest *w/c* ratio) and continuing formation of microstructure. Determining whether the AE activity is actually due to the formation of microcracks would require further research to verify that relationship. The lowest AE activity was recorded in mixture IV. This behaviour is connected with the rapid growth of strength which is typical for composites with a low *w/c* ratio with the addition of a superplasticizer (see Table 2 and Figure 2).

The AE responses are also presented in connection with the progress of relative deformations and mass losses of the mixtures. The results are presented in Figures 7(a), 7(b), and 8 showing curves representing the relationship between the relative length changes (ε) and mass losses (m) of the specimens during the first 72 hours of ageing together with the AE responses recorded during the same period. Figure 7 shows the results for mixtures without superplasticizer. The graphs show that the progress of the initial part of the $\varepsilon - m$ relationship is in both mixtures affected by their initial expansion (length increment) caused by thermal expansion and water reabsorption. Supposing that the increased initial AE activity due to plastic settlement and the initial formation of the composite microstructure are not taken into account, there are two other significant factors which lead to an increase in the AE activity during composite solidification: actual thermal conditions inside the test specimens and rapid changes in the progress of shrinkage.

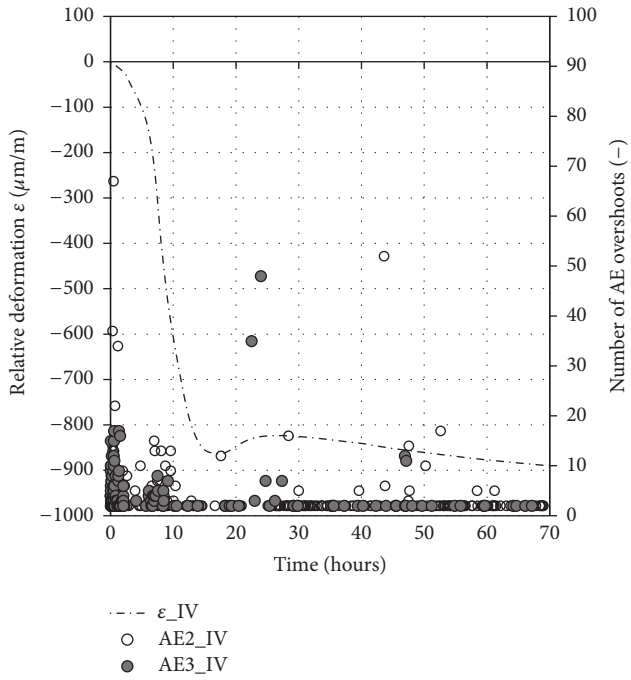

Figure 6: Relative deformations and AE overshoots measured during the first 72 hours of specimen ageing for mixture with a superplasticizer.

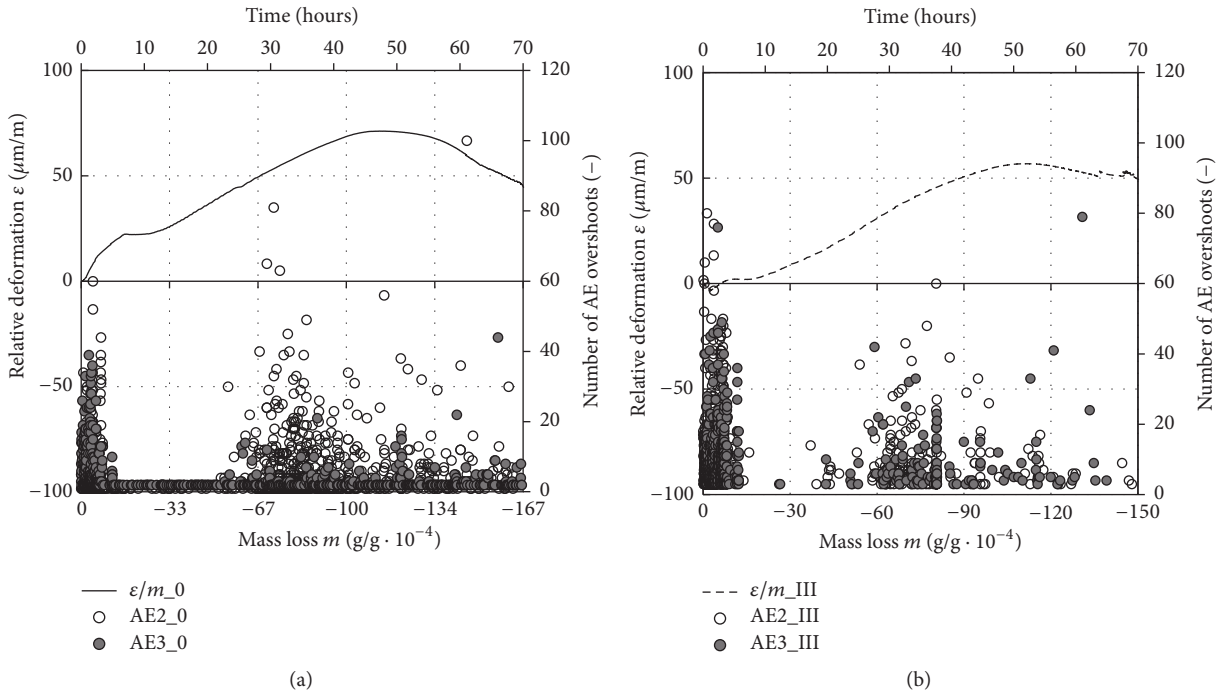

Figure 7: Relationship between deformations and mass losses together with the AE overshoots measured during the first 72 hours of specimen ageing for mixtures without a superplasticizer.

Figure 7(a) shows measurement results for the mixture with the highest *w/c* ratio. The first appearance of increased AE activity (a high number of overshoots) between 25 and 40 hours of age corresponds to the time when the temperature measured inside the test specimens dropped to its steady-state value. Within this time period, the temperature no longer contributes to the specimen expansion. The second period with high AE activity is visible at the time when the expansion (length increment) is changed to the shrinkage (length decrement). The curvature of the $\varepsilon - m$ relationship

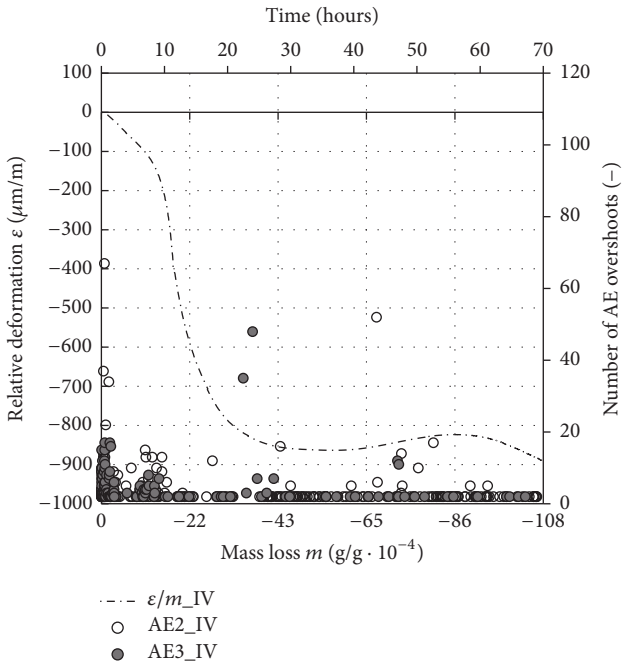

Figure 8: Relationship between deformations and mass losses together with the AE overshoots measured during the first 72 hours of specimen ageing for mixture with superplasticizer.

is also visibly changed. Similar results were recorded also in mixture III (see Figure 7(b)). Results obtained for mixture IV are rather different because the progress of shrinkage and mass losses were not affected by initial expansion and the temperature growth was delayed due to the presence of superplasticizer. Nevertheless, the results shown in Figure 8 indicate that the increased AE activity corresponds to the changes in curvature of the $\varepsilon - m$ relationship.

Concerning the results of long-term measurement, it can be stated that the addition of superplasticizer has a substantial influence on the total progress of relative deformations (see Figure 9). The initial rapid growth of shrinkage influences also its final values which are more than two times higher than the values recorded in the cement composite without the superplasticizer with a w/c ratio of 0.5. The period of expansion appears not to be very significant in terms of magnitude. However, the initial expansion delayed the start of shrinkage by more than 20 hours. This delay can be of great benefit to the later development of physical and mechanical properties of cement composites. The total progress of mass losses corresponds well with the water content of the mixtures (see Table 1). The lowest mass loss was recorded in the composite with the superplasticizer with a w/c ratio of 0.35.

The relationship between relative length changes and mass losses was observed over the whole time of the cement composite ageing (see Figure 10). However, the initial part of the curve is influenced by water reabsorption and thermal expansion.

4. Conclusion

The main aim of the experiments performed was to present comprehensive test techniques that can be used for the determination of shrinkage development in fine-grained cement-based composites and for monitoring structural changes throughout their ageing. The experimental investigation made use of advanced measurement equipment and procedure allowing the simultaneous measurement of length changes, mass losses, acoustic responses, and temperature development. The results were compared in terms of the overall behaviour of the studied materials with respect to a uniform setup of the test equipment (accuracy, sensitivity, curing conditions, etc.). Based on the results, it can be stated that the measurement technique described in the paper and used in the experiment fully satisfies the requirements for early-age diagnostics of the material's behaviour. The measurement of relative length changes together with the recorded progress of mass losses and temperature measured inside the test specimens provided comprehensive information about the behaviour of the material in the early stage of its setting and hardening. The possibility of continuing to measure the relative length changes as well as mass losses of the test specimens, after they were removed from moulds, provided data about the continuous progress of the investigated characteristics during the whole time of the composites' setting and hardening. The method of acoustic emission appears to be another suitable tool for continuous nondestructive monitoring of the structural changes taking place while the materials solidify. The conclusions presented in the article contain only a small fraction of the information contained in the AE data. The aim of the performed measurements was to compare the results obtained by measurements of three different mixtures manufactured, cured, stored, and measured under the same conditions. In this case, the absolute number of overshoots is not very important. Responses of the changes in the internal structure are strongly dependent on the material's composition (the same response can induce a different number of overshoots in different materials). More important for the presented measurements was to record the moment and time spectrum (interval) of the overshoots' appearance. Therefore, it was important to keep the same test setup across all measurements.

The possibility of determining the occurrence of microcracks during the setting and hardening of cement composites may be of great use in the early diagnostics of material failures in the future. The number of microcracks present in the cement composites substantially affects their final mechanical properties (i.e., strength, modulus of elasticity, fracture parameters, durability, etc.). The application of the AE method for continuous monitoring of cement composites during the setting and hardening can be useful for early detection of micro disruptions. This information about the behaviour of the material may be later used for improving the material composition or adjusting the curing method which can lead to the design of cement composite structures with better properties. Data obtained from the experiment are of great use in the creation of new and verification of existing computational models designed for the prediction of the

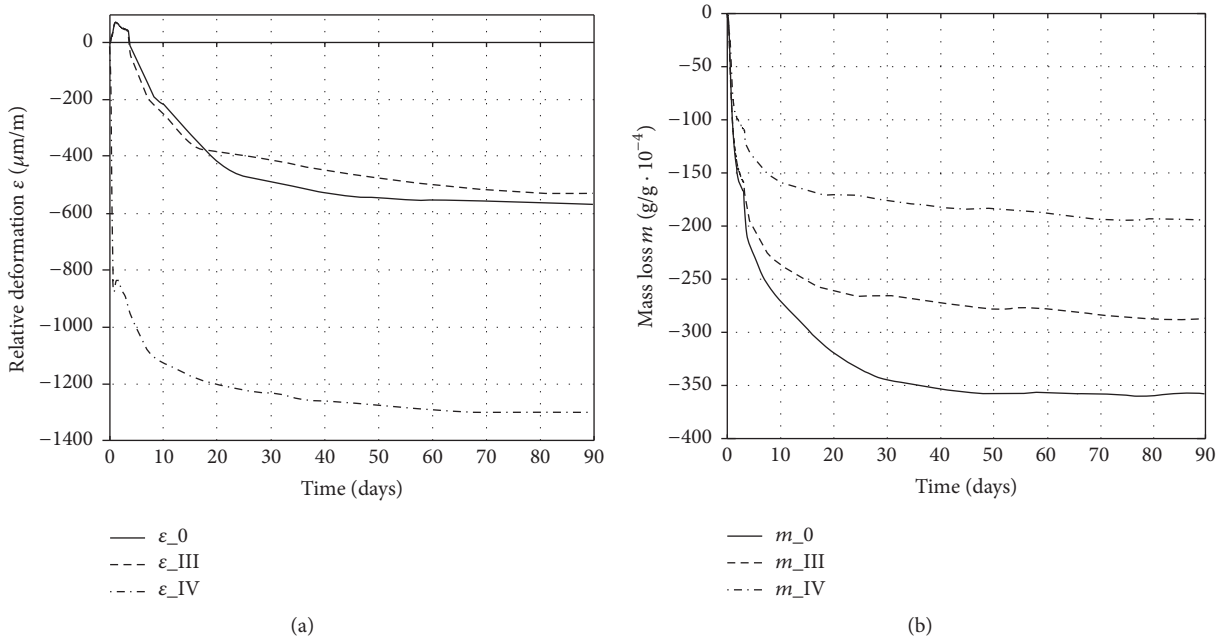

Figure 9: Progress of relative deformations and mass losses measured over the whole time of specimen ageing.

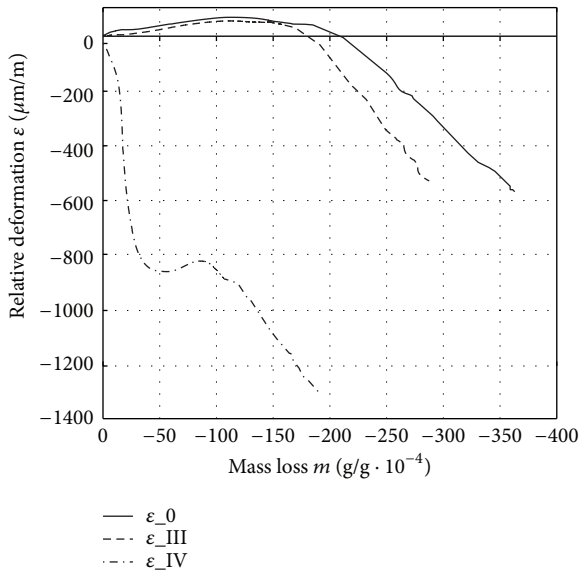

Figure 10: Relationship between deformations and mass losses measured over the whole time of specimen ageing.

progress of volume changes and microcrack development in cement-based composites.

Competing Interests

The authors declare that they have no competing interests.

Acknowledgments

This paper has been written as part of Project no. LO1408 "AdMaS UP, Advanced Materials, Structures and Technologies," supported by the Ministry of Education, Youth and Sports under the "National Sustainability Programme I."

References

[1] D. Čítek, M. Rydval, and J. Kolísko, "Volumetric changes of the UHPC matrix and its determination," *Applied Mechanics and Materials*, vol. 827, pp. 215–218, 2016.

[2] X.-M. Kong, Z.-L. Zhang, and Z.-C. Lu, "Effect of pre-soaked superabsorbent polymer on shrinkage of high-strength concrete," *Materials and Structures*, vol. 48, no. 9, pp. 2741–2758, 2014.

[3] L. Østergaard, L. Damkilde, and H. Stang, *Early age fracture mechanics and cracking of concrete: experiments and modelling [Ph.D. thesis]*, Department of Structural Engineering and Materials, Technical University of Denmark, Supervisor, 2003.

[4] A. Bentur, Ed., *Early Age Cracking in Cementitious Systems: Report of RILEM Technical Committee 181-EAS 'Early Age Shrinkage Induced Stresses and Cracking in Cementitious Systems'*, RILEM Publications, Bagneux, France, 2003.

[5] J. Zhang, Y. Gao, Y. Han, and J. Wang, "Evaluation of shrinkage induced cracking in early age concrete: from ring test to circular column," *International Journal of Damage Mechanics*, 2015.

[6] PCA: The Portland Cement Association, http://www.cement.org.

[7] P. Havlásek, *Creep and shrinkage of concrete subjected to variable environmental conditions. Prague [Ph.D. thesis]*, Czech

Technical University in Prague, Faculty of Civil Engineering, Supervisor, Jirásek Milan, Prague, Czech Republic, 2014.

[8] L. Topolář, P. Misák, D. Kocáb, and M. Matysik, "Applying method of acoustic emission for monitoring of different concrete mixture during setting and hardening," *Solid State Phenomena*, vol. 249, pp. 91–95, 2016.

[9] E. E. Holt, "Early age autogenous shrinkage of concrete," VTT Publications 446, Technical Research Centre of Finland, Espoo, Finland, 2001.

[10] "RILEM draft recommendation: TC-242-MDC multi-decade creep and shrinkage of concrete," *Materials and Structures*, vol. 48, no. 4, pp. 753–770, 2015.

[11] L. Topolář and L. Pazdera, "Acoustic emission in protected and non-protected concrete during the first 24 hours," *Applied Mechanics and Materials*, vol. 578-579, pp. 1149–1152, 2014.

[12] J. Newman and B. S. Choo, *Advanced Concrete Technology: Concrete Properties*, Elsevier, Amsterdam, The Netherlands, 2003.

[13] Schleibinger Testing Systems, http://www.schleibinger.com.

[14] H. W. Reinhardt and C. U. Grosse, *Advanced Testing of Cement Based Materials During Setting and Hardening*, RILEM Publications, Bagneux, France, 2005.

[15] M. Kratochvíl, M. Kadlec, I. Terzijski, and L. Zvolánek, "Autogenous Shrinkage and its Measurement since the Moment of Concrete Casting. (Autogenní smršťování a jeho měření od okamžiku uložení betonu)," *Beton: Technologie, Konstrukce, Sanace*, vol. 14, no. 3, pp. 64–67, 2014 (Czech).

[16] L. Barcelo, M. Moranville, and B. Clavaud, "Autogenous shrinkage of concrete: a balance between autogenous swelling and self-desiccation," *Cement and Concrete Research*, vol. 35, no. 1, pp. 177–183, 2005.

[17] A. M. Soliman and M. L. Nehdi, "Effect of drying conditions on autogenous shrinkage in ultra-high performance concrete at early-age," *Materials and Structures/Materiaux et Constructions*, vol. 44, no. 5, pp. 879–899, 2011.

[18] A. Mazzoli, S. Monosi, and E. S. Plescia, "Evaluation of the early-age-shrinkage of Fiber Reinforced Concrete (FRC) using image analysis methods," *Construction and Building Materials*, vol. 101, pp. 596–601, 2015.

[19] I. Norisham, P. Omenzetter, and P. Lipscombe, "Monitoring system for in-situ measurement of creep and shrinkage effects in a prestressed concrete bridge," in *Proceedings of the 20th Australasian Conference on the Mechanics of Structures and Materials*, pp. 767–771, Toowoomba, Australia, 2008.

[20] "Creep, shrinkage and durability mechanics of concrete and concrete structures," in *Proceedings of the Eighth International Conference on Creep, Shrinkage and Durability of Concrete and Concrete Structures, Ise-Shima, Japan, 30 September–2 October 2008*, R. Sato, K. Maekawa, T. Tanabe, K. Sakata, H. Nakamura, and H. Mihashi, Eds., CRC Press, Boca Raton, Fla, USA, 2009.

[21] J. Stráský, M. Zich, and P. Novotný, "Bridges with progressivelly erected decks ," in *Proceedings of the CIV-SPRING 2014*, pp. 19–22, Calgary, Canada, 2014.

[22] M. Zich, "The concept of a long-term monitoring of highway D47 bridges," *Prague: Czech Concrete Society*, vol. 11, no. 4, 2011 (Czech).

[23] R. Hofírek and M. Zich, "R35 Sedlice-R35 Sedlice-opatovice, construction of the flyover SO 206.2-monitoring of the stress in the load bearing structure," in *Proceedings of the 22nd Concrete Days 2015*, Czech Concrete Society ČSSI, Praha, Czech Republic, 2015 (Czech).

[24] RILEM Technical Committee TC-242-MDC, "RILEM draft recommendation: TC-242-MDC multi-decade creep and shrinkage of concrete," *Materials and Structures*, vol. 48, no. 4, pp. 753–770, 2015.

[25] A. Carpinteri, G. Lacidogna, G. Niccolini, and S. Puzzi, "Critical defect size distributions in concrete structures detected by the acoustic emission technique," *Meccanica*, vol. 43, no. 3, pp. 349–363, 2008.

[26] L. Topolár, K. Timcaková, P. Misák, L. Topolář, and K. Timčaková, "Influence of superplasticizer quantity on formation of micro-cracks during setting and hardening of concretes by acoustic emission method," *Advanced Materials Research*, no. 1124, pp. 219–224, 2015.

[27] C. Grosse and M. Ohtsu, *Acoustic emission testing*, Springer, Berlin, Germany, 2008.

[28] J. Blitz and G. Simpson, *Ultrasonic Methods of Non-Destructive Testing*, Chapman & Hall, London, UK, 1st edition, 1996.

[29] ČNI, "Methods of testing cement—part 1: determination of strength," ČSN EN 196-1:2005, ČNI, Prague, Czech Republic, 2005 (Czech).

[30] ČSN, "Methods of test for mortar for masonry—part 3: determination of consistence of fresh mortar (by flow table)," ČSN EN 1015-3:2000, CNI, Prague, Czech Republic, 2000 (Czech).

[31] ČSN EN 1015-6:1999, *Methods of Test for Mortar for Masonry-Part 6: Determination of Bulk Density of Fresh Mortar*, This standard is the Czech version of the European Standard EN 1015-6:1999, ČNI, Prague, Czech Republic, 1999 (Czech).

[32] OENORM, "Grout—requirements and test methods," OENORM B 3329:2009-06-01, OENORM, Vienna, Austria, 2009.

[33] B. Kucharczyková, P. Daněk, P. Misák, T. Vymazal, and P. Daněk, "Apparatus for measuring relative deformation of concrete and cement composites," Czech Republic. CZ 21600 U1 Utility model. Applied 13.10.2010. Granted 12.1.2011. Entered 3.1.2011, 2011, https://isdv.upv.cz/webapp/webapp.pts.det?xprim=15835-99&lan=en&s_majs=vysok%C3%A9%20u%C4%8Den%C3%AD%20technick%C3%A9%20v%20brn%C4%9B&s_puvo=kucharczykov%C3%A1&s_naze=&s_anot=.

[34] T. Vymazal, P. Daněk, B. Kucharczyková, and P. Misák, "Continuous measurement method of cement composite weight losses in early phase of setting and hardening, and apparatus for making the same," CZ 304898 B6 Patent, Czech Republic, 2015, https://isdv.upv.cz/webapp/webapp.pts.det?xprim=2083317&lan=en&s_majs=vysok%C3%A9%20u%C4%8Den%C3%AD%20technick%C3%A9%20v%20brn%C4%9B&s_puvo=vymazal-&s_naze=&s_anot=.

[35] Bleeding and segregation. The Concrete Society, http://www.concrete.org.uk/fingertips-nuggets.asp?cmd=display&id=832.

[36] P. Rovnaníková and O. Žalud, "Effect of admixtures and fine grain of aggregate on the portland cement hydration," in *Trvanlivost 2015. Brno: Faculty of Civil Engineering, BUT*, pp. 123–133, Faculty of Civil Engineering, Brno, Czech Republic, 2015.

[37] H. Justnes, E. J. Sellevold, A. Van Gemert, D. Van Gemert, and F. Verboven, "Influence of plasticizers and super-plasticizers on chemical shrinkage of cement," in *Proceedings of the 6th International Conference on Superplasticizers and Other Chemical Admixtures in Concrete*, CANMET/ACI SP-195, pp. 601–614, Nice, France, 2000.

Hindawi
Advances in Materials Science and Engineering
Volume 2017, Article ID 4214086, 8 pages
https://doi.org/10.1155/2017/4214086

Research Article

Rheological Method for Alpha Test Evaluation of Developing Superplasticizers' Performance: Channel Flow Test

Jae Hong Kim, Jin Hyun Lee, Tae Yong Shin, and Jin Young Yoon

School of Urban and Environmental Engineering, Ulsan National Institute of Science and Technology, Ulsan 44919, Republic of Korea

Correspondence should be addressed to Jae Hong Kim; jaekim@unist.ac.kr

Received 5 October 2016; Accepted 19 December 2016; Published 10 January 2017

Academic Editor: Doo-Yeol Yoo

Advance in high-range water-reducing admixture revolutionizes the workability and constructability of conventional vibrated concrete as well as self-consolidating concrete. Its need from construction fields has increased, and consequently a variety of new-type polycarboxylates, base polymers for the admixture, are being formulated in these days. Synthesizing new polymers needs a quick, but reliable, test to evaluate its performance on concrete. The test is also asked for selecting the best applicable brand of them before a test concrete will be mixed. This paper proposes a "channel flow test" and its usage for the purpose. The proposed procedure for the test includes the mix proportion of a test mortar, the test method, and rheological interpretation of the test results.

1. Introduction

Polycarboxylate- (PCE-) based high-range water-reducing admixture (HRWRA) was firstly introduced by Nippon Shokubai, Inc. (cement dispersant, JP 842,022; S59-018338; 1981), and then it became one of the most important polymers for chemical admixtures [1–3]. The merits of PCE, a raw material for HRWRA, can be found on its superior performance based on steric repulsion and its variability to control the time of its functioning. Changing its polymeric structure, such as trunk chain length and grafts' configuration, allows us to control the degree and speed of its absorption on cement grains, which results in controlling the time-dependent fluidity of cement-based materials.

A variety of polymeric structures have been developed to respond to needs from construction fields. A simple test to evaluate its performance in the middle of development is accordingly required in a polymer-synthesizing lab. Testing its application on concrete mixtures is certainly necessary at the end. The former can be called "alpha test," evaluating it in the producing lab, and the latter is "beta test" to evaluate its final blend with the field materials such as Portland cement and aggregates. A mini slump flow test [3–5] using a Hagerman cone has been widely used for the alpha test, but it has several limitations on considering the aggregate effect and the sensitivity on fluidity [6]. The cone used for the mini slump flow test was originally designed for a thick mortar. Its flow is triggered by dropping the sample using a so-called flow table.

This paper proposes the use of a channel flow test as an alpha test of PCEs. The volume of a sample increases compared to the mini slump flow test, which expects to get a stable measure of the test result. Finding the mix proportion for a test mortar is also one of the important tasks. The fluidity of the test mortar should represent that of concrete to be applied. Finally, a model functions to evaluate the rheological properties based on the results of channel flow test of the test mortar.

2. Channel Flow Test for a Test Mortar

2.1. Apparatus. The channel flow test is designed to sensitively measure the enhanced fluidity of a mortar sample. A volume of 100 mm × 100 mm × 100 mm (its total volume is 1 L) of a mortar sample is placed in the cubic space surrounded by a gate and walls, as shown in Figure 1. The higher volume of a sample, compared to the mini slump flow test (180 mL), increases the reliability of the measurements. Lifting up the gate induces the mortar flow by its self-weight. When the flow stops, the final length of the channel flow and the time to get the final length or 500 mm approach are measured. The channel guided to one-direction flow gives higher sensitivity

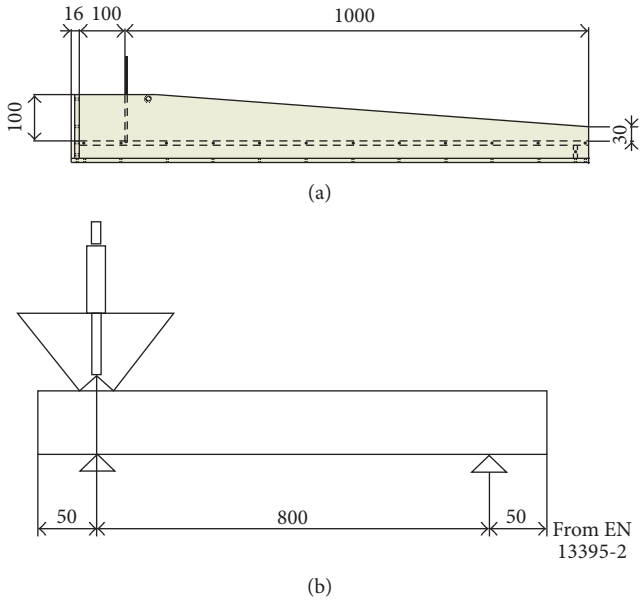

Figure 1: Equipment for (a) channel flow test and (b) grout flow test (dimensions are in mm).

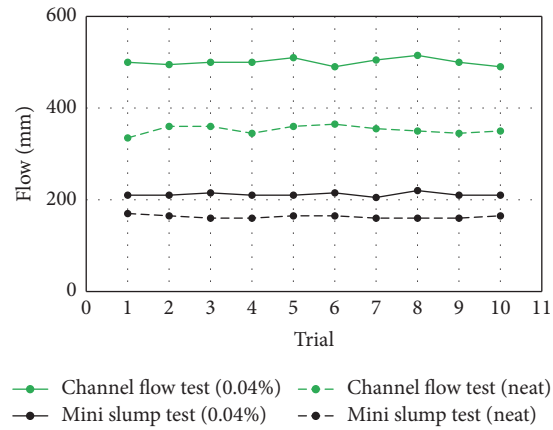

Figure 2: The result of resolution and repeatability.

than the radial flow by the mini slump flow test. The one-directional flow is based on the idea of the grout flow test (EN 13395-2. Products and systems for the protection and repair of concrete structures. Test methods. Determination of workability. Test for flow of grout or mortar). While the grout flow test permits the drop of a mortar sample from the charging hopper, a sample in the channel flow test is not subjected to such a dynamic motion. Note that the cross section of the grout flow apparatus is 130 mm in width by 75 mm in height and a one liter sample of grout is required for the test.

2.2. Resolution, Sensitivity, and Stability. The prototype of the channel flow test was priorly applied to only indicate the fluidity of mortar samples, where its application was acceptable [7, 8]. More pretests using various cement paste and mortar mixes support the fact that the range of 300 mm to 700 mm is acceptable for the channel flow. A sample showing less than 300 mm channel flow is so thick that it collapses when the gate opens. The collapse of a sample is not wanted to evaluate its flow behavior. On the other hand, a sample showing more than 700 mm channel flow is susceptible to segregation. Assuming a thin layer is composed at the end of the high channel flow, a sample showing the channel flow of 700 mm would be 14.3 mm thick (1 L-volume divided by the planer section 100 mm × 700 mm). The front-end thickness is lower than the calculation in practice because the top surface is inclined. Fine aggregates have the maximum grain of 5 mm, which is higher than the one-third of the thin layer thickness. The aggregate segregation is likely to occur in such a case. Note that the effective range of the mini slump flow is considered as 200 mm to 400 mm with the same reason.

A resolution test is accomplished in comparison to the mini slump flow test. Figure 2 shows the results of 10 replicated mixes, where two samples were used: one was a neat cement paste prepared by the water-to-cement ratio (w/cm) of 0.40 and the other having the same w/cm incorporated a HRWRA (0.04% dosage per cement mass). The superplasticzed cement paste gave the channel flow of 500 ± 13 mm, which is approximately ±3% variation on their average. Its mini slump flow was 210 ± 8 mm (±4% variation approximately). The neat cement paste showed the channel flow of 350 ± 15 mm (±4% variation) and the mini slump flow of 165 ± 5 mm (±3% variation). On the other hand, comparing the HRWRA effect on both flows indicates the sensitivity of the tests. While the mini slump flow showed 27% increase in its measurement (from 165 mm to 210 mm), the channel flow did 43% increase (from 350 mm to 500 mm). Therefore, it can be said that the channel flow test has better sensitivity on the fluidity of a sample and its resolution is in the same range, within ±4%, of the mini slump flow.

The viscosity of a sample is generally related to the time of spreading. One measure to consider the spreading time is the time to get 500 mm spread, similar to the slump flow test. The other measure for the viscosity evaluation is the time to get the final spread, which showed better correlation on the mini slump flow test [4]. The measuring stability of each time was compared in Figure 3. A total of 4 replicated mixes having w/cm = 0.35 and sand-to-cement ratio of 1.5 by mass were tested. A commercially available HRWRA (0.06% dosage per cement mass) was applied. For a single test, both times for 500 mm and the final spread were measured together. As can be compared in Figure 3, the times for the final spread and 500 mm spread showed 10 s variation (±22%) and 3 s variation (±23%), respectively. The value for 500 mm spread was more stable, even though the resolutions for each of the measurements are similar in percentage. Therefore, the use of the time for 500 mm spread is recommended because the viscosity is very sensitive to the value of spreading time.

2.3. Rheological Analysis for the Results. Developing a relationship between the rheological properties and the results of a field test allows us to have quantitative understanding on the flow behavior. A theoretical analysis [9] concluded an inverse relationship between the yield stress and the slump flow of a concrete mix. The relationships for the mini slump flow test and marsh cone test were summarized and compared [5],

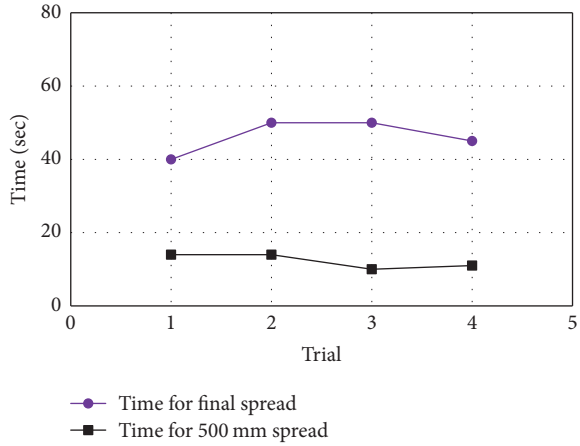

Figure 3: Repeatability on the measurement of the spreading time.

where the volume-of-fluid (VOF) simulation was adopted. For example, the yield stress (τ_y) and the plastic viscosity (η_p) can be obtained from the measurement of the mini slump flow test [4]:

$$\tau_y = 0.00660 D_f^{-5.81}, \quad (1)$$

$$\eta_p = \tau_y \left(0.00641 T_f - 0.00194\right), \quad (2)$$

where D_f and T_f are the mini slump flow, in meter, and the time to get the final mini slump flow, in second, respectively.

The volume-of-fluid (VOF) technique was also applied to simulate the channel flow test. A half-symmetric model was composed with 8-node hexagonal elements. The average mesh size was 10 mm, which is small enough to have an accuracy in the flow simulation of cement-based materials [10]. Thus, the number of elements was 2,700 for modeling an 800 mm long channel. The time increment for explicit computation was 0.1 s, and the channel flow was simulated for 65 s. Input variables for the flow simulation were yield stress and plastic viscosity assuming a mortar sample is a Bingham model fluid. Its density was set to 2,200 kg/m^3. Figure 4 shows an example result of flow simulation: (a) snapshots of the VOF simulation and (b) time spread curve for a Bingham fluid having 15 Pa yield stress (τ_y) and 30 Pa·s plastic viscosity (η_p). The front of the channel flow was determined by the volume fraction of each element.

In order to establish database of the flow simulation, each spread curve was fitted by a logarithmic function:

$$C(t) = \alpha + \beta \ln(t), \quad (3)$$

where α and β are the parameters related to the final length of spread and its damping, respectively. As shown in Figure 4(b), the logarithmic function showed a satisfactory fitting than an exponential function. The coefficient of determination was higher than 0.95 for most of spread curves. Assigning a cut-off velocity (V_f) of 1 mm/s allows us to catch the time for the Bingham fluid stops: its flow front stops

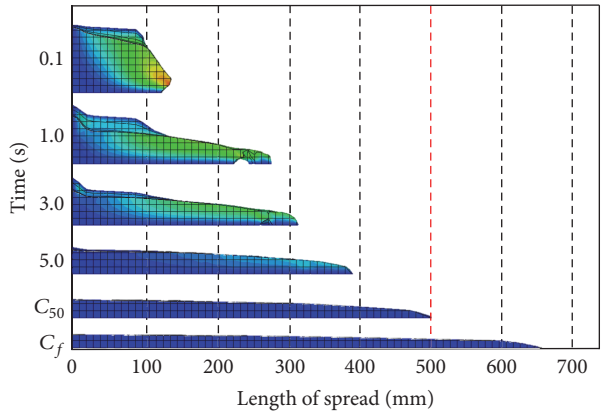

(a)

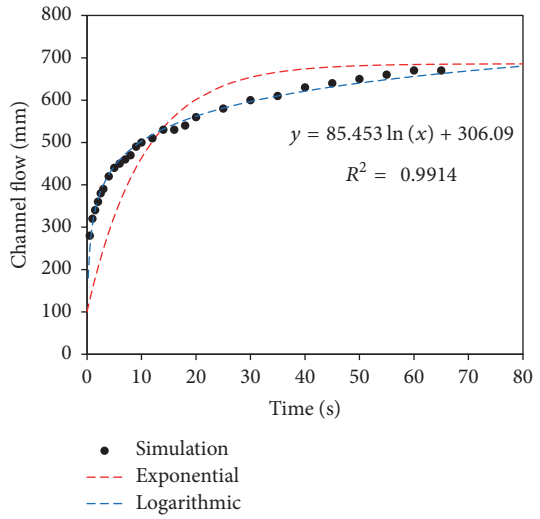

(b)

Figure 4: Simulation contour and spread curve of channel flow simulation.

moving at the time of β/V_f from the derivative of (1). The final spread of the channel flow test is then calculated by

$$C_f = \alpha + \beta \ln\left(\frac{\beta}{V_f}\right), \quad (4)$$

which is a measure of the channel flow (C_f). In addition, the time for its 500 mm flow is

$$C_{50} = \exp\left(\frac{500 - \alpha}{\beta}\right). \quad (5)$$

The flow simulations were conducted for the range of 1 to 60 Pa yield stress and 0 to 100 Pa·s plastic viscosity. A total of 48 combinations were parameterized by (3). Finally, the database composed of τ_y, η_p, C_f, and C_{50} developed using (4) and (5).

Figure 5(a) shows the correlation between the rheological properties and the results of the channel flow test. The channel flow (C_f) was inversely proportional to the yield stress of

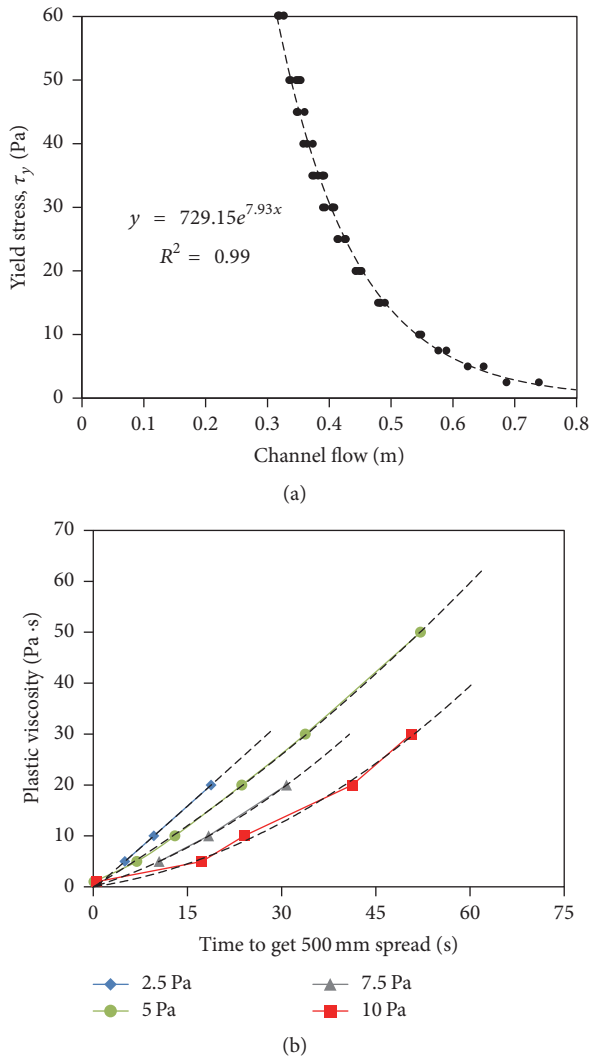

FIGURE 5: Correlation for the rheological evaluation.

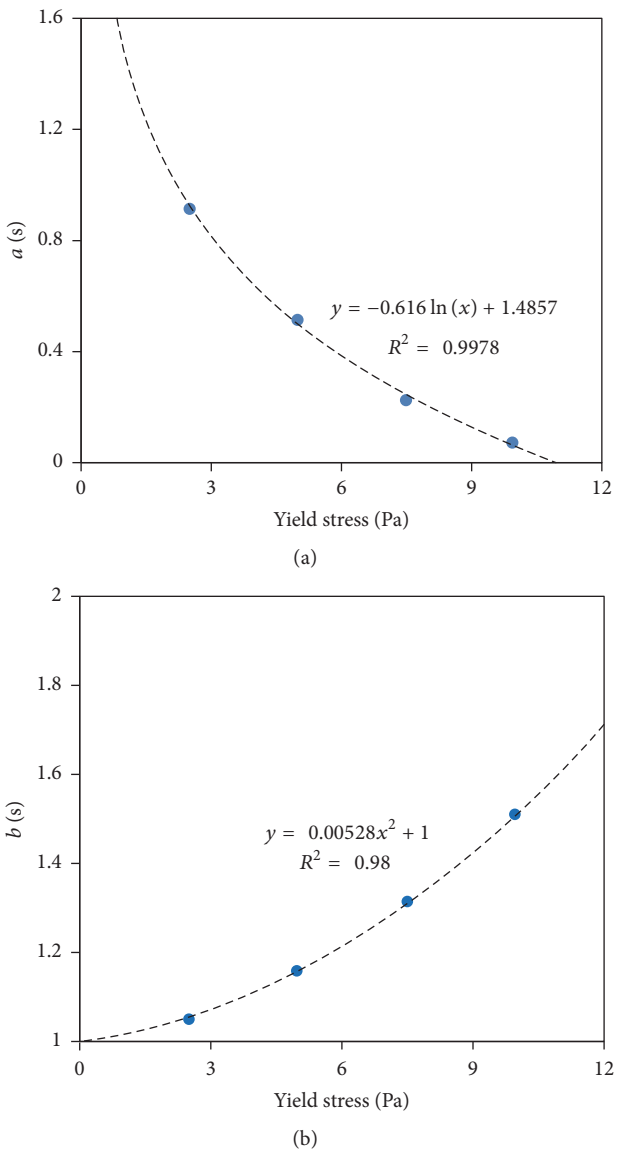

FIGURE 6: Regression analysis for the model parameters a and b.

a Bingham fluid, which is similar to the tendency for the slump flow. The inverse proportionality was modeled by

$$\tau_y = k_1 \exp\left(-\frac{C_f}{k_2}\right), \tag{6}$$

where k_1 and k_2 are fitting coefficients in the unit of "Pa" and "mm," respectively. Their values determined by a linear regression are listed in Table 1. In addition, as shown in Figure 5(b), the 500 mm flow time had a power-law relation with the plastic viscosity when the yield stress is fixed. Encapsulating the effect of the yield stress in the model parameters gave

$$\eta_p = a \cdot \left(\frac{C_{50}}{k_6}\right)^b, \tag{7}$$

where k_6 is a coefficient determining the unit of the plastic viscosity, here in "s." The model parameters, a and b, were then functions of the yield stress:

$$a = -k_3 \ln\left(\frac{\tau_y}{k_4}\right),$$
$$b = \left(\frac{\tau_y}{k_5}\right)^2 + 1, \tag{8}$$

where a and b were dimensionless parameters, and the units of k_3, k_4, and k_5 were determined to "Pa·s," "Pa," and "Pa," respectively, for nondimensionalization. Excepting the cases having a high yield stress ($\tau_y \geq 10$ Pa), the coefficients of determination were larger than 0.99 for a linear regression with respect to a and b. Figure 6 shows the results of the linear regression for the η_p-C_{50} relationship. The high yield stress cases also follow the trends in (8) with marginal errors.

Table 1: Coefficients for the correlating model.

k_1	k_2	k_3	k_4	k_5	k_6	k_7	k_8	k_9	k_{10}	k_{11}
729 Pa	126 mm	0.616 Pa·s	11.2 Pa	13.8 Pa	1.0 s	3.0 s	1568 Pa	46.1 s	11.6 Pa	1 Pa·s

In the same way as the η_p-C_{50} relationship, that for the time to get the final spread (η_p-C_{tf}) could be correlated. One may refer to the previous study [11]. Here, the result of the correlation is reported:

$$\eta_p = k_{11} \exp\left(\frac{C_{tf} - d}{c}\right),$$
$$c = -k_7 \ln\left(\frac{\tau_y}{k_8}\right), \quad (9)$$
$$d = k_9 \exp\left(\frac{-\tau_y}{k_{10}}\right),$$

where the value of each coefficient is listed in Table 1.

2.4. Mix Design of a Test Mortar. PCEs are usually applied for having the fluidity of self-consolidating concrete (SCC), and then a test mortar needs to represent the rheophysical state of SCC. The rheophysical state of a concentrated suspension is usually described by solid volume fraction [12]. Suspension models such as Krieger-Dougherty equation also indicate that the volume fraction of aggregates is critical [13, 14]. The aggregate volume fraction for SCC is intentionally reduced to decrease its yield stress, and its water-to-cement ratio is also reduced to have better stability. For example, an SCC's mix proportion by mass ratio is given by 0.33 : 1 : 1.63 (cementitious binder, water, and fine and coarse aggregates, resp.). The volume fraction of aggregates is 0.65 in the mix. In comparison, normal concrete is proportioned by 0.56 : 1 : 2.74 and the volume fraction of aggregates is 0.71. Finally, the mix proportion for a test mortar is regularized by 0.35 : 1 : 1.5 for considering the rheophysical state of SCC.

Using a bag of standard sand (ISO 679. Methods of testing cements. Determination of strength) makes it easy to prepare a sample. The mass of the bag is 1.35 kg, and then those of water and cement become 0.315 kg and 0.9 kg, respectively. Approximately 1.12 L of a test mortar is then produced. Note that ISO 679 provides the mix proportion of 0.5 : 1 : 3 for measuring the cement strength. The mix proportion for evaluating the PCE effect needs a higher water-to-cement ratio (0.35) and relatively smaller content of sand (1.5).

The optimal procedure to evaluate the performance of PCE is finally established:

(1) A test mortar sample is prepared with the cement-to-sand ratio of 1.5 and the water-to-cement ratio of 0.35. Approximately 1.12 L will be obtained with 0.315 kg-water, 0.9 kg-cement, and 1.35 kg-standard sand. The dosage of PCE needs to be adjusted to get the channel flow of 300 to 700 mm.

(2) The raw materials are mixed for 5 min using a planetary mixer.

(3) The channel flow test is followed. The final length of spread, C_f, the time taken for the sample to have 500 mm spread, C_{50}, and the time when the flow stops, C_{tf}, are measured.

(4) The channel flow test is repeated at an interval of 30 min, generally for 2 h, where it is important to remix the sample for 1 min before each repeating measurement. In between the measurements, the loss of water in the sample should be prevented using a plastic cover.

(5) The measured values of C_f and C_{50} at 0, 0.5, 1.0, 1.5, and 2.0 h are reported. Finally, the yield stress and plastic viscosity of a test mortar can be computed using the correlating equations.

3. Application

A total of 6 PCEs were tested. Monomers for their polymerization were the same, acrylic acid and polyethylene oxide. All of them were categorized in the MPEG-type [1]. Their molecular structures, however, varied by different process of polymerization, which results in showing various performance. Following their designed performance, the PCEs were divided into water-reducing type or consistency-maintaining type. The water-reducing PCEs, labeled by LA, LB, and LC, show fast adsorption on cement grains, and then a mix shows high fluidity with a small dosage. In terms of total solid content, a water-reducing PCE was incorporated in 0.12% of cement mass. The consistency-maintaining PCEs, labeled by LD, LE, and LF, were in 0.16% of cement mass. They were adsorbed rather slowly and the samples incorporating them show less fluidity.

Table 2 shows the results of the channel flow test accompanied with the mini slump flow test. The channel flow test was applied into the test mortar following the optimal procedure in Section 2.4, but the mini slump flow test was done with a cement paste having the water-to-cement ratio of 0.34. The dosage for each PCE was the same for both tests.

The channel flows for the water-reducing PCEs were similar to each other at 0 h, and they decreased over time. Only 71%, 54%, and 73% of channel flow of LA12, LB12 and LC12, respectively, were maintained for 2 h. However, the corresponding mini slump flows showed discrepancy: LB12 showed much less fluidity even at 0 h. Loss of mini slump flow was much smaller than that of channel flow. Their application in concrete mixes supports the trend of the channel flow, where the loss of slump flow was observed with all the water-reducing PCEs.

In the case of consistency-maintaining PCEs, LE16 and LF16 had rather lower initial channel flows, and then each of them had nearly doubled in 2 h. Note that the values in the parentheses exceed the limit of the measuring range, which was 300–700 mm for the channel flow and 200–400 mm

Table 2: Performance test results.

Label	Mini slump flow of pastes (mm)			Channel flow of mortars (mm)		
	0 h	1 h	2 h	0 h	1 h	2 h
LA12	400	390	360	635	555	450
LB12	290	260	260	645	430	350
LC12	360	350	340	640	610	470
LD16	280	300	310	520	360	320
LE16	260	370	400	(235)	430	510
LF16	310	(440)	(440)	300	530	560

Table 3: Rheological evaluation on the results of channel flow test.

Label	C_f (mm)	C_{50} (s)	τ_y (Pa)	η_p (Pa·s)
LA12	635	71	4.7	10.1
LB12	645	62	4.4	5.58
LC12	640	63	4.5	6.14
LD16	520	36	11.8	3.72
LE16	235	5	113	1.88
LF16	300	7	67.4	2.07

for mini slump flow as previously stated. The results of the mini slump flow corresponded with the increasing trend of fluidity and comparatively worse performance with LE16. LD16 showed a similar increase in the mini slump flow. However, its channel flow initially gave the highest values and it lost the fluidity within 1 h.

Figure 7 comparatively shows the channel flow of the test mortars and the mini slump flow of the test pastes. Each linear line provides a correlation between two measurements. The correlations for the water-reducing PCEs again indicate poor sensitivity of the mini slump flow of the test pastes: it did not reveal the loss of fluidity. Even though the results of consistency-maintaining PCE samples are on a single line, the right line in the figure, the other PCE samples are far from the coherent trend. Therefore, it can be concluded that the mini slump flow of the test pastes does not represent the flow behavior of the corresponding mortar samples. The use of a test mortar, accompanied with the channel flow test, is believed to better explain the fluidity of concrete mix.

More investigation on the performance of PCE could be made by rheological interpretation. For the initial measurement of channel flow test, (4) to (6) calculated the rheological properties of the test mortars. Table 3 reports the calculated properties. Even though the water-reducing PCEs show the same fluidity ($C_f \approx 640$ mm and $\tau_y \approx 4.5$ Pa), the plastic viscosity is different: 10.1, 5.58, and 6.14 Pa·s for LA12, LB12, and LC12, respectively. A PCE having lower plastic viscosity is preferable for higher workability of concrete.

4. Discussion

The channel flow of a test mortar is also dependent on the characteristics of constituting materials such as cement and

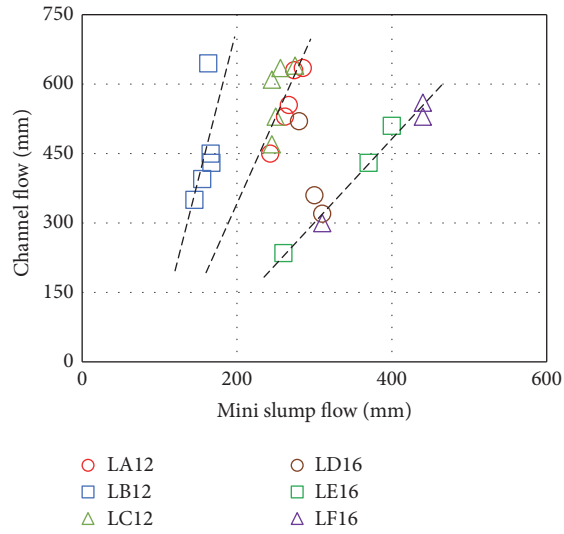

Figure 7: Comparison of channel flow and mini slump flow.

aggregates. Therefore, in order to compare the performance of PCEs, it is required to use the same materials for producing a test mortar. The variation according to the constituting materials is summarized here for future reference.

4.1. Batch of Portland Cement. Even if Portland cement, type I, is manufactured by an identical company, the mineral contents of cement can be different depending on the manufacturing time and process of production [15]. Table 4 shows the oxide composition of Portland cement from three different batches. The channel flows of LC12 using the three cements were in the range of 490 ± 150 mm (517.7 ± 5.91 in). The variation is approximately ±31%, which is beyond the resolution of the test (±4%) and then not an error factor.

4.2. Types of Binder. Blended cement is generally used to increase the fluidity [16] and the resistance against segregation. In this paper, a ternary binder (40% cement A, 50% ground-granulated blast furnace slag, and 10% fly ash) was compared. The test mortar using the ternary binder was segregated with LC12, while the channel flow of 100% cement A-LC12 was 550 mm (21.7 in), as reported in Table 4. When the PCE dosage was decreased, the channel flow of 100% cement A-LC10 was 340 mm (13.4 in) and that using the ternary binder was 900 mm (35.4 in). In addition, the channel

Table 4: Oxide composition of three batches.

Label	CaO	SiO_2	Al_2O_3	Fe_2O_3	SO_3	MgO	K_2O	Na_2O	TiO_2	C_f for LC12
Cement A	64.0%	19.3%	4.4%	3.8%	3.4%	2.4%	1.3%	0.4%	0.3%	550 mm
Cement B	64.6%	18.0%	4.8%	3.3%	3.7%	3.6%	1.1%	0.2%	0.3%	640 mm
Cement C	64.9%	17.9%	4.7%	3.3%	3.7%	3.6%	1.1%	0.2%	0.3%	345 mm

Table 5: The rheological properties of each mortar sample.

Type	TSC/C	τ_y (Pa)	η_p (Pa·s)
BE	0.18%	26.13	2.96
	0.21%	19.03	3.18
	0.24%	12.80	1.97
	0.27%	6.27	1.28
LC	0.10%	49.26	3.59
	0.12%	9.32	3.53
	0.14%	7.35	4.84

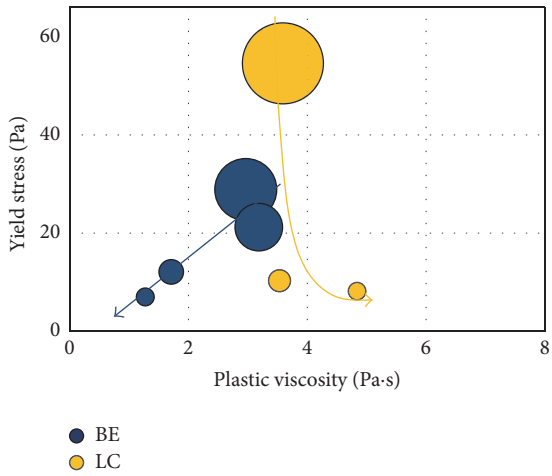

Figure 8: Rheograph showing the effect of PCE dosage.

flow of LC10 increases up to 780 mm (30.7 in) when the water-to-cement ratio increased from 0.35 to 0.40. Thus, the use of ternary binder is very effective in increasing the flow of cement-based materials.

4.3. Types of Sand. The standard sand is required for preparing a test mortar. The use of the other sand dramatically changes the channel flow even though its quality is "good" and its grading is comparable with the standard sand. A comparison was made with good-quality river sand. The average particle size and fineness modulus of river sand are 0.45 mm (0.0178 in) and 2.60, respectively, while those of standard sand were 0.77 mm (0.0303 in) and 2.51. Their difference was highlighted on the absorption rate: 0.79% versus 2.20% for the standard sand and the river sand, respectively. Adding 7.11 g (0.0157 lb; 0.79%-absorption) water to compensate the water adsorption of standard sand increased 10 mm channel flow of a test mortar, where the reference was 550 mm (21.7 in) for LC12, 100% cement A. However, the mortar proportioned with river sand did not flow in spite of adding 19.8 g (0.0437 lb; 2.20%-absorption) water. Inconsistency on the aggregate changes to a great extent the rheophysical state of a test mortar.

4.4. Dosage of PCE. The effect of PCE dosage can be compared with the results of channel flow test. For the mortar samples with a different dosage, the channel flow was firstly conducted. Table 5 shows the test results, where BE and LC are different-type PCEs. The dosage is reported in total solid content (TSC) per cement by mass. The rheograph, originally developed for SCC [17], was developed in Figure 8, where the PCE dosage is represented with the size of each symbol. A smaller dosage is depicted with a bigger circle symbol, which illustrates higher sensitivity to the dosage dependence. Adding more BE sample decreases both yields stress and plastic viscosity of a mix. However, LC sample dominantly decreases the yield stress first, and then its excessive dosage (0.12% to 0.14%) increases the plastic viscosity, while its yield stress holds a constant value.

5. Conclusions

This paper has introduced the alpha test to evaluate the performance of PCE or HRWRA before a test concrete is mixed. The alpha test needs to be quickly finished and less loaded in terms of labor. The mini slump flow test for a test paste, currently widely used, has the limit on its sensitivity and representing the aggregate effect. The channel flow test with a test mortar is therefore proposed. The final spread and the time to get the stoppage of the spread are measures of the test, and a model converting them into rheological properties is also developed. The mix proportion of a test mortar is taken to represent the aggregate volume fraction of SCC. Future work will focus on ways to stack performance data of various PCEs or HRWRAs and quantitatively evaluate their performance grade.

Competing Interests

The authors declare that they have no competing interests.

Acknowledgments

This research was supported by a grant from Smart Civil Infrastructure Research Program funded by Ministry of

Land, Infrastructure and Transport (MOLIT) of Korea government (13SCIPA02) and Korea Agency for Infrastructure Technology Advancement (KAIA).

References

[1] J. Plank, E. Sakai, C. W. Miao, C. Yu, and J. X. Hong, "Chemical admixtures—chemistry, applications and their impact on concrete microstructure and durability," *Cement and Concrete Research*, vol. 78, pp. 81–99, 2015.

[2] E. Sakai, A. Ishida, and A. Ohta, "New trends in the development of chemical admixtures in Japan," *Journal of Advanced Concrete Technology*, vol. 4, no. 2, pp. 211–223, 2006.

[3] S. Hanehara and K. Yamada, "Rheology and early age properties of cement systems," *Cement and Concrete Research*, vol. 38, no. 2, pp. 175–195, 2008.

[4] N. Tregger, L. Ferrara, and S. P. Shah, "Identifying viscosity of cement paste from mini-slump-flow test," *ACI Materials Journal*, vol. 105, no. 6, pp. 558–566, 2008.

[5] A. Bouvet, E. Ghorbel, and R. Bennacer, "The mini-conical slump flow test: analysis and numerical study," *Cement and Concrete Research*, vol. 40, no. 10, pp. 1517–1523, 2010.

[6] K. Yamada, T. Sugamata, and H. Nakanishi, "Fluidity performance evaluation of cement and superplasticizer," *Journal of Advanced Concrete Technology*, vol. 4, no. 2, pp. 241–249, 2006.

[7] J. H. Kim, H. J. Yim, and S. H. Kwon, "Quantitative measurement of the external and internal bleeding of conventional concrete and SCC," *Cement and Concrete Composites*, vol. 54, pp. 34–39, 2014.

[8] J. H. Lee, J. H. Kim, and M. K. Kim, "Fine aggregates size effect on rheological behavior of mortar," *Journal of the Korea Academia-Industrial cooperation Society*, vol. 16, no. 8, pp. 5636–5645, 2015.

[9] N. Roussel and P. Coussot, "'Fifty-cent rheometer' for yield stress measurements: from slump to spreading flow," *Journal of Rheology*, vol. 49, no. 3, pp. 705–718, 2005.

[10] J. H. Kim, H. R. Jang, and H. J. Yim, "Sensitivity and accuracy for rheological simulation of cement-based materials," *Computers and Concrete*, vol. 15, no. 6, pp. 903–919, 2015.

[11] T. Y. Shin, J. H. Lee, J. H. Kim, and M. K. Kim, "Correlation between channel-flow test results and rheological properties of freshly mixed mortar," *Journal of the Korea Academia*, vol. 17, no. 7, pp. 237–244, 2016 (Korean).

[12] P. Coussot and C. Ancey, "Rheophysical classification of concentrated suspensions and granular pastes," *Physical Review E*, vol. 59, no. 4, pp. 4445–4457, 1999.

[13] I. M. Krieger and T. J. Dougherty, "A mechanism for non-newtonian flow in suspensions of rigid spheres," *Journal of Rheology*, vol. 3, no. 1, pp. 137–152, 1959.

[14] L. Struble and G.-K. Sun, "Viscosity of Portland cement paste as a function of concentration," *Advanced Cement Based Materials*, vol. 2, no. 2, pp. 62–69, 1995.

[15] R. P. Ferron, A. Gregori, Z. Sun, and S. P. Shah, "Rheological method to evaluate structural buildup in self-consolidating concrete cement pastes," *ACI Materials Journal*, vol. 104, no. 3, pp. 242–250, 2007.

[16] J. H. Kim, H. J. Yim, and R. D. Ferron, "In situ measurement of the rheological properties and agglomeration on cementitious pastes," *Journal of Rheology*, vol. 60, no. 4, pp. 695–704, 2016.

[17] O. H. Wallevik and J. E. Wallevik, "Rheology as a tool in concrete science: the use of rheographs and workability boxes," *Cement and Concrete Research*, vol. 41, no. 12, pp. 1279–1288, 2011.

Hindawi
Advances in Materials Science and Engineering
Volume 2017, Article ID 1901459, 10 pages
https://doi.org/10.1155/2017/1901459

Research Article

Prediction of Time-Dependent Chloride Diffusion Coefficients for Slag-Blended Concrete

Ki-Bong Park,[1] Han-Seung Lee,[2] and Xiao-Yong Wang[1]

[1] *College of Engineering, Department of Architectural Engineering, Kangwon National University, Chuncheon-Si 200-701, Republic of Korea*
[2] *Department of Architectural Engineering, Hanyang University, Ansan-Si 426-791, Republic of Korea*

Correspondence should be addressed to Xiao-Yong Wang; wxbrave@kangwon.ac.kr

Received 25 August 2016; Accepted 10 November 2016; Published 1 January 2017

Academic Editor: Kazunori Fujikake

The chloride diffusion coefficient is considered to be a key factor for evaluating the service life of ground-granulated blast-furnace slag (GGBS) blended concrete. The chloride diffusion coefficient relates to both the concrete mixing proportions and curing ages. Due to the continuous hydration of the binders, the capillary porosity of the concrete decreases and the chloride diffusion coefficient also decreases over time. To date, the dependence of chloride diffusivity on the binder hydration and curing ages of slag-blended concrete has not been considered in detail. To fill this gap, this study presents a numerical procedure to predict time-dependent chloride diffusion coefficients for slag-blended concrete. First, by using a blended cement hydration model, the degree of the binder reaction for hardening concrete can be calculated. The effects of the water to binder ratios and slag replacement ratios on the degree of the binder reaction are considered. Second, by using the degree of the binder reaction, the capillary porosity of the binder paste at different curing ages can be determined. Third, by using the capillary porosity and aggregate volume, the chloride diffusion coefficients of concrete can be calculated. The proposed numerical procedure has been verified using the experimental results of concrete with different water to binder ratios, slag replacement ratios, and curing ages.

1. Introduction

Chloride ingress is considered to be one of the major factors in the deterioration mechanisms of reinforced concrete in marine environments. The resulting corrosion of steel reinforcements causes serious detrimental effects, such as concrete cover cracking, reduced reinforcement in cross sections, decreased bonding between the steel rebar and concrete, and reduced yield strength and ductility of the steel rebar in reinforced concrete structures. However, to improve the resistance of concrete against chloride ingress, slag is widely used as a mineral admixture. Generally, incorporating GGBS into blended binders can increase the total porosity but will refine the pore size. Slag-blended concrete presents a lower chloride diffusivity and higher chloride binding capacity than control concrete [1].

The chloride diffusion coefficient is a key factor in the service life evaluation of slag-blended concrete. As for the chloride diffusivity in ordinary Portland cement (OPC) concrete or slag-blended concrete, Papadakis [2] and Demis et al. [3] evaluated the chloride diffusivity of fully hardened concrete as a function of the ultimate porosity. Alexander and Thomas [4] evaluated the chloride diffusivity of concrete after 28 days of curing as a function of the water to binder ratios. The Life-365 program [5] also uses the Alexander and Thomas equation [4] to determine concrete diffusivity. However, the Papadakis [2], Demis et al. [3], and Alexander and Thomas [4] models are not perfect. The Papadakis [2] and Demis et al. [3] models assume that cement is completely hydrated (i.e., the hydration degree is 100%) regardless of the water to cement ratio. Wang and Lee [6] reported that concretes with lower water to cement ratios had slower rates of hydration and lower ultimate degrees of hydration. The chloride diffusivity calculated according to the Alexander and Thomas model [4] does not consider other factors, such as the binder content, binder reactivity, and curing methods.

The composition of hydration products, capillary porosity, and chloride diffusivity relate closely to the degree of

hydration in hardening or hardened concrete. Han [7] and Fan and Wang [8] proposed hydration-based chloride ingress models. Time-dependent chloride diffusivity was calculated by using the development of the capillary porosity of concrete over time. However, the Han [7] and Fan and Wang [8] models do not consider the reaction of mineral admixtures and are only valid for Portland cement concrete. In the literature, some models have been proposed that evaluate the chloride diffusivity of concrete containing mineral admixtures. Song et al. [9, 10] calculated the final degrees of reaction of cement and silica fume in silica fume-blended concrete. The capillary porosity, chloride diffusivity, and water permeability were determined by considering the final degrees of the binder reaction and the concrete mixing proportions. Oh and Jang [11] evaluated the chloride diffusivity of fly ash and slag-blended concrete by considering the final degrees of the binder reaction and the concrete porosity. However, Song et al. [9, 10] and Oh and Jang [11] studies are only valid for fully hardened concrete; they do not consider the dependence of chloride diffusivity on curing ages because their models do not account for the kinetic reaction processes of mineral admixtures.

As for the time dependence of chloride diffusivity, Nokken et al. [12] and Yu and Ye [13] found that chloride diffusion into concrete decreased over time. Concrete containing mineral admixtures has shown reduced chloride diffusivity compared to reference concrete. An empirical time parameter [14–16] has frequently been used to describe the age dependence of the chloride diffusion coefficient. However, this empirical time parameter cannot fully describe the evolution of the hardening concrete microstructure. The influence of various factors, such as the cement type, water to binder ratio, and slag replacement ratio, on this empirical time parameter requires further investigation [17].

To address the shortcomings of these current models, this paper presents a numerical procedure that analyzes the time dependence of the chloride diffusion coefficient. By using a blended cement hydration model, the degree of the reaction of binders and the capillary porosity of binder paste were calculated. Furthermore, the chloride diffusion coefficients at different curing ages were determined, considering the capillary porosity and aggregate volume.

2. Cement Hydration Model and Chloride Diffusion Coefficient Model

2.1. Cement Hydration Model. Wang and Lee [6, 18] proposed a hydration model for concrete containing supplementary cementitious materials, such as silica fume, fly ash, and slag. Hydration equations were proposed for cement and mineral admixtures, respectively, and the mutual interactions between cement hydration and mineral admixture reactions are considered with the capillary water content and calcium hydroxide content. The hydration model is valid for concrete with different water to binder ratios, mineral admixture replacement ratios, and curing temperatures [6, 18].

The reaction degrees of cement and mineral admixtures are used as fundamental indicators to evaluate the development of concrete properties. The degree of cement hydration (α) is defined as the ratio of the mass of hydrated cement to the mass of cement in the mixing proportion. The value of the degree of cement hydration (α) ranges between 0 and 1. A degree of cement hydration of $\alpha = 0$ means the absence of any hydration, and a degree of cement hydration of $\alpha = 1$ means that cement has fully hydrated.

By using an integration method, the degree of cement hydration can be determined as follows:

$$\alpha = \int_0^t \left(\frac{d\alpha}{dt} \right) dt, \tag{1}$$

where t is time and $d\alpha/dt$ is rate of cement hydration. The detailed equations for $d\alpha/dt$ are available in our former research [6, 18].

Similarly, the reaction degree of a mineral admixture (α_M) is defined as the ratio of the mass of reacted mineral admixture to the mass of the mineral admixture in the mixing proportion. The value of the degree of the mineral admixture reaction (α_M) ranges between 0 and 1. $\alpha_M = 0$ means the absence of any mineral admixture reaction, and $\alpha_M = 1$ indicates that the mineral admixture has reacted completely. The reaction degree of the mineral admixture reaction can also be determined using an integration method in the time domain as follows:

$$\alpha_M = \int_0^t \left(\frac{d\alpha_M}{dt} \right) dt, \tag{2}$$

where $d\alpha_M/dt$ is the rate of the mineral admixture reaction. The detailed equations for $d\alpha_M/dt$ are available in our former research [6, 18].

In cement-mineral admixture blends, the production of chemically bound water relates to both cement hydration and mineral admixture reactions. The chemically bound water content can be determined as follows:

$$W_{\text{cbm}}(t) = 0.25 * C_0 * \alpha + 0.3 * M_0 * \alpha_M, \tag{3}$$

where W_{cbm} is the chemically bound water content, C_0 is the mass of cement in the mixing proportion, and M_0 is the mass of the mineral admixture in the mixing proportions. The expression $0.25 * C_0 * \alpha$ is the mass of the chemically bound water from cement hydration, and the expression $0.3 * M_0 * \alpha_M$ is the mass of the chemically bound water from the slag reactions [6, 18].

In the cement-mineral admixture blends, both cement hydration and mineral admixture reactions contribute to the formation of gel water. The content of gel water can be calculated as follows:

$$W_{\text{gel}}(t) = 0.15 * C_0 * \alpha + 0.15 * \alpha_M * M_0, \tag{4}$$

where W_{gel} is the mass of gel water, $0.15 * C_0 * \alpha$ is the mass of gel water produced from cement hydration, and $0.15 * \alpha_M * M_0$ is the mass of gel water produced from slag reaction.

The mass of combined water equals the sum of chemically bound water and gel water. The mass of combined water can be determined as follows:

$$W_c(t) = W_{\text{gel}}(t) + W_{\text{cbm}}(t), \tag{5}$$

where $W_c(t)$ is the mass of combined water.

In cement-mineral admixture blends, capillary water is consumed by both cement hydration and mineral admixture reactions. The capillary water content can be calculated as follows:

$$W_{\text{cap}}(t) = W_0 - 0.4 * C_0 * \alpha - 0.45 * \alpha_M * M_0, \quad (6)$$

where W_{cap} is the mass of capillary water in the hardening concrete and W_0 is the mass of water in the mixing proportion. The expression $0.4 * C_0 * \alpha$ is the mass of capillary water consumed by cement hydration and the expression $0.45 * \alpha_M * M_0$ is the mass of the consumed capillary water from the slag reactions.

For hardened concrete, the capillary porosity equals the sum of capillary water and chemical shrinkage. The capillary porosity can be determined as follows:

$$\phi_{\text{cap}}(t) = W_{\text{cap}}(t) + 0.0625 * C_0 * \alpha + 0.1 * \alpha_M * M_0, \quad (7)$$

where $\phi_{\text{cap}}(t)$ is the capillary porosity of hardening concrete, $0.0625 * C_0 * \alpha$ is the chemical shrinkage from cement hydration, and $0.1 * \alpha_M * M_0$ is the chemical shrinkage from slag reactions.

2.2. Chloride Diffusion Coefficient Model. Concrete is a three-phase material consisting of a cement paste matrix, aggregate, and interfacial transition zones (ITZs) between the cement paste matrix and aggregate. The interfacial transition zone has a higher capillary porosity and contains higher calcium hydroxide volume fractions compared to the bulk matrix. Interfacial zones are formed due to the particle-packing effect and the one-sided growth effect [19]. The particle-packing effect arises because the cement particles cannot pack together as well near a flat edge as in a free space. The one-sided growth effect is reactive growth from the cement side, but not from the aggregate side. The cement paste matrix is interconnected through interfacial transition zones. Garboczi [19] found that when the aggregate volume fractions are greater than 50%, the interfacial transition zone will be fully percolated. This observation agrees with the experimental results from Principgallo et al. [20]. Because most concretes have aggregate volume fractions above 50%, the interfacial transition zones in the usual concrete are percolated.

Due to the cement particle-packing effect, the ITZ shows a higher water to cement ratio. Therefore, the effective water to cement ratio in the bulk cement paste will be reduced. Nadeau [20, 21] proposed a model to consider water to cement gradients between the aggregate and bulk cement paste. The model is a function of the overall water-cement ratio, volume fraction and radius of the aggregate, specific gravity of cement, and thickness of the ITZ. The equations for determining the effective water to binder ratio of bulk cement paste in concrete are given as follows [21, 22]:

$$\overline{V_C} = \frac{10(1 - V_a)}{(1 + (W_0/(C_0 + M_0))G_C)[a_c V_a \varepsilon \{\varepsilon^2 + 5\varepsilon + 10\} + 10(1 - V_a)]}, \quad (8)$$

$$\overline{W_C} = \frac{1 - \overline{V_C}}{G_C \overline{V_C}},$$

where $\overline{V_C}$ is the binder volume fraction in the bulk binder paste, V_a is the volume of the aggregate, $W_0/(C_0 + M_0)$ is the overall water to binder ratio of concrete, G_C is the specific gravity of the binder, a_c is a constant equal to approximately -0.5, and ε is the thickness ratio of ITZ. $\overline{W_C}$ is the effective water to binder ratio in the bulk binder paste, whereas $1 - \overline{V_C}$ indicates the water volume fraction in the bulk binder paste.

The diffusivity of the cement paste phase D_P is mainly dependent on the capillary pores in the cement paste, which can be determined as follows [8]:

$$D_P(t) = A_1 * \left(\phi_{\text{paste}}\right)^{A_2}, \quad (9)$$

$$\phi_{\text{paste}} = \frac{\phi_{\text{cap}}}{V_P}, \quad (10)$$

where A_1 and A_2 are the relation coefficients between the capillary porosity and chloride diffusivity, respectively; ϕ_{paste} is the capillary porosity in the binder paste; and V_P is volume of binder paste calculated from the effective water to binder ratio $\overline{W_C}$. In (9), the intrinsic diffusion coefficient A_1 relates to the type of binder, such as cement or slag. Exponent A_2 ($A_2 > 1$) relates to the pore size distribution or the complexity of the microstructure of the reaction products. As shown in (9) and (10), with the progress of binder hydration, the capillary porosity of concrete decreases and the chloride diffusion coefficient decreases correspondingly.

When the diffusivity of the aggregate particle inclusions is assumed to be zero, according to the composite sphere assemblage (CSA) model [11], the chloride diffusion coefficient of concrete can be determined as follows:

$$\frac{D}{D_P} = 1 + \frac{V_a}{1/(2(D_i/D_P)\varepsilon - 1) + (1 - V_a)/3}, \quad (11)$$

where D is the diffusivity of concrete and D_i is the diffusivity in the interfacial transition zone.

By using a hard core/soft shell model, Garboczi [19] evaluated the connectivity of the interfacial zones for different choices of interfacial zone thicknesses. Furthermore, by comparison with cement mortar mercury intrusion data [23], a choice of 20 μm for the interfacial zone thickness was found to give the best agreement with the mercury data. The mean radius of coarse aggregate is approximately 10 mm. Hence, in this study, a thickness ratio of ITZ of approximately $\varepsilon = 0.002$ is used.

Bentz and Garboczi [24] studied the effects of mineral admixtures on the interfacial transition zone. They found that smaller admixtures allow better packing nearer to the aggregate edge, and the reactivity of the mineral admixture controls the consumption of the calcium hydroxide. For fly ash blended mortar, the fraction ratio of CSH between ITZ and the bulk matrix is similar to plain cement mortar [22]. Similarly, based on an analysis of the chloride diffusivity of concrete with various fly ash and slag additions, Oh and Jang [11] proposed that, for Portland cement concrete, fly ash blended concrete, and slag-blended concrete, the ratios between D_i and D_P are almost the same ($D_i/D_P = 7$).

The effects of slag addition on the chloride diffusion coefficients of concrete are summarized as follows: first,

Table 1: Properties of binders [15].

Types	Chemical composition (mass%)							Physical properties	
	SiO_2	Al_2O_3	Fe_2O_3	CaO	MgO	SO_3	Lg. loss	Specific gravity (g/cm^3)	Blaine (cm^2/g)
Cement	21.96	5.27	3.44	63.41	2.13	1.96	0.79	3.16	3214
Slag	32.74	13.23	0.41	44.14	5.62	1.84	0.2	2.89	4340

Table 2: Mixing proportions of concrete [15].

W/B[1]	S/B[2]	Water	Cement (kg/m^3)	Slag (kg/m^3)	Sand (kg/m^3)	Gravel (kg/m^3)	Superplasticizer (% of binder)
0.37	0	168	454	0	767	952	1%
0.42	0	168	400	0	787	976	0.9%
0.47	0	168	357	0	838	960	0.85%
0.37	0.3	168	318	136	762	946	0.8%
0.42	0.3	168	280	120	783	972	0.75%
0.47	0.3	168	250	107	835	956	0.65%
0.37	0.5	168	227	227	760	943	0.75%
0.42	0.5	168	200	200	780	969	0.7%
0.47	0.5	168	178	179	832	853	0.6%

[1]Water to binder ratio. [2]Slag to binder ratio.

incorporating GGBS into blended binders can increase the total porosity because the reactivity of slag is lower than the reactivity of cement. This point is considered using slag-blended cement hydration models ((1) and (7)). Second, calcium silicate hydrate (CSH) gel produced from slag reactions has finer gel pores than the gel from cement hydration. This effect is considered using an intrinsic diffusion coefficient A_1 in (9). Third, the formation of slag reaction products can fill large capillary voids and reduce the average pore size. This effect is considered using a chloride diffusion exponent A_2 in (9). In our study, the evolution of the chloride diffusion coefficient over time is directly related to the time-dependent development of capillary porosity. We do not use the empirical time parameter [14–16] to describe the age dependence of the chloride diffusion coefficient. Compared with the empirical time parameter method [14–16], the physical meaning of the model proposed in this study is much clearer.

However, the proposed model in this study for the chloride diffusion coefficient of concrete shows some limits. First, the chloride diffusivity in the ITZ is dependent on the distance from the aggregate surface [25, 26]. The chloride diffusivity in the ITZ is not analyzed in detail in this study. Second, for hardening concrete, the moisture transport from the water-rich ITZ to the drying bulk paste is not considered [25]. Water transport plays a prominent role in the hardened ITZ microstructure [27]. Therefore, the present version of the proposed model is not perfect and needs to be improved.

3. Verification of the Proposed Model

The experimental results from Song and Kwon [15] were used to verify the proposed model. Song and Kwon [15] performed a systematic experimental study of the chloride diffusivity of slag-blended concrete. They measured a chloride diffusion coefficient for slag-blended concrete with various mixing proportions at different curing ages. Table 1 shows the chemical and physical properties of the cement and slag. Table 2 shows the mixing proportions of the concrete specimens. Concrete specimens with three different water to binder ratios of 0.47, 0.42, and 0.37 and two different slag contents of 30% and 50% were prepared. Concrete cylinder specimens were cured under moist conditions. At curing periods of 28 days (four weeks), 90 days (three months), 180 days (six months), and 270 days (nine months), the chloride diffusion coefficients were measured through an electrical accelerated method. After the electrical accelerated test, a silver nitrate solution ($AgNO_3$ with a concentration of 0.1 mol/L) was used as an indicator to measure the chloride penetration depth that was achieved, and the chloride diffusion coefficient was calculated according to the penetration depth [15]. The diffusion coefficient determined by this test is a migration coefficient, which does not include binding, among other effects.

3.1. Reaction Degree of Cement. The addition of slag presents a dilution effect on cement hydration. A dilution effect means that, in cement-slag blends, the addition of slag makes the water to cement ratio increase. As shown in Figures 1(a) and 1(b), in cement-slag blends, the reaction degree of cement is higher than in plain cement paste. The more the slag additions, the higher the reaction degree of cement. When the water to binder ratio increases from 0.37 (Figure 1(a)) to 0.47 (Figure 1(b)), the degree of cement hydration increases because the concentration of the capillary water and available deposit space of hydration products increases.

3.2. Reaction Degree of Slag. The slag reaction relates to both the water to binder ratios and slag replacement ratios. As shown in Figures 2(a) and 2(b), when the water to binder ratio increases from 0.37 to 0.47, the reaction degree of the slag increases because the concentration of capillary water and

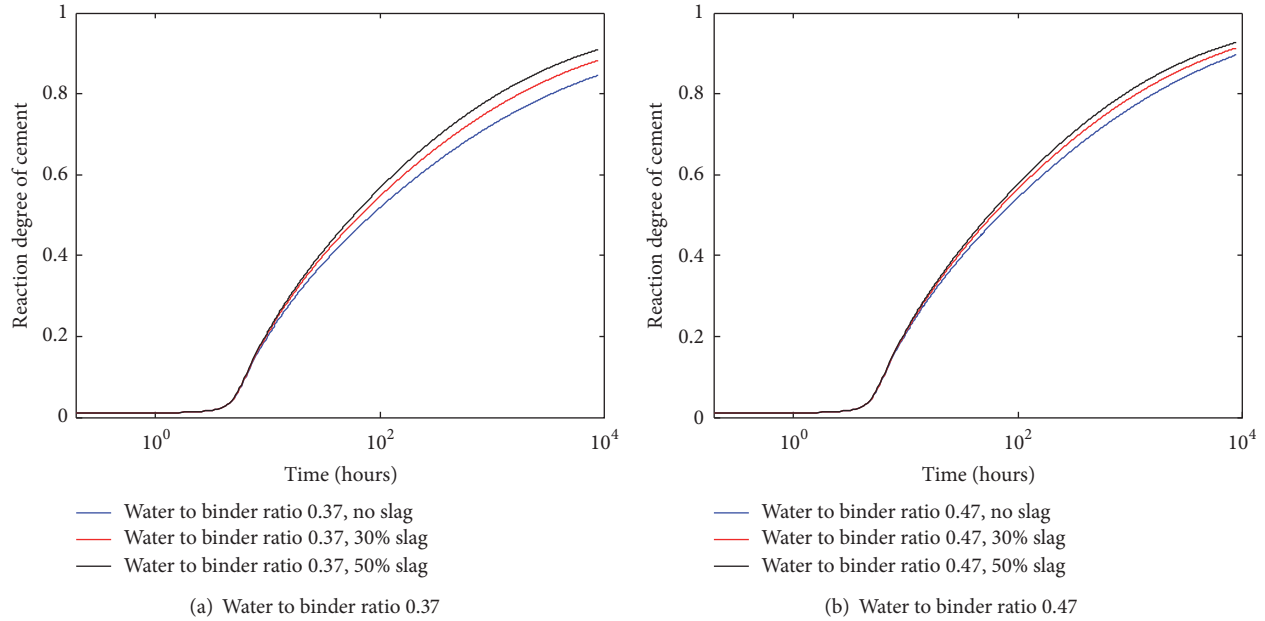

(a) Water to binder ratio 0.37

(b) Water to binder ratio 0.47

Figure 1: Reaction degree of cement.

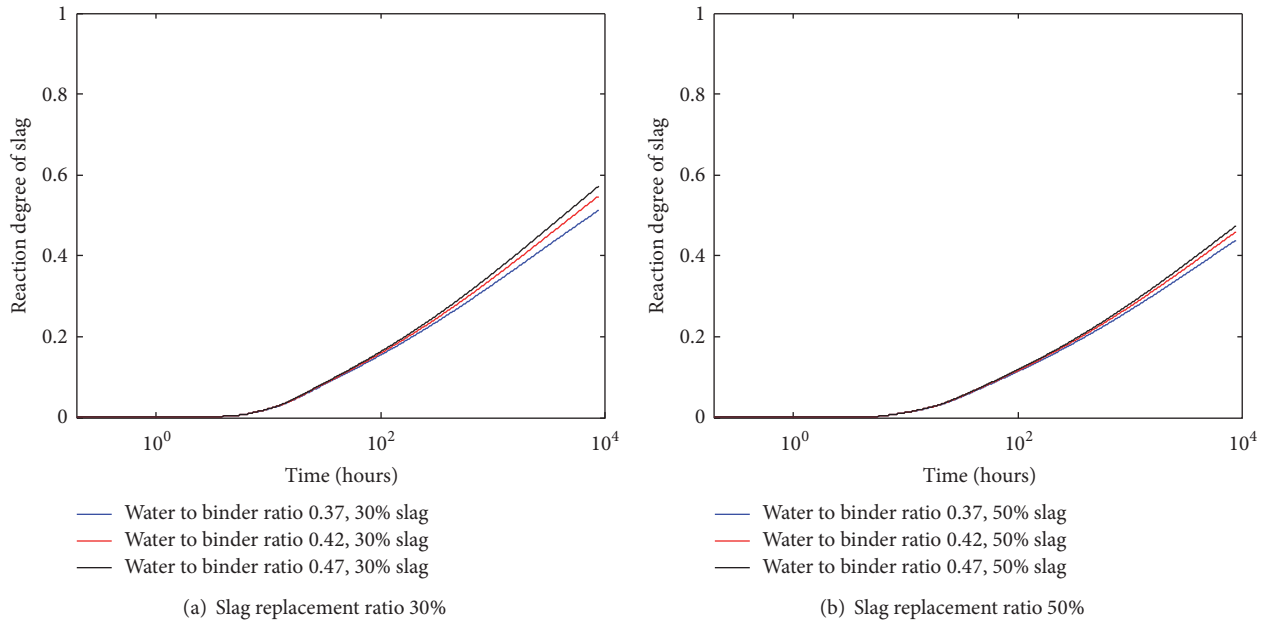

(a) Slag replacement ratio 30%

(b) Slag replacement ratio 50%

Figure 2: Reaction degree of slag.

available deposit space of the hydration products increases. However, when the slag replacement ratio increases from 30% (Figure 2(a)) to 50% (Figure 2(b)), the reaction degree of the slag decreases because the alkali activation effect on the slag reaction becomes weaker.

3.3. Combined Water. As shown in (3)–(5), both cement hydration and the slag reaction contribute to the production of combined water. Figure 3 shows the amount of combined water as a function of curing ages. As shown in Figures 3(a) and 3(b), when the water to binder ratio increases from 0.37 to 0.47, the amount of combined water decreases. For concrete containing 50% slag (Figure 3(b)), the amount of combined water is lower than in plain concrete (Figure 3(a)) because the reaction rate of slag (shown in Figure 2) is much slower than the reaction rate of cement (shown in Figure 1).

3.4. Capillary Porosity. In hydrating cement-slag blends, with the increase in combined water, the reaction products deposit in the capillary pore space and the capillary porosity decreases. Figure 4 shows the amount of capillary porosity in binder paste as a function of the curing ages. As shown in

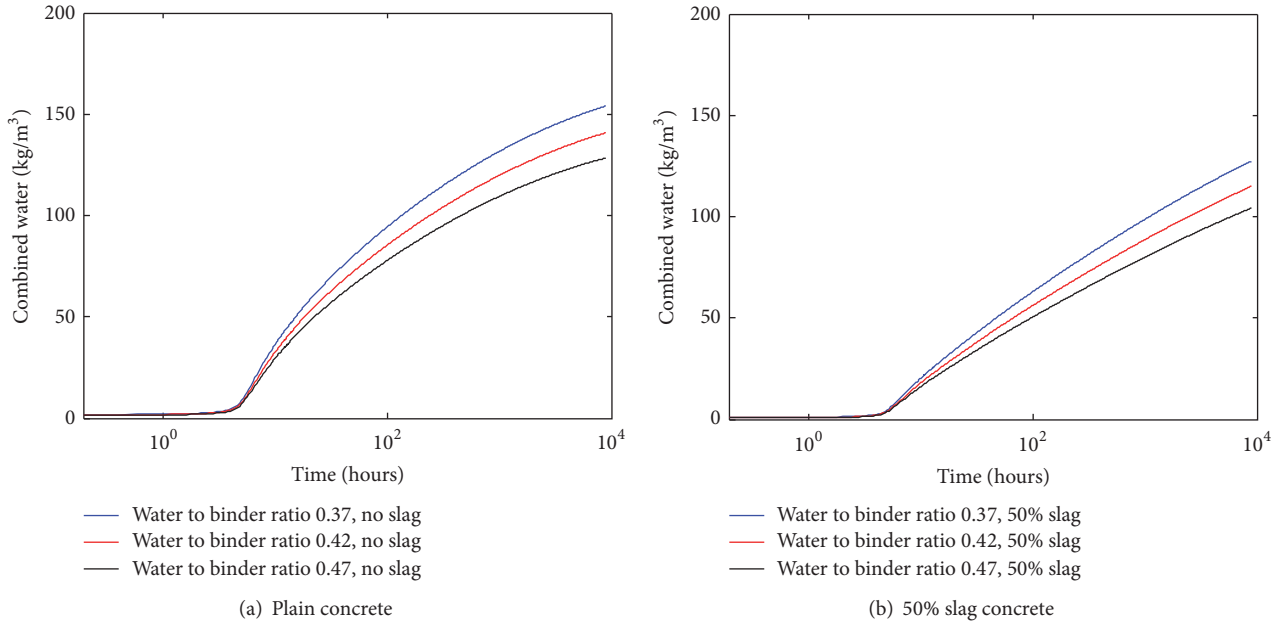

Figure 3: Combined water.

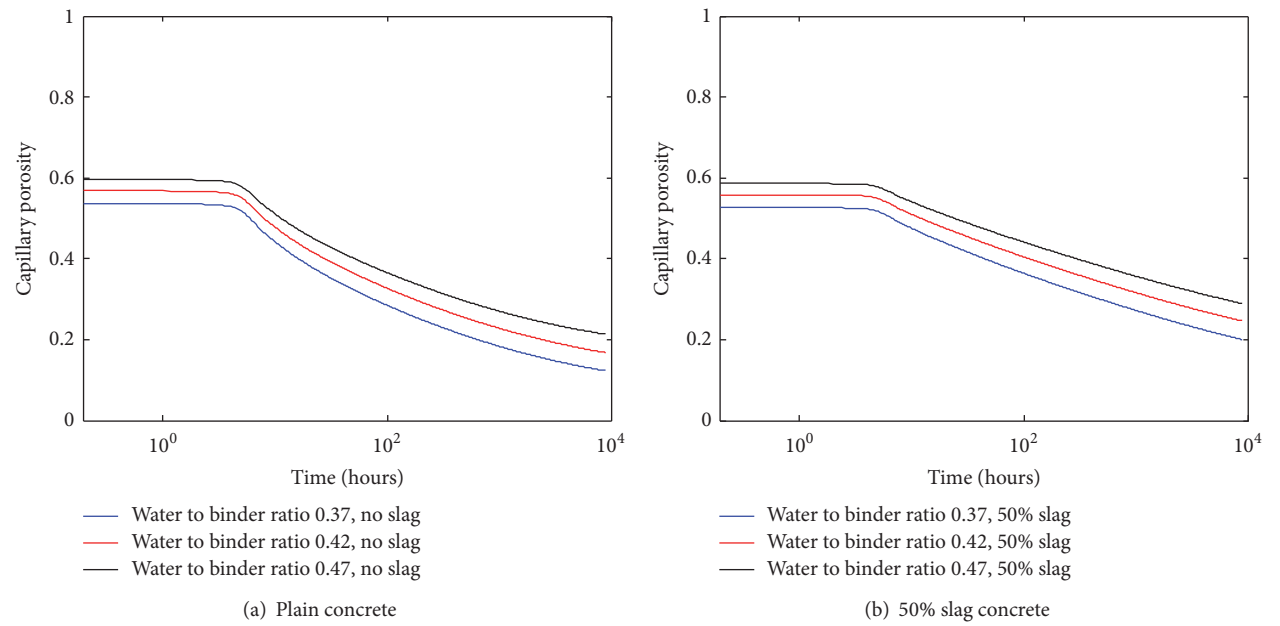

Figure 4: Capillary porosity.

Figure 4, when the water to binder ratio increases from 0.37 to 0.47, the amount of capillary porosity increases. For concrete containing 50% slag, the amount of capillary porosity is higher than in plain concrete.

3.5. General Equation of the Chloride Diffusion Coefficient for Slag-Blended Concrete. As mentioned in Section 2.2, the intrinsic diffusion coefficient A_1 and exponent A_2 in (9) are not dependent on the water to binder ratios and only relate to the type of binders. We assume that cement and slag contribute to both the intrinsic diffusion coefficient A_1 and the exponent A_2 relating to binder weight fractions as follows:

$$A_1 = B_1 * \frac{C_0}{C_0 + M_0} + B_2 * \frac{M_0}{C_0 + M_0}$$
$$A_2 = C_1 * \frac{C_0}{C_0 + M_0} + C_2 * \frac{M_0}{C_0 + M_0}, \quad (12)$$

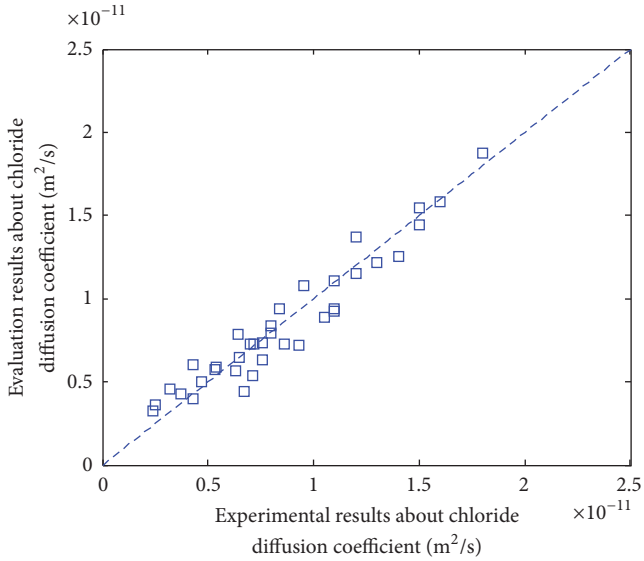

FIGURE 5: Comparisons between experimental results and analyzed results.

where B_1 and B_2 are the contributions of cement and slag, respectively, to the intrinsic diffusion coefficient A_1; C_1 and C_2 are the contributions of cement and slag, respectively, on the exponent A_2. $C_0/(C_0 + M_0)$ and $M_0/(C_0 + M_0)$ are the weight fractions of cement and slag, respectively, in cement-slag blends. As shown in (12), when the replacement ratio of slag equals zero, the chloride diffusion coefficient is only dependent on the values of B_1 and C_1, which relate to cement. When slag is used as a mineral admixture, the chloride diffusion coefficient is dependent on the values of B_1, B_2, C_1, and C_2.

Using the experimental results from chloride diffusion coefficients measured at different ages for various mixing proportions, the values of B_1, B_2, C_1, and C_2 are calibrated as $3.90e-10$, $0.72e-10$, 1.21, and 2.31, respectively. As shown in Figure 5, the analyzed results generally agree with the experimental results. The correlation coefficient between the analyzed results and experimental results is 0.96. The addition of slag can reduce the intrinsic chloride diffusion coefficient A_1 (because $B_1 > B_2$) because the gel produced from the slag reaction has finer gel pores than the gel produced from cement hydration. In addition, the addition of slag can increase the chloride diffusion exponent A_2 (because $C_1 < C_2$). This increase may be due to the pore size refinement effect resulting from the slag reactions. With the reduction of the intrinsic chloride diffusion coefficient A_1 and the increase of the chloride diffusion exponent A_2, the chloride diffusion coefficients decrease correspondingly.

The relationship between capillary porosity in the binder paste and the chloride diffusion coefficients is shown in Figure 6(a). As seen in Figure 6(a), given the same capillary porosity, the chloride diffusion coefficients of slag-blended concrete are much lower than the chloride diffusion coefficients of Portland cement concrete, possibly because the formation of slag reaction products can fill large capillary voids and reduce the average pore size [6]. As shown in Figures 6(b)–6(d), the analyzed results generally agree with the experimental results. With increasing slag replacement levels or decreasing water to binder ratios, the chloride diffusion coefficients decrease. By relating the chloride diffusion coefficients to binder hydration, the proposed model can generally reflect the dependence of chloride diffusion coefficients on the curing ages, water to binder ratios, and slag content. However, because the proposed model does not consider the evolution of the Ca/Si ratio in calcium silicate hydrate (CSH) during the binder hydration process [6], the analyzed results show slight deviations from experimental results (especially for 50% slag concrete).

3.6. Comparison with Life-365 Model. In addition to our analysis results, the analyzed results from the Life-365 program [5] are shown in Figure 7. In the Life-365 program, the time-dependent chloride diffusion coefficient is calculated as follows:

$$D(t) = D_{\text{ref}} \left(\frac{t_{\text{ref}}}{t} \right)^m,$$

$$D_{\text{ref}} = 10^{(-12.06+2.4\,\text{w/cm})}, \tag{13}$$

$$m = 0.2 + 0.4 \left(\frac{\%\ \text{FA}}{50} + \frac{\%\ \text{SG}}{70} \right),$$

where D_{ref} is the chloride diffusion coefficient at time t_{ref} = 28 days, m is the diffusion decay index, w/cm is the water-cementitious material ratio, and % FA and % SG are the levels of fly ash and slag, respectively, in the mixtures. The Life-365 program assumes that fly ash or slag does not affect the early age chloride diffusion coefficient D_{ref} (chloride diffusion coefficient at 28 days). The Life-365 program considers that fly ash and slag impact the rate of reduction in diffusivity only over time. With the increase of the slag or fly ash replacement levels, the value of m increases and more reduction in chloride diffusivity occurs over time. As shown in Figure 7, the trends of the calculation results from the Life-365 program are similar to our proposed model. However, for Portland cement concrete (Figure 7(a)) and 30% slag concrete (Figure 7(b)), the chloride diffusivity calculated from the Life-365 program is lower than the experimental results, possibly because the reactivity of cement and aggregate content in our study are different from those in the Life-365 program.

4. Conclusions

This study presents a numerical procedure to predict the time-dependent chloride diffusion coefficients of slag-blended concrete. This numerical procedure starts with a slag-blended cement hydration model. The reaction degree of the binders is calculated using this hydration model. By using the reaction degree of binders, the combined water

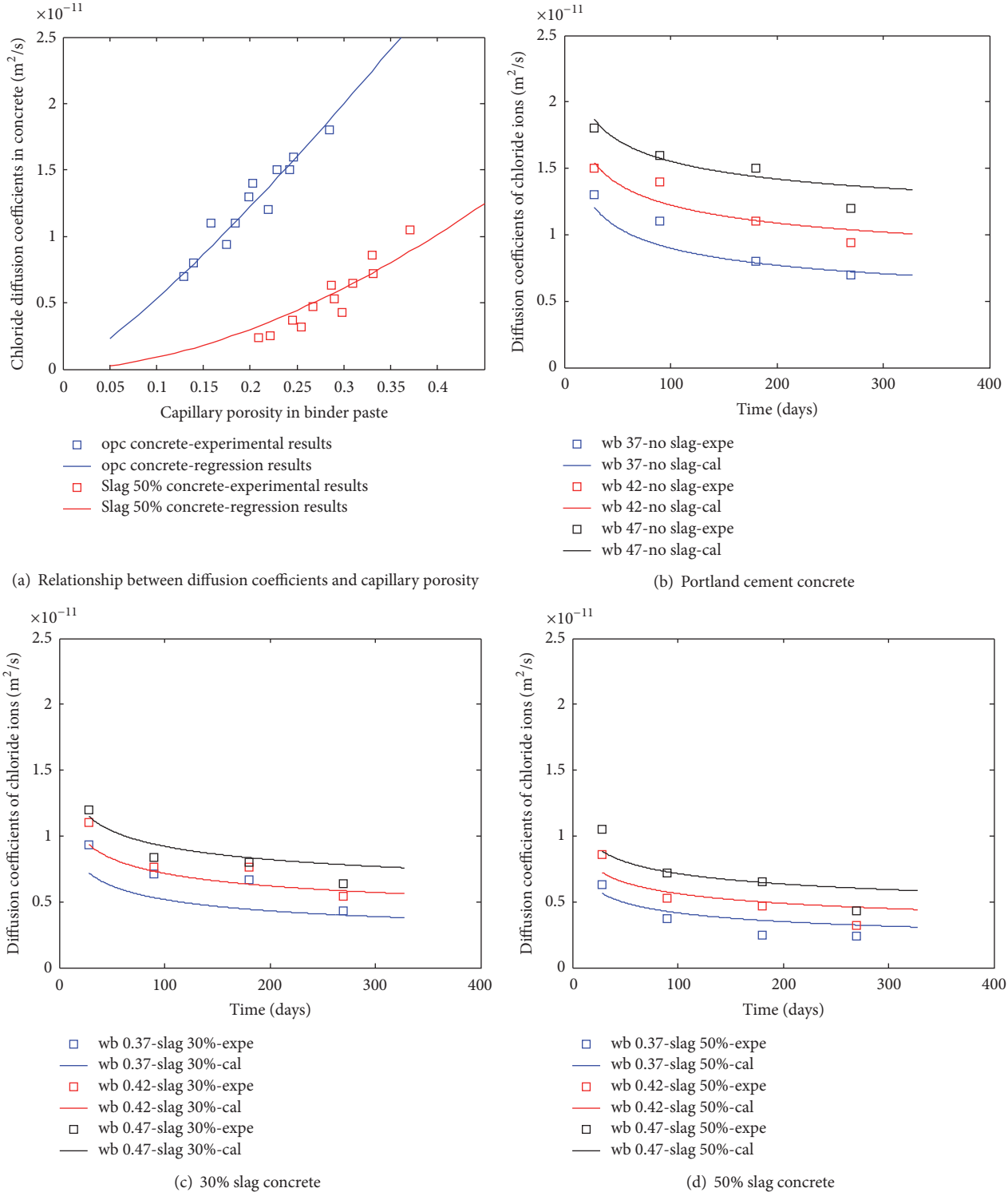

(a) Relationship between diffusion coefficients and capillary porosity

(b) Portland cement concrete

(c) 30% slag concrete

(d) 50% slag concrete

Figure 6: Chloride diffusion coefficients.

and capillary porosity of hardening concrete at different curing ages is determined. Furthermore, by using the capillary porosity and aggregate volume, the chloride diffusion coefficients are calculated. A general equation for the chloride diffusion coefficient for hardening slag-blended concrete is proposed. The increase of total porosity due to slag addition, pore refinement on the macroscale by slag due to the filling effect, and pore refinement on the microscale due to the

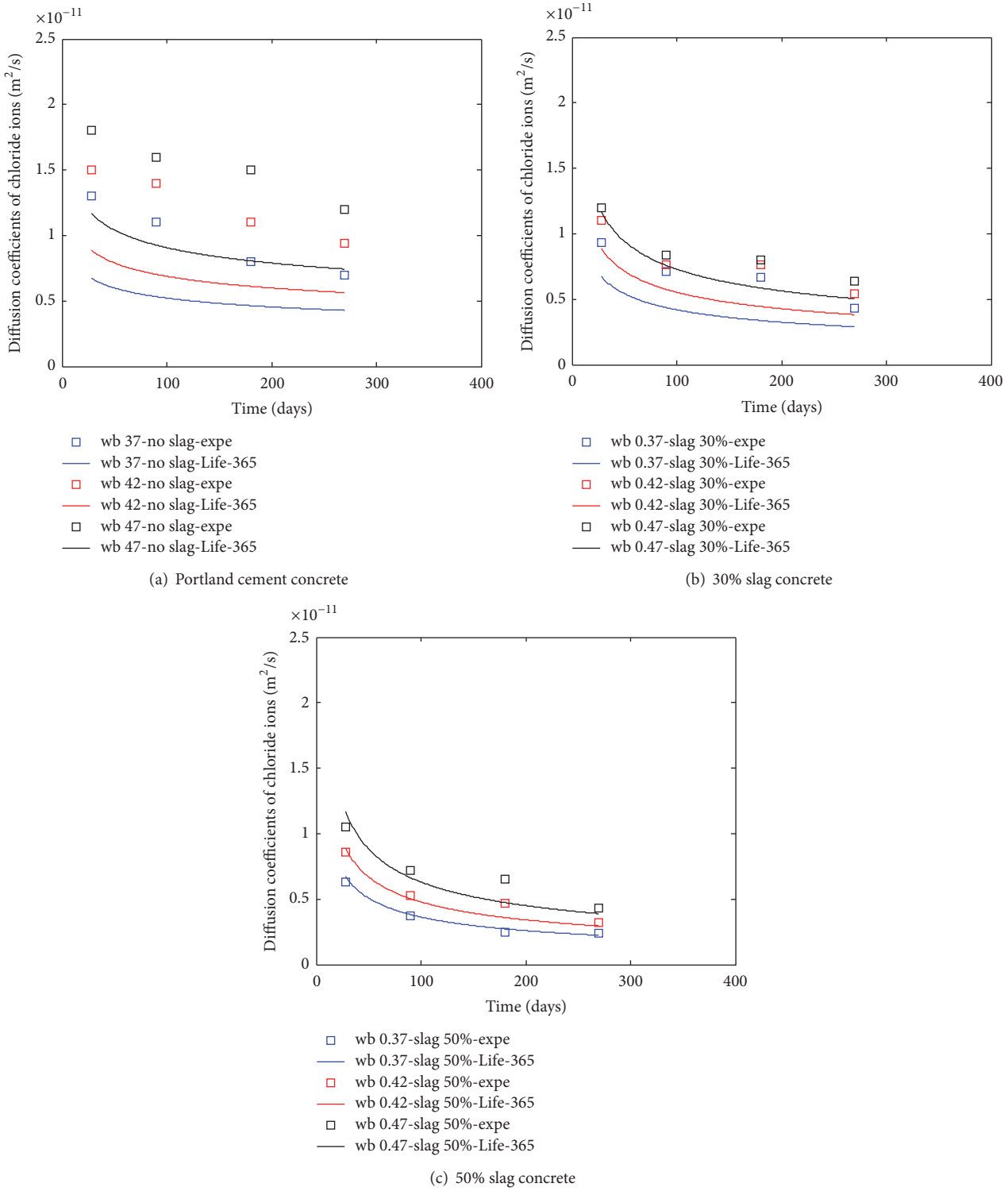

(a) Portland cement concrete

(b) 30% slag concrete

(c) 50% slag concrete

Figure 7: Chloride diffusion coefficients calculated from Life-365 model.

latent-hydraulic properties and pozzolanic reaction of slag are analyzed. The proposed model is valid for concrete with different water to binder ratios, slag replacement ratios, and curing ages.

Competing Interests

The authors declare that there is no conflict of interests regarding the publication of this paper.

Acknowledgments

This research was supported by Basic Science Research Program through the National Research Foundation of Korea (NRF) funded by the Ministry of Science, ICT and Future Planning (no. 2015R1A5A1037548).

References

[1] K. Maekawa, T. Ishida, and T. Kishi, *Multi-Scale Modeling of Structural Concrete*, Taylor & Francis, London, UK, 2009.

[2] V. G. Papadakis, "Effect of supplementary cementing materials on concrete resistance against carbonation and chloride ingress," *Cement and Concrete Research*, vol. 30, no. 2, pp. 291–299, 2000.

[3] S. Demis, M. P. Efstathiou, and V. G. Papadakis, "Computer-aided modeling of concrete service life," *Cement and Concrete Composites*, vol. 47, pp. 9–18, 2014.

[4] M. Alexander and M. Thomas, "Service life prediction and performance testing—current developments and practical applications," *Cement and Concrete Research*, vol. 78, pp. 155–164, 2015.

[5] http://www.life-365.org/.

[6] X.-Y. Wang and H.-S. Lee, "Modeling the hydration of concrete incorporating fly ash or slag," *Cement and Concrete Research*, vol. 40, no. 7, pp. 984–996, 2010.

[7] S.-H. Han, "Influence of diffusion coefficient on chloride ion penetration of concrete structure," *Construction and Building Materials*, vol. 21, no. 2, pp. 370–378, 2007.

[8] W.-J. Fan and X.-Y. Wang, "Prediction of chloride penetration into hardening concrete," *Advances in Materials Science and Engineering*, vol. 2015, Article ID 616980, 8 pages, 2015.

[9] H.-W. Song, J.-C. Jang, V. Saraswathy, and K.-J. Byun, "An estimation of the diffusivity of silica fume concrete," *Building and Environment*, vol. 42, no. 3, pp. 1358–1367, 2007.

[10] H.-W. Song, S.-W. Pack, S.-H. Nam, J.-C. Jang, and V. Saraswathy, "Estimation of the permeability of silica fume cement concrete," *Construction and Building Materials*, vol. 24, no. 3, pp. 315–321, 2010.

[11] B. H. Oh and S. Y. Jang, "Prediction of diffusivity of concrete based on simple analytic equations," *Cement and Concrete Research*, vol. 34, no. 3, pp. 463–480, 2004.

[12] M. Nokken, A. Boddy, R. D. Hooton, and M. D. A. Thomas, "Time dependent diffusion in concrete-three laboratory studies," *Cement and Concrete Research*, vol. 36, no. 1, pp. 200–207, 2006.

[13] Z. Yu and G. Ye, "New perspective of service life prediction of fly ash concrete," *Construction and Building Materials*, vol. 48, pp. 764–771, 2013.

[14] T. Luping and J. Gulikers, "On the mathematics of time-dependent apparent chloride diffusion coefficient in concrete," *Cement and Concrete Research*, vol. 37, no. 4, pp. 589–595, 2007.

[15] H.-W. Song and S.-J. Kwon, "Evaluation of chloride penetration in high performance concrete using neural network algorithm and micro pore structure," *Cement and Concrete Research*, vol. 39, no. 9, pp. 814–824, 2009.

[16] B. H. Oh and S. Y. Jang, "Effects of material and environmental parameters on chloride penetration profiles in concrete structures," *Cement and Concrete Research*, vol. 37, no. 1, pp. 47–53, 2007.

[17] W. Chalee and C. Jaturapitakkul, "Effects of W/B ratios and fly ash finenesses on chloride diffusion coefficient of concrete in marine environment," *Materials and Structures*, vol. 42, no. 4, pp. 505–514, 2009.

[18] X.-Y. Wang, "Properties prediction of ultra high performance concrete using blended cement hydration model," *Construction and Building Materials*, vol. 64, pp. 1–10, 2014.

[19] E. J. Garboczi, "Microstructure and transport properties of concrete," in *RILEM Report 12 Performance Criteria of Concrete Durability*, J. Kropp and H. K. Hilsdorf, Eds., pp. 198–212, E&FN Spon, London, UK, 1995.

[20] A. Principigallo, K. Van Breugel, and G. Levita, "Influence of the aggregate on the electrical conductivity of Portland cement concretes," *Cement and Concrete Research*, vol. 33, no. 11, pp. 1755–1763, 2003.

[21] J. C. Nadeau, "Water-cement ratio gradients in mortars and corresponding effective elastic properties," *Cement and Concrete Research*, vol. 32, no. 3, pp. 481–490, 2002.

[22] J. C. Nadeau, "A multiscale model for effective moduli of concrete incorporating ITZ water-cement ratio gradients, aggregate size distributions, and entrapped voids," *Cement and Concrete Research*, vol. 33, no. 1, pp. 103–113, 2003.

[23] D. N. Winslow, M. D. Cohen, D. P. Bentz, K. A. Snyder, and E. J. Garboczi, "Percolation and pore structure in mortars and concrete," *Cement and Concrete Research*, vol. 24, no. 1, pp. 25–37, 1994.

[24] D. P. Bentz and E. J. Garboczi, "Simulation studies of the effects of mineral admixtures on the cement paste-aggregate interfacial zone," *ACI Materials Journal*, vol. 88, no. 5, pp. 518–529, 1991.

[25] Y. Gao, G. De Schutter, G. Ye, Z. Tan, and K. Wu, "The ITZ microstructure, thickness and porosity in blended cementitious composite: effects of curing age, water to binder ratio and aggregate content," *Composites Part B: Engineering*, vol. 60, pp. 1–13, 2014.

[26] Y. Gao, G. De Schutter, G. Ye, H. L. Huang, Z. J. Tan, and K. Wu, "Characterization of ITZ in ternary blended cementitious composites: experiment and simulation," *Construction and Building Materials*, vol. 41, pp. 742–750, 2013.

[27] K. van Breugel, E. Koenders, Y. Guang, and P. Lura, "Modelling of transport phenomena at cement matrix—aggregate interfaces," *Interface Science*, vol. 12, no. 4, pp. 423–431, 2004.

Hindawi Publishing Corporation
Advances in Materials Science and Engineering
Volume 2016, Article ID 4730616, 8 pages
http://dx.doi.org/10.1155/2016/4730616

Research Article

Chloride Transport of High Alumina Cement Mortar Exposed to a Saline Solution

Hee Jun Yang, Sung Ho Jin, and Ki Yong Ann

Department of Civil and Environmental Engineering, Hanyang University, Ansan 15588, Republic of Korea

Correspondence should be addressed to Ki Yong Ann; kann@hanyang.ac.kr

Received 7 October 2016; Accepted 6 December 2016

Academic Editor: Paulo H. R. Borges

Chloride transport in different types of high alumina cement (HAC) mortar was investigated in this study. Three HAC cement types were used, ranging from 52.0 to 81.1% of aluminum oxides in clinker. For the development of the strength, the setting time of fresh mortar was measured immediately after mixing and the mortar compressive strength was cured in a wet chamber at 25 ± 2°C and then measured at 1–91 days. Simultaneously, to assess the rate of chloride transport in terms of diffusivity, the chloride profile was performed by an exposure test in this study, which was supported by further experimentation including an examination of the pore structure, chloride binding, and chemical composition (X-ray diffraction) analysis. As a result, it was found that an increase in the Al_2O_3 content in the HAC clinker resulted in an increase in the diffusion coefficient and concentration of surface chloride due to increased binding of chloride. However, types of HAC did not affect the pore distribution in the cement matrix, except for macro pores.

1. Introduction

High alumina cement (HAC), mainly consisting of aluminum oxide (Al_2O_3) from about 50 to 85% in cement clinker, could be often used for a special application, due to both high resistance to aggressive chemical ions (i.e., sewer concrete) and rapid development of strength within 24 hours [1–4]. However, its use in concrete structures has been severely restricted by the loss of strength in the process of conversion; metastable hydrates ($CaO{\cdot}Al_2O_3{\cdot}10H_2O$, CAH_{10}; $2CaO{\cdot}Al_2O_3{\cdot}8H_2O$, C_2AH_8) are transformed to stable ones ($3CaO{\cdot}Al_2O_3{\cdot}6H_2O$, C_3AH_6) as follows [5–8]:

$$3CAH_{10} \longrightarrow C_3AH_6 + 2AH_3 + 18H \quad (1)$$

$$3C_2AH_8 \longrightarrow 2C_3AH_6 + 2AH_3 + 9H \quad (2)$$

Due to the release of water molecules in the conversion, however, further hydration of anhydrous phases in cement matrix progresses steadily [1, 2, 9], thereby compensating for the reduced strength and thus the required performance in structural members. Thus, HAC may be used for structural concrete structures, under the condition that rapid hydration is arrested in situ by any means, together with reduced economic price.

It is also intuitively supported that the high portion of aluminum oxide in HAC, which is in fact related to formation of CA-type hydration, for example, C_3A, to remove free chlorides from the concrete pore solution, might be preferred to enhance resistance to chloride-induced corrosion of steel in concrete [10]. Steel embedment in concrete is usually protected by the passive layer (i.e., γ-Fe_2O_3), formed in a high alkaline environment, in which the value of pH accounts for about 12.0 up to 13.5 [11], although chloride ions at the depth of the steel in concrete would subsequently depassivate the steel surface, followed by corrosion propagation to the entire surface of steel [12, 13]. Simultaneously, corrosion of steel could be more or less mitigated by the removal of free chloride ions in the pore solution. In the majority of previous studies [14, 15], the increased binding capacity of HAC paste enabled more adsorption and binding of chloride ions in the pore solution to mitigate the risk of chloride-induced corrosion. In fact, the corrosion resistance of HAC in terms of critical chloride concentration for the onset of corrosion was increased up to 2.4%, whilst OPC concrete ranged from 0.2% to 1.0% for the chloride threshold [10].

Table 1: Oxide composition and chemical properties of different HAC types.

	Oxide composition (%)									Ignition loss (%)	Fineness (cm^2/g)	Density
	CaO	Al_2O_3	SiO_2	Fe_2O_3	SO_3	MgO	K_2O	Na_2O	MnO			
HAC I	38.83	52.03	5.02	0.86	0.09	0.42	0.68	0.17	0.03	0.50	5,150	3.03
HAC II	32.01	67.25	0.11	0.08	0.01	0.21	0.01	0.28	0.02	0.61	4,800	2.92
HAC III	18.35	81.09	0.06	0.06	0.01	0.08	0.01	0.32	0.01	1.21	8,540	3.19

When it comes to the corrosion-free service life of structures, the rate of chloride transport in HAC concrete, however, is of no concern to date. As chloride transport is affected by the distribution of pores and simultaneously the reactivity of the cement matrix with chloride ions, predicting the corrosion-free life must be accompanied by the rate of chloride transport. In particular, HAC concrete imposes the increased pores in the process of conversion from the hexagonal to cubic phases, which may accelerate the chloride permeation and offset the benefit in increasing the resistance to chloride-induced corrosion. Moreover, the binding capacity of HAC concrete may affect the buildup of chloride ions on the surface of concrete, when immersed in a salt solution, which subsequently would increase the diffusivity of chloride ions.

To ensure the characteristics of chloride transport in HAC concrete, the rate of chloride transport in terms of diffusivity was investigated by an exposure test in this study. Refinement of the pore structure was examined by the intrusion of mercury into a specimen to quantify the influence of conversion on the pore distribution. Simultaneously, the chloride binding capacity of HAC paste was determined to assess its effect on both corrosion resistance and chloride transport. Three different HAC types were used containing 52.0, 67.3, and 81.1% of aluminum oxides in HAC clinker.

2. Experimental Works

2.1. Compressive Strength and Penetration Resistance. The oxide composition of HAC used in the present study was determined by X-ray fluorescence (XRF) and physical properties of HAC are given in Table 1. For the development of the compressive strength, mortar specimens were fabricated in a cylindrical mould (Ø 100 × 200 mm). Mix proportion for the cement : water : sand (Grade M) was 1.00 : 0.40 : 2.45. The specific gravity of sand was 2.65. This mix proportion for mortar was subsequently used for the chloride profile and mercury intrusion porosimetry. The mortar specimens were demoulded in 12 hours after casting and then cured in a wet chamber at 25 ± 2°C to reduce the influence on the transformation of hexagonal to cubic phases in hydration products. The compressive strength for mortar specimens was measured at various ages to monitor the influence of the conversion process in the HAC mortar on the strength development.

A fresh mortar was poured in a cubic mould (100 × 100 × 400 mm) to determine the penetration resistance with time and was subsequently measured by a set of standard needles (16, 32, 65, 161, 312, and 645 mm^2 in diameter) at a given time interval. After interpolating the curve for the penetration resistance with time, the setting time was determined, assuming that the initial and final sets are defined as time for the penetration resistance to reach 3.43 and 27.46 MPa, respectively.

2.2. Chloride Profile. The mortar specimens fabricated in the cylindrical mould (Ø 100 × 200 mm) were cured in an identical wet chamber for 91 days to maximise the hydration degree, and then the specimens were cut into 50 mm thickness, in which all the surfaces were coated by epoxy resin except for one surface to induce one-way chloride penetration. Then, the mortar disks (Ø 100 × 50 mm) were immersed in a 1.0 M NaCl solution for 100 days, followed by grinding the specimens every 5 mm depth increments up to 20 mm from the specimen surface to measure chloride concentration in each sample. The obtained sample was stirred for 5 min in 50 mL distilled water at 50°C to extract the water-soluble chloride, and then, for reaching a chemical equivalent in solution, a further 30 min of standing was carried out. After filtering the sample, the concentration of chloride ion in sample was measured by the titration method using ion selective electrode (ISE) for chloride. An identical procedure was adopted to determine the acid soluble chloride concentration using 2.0 nitric acid (HNO_3) for solvent instead of distilled water.

Once the total and free chloride concentrations were obtained at all depths, the surface chloride (C_S) and an apparent diffusion coefficient (D_{app}) were determined by fitting to the error function solution to Fick's second law for nonsteady state, given by

$$C(x,t) = C_S\left(1 - \operatorname{erf}\frac{x}{2\sqrt{Dt}}\right), \tag{3}$$

where $C(x,t)$ is chloride concentration at depth x after time t (%/m^3), C_S is surface chloride concentration (%/m^3), x is depth (mm), D is apparent diffusion coefficient (m^2/s), and t is time of exposure (s).

When free chloride concentration was determined at a given total, the chloride binding capacity was represented by the Langmuir isotherm. In this study, water-soluble chlorides were taken as free, while acid soluble ones were taken as total chlorides. The concentration of bound chloride ions was determined by subtracting the free chloride concentration from the total.

2.3. Chlorides in the Matrix. The X-ray diffraction method was used to identify the bound chlorides in the HAC paste. To react with chlorides from an external environment, a thin layered HAC paste (Ø 100 × 5 mm) at 0.4 of a free

W/C was immersed in 1.0 M NaCl solution for 100 days. Then, the specimens were immersed in isopropanol for 7 days to prevent further hydration, followed by remaining in a dessicator for 1 day to remove/evaporate the residual water-based solvent. After removing water, the paste specimen was ground and sieved with the 300 μm sieve to obtain the dust sample, which was analysed with D/MAX-2500 model (Rigaku) and Jade 9.5 software. The scan range was from 5 to 45° of 2θ at a scan rate of 4°/min.

2.4. Pore Structure Examination. To examine the pore distribution at a given pore diameter, the HAC mortar specimens were fabricated in a cylindrical mould (Ø 10 × 10 mm) and cured for 91 days in the wet chamber at 25 ± 2°C. Prior to examining the pore structure, the residual water in the specimen was removed by an identical method for the X-ray diffraction test. The porosimeter used in this study was Autopore IV 9500 model (Micromeritics Instrument) to fit the low and high pressure. The first step was applied by low pressure of mercury (Hg) up to 0.51 psia using nitrogen gas to measure macroporosity, and then the maximum pressure was gradually increased to 33,000 psia for microporosity. The pore volume versus pore diameter calculated by the Washburn equation at a given pressure was plotted in the cumulative pore volume and incremental curve. Hence,

$$d = \frac{-4\gamma \cos\theta}{P}, \tag{4}$$

where d is pore diameter (m), γ is surface tension (N), θ is contact angle (°), and P is pressure (MPa).

3. Results and Discussion

3.1. Compressive Strength and Penetration Resistance. The penetration resistance of fresh HAC mortar with time is given in Figure 1. The initial and final sets were determined by the best-fitted curve for the penetration resistance with time ($y = ae^{bx}$). It was seen that the setting time was strongly dependent on the HAC type; an increase in the Al_2O_3 content in clinker resulted in an increase in the time for the initial and final sets. For example, the time for the initial and final sets of HAC I imposed the rapid hardening, accounting for 185 and 230 min for the initial and final sets, respectively, while HAC III indicated 291 min and 409 min, respectively. The HAC is usually divided into three groups: (1) low alumina (50–60% in Al_2O_3), (2) medium alumina (65–75% in Al_2O_3), and (3) high alumina (>80% in Al_2O_3). The anhydrous phases consist of CA, a main hydraulic constituent in HAC, α-Al_2O_3, $C_{12}A_7$, and CA_2, being significant, according to raw materials. Guirado and Galí [16] showed that an increase in ratio of CaO/Al_2O_3 (hereinafter C/A) resulted in both an increase in CA_2 content and a decrease in CA ones, measured by the Rietveld analysis. As the hydration process in HAC is governed by the amount of Ca^{2+} and $Al(OH)_4^-$ ions in solution, the quantities and solubility in each clinker could be influencing the development of the strength. Klaus et al. [17] investigated the hydration of mixture of CA and CA_2 (W/C ratio: 0.45; curing temp.: 23 ± 0.2°C) in terms of their dissolution. They found that the dissolution of CA progressively appeared at the initial stage (up to about 6 hours), followed by that of CA_2. Moreover, the dissolution behaviour of CA was constant in the presence of various CA_2 content. In addition, it was reported that CA in HAC clinker is reactive more than CA_2 at ambient temperature (20–30°C) [18]. Consequently, as CA leads to rapid setting and hardening at the early stage in the process of hydration, it is possible to control the setting behaviour for HAC by modifying the C/A ratio in clinker at the manufacturing step.

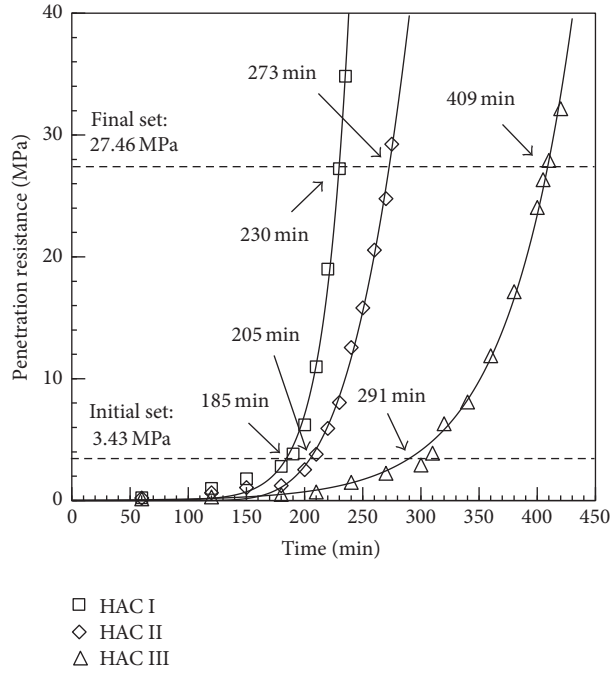

Figure 1: Penetration resistance of fresh concrete with time to determine the setting time for different HAC types.

The compressive strength of mortar with different HAC types was measured at 1–91 days as shown in Figure 2. As expected, the strength for HAC mortar rapidly increased with time at an early age, regardless of types, up to 7 days, and then decreased at 14 days, except for HAC I. In particular, the strength of HAC I mortar showed a considerable high strength at an early age, reaching beyond 66.3 MPa at 7 days, and then gradually decreased to 47.7 MPa at 56 days, while HAC III mortar faced a sudden decease from 65.1 MPa at 7 days to 51.4 MPa at 14 days. The high early compressive strength is attributed to an inherent characteristic of HAC, which may be attributed to rapidly elevated heat (up to about 90°C in adiabatic temperature) during hydration within 10–12 hours [1]. A reduction of the compressive strength may reflect the conversion process from the hexagonal (CAH_{10} and C_2AH_8) to cubic (C_3AH_6) phases during hydration of HAC paste, accompanying the densified matrix, and thus in turn increased porosity in the cement matrix [6, 7]. It is notable that a marginal increase for compressive strength was observed after 14 days of curing in all types. It is evident that further hydration of anhydrous phases, such as CA, CA_2, and $C_{12}A_7$, may maintain a certain strength, despite a risk of the

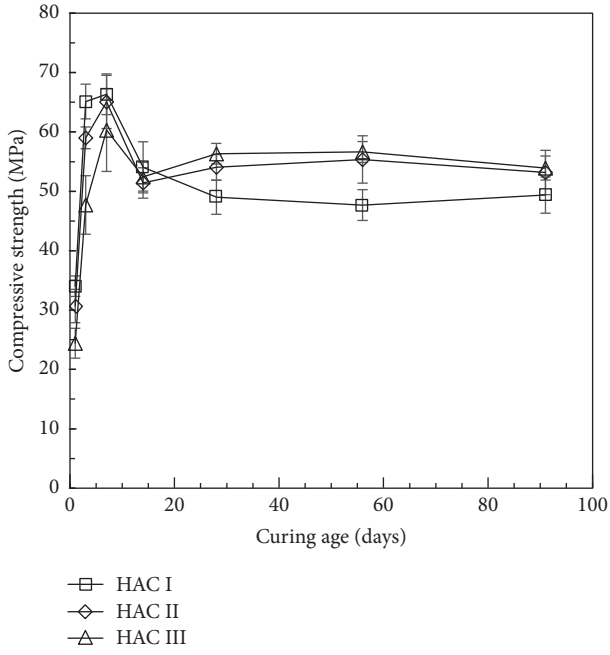

Figure 2: Development of compressive strength of mortar for different HAC types with curing age.

conversion process, which is, in fact, related to generation of porosity and in turn may decrease the concrete strength [6, 7]. Substantially, all the mortar compressive strengths achieved a high level of their ultimate compressive strength, exceeding about 50 MPa at 91 days, which could not seem to further increase or decrease. Thus, it can be said that there would be no adverse effect in using the HAC for structural concrete, presumably due to the unstable development of the compressive strength.

3.2. Chloride Transport. After exposure of mortar specimens to the 1.0 NaCl solution for 100 days, the chloride concentration was measured at each depth with increments of 5.0 mm for the acid- and water-soluble chlorides, corresponding to total and free chlorides, respectively. Then, the chloride profile was used to determine the apparent diffusion coefficient of chlorides and the surface chloride content for nonsteady state by fitting to the error function solution to Fick's second law, as shown in Figure 3. It is obvious that an increase in the C/A ratio (i.e., lower content of Al_2O_3 in oxides in HAC clinker) resulted in a decrease in the chloride ingress at every depth. In particular, the concentration of total surface chloride was strongly dependent on the C/A ratio in cement. For example, HAC I at the higher C/A ratio produced 0.84% of the surface chloride by weight of cement, while HAC III increased up to 2.08%. This may be ascribed to the chemical equilibrium for chloride ions at the interface between specimen surface and solution. The higher Al_2O_3 content in cement clinker would enhance the formation of chloroaluminate hydrates, which often would result from a reaction between cement paste and free chlorides to remove/immobilise them from the pore solution [10, 19]. The higher chloride binding capacity, resulting from increased C_3A content, may impose increased concentration of bound chloride on the surface of concrete at a given free chloride concentration due to the chemical balance between concrete surface and saline media [20]. Thus, the lower C/A ratio in HAC may enhance the buildup of chlorides on the concrete surface, leading to an increase in the concentration gradient to accelerate the rate of chloride transport.

It is evident that the diffusion coefficient of chlorides was much affected by the C/A ratio in HAC. In fact, an increase in the C/A resulted in a decrease in the diffusion coefficient. For example, the HAC I produced the lowest diffusivity of 1.61×10^{-11} m^2/s, while HAC II and HAC III indicated 1.85×10^{-11} m^2/s and 2.17×10^{-11} m^2/s, respectively. However, the diffusion coefficient calculated for free chloride transport had no significant effect arising from different C/A ratios; the diffusion coefficient for free chlorides in HAC was in a small range from 1.31×10^{-11} to 1.43×10^{-11} m^2/s, irrespective of types of HAC. The rate of chloride transport is affected by the pore structure (i.e., distribution of capillary pores in the cement matrix) and chemical reactivity between cement paste and chloride ions, such as chloride binding. The HAC paste is always subjected to the conversion process from the hexagonal phases (CAH_{10} and C_2AH_8) to cubic phases (C_3AH_6), depending on the curing regime, temperature, and C/A ratio, which subsequently may govern the pore structure. Simultaneously, the reactivity between cement paste and chloride ions in HAC would be very accelerated rather than in OPC, due to increased formation of reactive hydration products such as CA, CA_2, and $C_{12}A_7$. Thus, these influencing factors must be quantified to determine the chloride transport in HAC concrete. For example, examination of the chloride binding capacity and the pore structure must be accompanied.

3.3. Chloride Binding. To render the binding isotherm, the relation between free and bound chlorides for different HAC types was depicted in Figure 4, using the Langmuir isotherm. The concentration of free and bound chloride was determined in the process of chloride profiling at different depths and at different total chloride concentrations. As expected, an increase in the free chloride concentration resulted in an increase in the bound chlorides, regardless of the HAC types. It is evident that the C/A ratio was significantly influencing the chloride binding capacity at a given total chloride concentration. In fact, HAC III was ranked the highest chloride binding capacity, presumably arising from increased Al-based clinkers, which subsequently would form the CA-type hydrates to arrest chlorides into Friedel's salt. Due to a marginal difference in the pH of the pore solution, the pH seems to be less influencing on the chloride binding capacity [15], and the conversion process in the HAC matrix is, moreover, less affected. Substantially, the binding of chlorides into a crystallised form may solely be affected by the concentration of Al_2O_3 in clinker, although other hydration products may contribute to the reaction with chlorides in a limited margin.

The HAC paste immersed in the NaCl solution was analysed by X-ray diffraction as seen in Figure 5. It is seen that the peaks for hydration products were mostly

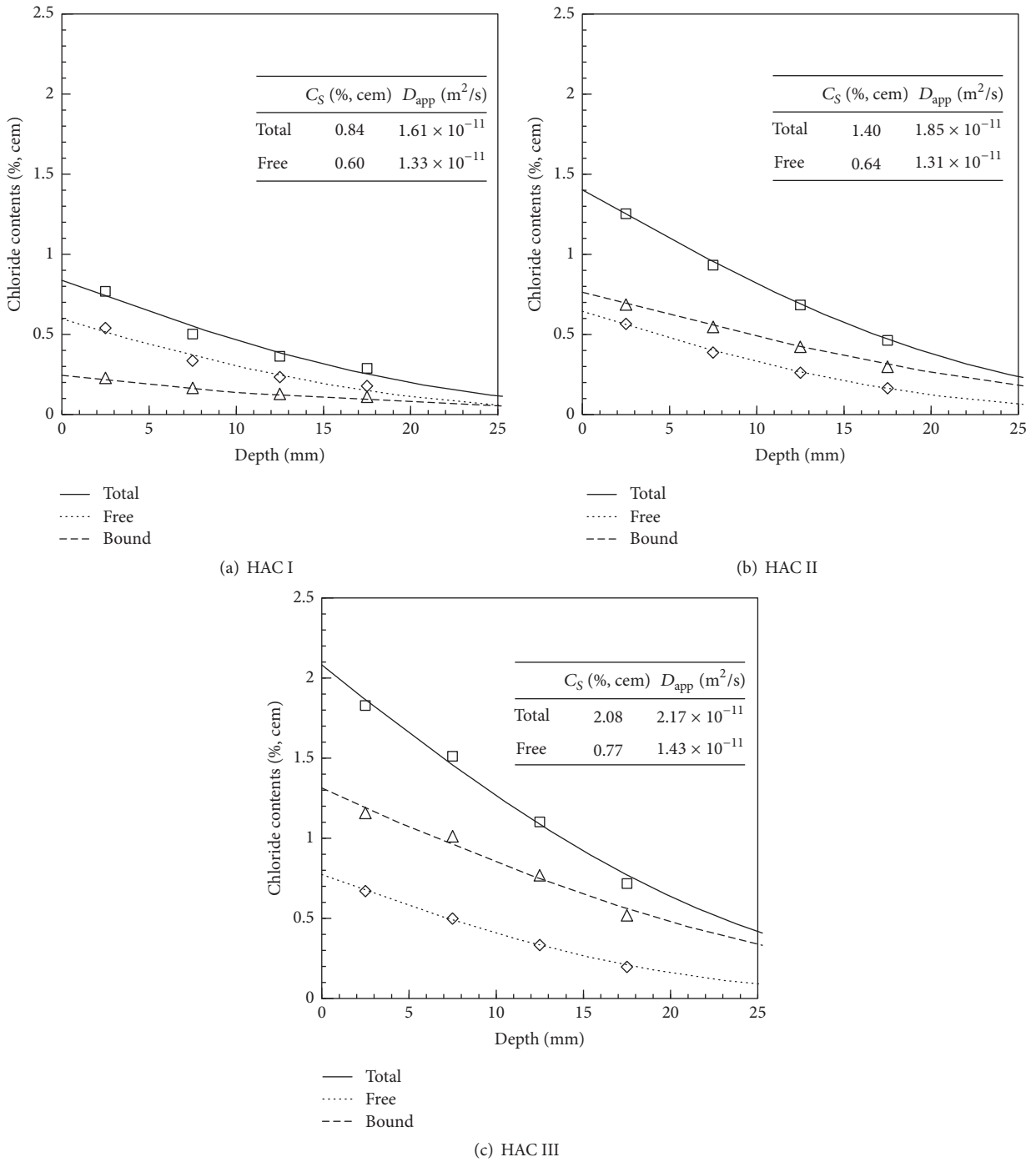

Figure 3: Chloride profiles of mortar for different HAC types after 100 days of exposure to 1.0 M NaCl solution.

identical between HAC pastes, imposing similar generation of hydration, except for unreactive α-Al_2O_3 in HAC III. It is notable that no metastable crystals (CAH_{10} and C_2AH_8) were identified for all the HAC types in the X-ray diffraction curves, implying that the hexagonal phases formed in the cement matrix were completely converted to cubic phases during curing consisting of 91 days of wet curing and 100 days of exposure to a salt solution at 25 ± 2°C. The high intensity was commonly observed at 11.0–11.2° of 2θ in HAC pastes, indicating that Friedel's salt was quite formed, depending on the C/A ratio. In fact, an increase in the C/A resulted in a decrease in Friedel's salt. This may confirm that the high content of Al_2O_3 may be of benefit in forming Friedel's salt, due to increased possibilities of the formation of chloride-reactive CA hydration products.

3.4. Pore Structure. The pore distribution in the HAC mortar was determined by mercury intrusion porosimetry, as given

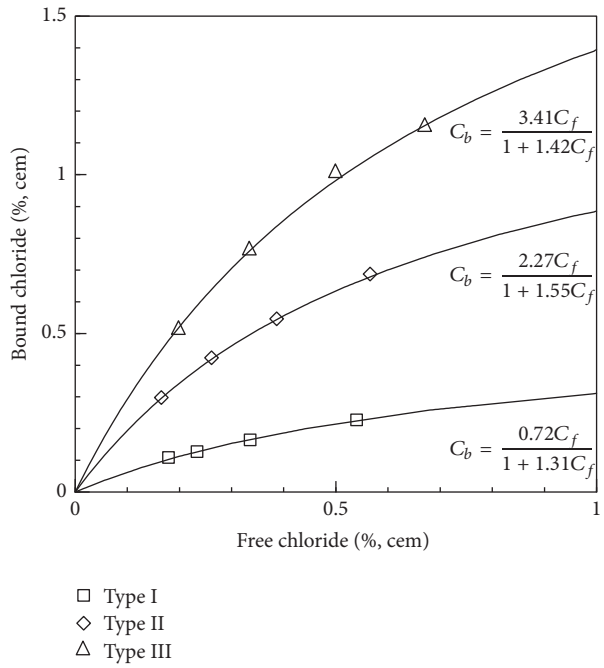

Figure 4: Relation between free and bound chlorides at a given total chloride concentration in cement mortar with different HAC types after 100 days of exposure to 1.0 M NaCl solution (expressed by the Langmuir isotherm).

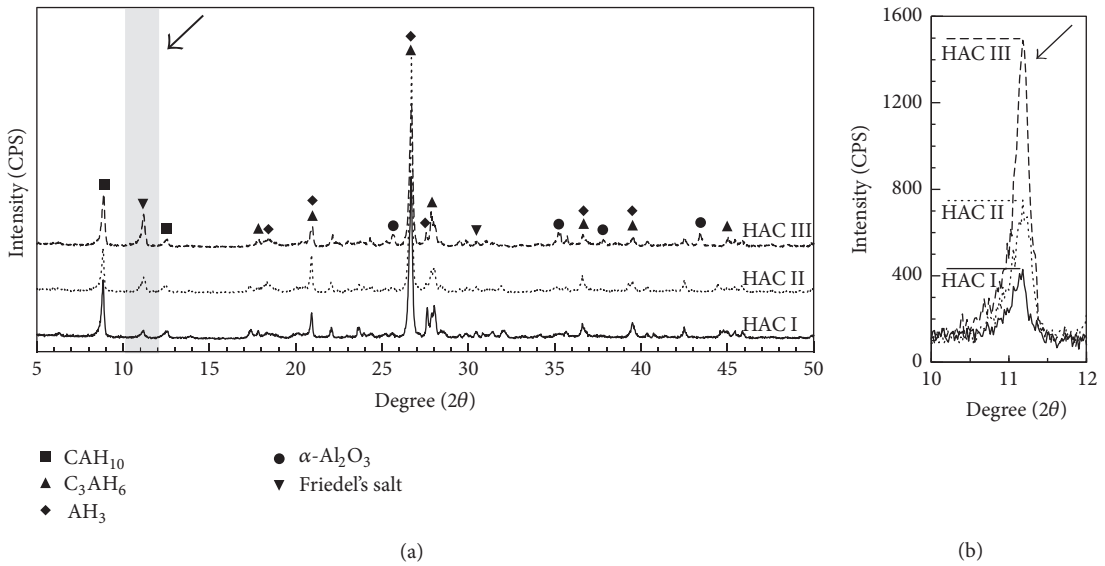

Figure 5: X-ray diffraction pattern of cement paste with different HAC types after 100 days of exposure to 1.0 M NaCl solution. (a) Hydration products and (b) Friedel's salt.

in Figure 6, together with incremental pores at different sizes. Irrespective of types of HAC, the total pore volume was in the range of 0.076–0.088 mL/g. The distribution of capillary pore was not much affected by the types of HAC, which would provide paths for ions to transport in the form of interrelated network. However, macro pore distribution was dependent on the HAC types; an increase in the C/A resulted in an increase in the volume of macro pores, which are not interconnected with the capillary pore and thus may block the ionic transport [21]. As seen in Figure 3, the HAC III produced the highest rate of chloride transport in terms of apparent chloride diffusion coefficient. This may be attributed to a lower volume of the macro pores, enhancing the connectivity between pores and thus chloride transport. Moreover, a reduction of the macro pore volume may increase the development of the concrete strength at a given hydration degree; in fact, HAC III was ranked the highest strength as seen in Figure 2 after 14–28 days of curing. Despite further generation of the pores in the conversion process from the hexagonal to cubic phases, a modified pore structure after the

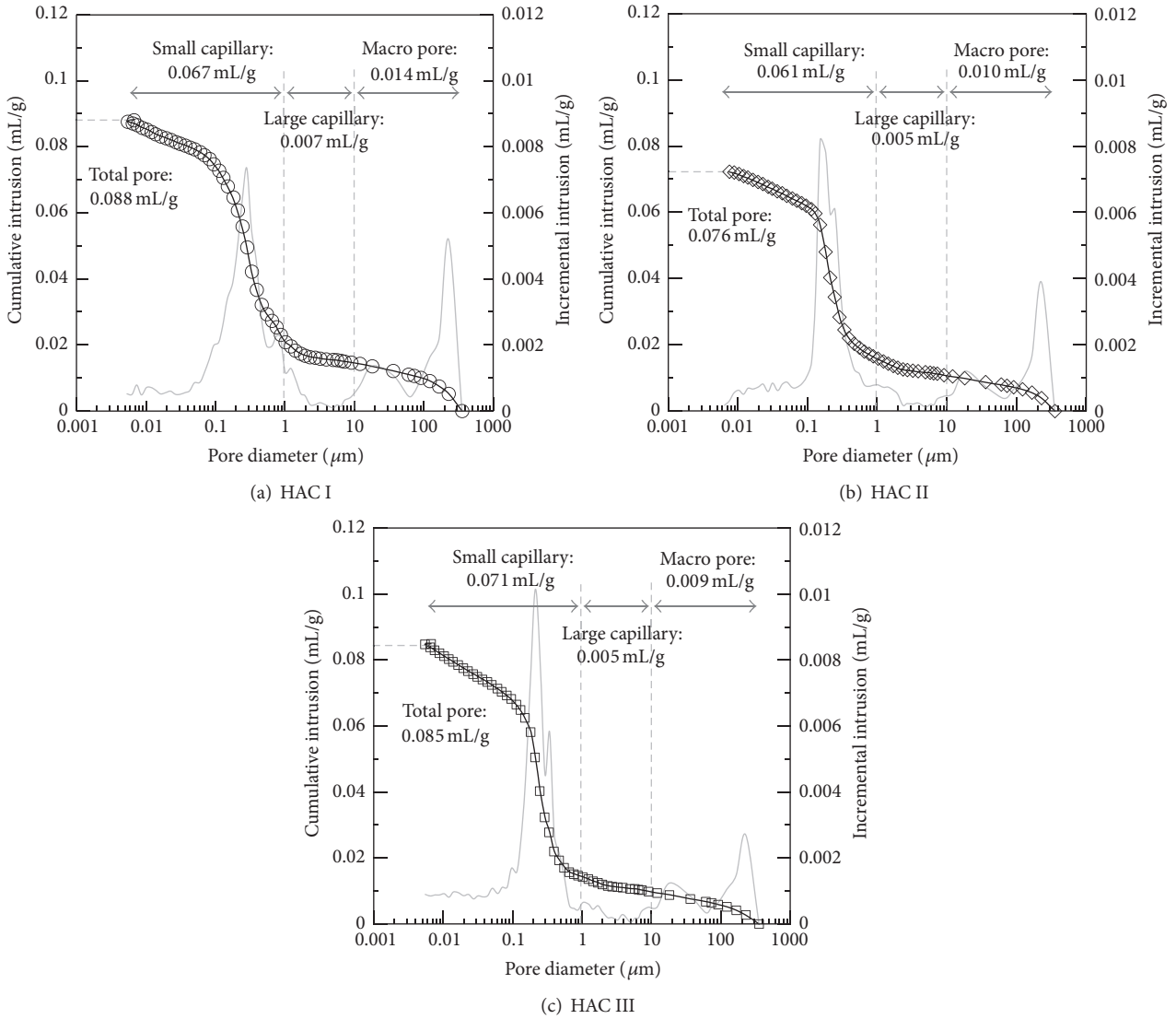

Figure 6: Pore size distribution of mortar to a given pore diameter with different HAC types.

conversion was not identified in this study, because the pore distribution before the conversion process, presumably at a very early age, was not obtained.

4. Conclusion

In this study, the ionic transport in different types of HAC mortar was investigated by the chloride profile, which was supported by further experimentation including an examination of the pores structure, chloride binding capacity, and chemical microscopic analysis (X-ray diffraction analysis). The HAC was classified by the content of Al_2O_3 in cement clinker ranging from 52.0 to 81.1%. Simultaneously, development of the compressive strength and setting time were measured to secure their applicability in situ. Detailed experimental results and conclusion derived from the study are given as follows:

(1) An increase in the Al_2O_3 in the HAC clinker resulted in an increase in the setting time, and, moreover, the gap between initial and final sets was also increased, due to increased CA_2 formation. HAC mortars gained rapidly the compressive strength at an early age, accounting for 66.3 MPa at 7 days, which was reduced at 14 days of curing presumably due to the conversion process from the hexagonal to cubic phases and then again marginally increased or/and converged to a certain level up to 91 days, ranging from 49.36 to 53.92 MPa.

(2) The apparent diffusion coefficient and surface chloride concentration of HAC mortars immersed in a salt solution were obtained by profiling of chloride concentration at each depth. An increase in the Al_2O_3 in HAC clinker resulted in an increase in the surface chloride and diffusion coefficient, due to increased chloride binding capacity and modified pore structure. The surface chloride ranged from 0.84 to 2.08%, while the diffusion coefficient of chlorides in HAC mortar was in the range of 1.61–2.17 m^2/s.

(3) The chloride binding capacity, rendered by the Langmuir isotherm, was increased by Al_2O_3 in HAC clinker, which would form CA-type hydration products to react with chloride ions into Friedel's salt. However, types of HAC did not have an influence on the pore distribution in the cement matrix, except for macro pores.

Competing Interests

The authors declare that they have no competing interests.

Acknowledgments

This research was supported by the research fund of Hanyang University (HY-2012-N).

References

[1] P. C. Hewlett, *Lea's Chemistry of Cement and Concrete*, Elsevier, 4th edition, 2013.

[2] J. Newman and B. S. Choo, *Advanced Concrete Technology—Constituent Materials*, Elsevier, 2003.

[3] H. Pöllmann, "Calcium aluminate cements—raw materials, differences, hydration and properties," *Reviews in Mineralogy & Geochemistry*, vol. 74, no. 1, pp. 1–82, 2012.

[4] S. M. Bushnell-Watson and J. H. Sharp, "The effect of temperature upon the setting behaviour of refractory calcium aluminate cements," *Cement and Concrete Research*, vol. 16, no. 6, pp. 875–884, 1986.

[5] A. M. Neville, *Properties of Concrete*, Longman Group, 4th edition, 1995.

[6] H. G. Midgley and A. Midgley, "The conversion of high alumina cement," *Magazine of Concrete Research*, vol. 27, no. 91, pp. 59–77, 1975.

[7] C. Bradbury, P. M. Callaway, and D. D. Double, "The conversion of high alumina cement/concrete," *Materials Science and Engineering*, vol. 23, no. 1, pp. 43–53, 1976.

[8] R. J. Collins and W. Gutt, "Research on long-term properties of high alumina cement concrete," *Magazine of Concrete Research*, vol. 40, no. 145, pp. 195–208, 1988.

[9] J. Bensted and P. Barnes, *Structure and Performance of Cements*, Taylor & Francis Group, 2nd edition, 2002.

[10] K. Y. Ann, T.-S. Kim, J. H. Kim, and S.-H. Kim, "The resistance of high alumina cement against corrosion of steel in concrete," *Construction and Building Materials*, vol. 24, no. 8, pp. 1502–1510, 2010.

[11] C. L. Page, "Mechanism of corrosion protection in reinforced concrete marine structures," *Nature*, vol. 258, no. 5535, pp. 514–515, 1975.

[12] M. Saremi and E. Mahallati, "A study on chloride-induced depassivation of mild steel in simulated concrete pore solution," *Cement and Concrete Research*, vol. 32, no. 12, pp. 1915–1921, 2002.

[13] K. Y. Ann and H.-W. Song, "Chloride threshold level for corrosion of steel in concrete," *Corrosion Science*, vol. 49, no. 11, pp. 4113–4133, 2007.

[14] A. Macias, A. Kindness, and F. P. Glasser, "Corrosion behaviour of steel in high alumina cement mortar cured at 5, 25 and 55°C: chemical and physical factors," *Journal of Materials Science*, vol. 31, no. 9, pp. 2279–2289, 1996.

[15] M. A. Sanjuán, "Formation of chloroaluminates in calcium aluminate cements cured at high temperatures and exposed to chloride solutions," *Journal of Materials Science*, vol. 32, no. 23, pp. 6207–6213, 1997.

[16] F. Guirado and S. Galí, "Quantitative Rietveld analysis of CAC clinker phases using synchrotron radiation," *Cement and Concrete Research*, vol. 36, no. 11, pp. 2021–2032, 2006.

[17] S. R. Klaus, J. Neubauer, and F. Goetz-Neunhoeffer, "Hydration kinetics of CA_2 and CA-investigations performed on a synthetic calcium aluminate cement," *Cement and Concrete Research*, vol. 43, no. 1, pp. 62–69, 2013.

[18] A. Rettel, R. Seydel, W. Gessner, J. P. Bayoux, and A. Capmas, "Investigations on the influence of alumina on the hydration of monocalcium aluminate at different temperatures," *Cement and Concrete Research*, vol. 23, no. 5, pp. 1056–1064, 1993.

[19] K. Y. Ann and C.-G. Cho, "Corrosion resistance of calcium aluminate cement concrete exposed to a chloride environment," *Materials*, vol. 7, no. 2, pp. 887–898, 2014.

[20] G. K. Glass and N. R. Buenfeld, "The influence of chloride binding on the chloride induced corrosion risk in reinforced concrete," *Corrosion Science*, vol. 42, no. 2, pp. 329–344, 2000.

[21] G. K. Glass and N. R. Buenfeld, "Chloride-induced corrosion of steel in concrete," *Progress in Structural Engineering and Materials*, vol. 2, no. 4, pp. 448–458, 2000.

Hindawi Publishing Corporation
Advances in Materials Science and Engineering
Volume 2016, Article ID 7529382, 15 pages
http://dx.doi.org/10.1155/2016/7529382

Research Article

Simulated Experiment Study of Factors Influencing the Hydration Activity of f-CaO in Basic Oxygen Furnace Slag

Ruiquan Jia and Jiaxiang Liu

Beijing Key Laboratory of Electrochemical Process and Technology for Materials, Beijing University of Chemical Technology, Beijing 100029, China

Correspondence should be addressed to Jiaxiang Liu; ljxpost@263.net

Received 26 June 2016; Revised 17 September 2016; Accepted 17 October 2016

Academic Editor: Paulo H. R. Borges

The compositions and formation process of f-CaO in BOF slag were revealed and simulated to understand its expansion rules and why its hydration activity is low. BSE showed the compositions of f-CaO, which included calcium iron phase and calcium iron manganese phase, were diverse. The hydration activity sequence was $Ca_2Fe_2O_5$ and $Ca_3Fe_{1.5}Mn_{1.5}O_8$ in tricomponent f-CaO < CaO in tricomponent f-CaO < monocomponent f-CaO; only $Ca_2Fe_2O_5$ and $Ca_3Fe_{1.5}Mn_{1.5}O_8$ were hard to hydrate, and the volume expansion rates of the tricomponent f-CaO varied with different compositions. Inductively, in BOF slag, the hydration activity sequence was solid solutions CaO-FeO_x and CaO-FeO_x-MnO_y in tricomponent f-CaO < CaO in tricomponent f-CaO < monocomponent f-CaO; the volume expansion rates of tricomponent f-CaO changed with different compositions, and CaO-FeO_x and CaO-FeO_x-MnO_y were difficult to hydrate. The reason why solid solutions CaO-FeO_x and CaO-FeO_x-MnO_y were hard to hydrate was that their hydration reaction driving force, which is the absolute value of standard molar reaction Gibbs functions, decreased.

1. Introduction

Basic Oxygen Furnace (BOF) slag is the industrial by-product from the steel-refining process in a conversion furnace, and its output accounts for 15~20% by mass of the total output of crude steel [1]. In China, 1.5×10^8 tons of BOF slag was produced in 2015 [2]. However, the current utilization rate of BOF slag in China is only 22%. Massive amounts of BOF slag have been dumped as waste, which not only leads to the occupation of farm land and serious pollution to the environment but is also an extreme waste of resources. This situation also has a very negative effect on steel enterprise regarding sustainable development [3]. In China, approximately two billion tons of Ordinary Portland Cement (OPC) is produced every year [4, 5]. BOF slag and OPC possess the same chemical and mineral compositions, and it is possible to use BOF slag in cement and concrete industry as a resource; meanwhile, this use is effective to realize a high added value application and sustainable development. However, its low hydration activity [6, 7] and the volume expansion that occurs after blended OPC binder containing BOF slag (CBS) hardens [8–10] have restricted the application of BOF slag in cement and concrete industry. It is imperative to find ways to stimulate its hydration activity and resolve the volume expansion of BOF slag.

There have been a great number of studies on stimulating the hydration activity of BOF slag, but there have been very limited studies on resolving the volume expansion of BOF slag. Currently, it is universally acknowledged that there is the possibility that f-CaO and f-MgO, which are in a dead-burnt state and whose hydration activity is very low, will continue to slowly hydrate in BOF slag after CBS hardens, causing a volume expansion, which may damage the construction. In this study, f-CaO was considered to be the major factor of the volume expansion of BOF slag. F-CaO, which will cause the volume expansion after CBS hardens, is a mineral phase in BOF slag, and its main composition is CaO [11–13]. To address the volume expansion caused by f-CaO, Wang et al. [8] have found a theoretical equation based on both chemical reaction and physical changes of f-CaO in BOF slag during the hydration process to predict the volume expansion of BOF slag. The calculated volume expansion data can be

used as evaluation criteria for a given slag that is used in an engineering application, which is significant to applying BOF slag in OPC. At the same time, Wang [9] has noted that the volume expansion data of BOF slag tested by the current ASTM (2006) standard test method [10] are not directly related to the expansion behavior of BOF slag under confined conditions. The expansion force is the direct factor, and the allowable stress of a rigid matrix should also be considered when BOF slag is applied in OPC. Kuo et al. [14, 15] have put forward that high temperature rapid catalytic technology can accelerate f-CaO hydration and forecast the volume expansion within a short time. Moreover, it can verify the volumetric stability of a steel material, identify the possible expansion risk before use, and forecast the durability of concrete mixed with different amounts of BOF slag.

So far, the literature has shown that there has been a great amount of attention paid by exploring the relationship between a certain amount of f-CaO and the volume expansion that is caused. However, a limited number of studies have revealed a clear explanation of the causes related to the low hydration activity of f-CaO. Therefore, the current aims to resolve volume expansion and establish evaluation criteria are difficult and, to a certain extent, rely on experience. Therefore, it is theoretically and practically significant to study how the factors that influence the hydration activity of f-CaO lead to a minimal hydration activity of f-CaO.

Through a molten temperature of approximately 1600°C, f-CaO in BOF slag is in a dead-burnt state, and the compositions and the distribution of f-CaO are heterogeneous. It is possible that iron oxide (FeO_x) and manganese oxide (MnO_y) may dissolve in f-CaO during the steelmaking process [11–13]. The steelmaking process occurs at a high temperature (about 1600°C) and oxidation state [16]. Under this condition, transition metals, such as Fe and Mn, often form nonstoichiometric oxides [17, 18]. If f-CaO is transformed into the combination of metal oxides, it will present with the form of $CaO{\cdot}aFeO_x{\cdot}bMnO_y$ [12]. The values of a, b, x, and y of f-CaO in different areas of BOF slag are different and uncertain.

Taking the formation process and the compositions of f-CaO into consideration, the factors that influence the hydration activity of f-CaO are absolutely connected with both the time of high temperature process and dissolved FeO_x and MnO_y. Under the influence of these factors, the hydration activity of f-CaO may become low. Since the system of BOF slag is very complex, the relationship between the hydration activity of f-CaO and the duration of the high temperature process, especially the quantitative relationship between the hydration activity of f-CaO and its compositions, is still not definite.

With the aim of better understanding the compositions of f-CaO in BOF slag, why the hydration activity of f-CaO is low, and its expansion rules, as well as providing theoretical support to address the volume expansion caused by f-CaO, first, the compositions and formation process of f-CaO in different BOF slags were revealed using backscattered electron images (BSE) and energy dispersive analysis (EDS) of scanning electron microscope (SEM) images. Secondly, based on these observations, the formation process and compositions of f-CaO were simply simulated through the calcination experiment. Simulated monocomponent f-CaO is not the same but it is similar to monocomponent f-CaO in BOF slag and tricomponent f-CaO of $CaO{\cdot}aFeO_{1.5}{\cdot}bMnO_2$ system is not the same but it is similar to the tricomponent f-CaO of $CaO{\cdot}aFeO_x{\cdot}bMnO_y$ system in BOF slag. These components were thoroughly studied by scanning electron microscope (SEM), X-ray diffraction (XRD), energy dispersive spectrometer mapping (EDS-mapping), and hydration heat evolution test. The latter was used to explore the influence mechanisms of the calcination time on the hydration activity of monocomponent f-CaO and dissolved Fe_2O_3 and MnO_2 on the hydration activity of tricomponent f-CaO of $CaO{\cdot}aFeO_{1.5}{\cdot}bMnO_2$ system. The aim of this study was to provide useful fundamental knowledge regarding complex systems by studying simplified systems. Then, the influence mechanisms were extended to monocomponent f-CaO and tricomponent f-CaO of $CaO{\cdot}aFeO_x{\cdot}bMnO_y$ system because of their similarity. Finally, the main mechanisms behind tricomponent f-CaO of $CaO{\cdot}aFeO_x{\cdot}bMnO_y$ system were confirmed by thermodynamic theory. Thermodynamic theory was applied to confirm why the hydration activity of solid solutions CaO-FeO_x and CaO-FeO_x-MnO_y in tricomponent f-CaO in BOF slag was low and weaker than that of CaO.

2. Materials and Methods

2.1. Materials. Four types of BOF slags were obtained from Jiangsu Tieben Steel and Iron Co., Ltd.; Ma'anshan Steel and Iron Co., Ltd.; Cangzhou Steel and Iron Co., Ltd.; and Baoshan Steel and Iron Co., Ltd., being denominated as SS, MS, CS, and BS, respectively. They were treated by heat-stewed process and then underwent natural cooling in warehouse. The chemical compositions of the BOF slags were determined by wavelength dispersive X-ray fluorescence (XRF) spectrometry (Thermo Electron ADVANT' XP). The samples were scanned over a range of 5° and 90° 2θ. The scans were measured in step scan mode at 2 s per 0.02° 2θ. Their chemical compositions and the average chemical compositions of BOF slag in China are given in Table 1 [2, 3]. From Table 1, it can be seen that the four types of BOF slags are representative in China.

The commercial materials used in this study included analytical grade CaO (Sinopharm Chemical Reagent Co., Ltd.), Fe_2O_3 (Xilong Chemical Co., Ltd.), MnO_2 (Xilong Chemical Co., Ltd.), and deionized water (self-manufacture).

2.2. Sample Preparation. BOF slag particles were crushed, rubbed, and inserted in a mould to be polished achieving a smoothness ≤ 0.5 um. Subsequently, the samples were washed and coated by carbon film.

Analytical grade CaO was placed in a φ50 mm × 10 mm cylindrical mould under a pressure of 20 MPa for 3 min and then demoulded; calcinated for 1, 3, 5, and 7 h at 1600°C in the electric furnace (Luoyang Shenjia Kiln Co., Ltd., SSJ-17); and cooled in air rapidly to prepare the four monocomponent f-CaO samples. After the calcinations, the samples were fractured, milled, and sieved below 180 um. Finally, the samples were stored in a dryer for the tests.

Table 1: Chemical composition of BOF slag from different steel plants and the average composition in China.

Source	Chemical composition (w/%)									
	CaO	SiO_2	Al_2O_3	Fe_2O_3 (FeO)	MgO	MnO	P_2O_5	TiO_2	Others	f-CaO
SS	43.29	13.63	3.23	24.34	10.37	1.05	2.78	0.56	0.75	5.68
MS	41.4	9.79	2.69	25.25	13.6	4.67	0.98	0.79	0.83	6.29
CS	37.37	12.21	1.01	27.90	11.5	3.32	4.10	1.02	1.37	4.19
BS	39.42	11.63	0.83	30.43	8.50	2.21	3.23	0.67	3.08	4.81
BOF slag	40~50	10~15	1~5	24~28	10~12	<5	<8	<2	/	<10

The three samples of tricomponent f-CaO of $CaO{\cdot}aFeO_{1.5}\cdot bMnO_2$ system were prepared from mixing analytical grade CaO, Fe_2O_3, and MnO_2 according to a and b that were equal to 0.17 and 0.03, 0.14 and 0.06, 0.1, and 0.1, separately, and then, the other procedures were the same as above, except that the calcination time was 3 h. The nomenclature used for the three samples of the tricomponent f-CaO of $CaO{\cdot}aFeO_{1.5}{\cdot}bMnO_2$ system is C·0.17F·0.03M, C·0.14F·0.06M, and C·0.1F·0.1M according to the difference of a and b. C, F, and M represent CaO, $FeO_{1.5}$, and MnO_2, respectively. $Ca_2Fe_2O_5$, whose molar ratio of CaO to Fe_2O_3 was 2, and $Ca_3Fe_{1.5}Mn_{1.5}O_8$, whose molar ratio of CaO, Fe_2O_3, and MnO_2 was 4 : 1 : 2, was prepared by similar procedures.

2.3. Methods

2.3.1. The Compositions of f-CaO in the Four Types of BOF Slags. The backscattered electron image (BSE) was used to observe the micromorphology of the mineral phase in solid matter, in which brighter area corresponds to higher atomic number. The morphology and distribution of the mineral phase in BOF slags were observed using BSE, and, with the energy dispersive spectrometer analysis (EDS), the element compositions of f-CaO in BOF slags were revealed by frequency histogram method in statistics.

2.3.2. Simulated Monocomponent f-CaO Calcinated for Different Times

(1) XRD Characterization. The monocomponent f-CaO samples were ground to 45 um, and then the sieved samples were used for XRD (Siemens D5000) with a scanning range between 5° and 90° 2θ at a scanning speed of 1 s/step and a resolution of 0.05°/step. The X-ray diffraction patterns were analyzed by the diffraction software Jade-6 equipped with the ICCD (International Centre for Diffraction Data) PDF-2 database to calculate the crystalline sizes of the monocomponent f-CaO samples using the Scherrer equation [19].

(2) SEM Characterization. The fractured monocomponent f-CaO samples were coated with gold and observed by a SEM (Japanese Electronics Co., Ltd., JSW-780f) to analyse the influence of the calcination time on the microtopography of the monocomponent f-CaO samples.

(3) Hydration Heat Evolution Test. The monocomponent f-CaO samples, whose initial masses were 0.6 g, were for the hydration heat evolution test at a water/powder mass ratio = 10/3 at 20°C with isothermal calorimetry (Toni Technik GmBH, Germany, ToniDCA7338, sensitivity ratio 0.2 J/g). The results represent the hydration activity of the samples.

2.3.3. Simulated Tricomponent f-CaO of $CaO{\cdot}aFeO_{1.5}{\cdot}bMnO_2$ System

(1) XRD Characterization. The samples of tricomponent f-CaO of $CaO{\cdot}aFeO_{1.5}{\cdot}bMnO_2$ system were ground below 45 um. Then, the sieved samples were dehydrated, hydrated at 20°C after 36 h, and autoclaved after 3 h (P = 2.0 MP, T = 216°C). The samples were used for XRD (Siemens D5000) with a scanning range between 10° and 50° 2θ, a scanning speed of 1 s/step, and a resolution of 0.02°/step. $Ca_2Fe_2O_5$ and $Ca_3Fe_{1.5}Mn_{1.5}O_8$ and the products of $Ca_2Fe_2O_5$ and $Ca_3Fe_{1.5}Mn_{1.5}O_8$ hydrated at 20°C after 28 d were also used for XRD under the similar condition, except that the scanning range was between 20° and 70° 2θ. The X-ray diffraction patterns were analyzed by the diffraction software Jade-6 in Section 2.3.2(1). The differences in the compositions of the samples were analysed before and after hydration under different conditions.

(2) EDS-Mapping Characterization. The fractured samples were observed by EDS-mapping (Hitachi Co., Ltd., HITACHIS-47000) to identify the *distribution patterns* and *interactions* of different phases in tricomponent f-CaO of $CaO{\cdot}aFeO_{1.5}{\cdot}bMnO_2$ system.

(3) Hydration Heat Evolution Test. This test was the same as in Section 2.3.2 (3), except that the samples were tricomponent f-CaO of $CaO{\cdot}aFeO_{1.5}{\cdot}bMnO_2$ system.

3. Results and Discussion

3.1. The Morphology of Mineral Phase and the Element Compositions of f-CaO in BOF Slags

3.1.1. The Morphology of Mineral Phase in BOF Slags. Figure 1 shows the BSE images of the four types of BOF slags. With EDS for every unique area, it can be found that the black calcium silicate phase marked by A had a round or leaf shape;

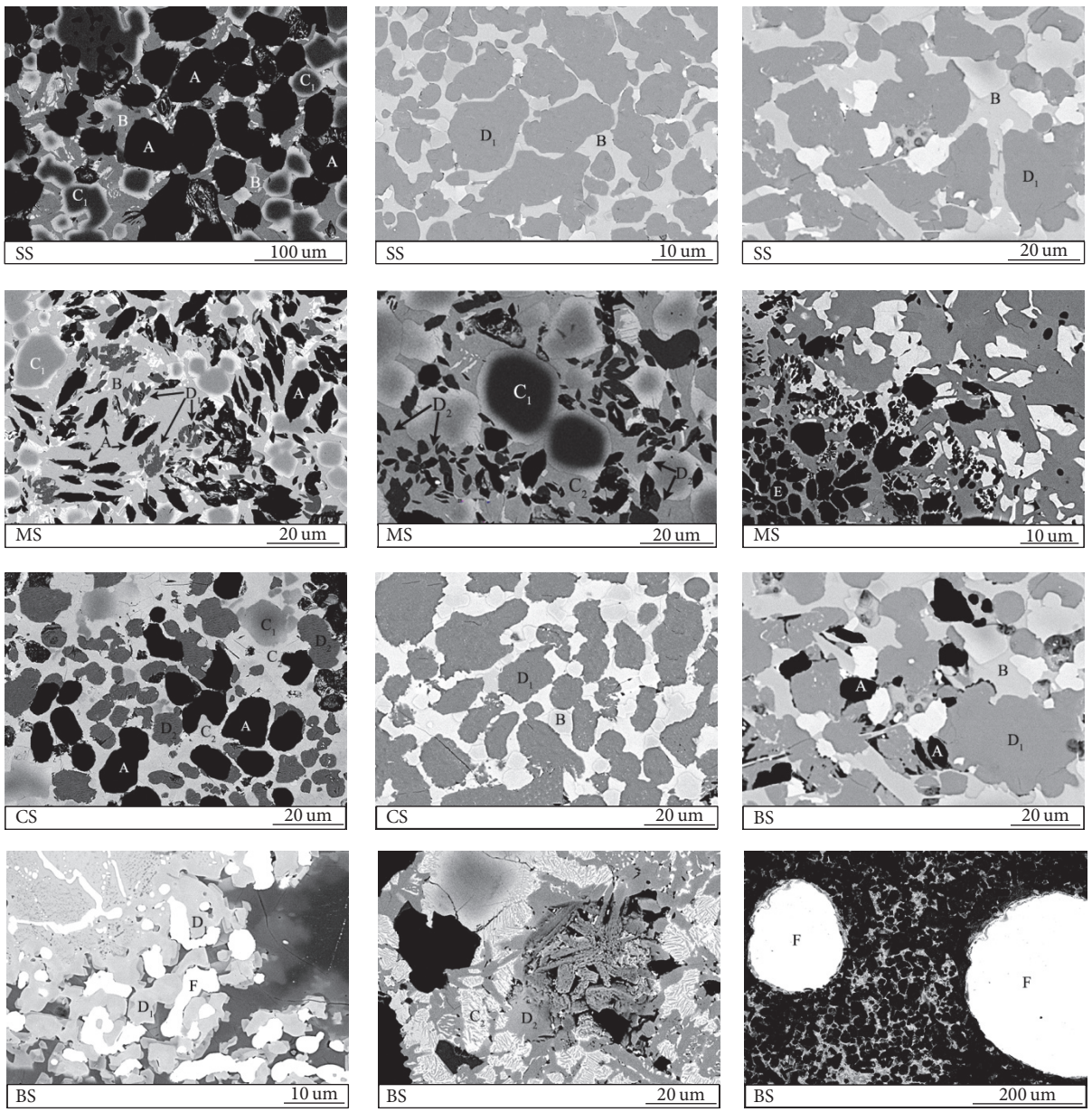

Figure 1: BSE images of the four types of BOF slag.

the white calcium iron aluminium phase indicated by B had a crosslinked shape; the iron magnesium phase, which is labelled by C_1, was black in the center and white at the edge; the iron magnesium manganese calcium phase labelled by C_2 was light grey and in an irregular or striation shape; the calcium iron phase marked by D_1 had a large particle shape; and the gathering calcium iron manganese phase shown as D_2 had a grey small particle shape. There was a small amount of f-MgO, labelled by E that is shown by a black small particle shape as well as Fe particles, indicated as F, that had a light and round shape. As shown in Figure 1, the mineral phase distribution is not uniform. Although they were in the same phase, for example, the black calcium silicate phase, their morphology, and distribution were different in different BOF slags.

F-CaO in BOF slag was considered as a phase which includes not only main CaO but also some iron oxide (FeO_x) and manganese oxide (MnO_y) [11–13]. From the above observations, there was the possibility that calcium iron phase (D_1) and calcium iron manganese phase (D_2) were classified as f-CaO. In the following section, the element compositions of calcium iron phase and calcium iron manganese phase were analysed by frequency histogram method in statistics to identify whether the calcium iron phase and calcium iron manganese phase could be regarded as f-CaO or not.

3.1.2. The Element Compositions of the Calcium Iron Phase and Calcium Iron Manganese Phase in BOF Slags. Frequency histogram method in statistics was used to reveal the element

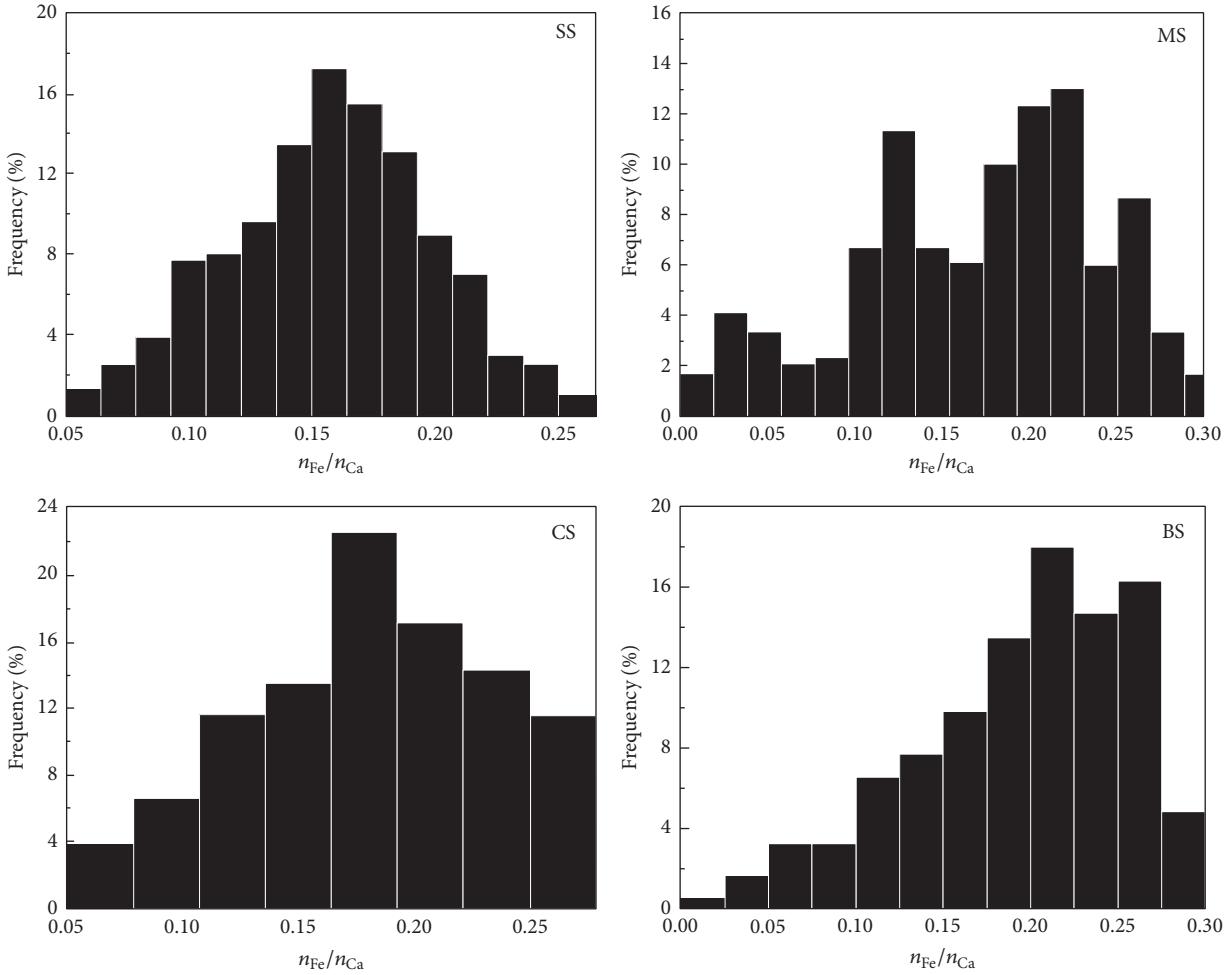

Figure 2: Frequency patterns of n_{Fe}/n_{Ca} in calcium iron phase of the four types of BOF slag.

compositions of calcium iron phase and calcium iron manganese phase in BOF slags.

(1) The Element Compositions of Calcium Iron Phase. Figure 2 presents frequency histograms of the mole ratio of Fe to Ca in the calcium iron phase of the four types of BOF slags. In the BSE images, 70 microareas in BS, 90 microareas in MS, 50 microareas in CS, and 70 microareas in BS were analysed by EDS, producing the frequency histograms of the mole ratio of Fe to Ca. Figure 2 indicated that the frequency histograms of n_{Fe}/n_{Ca} in the calcium iron phase were irregular and varied in different BOF slags, but their values were all less than 0.3. Therefore, the calcium iron phase in BOF slags was a phase of $CaO{\cdot}aFeO_x$ system, whose compositions were not fixed.

(2) The Element Compositions of Calcium Iron Manganese Phase. Figure 3 shows frequency histograms of the mole ratio of (Fe + Mn) to Ca in the calcium iron manganese phase of the three types of BOF slags. In BSE images, the calcium iron manganese phase was not found in SS, and 70 microareas in MS, 90 microareas in CS, and 50 microareas in BS were analysed by EDS, producing the frequency histograms of the mole ratio of (Fe + Mn) to Ca. Based on Figure 2, it can be obtained that Figures 3 and 2 possess similar characteristics. The frequency histograms of $(n_{Fe} + n_{Mn})/n_{Ca}$ in the calcium iron manganese phase were irregular and varied in different BOF slags, and the values were all less than 0.5. Therefore, the calcium iron manganese phase in BOF slags was a phase of $CaO{\cdot}aFeO_x{\cdot}bMnO_y$ system, whose compositions were diverse.

It can be concluded that the calcium iron phase and calcium iron manganese phase could be regarded as f-CaO because CaO was the main component and FeO_x and MnO_y were minor components.

Table 2 is frequency table of elements in the calcium iron manganese phase of the three types of BOF slags. It is evident that the average contents of Ca, Fe, and Mn decreased gradually, and although Figure 3 gives that the frequency histogram of $(n_{Fe} + n_{Mn})/n_{Ca}$ in the calcium iron manganese phase was irregular, the average values of $(n_{Fe} + n_{Mn})/n_{Ca}$ were about 0.2. From Figure 1, it is clear that the f-CaO of the calcium iron phase was adjacent to the calcium iron aluminium phase or Fe and that the f-CaO of the calcium iron manganese phase was close to the iron magnesium manganese calcium phase. From this, it can be speculated that the compositional difference between the f-CaO of

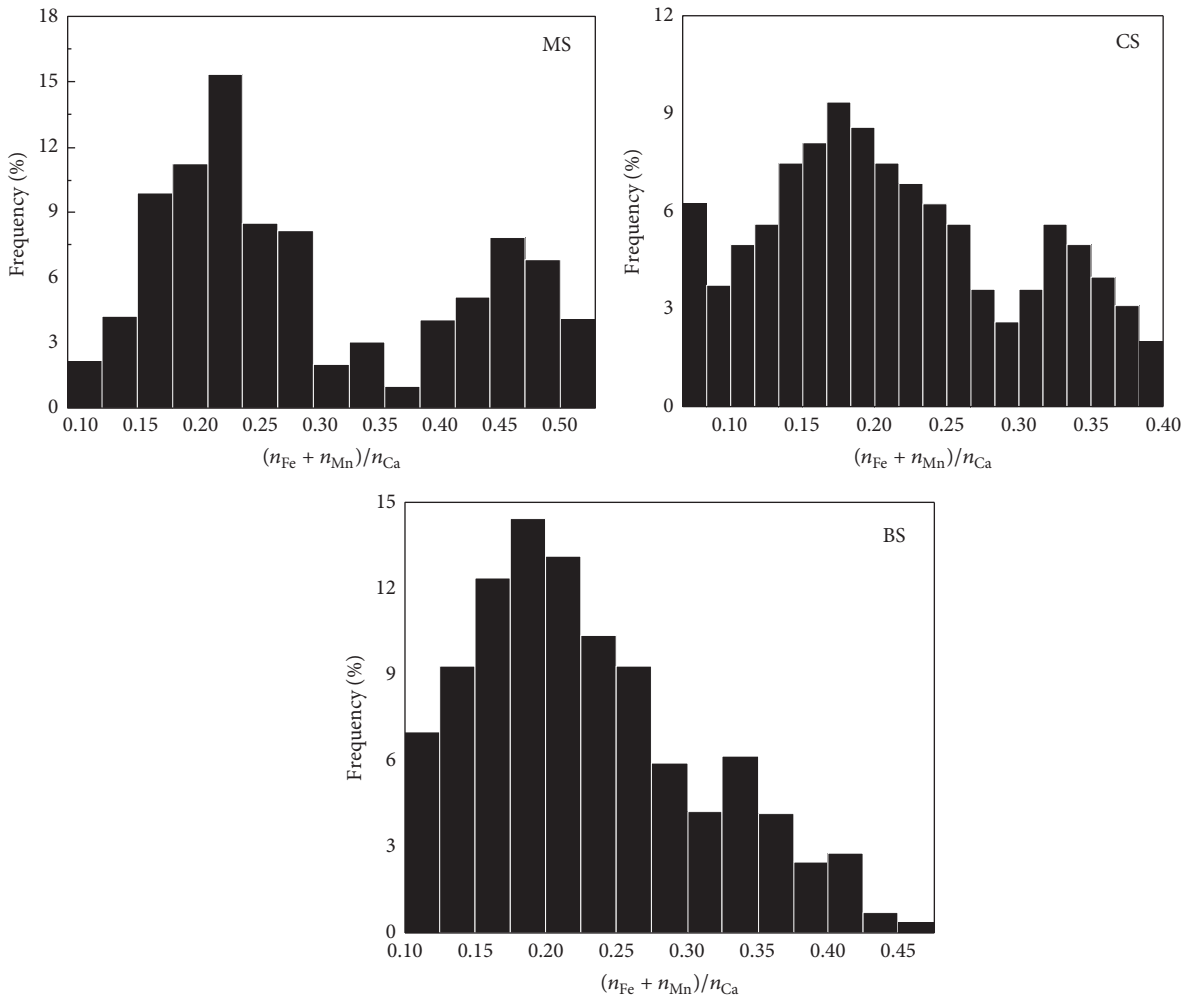

Figure 3: Frequency patterns of $(n_{Fe} + n_{Mn})/n_{Ca}$ in calcium iron manganese phase of the three types of BOF slag.

Table 2: Frequency table of elements in calcium iron manganese phase of BOF slags from different steel plants.

Type	Microarea number	Parameter	Element number/%			Molar ratio
			Ca	Fe	Mn	(Fe + Mn)/Ca
MS	100	Range	30.13–47.41	2.81–9.70	0.78–6.51	**0.09–0.52**
		Average	45.28	5.85	4.20	**0.22**
CS	150	Range	32.71–48.27	1.92–7.81	1.29–5.71	**0.07–0.40**
		Average	41.50	4.56	3.06	**0.18**
BS	110	Range	29.42–45.91	3.71–10.07	0.63–4.62	**0.10–0.47**
		Average	37.59	5.26	2.61	**0.21**

the calcium iron phase and the f-CaO of the calcium iron manganese phase was due to the difference of the phases adjacent to different f-CaO. In the high temperature process of steelmaking, some FeO_x dissolved in CaO, which was next to the calcium iron aluminium phase or Fe, forming f-CaO of the calcium iron phase, and both FeO_x and MnO_y dissolved in CaO adjacent to the iron magnesium manganese calcium phase to form the f-CaO of the calcium iron manganese phase. In the process of solid solution formation, compared with the radii of Mg^{2+} in MgO and Al^{3+} in Al_2O_3, the radii of Fe^{2x+} in FeO_x and Mn^{2y+} in MnO_y may be closer to Ca^{2+} (there is a special example: Ca^{2+}: 0.099 nm, Mn^{2+}: 0.091 nm, Fe^{2+}: 0.083 nm, and Mg^{2+}: 0.078 nm, Al^{3+}: 0.057 nm) [11, 12]. Therefore, FeO_x and MnO_y may be easier to dissolve in CaO than MgO and Al_2O_3, and the main compositions dissolved in f-CaO were FeO_x and MnO_y, but not MgO and Al_2O_3.

The formation mechanism of f-CaO was achieved by dissolving FeO_x and MnO_y in CaO by using high temperature process of steelmaking. So two factors influencing the hydration activity of f-CaO in BOF slag can be considered: the

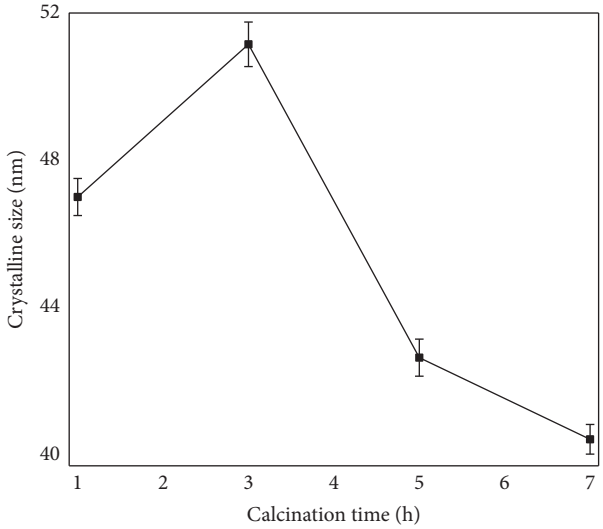

Figure 4: Crystalline sizes of monocomponent f-CaO calcinated for different times.

duration of the high temperature process and the dissolved FeO_x and MnO_y. Since the system of BOF slag is very complex, the influence of these factors on hydration activity of f-CaO was simply studied through the calcination experiment.

So far, the majority of the published literatures have thought that both FeO_x and MnO_y dissolve in f-CaO [11, 12], so in the following section, the influence of the duration of the high temperature process and the components of both FeO_x and MnO_y on hydration activity of f-CaO was simply studied firstly. If it is necessary, the influence of FeO_x on the hydration activity of f-CaO will be further explored in later studies.

F-CaO was divided into two categories: monocomponent f-CaO and tricomponent f-CaO of $CaO{\cdot}aFeO_x{\cdot}bMnO_y$ system. F-CaO, composed of only CaO, was called monocomponent f-CaO, and f-CaO, composed of CaO, Fe_2O_3 and MnO_2, was called tricomponent f-CaO of $CaO{\cdot}aFeO_{1.5}{\cdot}bMnO_2$ system. Monocomponent CaO, which is not the same but is similar to monocomponent f-CaO in BOF slag, was prepared to explore the influence mechanisms of the calcination time on the hydration activity of monocomponent f-CaO, and tricomponent f-CaO of $CaO{\cdot}aFeO_{1.5}{\cdot}bMnO_2$ system, which is not the same but similar to tricomponent f-CaO of $CaO{\cdot}aFeO_x{\cdot}bMnO_y$ system in BOF slag, was prepared to study the influence mechanisms of the dissolved Fe_2O_3 and MnO_2 on the hydration activity of the tricomponent f-CaO of $CaO{\cdot}aFeO_{1.5}{\cdot}bMnO_2$ system. The aim of this study was to provide useful fundamental knowledge for complex system through studying simplified systems.

3.2. Microtopography and Hydration Heat Evolution Rate Curves of Monocomponent f-CaO Calcinated for Different Times. Figure 4 shows the crystalline sizes of monocomponent f-CaO calcinated for 1, 3, 5, and 7 h, and Figure 5 presents their microtopography. With the development of the calcination time, the crystalline sizes of monocomponent f-CaO initially increased but ultimately decreased, and the crystalline size of the monocomponent f-CaO calcinated for 3 h was 51 nm, which was the largest size. Figure 5 indicates that, compared with monocomponent f-CaO calcinated for 1, 5, and 7 h, the microtopography of monocomponent f-CaO calcinated for 3 h was more complete and its microstructure was denser. This was probably because the calcination time affects the crystal growth, and the degree of growth will increase with calcination time; however, an unreasonable extension of the calcination time would aggravate secondary recrystallization, which can damage the crystal structure, increasing the number of crystal defects [20].

Figure 6 shows the hydration heat evolution rate curves of monocomponent f-CaO calcinated for 1, 3, 5, and 7 h. Figure 6 shows that all of the samples were still not fully hydrated after 3 h. It can be inferred that calcination at 1600°C could restrain the hydration activity of CaO to a certain extent. Compared with monocomponent f-CaO calcinated for 1, 5, and 7 h, the hydration heat evolution peaks of monocomponent f-CaO calcinated for 3 h fell behind. This was probably because the better the degree of the growth of the crystal, the lower the hydration activity. Figures 4 and 5 show that the crystallinity of monocomponent f-CaO calcinated for 3 h was more complete and its microstructure was denser than those of monocomponent f-CaO calcinated for 1, 5, and 7 h.

3.3. Characterization of Simulated Tricomponent f-CaO of $CaO{\cdot}aFeO_{1.5}{\cdot}bMnO_2$ System. Figure 3 indicated that the frequency histograms of $(n_{Fe} + n_{Mn})/n_{Ca}$ in the calcium iron manganese phase were irregular and varied in different BOF slags, but Table 2 shows the average contents of Ca, Fe, and Mn decreased gradually with the sequence of Ca, Fe, and Mn, and the average values of $(n_{Fe} + n_{Mn})/n_{Ca}$ were about 0.2. Therefore, the metal oxides compositions of tricomponent f-CaO samples were $CaO{\cdot}0.17FeO_{1.5}{\cdot}0.03MnO_2$, $CaO{\cdot}0.14FeO_{1.5}{\cdot}0.06MnO_2$, and $CaO{\cdot}0.1FeO_{1.5}{\cdot}0.1MnO_2$ in this study. To explore the influence mechanisms of dissolved Fe_2O_3 and MnO_2 on their hydration activity, the following tests were carried out.

3.3.1. XRD Analyses. Figure 7 shows the X-ray diffraction patterns of the three samples of tricomponent f-CaO of $CaO{\cdot}aFeO_{1.5}{\cdot}bMnO_2$ system, samples hydrated at 20°C for 36 h and samples autoclaved for 3 h. The phases present in samples C·0.17F·0.03M and C·0.14F·0.06M were the same, CaO, $Ca_3Fe_{1.5}Mn_{1.5}O_8$, and $Ca_2Fe_2O_5$. After they had hydrated at 20°C for 36 h, the detected phases were $Ca(OH)_2$, $Ca_3Fe_{1.5}Mn_{1.5}O_8$, and $Ca_2Fe_2O_5$. After they had been autoclaved for 3 h, $Ca(OH)_2$, $Ca_3Fe_{1.5}Mn_{1.5}O_8$, $Ca_2Fe_2O_5$, $FeMnO_3$, and Fe_2O_3 were detected in both samples. The phases present in sample C·0.1F·0.1M were CaO and $Ca_3Fe_{1.5}Mn_{1.5}O_8$. After it had hydrated at 20°C for 36 h, the detected phases were $Ca(OH)_2$ and $Ca_3Fe_{1.5}Mn_{1.5}O_8$. After it had been autoclaved for 3 h, $Ca(OH)_2$, $Ca_3Fe_{1.5}Mn_{1.5}O_8$, and $FeMnO_3$ were detected.

Figure 8 shows the X-ray diffraction patterns of samples $Ca_2Fe_2O_5$ and $Ca_3Fe_{1.5}Mn_{1.5}O_8$ and they hydrated at 20°C after 28 d. There were no new peaks after $Ca_2Fe_2O_5$ and $Ca_3Fe_{1.5}Mn_{1.5}O_8$ were hydrated at 20°C for 28 d. This may be because the hydration activity of $Ca_2Fe_2O_5$ and $Ca_3Fe_{1.5}Mn_{1.5}O_8$ was so low that Fe_2O_3 and $FeMnO_3$

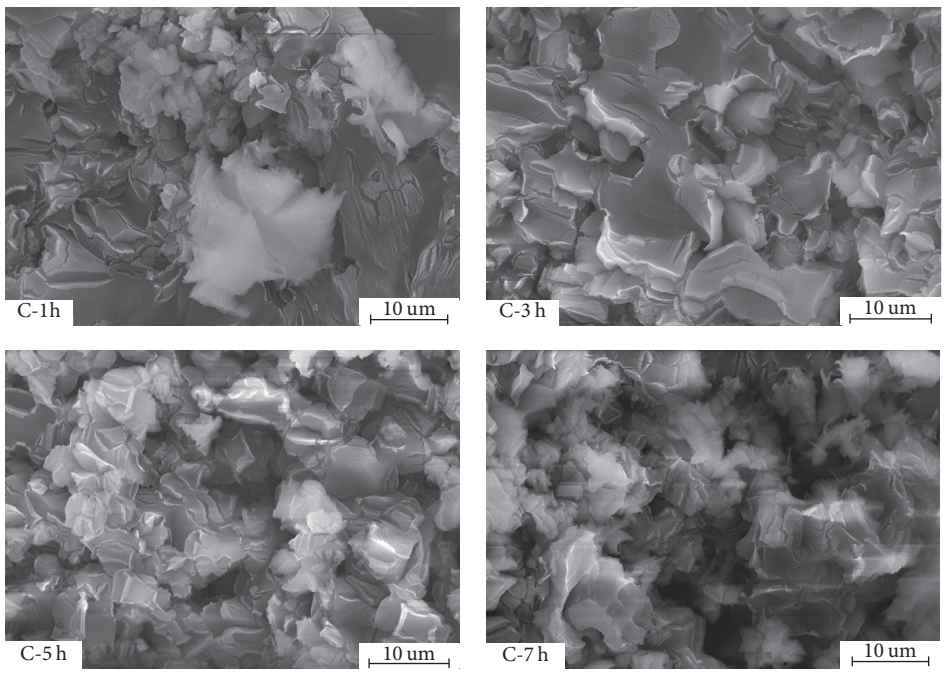

Figure 5: SEM images of monocomponent f-CaO calcinated for different times.

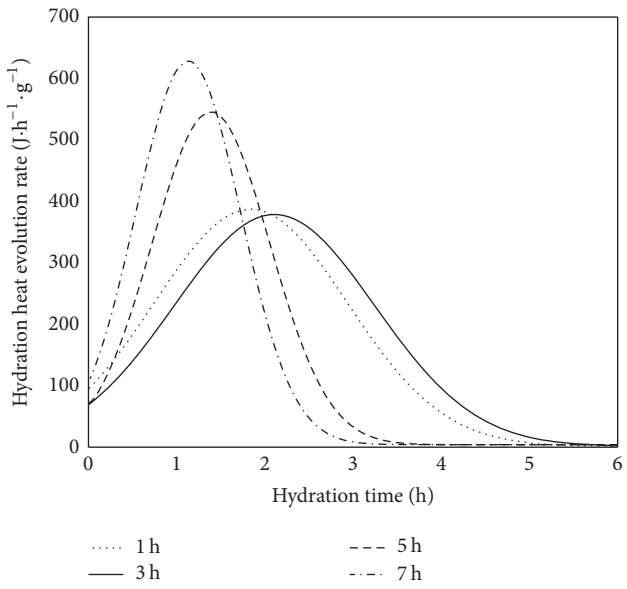

Figure 6: Hydration heat evolution rate curves of monocomponent f-CaO calcinated for different times.

contents in their hydration products were less than the detection limit of XRD.

From Figures 7 and 8, it can be concluded that CaO in the tricomponent f-CaO can fully hydrate at 20°C after 36 h, even though it went through the calcination at 1600°C, but $Ca_3Fe_{1.5}Mn_{1.5}O_8$ and $Ca_2Fe_2O_5$, which were autoclaved for 3 h, were only slightly hydrated. The hydration activity of both $Ca_3Fe_{1.5}Mn_{1.5}O_8$ and $Ca_2Fe_2O_5$ was so low that hydration was undetected at 20°C after 28 d. The hydration products of $Ca_2Fe_2O_5$ were $Ca(OH)_2$ and Fe_2O_3, and the hydration products of $Ca_3Fe_{1.5}Mn_{1.5}O_8$ mainly contained $Ca(OH)_2$ and $FeMnO_3$. $Ca_2Fe_2O_5$ and $Ca_3Fe_{1.5}Mn_{1.5}O_8$ formed by CaO, Fe_2O_3, and MnO_2 were difficult to hydrate.

Because the hydration reactions occurred in different phases in the tricomponent f-CaO, the volume expansion rates of the solid phases can be calculated and are presented in Table 3. From Table 3, because of the hydration reactions of CaO, $Ca_2Fe_2O_5$, and $Ca_3Fe_{1.5}Mn_{1.5}O_8$, the volumes of the solid phases increased by 97.88%, 43.44%, and 52.02%, respectively. Their volume expansion rates were different, so the volume expansion rates of the tricomponent f-CaO varied with different proportions of CaO, $Ca_2Fe_2O_5$, and $Ca_3Fe_{1.5}Mn_{1.5}O_8$.

3.3.2. EDS-Mapping Analyses. Figure 9 shows EDS-mapping of the tricomponent f-CaO of $CaO{\cdot}aFeO_{1.5}{\cdot}bMnO_2$ system. From Figure 7, it can be observed that the main phases in the tricomponent f-CaO were CaO, $Ca_3Fe_{1.5}Mn_{1.5}O_8$, and $Ca_2Fe_2O_5$. Figure 9 shows CaO was widespread, $Ca_2Fe_2O_5$ distributed as dendritic patterns, and $Ca_3Fe_{1.5}Mn_{1.5}O_8$ irregularly distributed in the tricomponent f-CaO. $Ca_3Fe_{1.5}Mn_{1.5}O_8$ is distributed with widespread diffusion patterns in C·0.1F·0.1M sample.

In order to study the influence of dissolved Fe_2O_3 and MnO_2 on the hydration activity of the tricomponent f-CaO of $CaO{\cdot}aFeO_{1.5}{\cdot}bMnO_2$ system, except for $Ca_2Fe_2O_5$ and $Ca_3Fe_{1.5}Mn_{1.5}O_8$ in the tricomponent f-CaO that were hard to hydrate, the hydration activity of CaO in tricomponent f-CaO should also be investigated. It is meaningful to identify whether and how the distribution of the patterns of $Ca_2Fe_2O_5$ and $Ca_3Fe_{1.5}Mn_{1.5}O_8$ influenced the hydration activity of CaO in the tricomponent f-CaO.

Table 3: Volume expansion of the solid phases after the hydration of different phases in tricomponent f-CaO of $CaO{\cdot}aFeO_{1.5}{\cdot}bMnO_2$ system.

Equations of reaction	Molecular mass			Specific gravity (g/cm^3)			Solid phase volume (cm^3)		Volume expansion rate (%)
							Before reaction	After reaction	
$CaO + H_2O \rightarrow Ca(OH)_2$	CaO: 56.08	$Ca(OH)_2$: 74.09		CaO: 3.34	$Ca(OH)_2$: 2.23		16.79	33.22	**97.88**
$Ca_2Fe_2O_5 + 2H_2O \rightarrow 2Ca(OH)_2 + Fe_2O_3$	$Ca_2Fe_2O_5$: 271.83	$Ca(OH)_2$: 74.09	Fe_2O_3: 159.68	$Ca_2Fe_2O_5$: 4.03	$Ca(OH)_2$: 2.23	Fe_2O_3: 5.27	67.45	96.75	**43.44**
$4Ca_3Fe_{1.5}Mn_{1.5}O_8 + 12H_2O \rightarrow 12Ca(OH)_2 + 6FeMnO_3 + O_2$	$Ca_3Fe_{1.5}Mn_{1.5}O_8$: 414.4	$Ca(OH)_2$: 74.09	$FeMnO_3$: 158.78	$Ca_3Fe_{1.5}Mn_{1.5}O_8$: 4.26	$Ca(OH)_2$: 2.23	$FeMnO_3$: 4.94	389.11	591.54	**52.02**

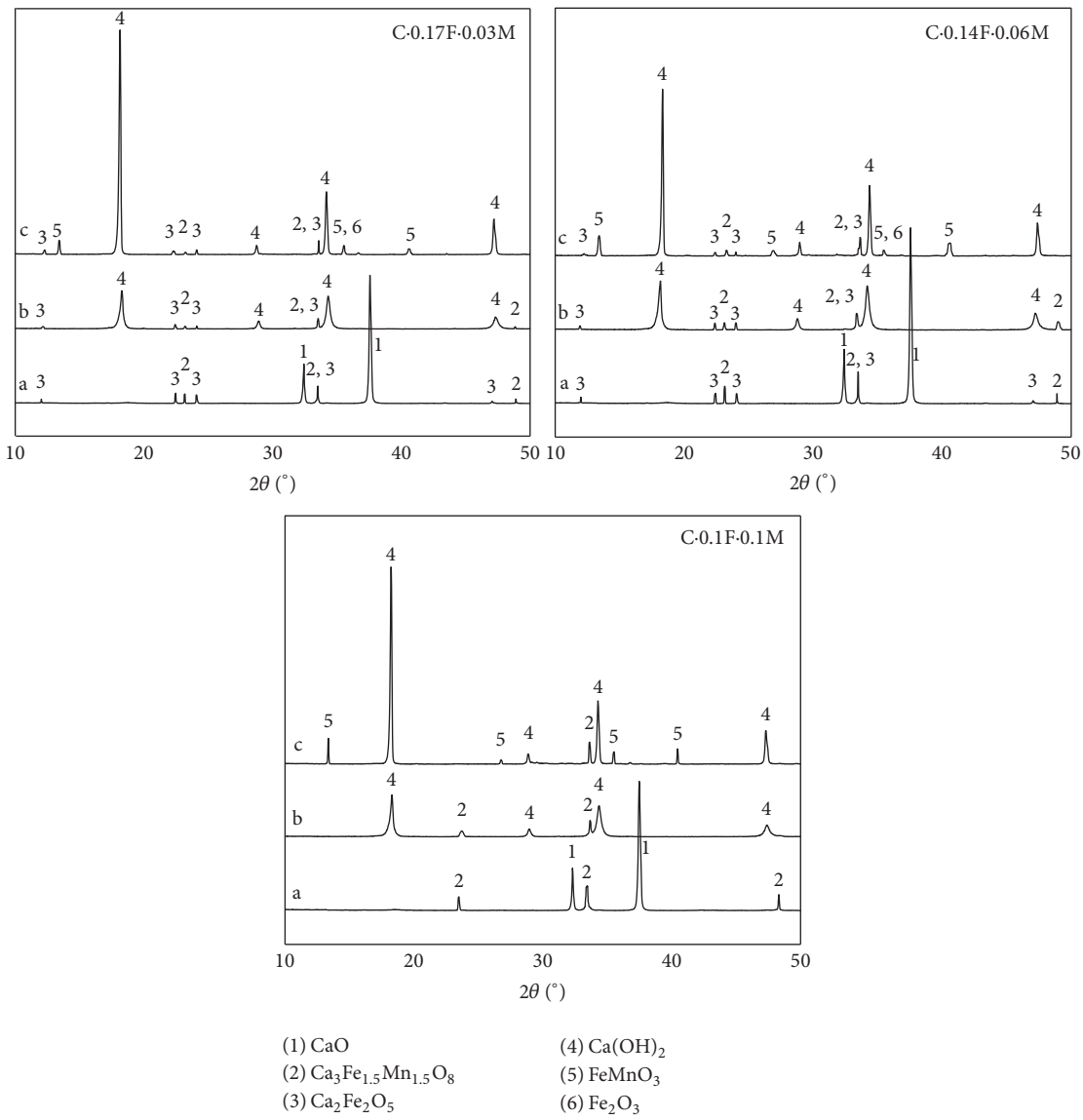

Figure 7: X-ray diffraction patterns of tricomponent f-CaO of CaO·aFeO$_{1.5}$·bMnO$_2$ system and their hydration products under different hydration conditions (a: no hydration, b: hydration at 20°C for 36 h, and c: autoclave hydration for 3 h).

3.3.3. Hydration Heat Evolution Analyses. The increasing curves shown in Figure 10 are the cumulative hydration heat curves of the monocomponent f-CaO and tricomponent f-CaO of CaO·aFeO$_{1.5}$ ·bMnO$_2$ system. There were no increases in the cumulative hydration heats of C·0.17F·0.03M, C·0.14F·0.06M, and C·0.1F·0.1M after 30 h, and the cumulative hydration heats of them were similar after 30 h. When their initial masses were 0.6 g, the contents, expressed by the amount of substance with different compositions, could be calculated as shown in Table 4. Table 4 shows the CaO contents related to C·0.17F·0.03M, C·0.14F·0.06M, and C·0.1F·0.1M being 0.0064, 0.0061, and 0.0057 mol, respectively. It was clear that their CaO contents were similar. Since CaO was totally hydrated, but no hydration was detected in $Ca_2Fe_2O_5$ and $Ca_3Fe_{1.5}Mn_{1.5}O_8$ when the tricomponent f-CaO took part in the hydration process at room temperature within a short time, the final cumulative hydration heat of C·0.17F·0.03M, C·0.14F·0.06M, and C·0.1F·0.1M was similar.

The single peak type curves shown in Figure 10 are the hydration heat evolution rate curves of monocomponent f-CaO and tricomponent f-CaO of CaO·aFeO$_{1.5}$ ·bMnO$_2$ system. Compared with the narrow and high hydration heat evolution peak of monocomponent f-CaO, the hydration heat evolution peaks of the tricomponent f-CaO were wide and low. Compared with monocomponent f-CaO, the hydration heat evolution peaks of tricomponent f-CaO fell slightly behind, and the larger the b/a was, the further its hydration heat evolution peak fell behind. It is clearly indicated that, compared with monocomponent f-CaO, the hydration activity of CaO in the tricomponent f-CaO decreased continuously with increasing b/a. When the contact of CaO and H_2O became more difficult, the hydration activity of CaO reduced

Table 4: The compositions of tricomponent f-CaO of CaO·aFeO$_{1.5}$·bMnO$_2$ system.

Tricomponent f-CaO	CaO·0.17FeO$_{1.5}$·0.03MnO$_2$			CaO·0.14FeO$_{1.5}$·0.06MnO$_2$			CaO·0.1FeO$_{1.5}$·0.1MnO$_2$	
Mass (g)				**0.6**				
molecular mass	72.26			72.47			72.76	
Amount of substance (mol)	0.0083			0.0083			0.0082	
Phase composition	$Ca_3Fe_{1.5}Mn_{1.5}O_8$	$Ca_2Fe_2O_5$	CaO	$Ca_3Fe_{1.5}Mn_{1.5}O_8$	$Ca_2Fe_2O_5$	CaO	$Ca_3Fe_{1.5}Mn_{1.5}O_8$	CaO
Amount of substance (mol)	0.0002	0.0006	**0.0064**	0.0005	0.0003	**0.0061**	0.0008	**0.0057**

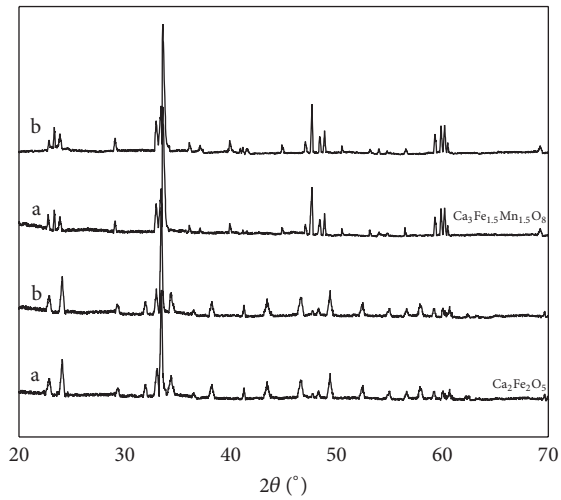

Figure 8: X-ray diffraction patterns of $Ca_2Fe_2O_5$, $Ca_3Fe_{1.5}Mn_{1.5}O_8$, and their hydration products (a: no hydration and b: hydration at 20°C for 28 d).

[21], so it may be that the distribution patterns of $Ca_2Fe_2O_5$ and $Ca_3Fe_{1.5}Mn_{1.5}O_8$ in tricomponent f-CaO can restrain the contact between CaO and H_2O in the hydration process of tricomponent f-CaO; the effect became more serious with increasing $Ca_3Fe_{1.5}Mn_{1.5}O_8$ contents and decreasing of $Ca_2Fe_2O_5$ contents. Combined with the analyses of Figure 7, the sequence of the hydration activity of monocomponent f-CaO and tricomponent f-CaO was as follows: $Ca_2Fe_2O_5$ and $Ca_3Fe_{1.5}Mn_{1.5}O_8$ in tricomponent f-CaO < CaO in tricomponent f-CaO < monocomponent f-CaO.

Since simulated monocomponent CaO and tricomponent f-CaO of CaO·aFeO$_{1.5}$ ·bMnO$_2$ system in this study are similar to monocomponent f-CaO and tricomponent f-CaO of CaO·aFeO$_x$ ·bMnO$_y$ system in BOF slag, the conclusions of this study can be extended to monocomponent f-CaO and tricomponent f-CaO of CaO·aFeO$_x$ ·bMnO$_y$ system in BOF slag. The following deductions can be made: (i) the volume expansion rates of tricomponent f-CaO of CaO·aFeO$_x$ ·bMnO$_y$ system in BOF slag, due to the different volume expansion rates of CaO and solid solutions CaO-FeO$_x$ and CaO-FeO$_x$-MnO$_y$, varied with different proportions of CaO and solid solutions CaO-FeO$_x$ and CaO-FeO$_x$-MnO$_y$, which was different from the current view that the volume expansion rate, due to f-CaO hydration, is merely 97.88% [8]; this study showed that 97.88% was only suitable for monocomponent f-CaO; (ii) in BOF slag, the sequence of the hydration activity of monocomponent f-CaO and tricomponent f-CaO of CaO·aFeO$_x$ ·bMnO$_y$ system should be solid solutions CaO-FeO$_x$ and CaO-FeO$_x$-MnO$_y$ in tricomponent f-CaO < CaO in tricomponent f-CaO < monocomponent f-CaO; (iii) monocomponent f-CaO and CaO in tricomponent f-CaO of CaO·aFeO$_x$ ·bMnO$_y$ system, which underwent calcination at 1600°C, could hydrate fully in the hydration process at room temperature within a short time, but solid solutions CaO-FeO$_x$ and CaO-FeO$_x$-MnO$_y$ were hard to hydrate. In the following section, the reason why solid solutions CaO-FeO$_x$ and CaO-FeO$_x$-MnO$_y$ in tricomponent f-CaO in BOF slag were hard to hydrate was explained by theoretical analysis.

4. Theoretical Analysis of the Reason Why the Solid Solutions CaO-FeO$_x$ and CaO-FeO$_x$-MnO$_y$ in Tricomponent f-CaO Were Hard to Hydrate

AO$_n$, BO$_m$, and A(OH)$_{2n}$ were used to represent metal oxides and the hydration product, and (1) and (2) represent the hydration reaction of AO$_n$ and the solid solution reaction of AO$_n$ and BO$_m$, separately.

$$\mathrm{AO}_n + n\mathrm{H}_2\mathrm{O} \longrightarrow \mathrm{A(OH)}_{2n}, \quad \Delta_r G^{\theta}_{m,\mathrm{A}} \tag{1}$$

$$x\mathrm{AO}_n + y\mathrm{BO}_m \longrightarrow x\mathrm{AO}_n\text{-}y\mathrm{BO}_m, \quad \Delta_r G^{\theta}_m, \tag{2}$$

where xAO$_n$-yBO$_m$, $\Delta_f G^{\theta}_m$, $\Delta_r G^{\theta}_m$, and $(\partial \Delta_r G^{\theta}_m / \partial x)_y$ represent bicomponent metal oxide solid solution with a certain proportion of x/y, standard molar formation Gibbs function, standard molar reaction Gibbs function, and partial molar quantity of standard molar reaction Gibbs function of bicomponent metal oxide solid solution, respectively.

The hydration of xAO$_n$-yBO$_m$ gradually proceeded. The first stage was associated with the hydration of AO$_n$ whose hydration activity was higher than that of BO$_m$. The hydration reaction of this stage is described by

$$x\mathrm{AO}_n\text{-}y\mathrm{BO}_m + nx\mathrm{H}_2\mathrm{O} \longrightarrow x\mathrm{A(OH)}_{2n} + y\mathrm{BO}_m. \tag{3}$$

The second stage was related to the hydration of BO$_m$ if its hydration was possible. The hydration reaction of this stage is described by

$$\mathrm{BO}_m + m\mathrm{H}_2\mathrm{O} \longrightarrow \mathrm{B(OH)}_{2m}. \tag{4}$$

The overall hydration reaction of xAO$_n$-yBO$_m$ was as follows:

$$x\mathrm{AO}_n\text{-}y\mathrm{BO}_m + (nx + my)\,\mathrm{H}_2\mathrm{O} \longrightarrow x\mathrm{A(OH)}_{2n} + y\mathrm{B(OH)}_{2m}. \tag{5}$$

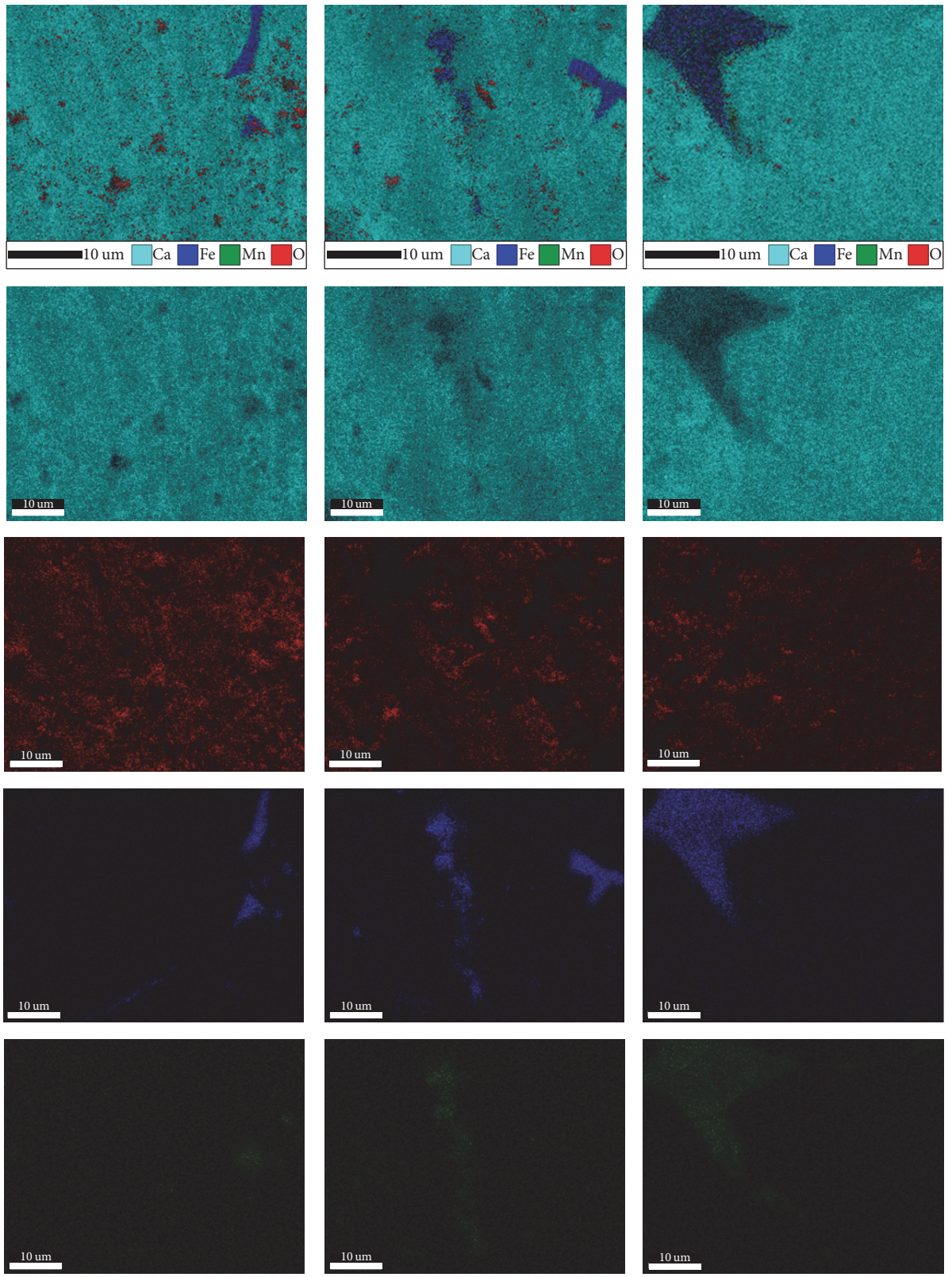

$a = 0.17, b = 0.03$ $a = 0.14, b = 0.06$ $a = 0.1, b = 0.1$

Figure 9: EDS-mapping images of fractured tricomponent f-CaO of $CaO{\cdot}aFeO_{1.5}{\cdot}bMnO_2$ system.

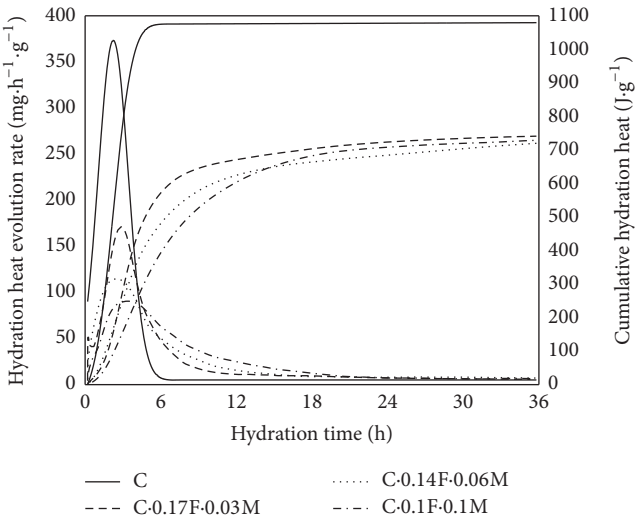

Figure 10: Hydration heat curves of monocomponent f-CaO and tricomponent f-CaO of CaO·aFeO$_{1.5}$·bMnO$_2$ system.

For first stage, the hydration of AO_n in xAO_n-yBO_m can be classified into two types.

The first type was related to the fact that all AO_n in xAO_n-yBO_m took part in hydration reaction. The hydration reaction was as follows:

$$xAO_n\text{-}yBO_m + nxH_2O \longrightarrow xA(OH)_{2n} + yBO_m, \quad \Delta_r G^{\theta}_{m,A(mix)}. \tag{6}$$

After calculation,

$$\begin{aligned}\Delta_r G^{\theta}_{m,A(mix)} &= \sum_C \nu_C \Delta_f G^{\theta}_m(C)\\ &= y\Delta_f G^{\theta}_m(BO_m) + x\Delta_f G^{\theta}_m(A(OH)_{2n})\\ &\quad - nx\Delta_f G^{\theta}_m(H_2O)\\ &\quad - \Delta_f G^{\theta}_m(xAO_n\text{-}yBO_m)\\ &= x\Delta_r G^{\theta}_{m,A} - \Delta_r G^{\theta}_m.\end{aligned} \tag{7}$$

So (8) showed the standard molar reaction Gibbs function of the hydration reaction of AO_n in xAO_n-yBO_m for this type.

$$\Delta_r G^{\theta}_{m,A(mix,1)} = \Delta_r G^{\theta}_{m,A} - \frac{\Delta_r G^{\theta}_m}{x}. \tag{8}$$

The second type was associated with the fact that part of AO_n in xAO_n-yBO_m took part in hydration reaction. The hydration reaction was expressed as

$$xAO_n\text{-}yBO_m + ndxH_2O \longrightarrow dxA(OH)_{2n} + (x-dx)AO_n\text{-}yBO_m, \quad \Delta_r G^{\theta}_{m,A(d)}. \tag{9}$$

After calculation,

$$\begin{aligned}\Delta_r G^{\theta}_{m,A(d)} &= \sum_C \nu_C \Delta_f G^{\theta}_m(C)\\ &= \Delta_f G^{\theta}_m((x-dx)AO_n\text{-}yBO_m)\\ &\quad + dx\Delta_f G^{\theta}_m(A(OH)_{2n})\\ &\quad - ndx\Delta_f G^{\theta}_m(H_2O)\\ &\quad - \Delta_f G^{\theta}_m(xAO_n\text{-}yBO_m).\end{aligned} \tag{10}$$

So (11) showed the standard molar reaction Gibbs function of the hydration reaction of AO_n in xAO_n-yBO_m for this type.

$$\Delta_r G^{\theta}_{m,A(d,1)} = -\left(\frac{\partial \Delta_r G^{\theta}_m}{\partial x}\right)_y + \Delta_r G^{\theta}_{m,A}. \tag{11}$$

In general, the values of $\Delta_r G^{\theta}_m$ and $(\partial\Delta_r G^{\theta}_m/\partial x)_y$ of the bicomponent metal oxide solid solution are negative [22]. It can be deduced that whether all or part of AO_n in xAO_n-yBO_m took part in the first stage of the hydration of xAO_n-yBO_m, the absolute values of $\Delta_r G^{\theta}_{m,A(mix,1)}$ and $\Delta_r G^{\theta}_{m,A(d,1)}$ both were smaller than the absolute value of $\Delta_r G^{\theta}_{m,A}$ of the hydration reaction of AO_n alone. It can be speculated that the first stage of the hydration of xAO_n-yBO_m was more difficult than the hydration of AO_n alone, so the overall hydration of xAO_n-yBO_m must be more difficult than that of AO_n alone. Tricomponent metal oxide solid solution xAO_n-yBO_m-zCO_k was the product of the solid solution reaction among AO_n, BO_m, and CO_k with a certain proportion of $x/y/z$. Tricomponent metal oxide solid solution xAO_n-yBO_m-zCO_k can be seen as a pseudo-bi-component metal oxide solid solution of AO_n and yBO_m-zCO_k with a proportion of $x/1$. If the values of $\Delta_r G^{\theta}_m$ and $(\partial\Delta_r G^{\theta}_m/\partial x)_{y,z}$ of pseudo-bi-component metal oxide solid solution xAO_n-yBO_m-zCO_k were still negative, its hydration must also be more difficult than that of AO_n alone. Therefore, there was the possibility that solid solutions CaO-FeO$_x$ and CaO-FeO$_x$-MnO$_y$ in tricomponent f-CaO in BOF slag were difficult to hydrate because of the decreased hydration reaction driving force, namely, the absolute value of standard molar reaction Gibbs function.

This study indicated that only solid solutions CaO-FeO$_x$ and CaO-FeO$_x$-MnO$_y$ in tricomponent f-CaO were hard to hydrate, and their hydration activity was very low. Therefore, if f-CaO can make contact with H_2O during the hydration process of CBS, all of the monocomponent f-CaO and CaO in tricomponent f-CaO of CaO·aFeO$_x$·bMnO$_y$ system undergo hydration within a short time, which will not lead to a volume expansion of BOF slag after the CBS hardens; however, solid solutions CaO-FeO$_x$ and CaO-FeO$_x$-MnO$_y$ will continue to slowly hydrate after the CBS hardens, resulting in the volume expansion.

5. Conclusions

The following conclusions can be drawn from the test results and discussion.

In BOF slag, f-CaO included at least the calcium iron phase and calcium iron manganese phase whose compositions were diverse. The reason why f-CaO had different compositions was that different compositions of f-CaO were found in different phases.

Simulated experiment indicated that high temperature calcination can restrain the hydration activity of CaO. Since the volume expansion rates of CaO, $Ca_2Fe_2O_5$, and $Ca_3Fe_{1.5}Mn_{1.5}O_8$ in tricomponent f-CaO of $CaO{\cdot}aFeO_{1.5}{\cdot}bMnO_2$ system were 97.88%, 43.44%, and 52.02%, respectively, the volume expansion rates of tricomponent f-CaO varied with different proportions of CaO, $Ca_2Fe_2O_5$, and $Ca_3Fe_{1.5}Mn_{1.5}O_8$. The hydration activity sequence was as $Ca_2Fe_2O_5$ and $Ca_3Fe_{1.5}Mn_{1.5}O_8$ in tricomponent f-CaO < CaO in tricomponent f-CaO < mono-component f-CaO. Monocomponent f-CaO and CaO in tricomponent f-CaO of $CaO{\cdot}aFeO_{1.5}{\cdot}bMnO_2$ system can hydrate fully at room temperature within a short time, but $Ca_2Fe_2O_5$ and $Ca_3Fe_{1.5}Mn_{1.5}O_8$ were difficult to hydrate.

In BOF slag, the volume expansion rates of tricomponent f-CaO of $CaO{\cdot}aFeO_x{\cdot}bMnO_y$ system changed with different proportions of CaO and solid solutions CaO-FeO_x and CaO-FeO_x-MnO_y. The hydration activity sequence of monocomponent f-CaO and tricomponent f-CaO of $CaO{\cdot}aFeO_x{\cdot}bMnO_y$ system was solid solutions CaO-FeO_x and CaO-FeO_x-MnO_y in tricomponent f-CaO < CaO in tricomponent f-CaO < monocomponent f-CaO. If f-CaO can make contact with H_2O during the hydration process of CBS, only CaO-FeO_x and CaO-FeO_x-MnO_y in bicomponent f-CaO, due to its low hydration activity, will lead to volume expansion after the CBS hardens. The reason why solid solutions CaO-FeO_x and CaO-FeO_x-MnO_y were difficult to hydrate was that their hydration reaction driving force, the absolute value of standard molar reaction Gibbs function, decreased.

Competing Interests

The authors declare that there is no conflict of interests regarding the publication of this paper.

Acknowledgments

The authors acknowledge the support from National Natural Science Foundation of China (Grant no. 51174011) and the Research Fund of Collaborative Innovation Center for Ecological Building Materials and Environmental Protection Equipments (Grant no. YCXT201613).

References

[1] F. H. Han, Z. Q. Zhang, D. M. Wang, and P. Yan, "Hydration heat evolution and kinetics of blended cement containing steel slag at different temperatures," *Thermochimica Acta*, vol. 605, pp. 43–51, 2015.

[2] Opsteel.cn, "Analysis of steel production through diagram," 2015, http://www.opsteel.cn/news/2015-01/0DBFD459DAF8413DE050080A7DC97F83.html.

[3] H. Yi, G. P. Xu, and H. G. Cheng, "An overview of utilization of steel slag," *Procedia Environmental Sciences*, vol. 16, pp. 791–801, 2012.

[4] W. Chen, J. Hong, and C. Xu, "Pollutants generated by cement production in China, their impacts, and the potential for environmental improvement," *Journal of Cleaner Production*, vol. 103, pp. 61–69, 2015.

[5] Q. Wang, J. W. Yang, and P. Y. Yan, "Influence of initial alkalinity on the hydration of steel slag," *Science China Technological Sciences*, vol. 55, no. 12, pp. 3378–3387, 2012.

[6] Q. Wang and P. Yan, "Hydration properties of basic oxygen furnace steel slag," *Construction and Building Materials*, vol. 24, no. 7, pp. 1134–1140, 2010.

[7] Q. Wang, P. Yan, J. Yang, and B. Zhang, "Influence of steel slag on mechanical properties and durability of concrete," *Construction and Building Materials*, vol. 47, pp. 1414–1420, 2013.

[8] G. Wang, Y. Wang, and Z. Gao, "Use of steel slag as a granular material: volume expansion prediction and usability criteria," *Journal of Hazardous Materials*, vol. 184, no. 1–3, pp. 555–560, 2010.

[9] G. Wang, "Determination of the expansion force of coarse steel slag aggregate," *Construction and Building Materials*, vol. 24, no. 10, pp. 1961–1966, 2010.

[10] American Society for Testing and Materials, "Standard test method for potential expansion of aggregate from hydration reactions," ASTM D4792-00p, 2006.

[11] M. S. Tang, M. Q. Yuan, and X. Shen, "The crystalline state of MgO, FeO and MnO in steel slag and the soundness of steel slag cement," *Journal of the Chinese Ceramic Society*, vol. 7, pp. 35–46, 1979 (Chinese).

[12] X.-K. Hou, D.-L. Xu, B. Xue, and H.-S. Li, "Study on volume stability problems of cement caused by steel slag," *Journal of Building Materials*, vol. 15, no. 5, pp. 588–595, 2012 (Chinese).

[13] H. S. Shi, "Microstructure and hydration activity of CaO," *Journal of the Chinese Ceramic Society*, vol. 22, pp. 117–123, 1994 (Chinese).

[14] W.-T. Kuo, C.-Y. Shu, and Y.-W. Han, "Electric arc furnace oxidizing slag mortar with volume stability for rapid detection," *Construction and Building Materials*, vol. 53, pp. 635–641, 2014.

[15] W.-T. Kuo and C.-Y. Shu, "Application of high-temperature rapid catalytic technology to forecast the volumetric stability behavior of containing steel slag mixtures," *Construction and Building Materials*, vol. 50, pp. 463–470, 2014.

[16] E. Belhadj, C. Diliberto, and A. Lecomte, "Properties of hydraulic paste of basic oxygen furnace slag," *Cement and Concrete Composites*, vol. 45, pp. 15–21, 2014.

[17] L. B. Liao and G. Z. Xia, *Crystal Chemistry and Crystal Physics*, Science Press, Beijing, China, 2013 (Chinese).

[18] P. S. Liu, *The Foundation of Crystal Point Defect*, Science Press, Beijing, China, 2010 (Chinese).

[19] S. T. Li, X. L. Qiao, J. G. Chen, H. S. Wang, F. Jia, and X. L. Qiu, "Effects of temperature on indium tin oxide particles synthesized by co-precipitation," *Journal of Crystal Growth*, vol. 289, no. 1, pp. 151–156, 2006.

[20] A. Q. Ma, Y. Ren, and F. Duan, *The Foundation of Inorganic Nonmetallic Material Science*, Metallurgical Industry Press, Beijing, China, 2010, 2010 (Chinese).

[21] T. Higuchi, M. Eguchi, M. Morioka, and E. Sakai, "Hydration and properties of expansive additive treated high temperature carbonation," *Cement and Concrete Research*, vol. 64, pp. 11–16, 2014.

[22] T. Sugiyama, *Metal Oixide and Catalysis*, Press of University of Science and Technology of China, Hefei, China, 1991 (Chinese).

Hindawi Publishing Corporation
Advances in Materials Science and Engineering
Volume 2016, Article ID 7645954, 8 pages
http://dx.doi.org/10.1155/2016/7645954

Research Article

Fractal Modeling of Pore Structure and Ionic Diffusivity for Cement Paste

Yun Gao,[1] Jin-yang Jiang,[1] and Kai Wu[2]

[1]*School of Materials Science and Engineering, Southeast University, Nanjing 211189, China*
[2]*School of Materials Science and Engineering, Tongji University, Shanghai 201804, China*

Correspondence should be addressed to Yun Gao; gaoyun3888@126.com

Received 27 July 2016; Revised 17 October 2016; Accepted 16 November 2016

Academic Editor: Kazunori Fujikake

Pore structure in cement based composites is of paramount importance to ionic diffusivity. In this paper, pore structure in cement paste is modeled by means of the recently proposed solid mass fractal model. Moreover, an enhanced Maxwell homogenization method that incorporates the solid mass fractal model is proposed to determine the associated ionic diffusivity. Experiments are performed to validate the modeling, that is, mercury intrusion porosimetry and rapid chloride migration. Results indicate that modeling agrees well with those obtained from experiments.

1. Introduction

Ionic (i.e., chloride ion) diffusivity is one of the critical parameters in service life design of cement based composites for coastal infrastructures [1]. In recent years, much attention has been drawn to the direct assessment of ionic diffusivity on a basis of pore structure which could be obtained from experiment or modeling [2]. However, a practical challenge still exists as a result of the intrinsic complexity of cement based composites. In particular, the pore size distribution may range from nanometer (C-S-H gel pore) to micrometer (capillary pore) of several orders [3]. The multiscale approach is therefore an option, which deals with C-S-H gel and capillary pore in terms of the packing of basic globules and hydration products, respectively [4, 5]. Nevertheless, as it has to assign a large number of parameters and assumptions, the multiscale approach often leads to substantial disadvantages in efficiency and viability. More robust approaches would be beneficial to describe the complex pore structure as well as ionic diffusivity for cement based composites.

The fractal characters have been recognized among natural and artificial porous materials such as limes, soils, rocks, and ceramics [6–10]. In essence, fractal describes a natural phenomenon or object that exhibits similar pattern at different scales [11]. Usually, if one-dimensional length of fractal is magnified, the occupied space of fractal is then magnified by a noninteger power. This power is called the fractal dimension. For a fractal phenomenon or object, the character of similarity at different scales facilitates property characterization.

In an early work, Winslow reported the fractal nature of internal surface for cement paste [12]. Thereafter, the fractal characters in cement paste have been discussed a lot during past decades [13–20]. It was revealed that three types of fractal might be present in cement paste, that is, the pore mass fractal, the pore surface fractal, and the solid mass fractal [21]. Based on the fractal geometry theory, the complex pore structure in cement paste could be modeled via simple iterations, as done in literatures [9, 10, 17, 21]. Moreover, the fractal geometry theory was able to account for various transport properties for porous materials such as permeability [22, 23] and electrical or thermal conductivity [24–28]. In this regard, the fractal modeling shows a great potential to well describe the complex pore structure as well as ionic diffusivity for cement based composites.

In this paper, pore structure in cement paste is modeled by means of the recently proposed solid mass fractal model [21]. Moreover, an enhanced Maxwell homogenization method that incorporates the solid mass fractal model is proposed to determine the associated ionic diffusivity.

Figure 1: Schematic illustration of the solid mass fractal model with $E = 2$, $n = 3$, and $b = 5$. Gray denotes the iterating phase and black denotes the pore phase.

Experiments are performed to validate the modeling, that is, mercury intrusion porosimetry (MIP) and rapid chloride migration (RCM).

2. Solid Mass Fractal Model

As shown in Figure 1, for the solid mass fractal to model porous medium, the generator refers to two distinct phases, that is, the pore phase and the iterating phase. At the initial step, a blank region with linear length L is defined in E-dimension Euclidean space which can further be divided into N identical subregions. Let n be the number of subregions in each dimension such that $N = n^E$. Moreover, let w and b, respectively, be the proportion and number of iterating phase in the generator such that $b = wN$. Upon successive iterations, the pattern of generator is repeated for the iterating phase at different scales. The generated pore structure can be analyzed as follows.

Step 1. The number of iterating phase and pore phase with the size $a_1 = L/n$ reads wN and $(1 - w)N$, respectively.

Step 2. The number of iterating phase and pore phase with the size $a_2 = L/n^2$ reads $(wN)^2$ and $(1 - w)wN^2$, respectively.

Step i. The number of iterating phase and pore phase with the size $a_i = L/n^i$ reads $(wN)^i$ and $(1 - w)N^i w^{(i-1)}$, respectively.

For the generated porous medium, the solid fraction or density χ is defined as the ratio of solid volume to the total volume that

$$\chi = \frac{V_{\text{tot}} - V}{V_{\text{tot}}}, \tag{1}$$

where V_{tot} is the total volume and V is the resultant volume of pore phase. As a result, the solid fraction at Step i of iteration holds that $\chi_i = w^i$. If a constant $D = \log(Nw)/\log(n)$ is defined, the solid fraction χ_i can then be rewritten as follows with respect to $a_i = L/n^i$ and $N = n^E$:

$$\chi_i = \left(\frac{a_i}{L}\right)^{E-D}. \tag{2}$$

Equation (2) suggests that the generated porous medium is a solid mass fractal with the dimension of D. In a log-log diagram, the linearity shall be detected for the solid fraction χ_i against the pore size a_i. In addition, the pore size distribution in terms of f versus a_i, that is, the cumulative porosity f that counts from the large to the small pores, can be expressed as follows:

$$f\left(\geq a_i\right) = 1 - \chi_i = 1 - \left(\frac{a_i}{L}\right)^{E-D}. \tag{3}$$

3. Modeling of Pore Structure

The MIP test was performed to validate the solid mass fractal model [29]. Figure 2 shows the pore size distribution of cement paste with water cement (w/c) of 0.4 and age of 28 days, which was cured at the condition of 95% ± 10% relative humidity and 20°C ± 1°C temperature. For the solid fractal mass model, solid fraction is plotted against pore diameter in the log-log diagram, as shown in Figure 3. It can be noted that the sound piecewise linearity exists. Moreover, the slope of linearity varies within two pore ranges. Let d_{low} and d_{upp} be the lower and upper limit of pore diameter, and let d_{thr} be the threshold of pore diameter for the two pore ranges. The values of d_{low}, d_{thr}, and d_{upp} can be determined as $d_{\text{low}} = 0.004\,\mu$m, $d_{\text{thr}} = 0.1\,\mu$m, and $d_{\text{upp}} = 2\,\mu$m. In other words, the two pore ranges, that is, the large and the small pore range, are located as $d_{\text{upp}} \sim d_{\text{thr}}$ and $d_{\text{thr}} \sim d_{\text{low}}$, that is, $2 \sim 0.1\,\mu$m and $0.1 \sim 0.004\,\mu$m. The large pore range corresponds to capillary pores, while the small pore range corresponds to C-S-H gel pores.

With the determined pore ranges ($d_{\text{upp}} \sim d_{\text{thr}}$, $d_{\text{thr}} \sim d_{\text{low}}$), the least square method is then applied to fit the associated slopes ($k_{\text{upp}} = 0.0206$, $k_{\text{low}} = 0.0607$) as well as

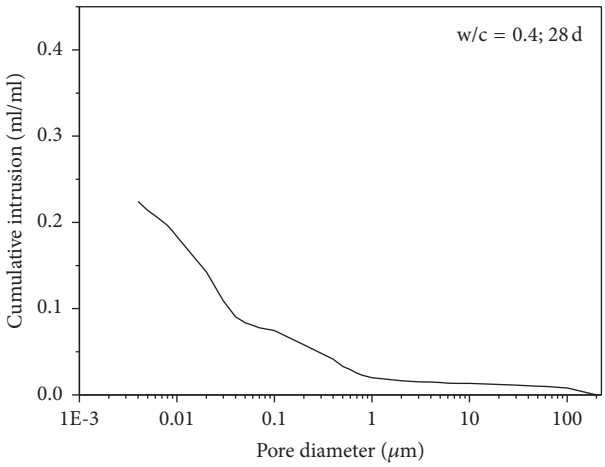

Figure 2: Porosimetric data example: cumulative intrusion volume against pore diameter.

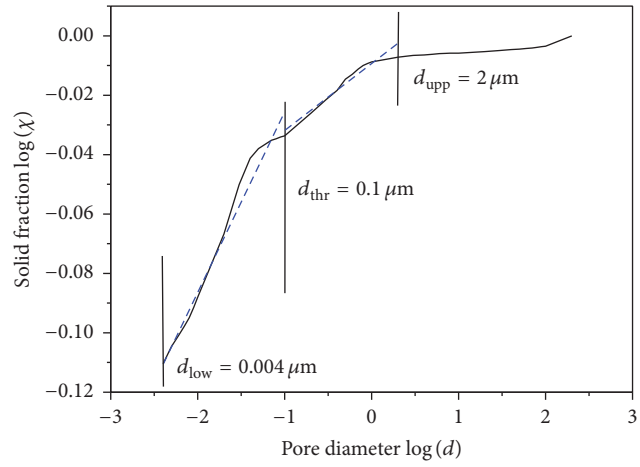

Figure 3: Parametric analysis: log-log diagram of solid fraction against pore diameter.

the fractal dimensions (D_{upp} = 2.9794, D_{low} = 2.9393) since $D_{upp} = E - k_{upp}$, $D_{low} = E - k_{low}$, and $E = 3$. Meanwhile, it is possible to specify the partial porosity of large and small pore range (f_{upp} = 0.0746, f_{low} = 0.1497) with the total porosity f holding that $f = f_{upp} + f_{low}$. In rough comparison, the fractal dimension of small pore range is smaller than that of large pore range, that is, $D_{low} < D_{upp}$. The partial porosity of small pore range is larger than that of large pore range, that is, $f_{low} > f_{upp}$. The fractal modeling of pore structure in cement paste refers to two specific structures, that is, two fractal generators for the large and the small pore range.

For the large pore range, let two integers i_{upp} and n_{upp} be the step of iterations and the number of subregions such that $i_{upp} = \log(d_{upp}/d_{thr})/\log(n_{upp})$. The solid mass fractal model requires $n_{upp} \geq 2$, $i_{upp} \geq 2$, and $n_{upp}\cdot\hat{}D_{upp} \geq 1$. In this paper, the symbol $\cdot\hat{}$ denotes the power operator. Without complicated mathematical analysis, it leads to $n_{upp} = 4$ and $i_{upp} = 3$. The value of w_{upp} is obtained via $\log(w_{upp}) = (D_{upp} - 3)\cdot\log(n_{upp})$. The number of iterating phase b_{upp} holds that $b_{upp} = w_{upp}\cdot(n_{upp})^3$. The intrinsic porosity of generated pore structure f^*_{upp} holds that $f^*_{upp} = 1 - [b_{upp}/(n_{upp})^3]\cdot\hat{}i_{upp}$. Details of analysis for the example are shown as follows:

The large pore range: $n_{upp} = 4$, $i_{upp} = 3$

The proportion of iterating phase: $w_{upp} = n_{upp}\cdot\hat{}(D_{upp} - 3) = 4\cdot\hat{}(-0.0206) = 0.9718$

The number of iterating phases: $b_{upp} = w_{upp}\cdot(n_{upp})^3 = 0.9718 * 4\cdot\hat{}3 = 62$

The intrinsic porosity: $f^*_{upp} = 1 - [b_{upp}/(n_{upp})^3]\cdot\hat{}i_{upp} = 1 - (62/64)\cdot\hat{}3 = 0.0909$

For the small pore range, let two integers i_{low} and n_{low} be the step of iterations and the number of subregions, which holds that $i_{low} = \log(d_{thr}/d_{low})/\log(n_{low})$. The solid mass fractal model requires $n_{low} \geq 2$, $i_{low} \geq 2$, and $n_{low}\cdot\hat{}D_{low} \geq 1$. It leads to $n_{low} = 3$ and $i_{low} = 3$. The value of w_{low} is obtained via $\log(w_{low}) = (D_{low} - 3)\cdot\log(n_{low})$. The number of iterating phase b_{low} holds that $b_{low} = w_{low}\cdot(n_{low})^3$. The intrinsic porosity of generated pore structure f^*_{low} holds that $f^*_{low} = 1 - [b_{low}/(n_{low})^3]\cdot\hat{}i_{low}$. Details of analysis for the example are shown as follows:

The small pore range: $n_{low} = 3$, $i_{low} = 3$

The proportion of iterating phase: $w_{low} = n_{low}\cdot\hat{}(D_{low} - 3) = 3\cdot\hat{}(-0.0607) = 0.9355$

The number of iterating phases: $b_{low} = w_{low}\cdot(n_{low})^3 = 0.9355 * 3\cdot\hat{}3 = 25$

The intrinsic porosity: $f^*_{low} = 1 - [b_{low}/(n_{low})^3]\cdot\hat{}i_{low} = 1 - (25/27)\cdot\hat{}3 = 0.2062$

The build-up of pore structure in cement paste follows from the large to the small pore range. In particular, after i_{upp} steps of iteration to generate the large pore range, the size and number of iterating phase is d_{thr} and $(b_{upp})\cdot\hat{}i_{upp}$, respectively. *Note that during the process to generate the small pore range, not all the iterating phases with size of* d_{thr} *are to be further iterated but a proportion of* γ ($\gamma \leq 1$). In other words, the $1-\gamma$ proportion of iterating phases with size of d_{thr} shall not be performed with further iterations. With respect to the chemical composition of cement paste, such γ and $1 - \gamma$ proportion of iterating phases are introduced as C-S-H gel and solid phases, respectively. The solid phases may be anhydrous cement, calcium hydroxide crystal, Aft, and gypsum. It is necessary to determine γ to fulfill the build-up of pore structure in cement paste. Herewith, consider the total porosity f satisfying $f = f^*_{upp} + f^*_{low}\cdot\gamma\cdot(w_{upp})\cdot\hat{}i_{upp}$. Then, f = 0.2243, f^*_{upp} = 0.0909, f^*_{low} = 0.2062, w_{upp} = 0.9718, and $i_{upp} = 3$ lead to γ = 0.7115. Figure 4 shows one realization of modeled pore structure in cement paste. In particular, it refers to two specific structures, that is, the capillary structure and the C-S-H gel structure. The capillary structure of large pore range consists of three phases, that is, the (capillary) pore phase, the solid phase (anhydrous cement, calcium hydroxide crystal, AFt, and gypsum), and the C-S-H gel phase. The C-S-H gel structure of small pore range consists of two phases, that

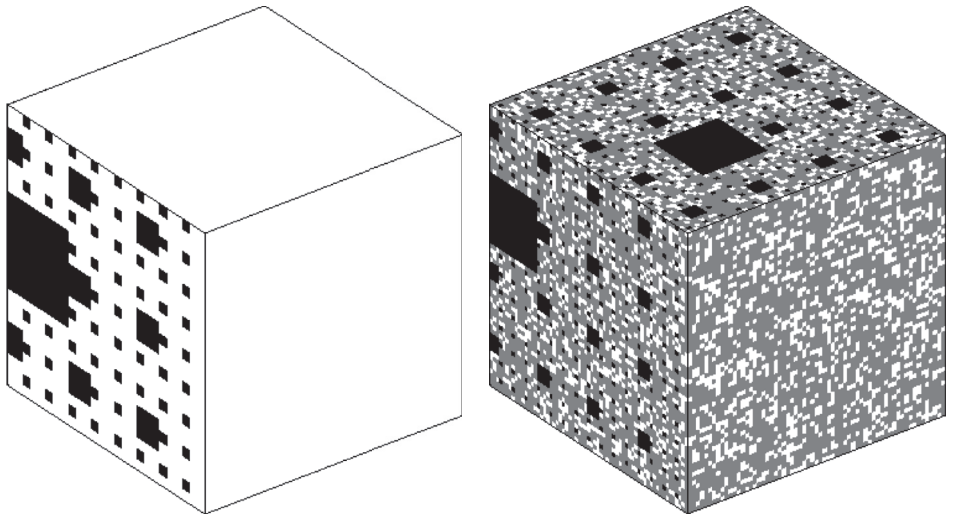

(a) (b)

Figure 4: Realization of pore structure in cement paste (a) C-S-H gel structure ($n_{low} = 3$, $i_{low} = 3$, $b_{low} = 25$) with element size of 0.004 μm; (b) capillary structure of cement paste ($n_{upp} = 4$, $i_{upp} = 3$, $b_{upp} = 62$, $\gamma = 0.7115$) with element size of 0.1 μm. Black denotes the pore phase, white denotes the solid phase, and gray denotes the C-S-H gel phase.

is, the (gel) pore phase and the solid phase (molecule layers within C-S-H gel). The pore size distribution can be written in terms of the piecewise form:

$$\text{for } d > d_{thr},\ d = d_{upp}/(n_{upp}.\hat{}\, j),\ f(\geq d) = 1 - w_{upp}.\hat{}\, j,\ j = 1, \ldots, i_{upp};$$

$$\text{for } d \leq d_{thr},\ d = d_{thr}/(n_{low}.\hat{}\, j),\ f(\geq d) = (1 - w_{upp}.\hat{}\, i_{upp}) + (1 - w_{low}.\hat{}\, j) \cdot \gamma \cdot (w_{upp}.\hat{}\, i_{upp}),\ j = 1, \ldots, i_{low}.$$

In particular, for example, it holds that

$$\text{for } d > 0.1\,\mu\text{m},\ d = d_{upp}/(4.\hat{}\, j),\ f(\geq d) = 1 - (62/64).\hat{}\, j,\ j = 1, 2, 3;$$

$$\text{for } d \leq 0.1\,\mu\text{m},\ d = d_{thr}/(3.\hat{}\, j),\ f(\geq d) = 1 - (62/64).\hat{}\, 3 + [1 - (25/27).\hat{}\, j] \cdot \gamma \cdot (62/64).\hat{}\, 3,\ j = 1, 2, 3.$$

4. Enhanced Maxwell Homogenization Method

The calculation of effective properties of heterogeneous materials that contain inclusions of diverse shape and/or properties withstands a long history. Numerous homogenization schemes have been developed so far [30–32]. Among them, the Maxwell homogenization method is probably the oldest and also most famous one [33]. It considers heterogeneous materials with unknown effective ionic diffusivity (D_{eff}) consisting of bulk phase with ionic diffusivity (D_B) and inclusion phase with ionic diffusivity (D_I). Mathematically, the Maxwell homogenization method can be described as follows:

$$D_{eff} = \frac{D_I + 2D_B + 2(D_I - D_B)c}{D_I + 2D_B - (D_I - D_B)c} D_B, \tag{4}$$

where c is the volume fraction of inclusions.

An enhanced Maxwell homogenization method is proposed that incorporates the solid mass fractal model to calculate ionic diffusivity of cement paste. In particular, cement paste is viewed as the composite material consisting of two phases. One refers to the low-diffusivity C-S-H gel structure being bulk. The other refers to the high-diffusivity capillary structure being inclusions. The treatment of two distinct phases was also applied in the general effective media theory [34–36]. For bulk (C-S-H gel structure) and inclusion (capillary structure), the associated ionic diffusivity can be approximated in a power form of intrinsic porosity [37, 38]:

$$D_B = \gamma D_1 \left(f^*_{low}\right)^{\delta_1},$$
$$D_I = D_2 \left(f^*_{upp}\right)^{\delta_2}, \tag{5}$$

where D_1 and D_2 are constants, that is, ionic diffusivities in water corresponding to C-S-H gel and capillary structures. δ_1 and δ_2 are the cementation exponent in Archie's law for C-S-H gel and capillary structures. Other parameters, that is, f^*_{upp}, f^*_{low}, and γ are defined in the solid mass fractal model. In addition, the volume fraction of inclusions is derived from

$$c = \frac{f_{upp}}{f_{upp} + f_{low}}. \tag{6}$$

As presented above, the Maxwell homogenization method is enhanced with critical parameters determined from the solid mass fractal model and Archie's law. Then, the enhanced Maxwell homogenization method can be applied to predict effective ionic diffusivity of cement paste.

5. Rapid Chloride Migration Test

The RCM test was performed to measure ionic (chloride) diffusivity of cement paste [39, 40]. Cement paste samples

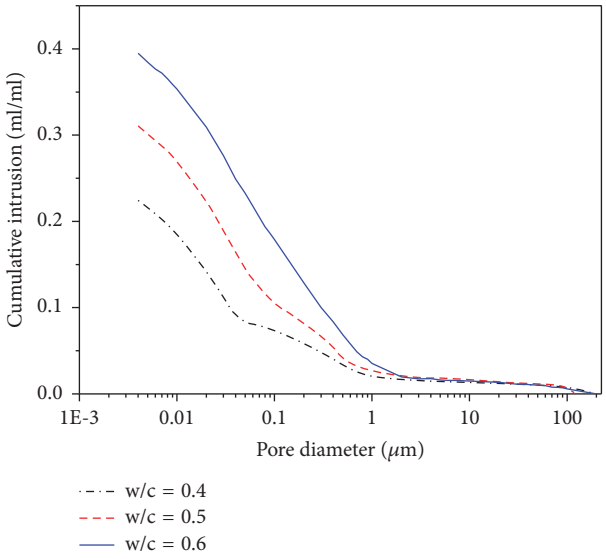

Figure 5: Porosimetric data of cement pastes with varying w/c ratios.

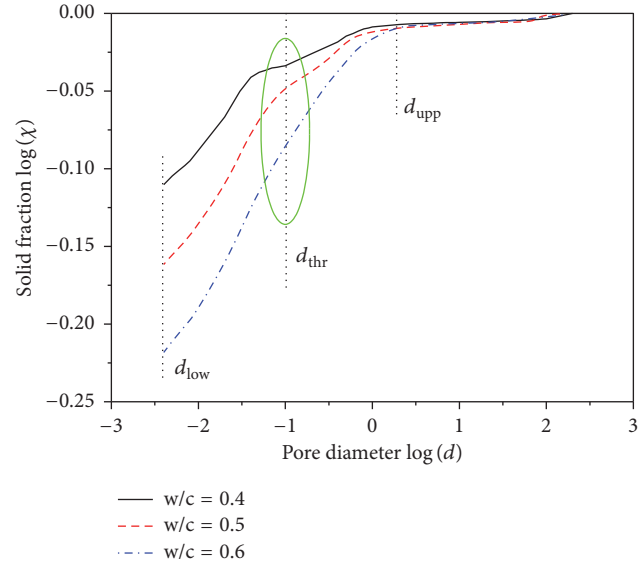

Figure 6: Parametric analysis of cement pastes with varying w/c ratios.

of 50 mm in thickness and 100 mm in diameter were prepared. Samples were then subjected to the vacuum saturation treatment. The saturated samples were treated to be surface-dry. Three samples of replicates were tested at the same time. Power sources with constant voltage outputs (adjustable in the range of 0 ~ 80 V, accuracy of 0.05 V) were applied. The used catholyte and anolyte were 10% NaCl solution and 0.3 M NaOH solution, respectively. The electrolytes were refreshed after each series of tests. After the migration test, the samples were split and sprayed with a 0.1 M $AgNO_3$ solution in order to determine the penetration depth of chlorides. The non-steady-state migration coefficient D_{RCM}, that is, ionic (chloride) diffusivity, was calculated according to the NT Build 492 as follows:

$$D_{RCM} = \frac{0.0239\,(273+T)\,l}{(U-2)\,t_d}\left(x_d - 0.0238\sqrt{\frac{(273+T)\,l x_d}{U-2}}\right), \quad (7)$$

where D_{RCM} is the non-steady-state migration coefficient, $\times 10^{-12}$ m^2/s; U is absolute value of the applied voltage, V; T is average value of the initial and final temperatures in the anolyte solution, °C; l is thickness of the specimen, mm; x_d is average value of the penetration depth, mm; and t_d is the test duration, h.

6. Results and Discussions

Cement pastes with w/c ratios of 0.4, 0.5, and 0.6 were compared, as shown in Figure 5. All samples were cured at the same condition (28 days, 95% ± 10% relative humidity, 20°C ± 1°C temperature). Figure 6 shows the parametric analysis with respect to the solid mass fractal model. Results

Table 1: Fractal dimensions and the associated porosities.

w/c ratio	D_{low}	f_{low}	D_{upp}	f_{upp}
0.4	2.9393	0.1497	2.9794	0.0746
0.5	2.9089	0.1769	2.9701	0.1052
0.6	2.9008	0.2161	2.9467	0.1789

Table 2: Parameters of the solid mass fractal model.

w/c ratio	b_{low}	n_{low}	i_{low}	γ	b_{upp}	n_{upp}	i_{upp}
0.4	25			0.7115	62		
0.5	24	3	3	0.8123	62	4	3
0.6	24			0.8928	60		

Table 3: Parameters used for the enhanced Maxwell homogenization method.

D_1	D_2	δ_1	δ_2
1.25×10^{-10} m^2/s	1.25×10^{-9} m^2/s	1.8	1.5

are summarized in Tables 1 and 2. Table 1 suggests that as w/c ratio increases, the partial porosities (f_{upp}, f_{low}) increase, while the fractal dimensions (D_{upp}, D_{low}) decrease. Table 2 suggests that some parameters, that is, n_{low}, i_{low}, n_{upp}, and i_{upp}, do not change with w/c ratio, while some parameters, that is, b_{upp}, b_{low}, and γ, do. That means the three parameters (b_{upp}, b_{low}, γ) are critical to characterize the effect of w/c ratio on geometry of capillary and C-S-H gel structure. Figure 7 shows the comparison of modeled and measured pore size distributions of cement pastes.

With the enhanced Maxwell homogenization method, ionic diffusivity of cement paste can be obtained. The parameters listed in Tables 1 and 2 are used, that is, (f_{upp}, f_{low}) and (n_{low}, i_{low}, n_{upp}, i_{upp}, b_{upp}, b_{low}, γ). Besides, values of the parameters ($D_1, D_2, \delta_1, \delta_2$) are suggested in Table 3. In

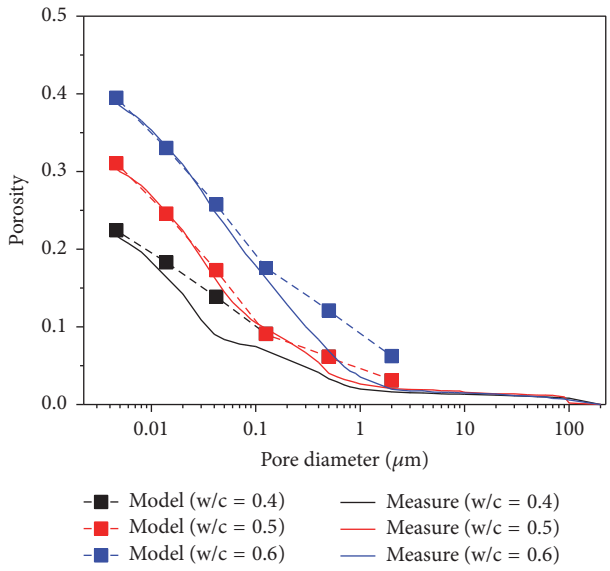

FIGURE 7: Modeled and measured pore size distribution of cement pastes with varying w/c ratios.

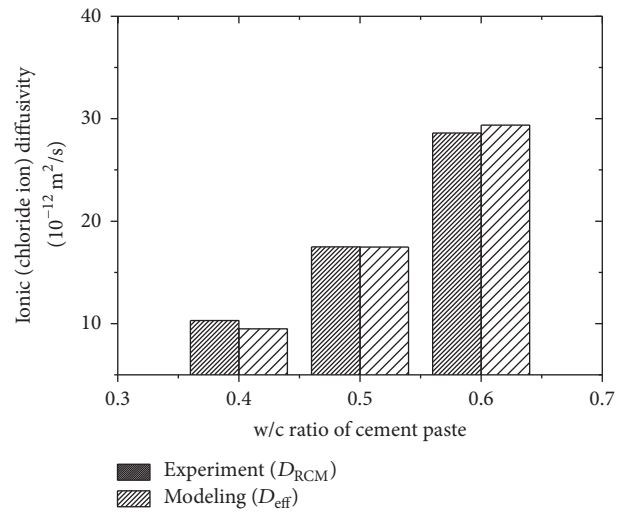

FIGURE 8: Modeled and measured ionic diffusivity of cement pastes with varying w/c ratios.

TABLE 4: Parameters measured in RCM test of cement pastes.

w/c ratio	T (°C)	U (V)	t_d (hour)	l (mm)	x_d (mm)
0.4	26.0	25	24	49.6	18.7
0.5	25.1	15	24	49.8	18.9
0.6	23.5	15	24	50.2	29.5

particular, $D_1 = 1.25 \times 10^{-10}$ m^2/s is empirical. It leads to the ionic (chloride) diffusivity of C-S-H gel around 8×10^{-12} m^2/s, which is comparable to the value suggested in [41]. $D_2 = 1.25 \times 10^{-9}$ m^2/s is taken after [42]. The cementation exponents of $\delta_1 = 1.8$ and $\delta_2 = 1.5$ for C-S-H gel and capillary structures are suggested from extensive tests, which differs from the usual range of 1.8–2.0 for consolidated sandstones [37].

For the RCM test, the measured parameters are listed in Table 4, which leads to an easy calculation of the non-steady-state migration coefficient D_{RCM}. As shown in Figure 8, results of the fractal modeling (D_{eff}) agree well with those obtained from experiment (D_{RCM}). In this regard, the present fractal modeling provides an optional description of pore structure as well as ionic diffusivity for cement paste.

7. Concluding Remarks

In this paper, modeling of pore structure as well as ionic diffusivity for cement paste is performed based on the fractal geometry theory. The solid mass fractal model is applied to model pore structure, and an enhanced Maxwell homogenization method that incorporates the solid mass fractal model is proposed to calculate the associated ionic diffusivity. Some general conclusions are drawn as follows:

(1) The solid mass fractal model well describes pore structure in cement paste in terms of two pore ranges, that is, the large (capillary) and the small (C-S-H gel) pore range. The fractal generator varies with the pore range.

(2) The enhanced Maxwell homogenization method considers cement paste consisting of low-diffusivity C-S-H gel structure and high-diffusivity capillary structure. Archie's law is applicable to approximate ionic diffusivity for C-S-H gel and capillary structures.

Nomenclature

L: Linear length of modeling space
E: Dimension of Euclidean space
N: Total number of identical subregions
n: Number of identical subregions in one dimension
w: Proportion of iterating phase in generator
b: Number of iterating phases in generator
i: Step of iteration
a_i: Size of iterating phase
χ: Solid fraction or density
V_{tot}: Total volume of porous medium
V: Volume of pore phase
D: Fractal dimension
f: Cumulative porosity f that counts from large to small pore
d: Equivalent pore diameter
d_{low}, d_{thr}, d_{upp}: Lower, threshold, and upper limit of equivalent pore diameter
k_{upp}, k_{low}: Slope of large and small pore range
D_{upp}, D_{low}: Fractal dimension of large and small pore range

f_{upp}, f_{low}: Partial porosity of large and small pore range
i_{upp}, i_{low}: Step of iteration to generate large and small pore range
n_{upp}, n_{low}: One-dimension number of subregions for large and small pore range
w_{upp}, w_{low}: Proportion of iterating phase in generator for large and small pore range
b_{upp}, b_{low}: Number of iterating phases in generator for large and small pore range
f^*_{upp}, f^*_{low}: Intrinsic porosity of large and small pore range
γ: Proportion of iterating phase being C-S-H gel
D_{eff}: Effective ionic diffusivity of porous medium
D_B, D_I: Ionic diffusivity of bulk and inclusion phase
c: Volume fraction of inclusions
D_1, D_2: Ionic diffusivity in water corresponding to gel and capillary pore
δ: Cementation exponent in Archie's law
D_{RCM}: Non-steady-state migration coefficient
U: Absolute value of the applied voltage
T: Average value of the initial and final temperatures in anolyte solution
l: Thickness of the specimen
x_d: Average value of the penetration depth
t_d: Test duration.

Competing Interests

The authors declare that they have no competing interests.

Acknowledgments

The authors gratefully acknowledge the financial support from Key Basic Research Project (Grant No. 2015CB655105), State Key Laboratory for Track Technology of High-speed Railway (Grant no. 2014G004-F), and Jiangsu Natural Science Foundation (Grant no. BK20150621).

References

[1] L. Tang, "Electrically accelerated methods for determining chloride diffusivity in concrete—current development," *Magazine of Concrete Research*, vol. 48, no. 176, pp. 173–179, 1996.

[2] E. J. Garboczi and D. P. Bentz, "Multiscale analytical/numerical theory of the diffusivity of concrete," *Advanced Cement Based Materials*, vol. 8, no. 2, pp. 77–88, 1998.

[3] H. M. Jennings, J. W. Bullard, J. J. Thomas, J. E. Andrade, J. J. Chen, and G. W. Scherer, "Characterization and modeling of pores and surfaces in cement paste: correlations to processing and properties," *Journal of Advanced Concrete Technology*, vol. 6, no. 1, pp. 5–29, 2008.

[4] K. Maekawa, T. Ishida, and T. Kishi, "Multiscale modeling of concrete performance integrated material and structural mechanics," *Journal of Advanced Concrete Technology*, vol. 1, no. 2, pp. 91–126, 2003.

[5] G. W. Sun, W. Sun, Y. S. Zhang, and Z. Y. Liu, "Prediction of the effective diffusion coefficient of chloride ions in cement-based composite materials," *Journal of Materials in Civil Engineering*, vol. 24, no. 9, pp. 1245–1253, 2012.

[6] D. Giménez, E. Perfect, W. J. Rawls, and Y. Pachepsky, "Fractal models for predicting soil hydraulic properties: a review," *Engineering Geology*, vol. 48, no. 3-4, pp. 161–183, 1997.

[7] J. L. Pérez Bernal and M. A. Bello, "Fractal geometry and mercury porosimetry. Comparison and application of proposed models on building stones," *Applied Surface Science*, vol. 185, no. 1-2, pp. 99–107, 2001.

[8] M. Arandigoyen, J. L. Perez Bernal, M. A. Bello López, and J. I. Alvarez, "Lime-pastes with different kneading water: pore structure and capillary porosity," *Applied Surface Science*, vol. 252, no. 5, pp. 1449–1459, 2005.

[9] C. Atzeni, G. Pia, and U. Sanna, "Fractal modelling of medium-high porosity SiC ceramics," *Journal of the European Ceramic Society*, vol. 28, no. 14, pp. 2809–2814, 2008.

[10] C. Atzeni, G. Pia, U. Sanna, and N. Spanu, "A fractal model of the porous microstructure of earth-based materials," *Construction and Building Materials*, vol. 22, no. 8, pp. 1607–1613, 2008.

[11] B. B. Mandelbrot, P. Pfeifer, O. Biham, O. Malcai, D. A. Lidar, and D. Avnir, "Is nature fractal?" *Science*, vol. 279, no. 5352, pp. 783–786, 1998.

[12] D. N. Winslow, "The fractal nature of the surface of cement paste," *Cement and Concrete Research*, vol. 15, no. 5, pp. 817–824, 1985.

[13] D. Pearson and A. J. Allen, "A study of ultrafine porosity in hydrated cements using small angle neutron scattering," *Journal of Materials Science*, vol. 20, no. 1, pp. 303–315, 1985.

[14] M. Kriechbaum, G. Degovics, J. Tritthart, and P. Laggner, "Fractal structure of portland cement paste during age hardening analyzed by small-angle X-ray scattering," *Progress in Colloid and Polymer Science*, vol. 79, pp. 101–105, 1989.

[15] D. A. Lange, H. M. Jennings, and S. P. Shah, "Image analysis techniques for characterization of pore structure of cement-based materials," *Cement and Concrete Research*, vol. 24, no. 5, pp. 841–853, 1994.

[16] D. N. Winslow, J. M. Bukowski, and J. F. Young, "The fractal arrangement of hydrated cement paste," *Cement and Concrete Research*, vol. 25, no. 1, pp. 147–156, 1995.

[17] X. Ji, S. Y. N. Chan, and N. Feng, "Fractal model for simulating the space-filling process of cement hydrates and fractal dimensions of pore structure of cement-based materials," *Cement and Concrete Research*, vol. 27, no. 11, pp. 1691–1699, 1997.

[18] A. Heinemann, H. Hermann, and F. Häussler, "SANS analysis of fractal microstructures in hydrating cement paste," *Physica B: Condensed Matter*, vol. 276–278, pp. 892–893, 2000.

[19] Y. Wang and S. Diamond, "A fractal study of the fracture surfaces of cement pastes and mortars using a stereoscopic SEM method," *Cement and Concrete Research*, vol. 31, no. 10, pp. 1385–1392, 2001.

[20] Q. Zeng, K. F. Li, T. Fen-Chong, and P. Dangla, "Surface fractal analysis of pore structure of high-volume fly-ash cement pastes," *Applied Surface Science*, vol. 257, no. 3, pp. 762–768, 2010.

[21] Y. Gao, K. Wu, and J. Jiang, "Examination and modeling of fractality for pore-solid structure in cement paste: starting from the mercury intrusion porosimetry test," *Construction and Building Materials*, vol. 124, pp. 237–243, 2016.

[22] T. J. Miao, B. Yu, Y. G. Duan, and Q. T. Fang, "A fractal analysis of permeability for fractured rocks," *International Journal of Heat and Mass Transfer*, vol. 81, pp. 75–80, 2015.

[23] S. Wang, T. Wu, H. Qi, Q. Zheng, and Q. Zheng, "A permeability model for power-law fluids in fractal porous media composed of arbitrary cross-section capillaries," *Physica A*, vol. 437, pp. 12–20, 2015.

[24] G. Pia and U. Sanna, "Intermingled fractal units model and electrical equivalence fractal approach for prediction of thermal conductivity of porous materials," *Applied Thermal Engineering*, vol. 61, no. 2-3, pp. 186–192, 2013.

[25] W. Wei, J. Cai, X. Hu, and Q. Han, "An electrical conductivity model for fractal porous media," *Geophysical Research Letters*, vol. 42, no. 12, pp. 4833–4840, 2015.

[26] H.-Q. Jin, X.-L. Yao, L.-W. Fan, X. Xu, and Z.-T. Yu, "Experimental determination and fractal modeling of the effective thermal conductivity of autoclaved aerated concrete: effects of moisture content," *International Journal of Heat and Mass Transfer*, vol. 92, pp. 589–602, 2016.

[27] S. Negrelli, R. P. Cardoso, and C. J. Hermes, "A finite-volume diffusion-limited aggregation model for predicting the effective thermal conductivity of frost," *International Journal of Heat and Mass Transfer*, vol. 101, pp. 1263–1272, 2016.

[28] G. Pia, "High porous yttria-stabilized zirconia with aligned pore channels: morphology directionality influence on heat transfer," *Ceramics International*, vol. 42, no. 10, pp. 11674–11681, 2016.

[29] R. A. Cook and K. C. Hover, "Mercury porosimetry of hardened cement pastes," *Cement and Concrete Research*, vol. 29, no. 6, pp. 933–943, 1999.

[30] R. W. Zimmerman, "Elastic moduli of a solid containing spherical inclusions," *Mechanics of Materials*, vol. 12, no. 1, pp. 17–24, 1991.

[31] M. Kachanov, I. Tsukrov, and B. Shafiro, "Effective moduli of solids with cavities of various shapes," *Applied Mechanics Reviews*, vol. 47, no. 1, pp. 151–174, 1994.

[32] S. K. Kanaun and D. Jeulin, "Elastic properties of hybrid composites by the effective field approach," *Journal of the Mechanics and Physics of Solids*, vol. 49, no. 10, pp. 2339–2367, 2001.

[33] I. Sevostianov and A. Giraud, "Generalization of Maxwell homogenization scheme for elastic material containing inhomogeneities of diverse shape," *International Journal of Engineering Science*, vol. 64, pp. 23–36, 2013.

[34] L. Cui and J. H. Cahyadi, "Permeability and pore structure of OPC paste," *Cement and Concrete Research*, vol. 31, no. 2, pp. 277–282, 2001.

[35] J. Zhang and Z. J. Li, "Application of GEM equation in microstructure characterization of cement-based materials," *Journal of Materials in Civil Engineering*, vol. 21, no. 11, pp. 648–656, 2009.

[36] J. Zhao, J.-J. Zheng, and G.-F. Peng, "An effective medium approach for predicting the intrinsic permeability of heated cement paste," *Advances in Cement Research*, vol. 27, no. 4, pp. 240–246, 2015.

[37] G. E. Archie, "Introduction to petrophysics of reservoir rocks," *American Association of Petroleum Geologists Bulletin*, vol. 34, no. 5, pp. 943–961, 1950.

[38] H. S. Salem and G. V. Chilingarian, "The cementation factor of Archie's equation for shaly sandstone reservoirs," *Journal of Petroleum Science and Engineering*, vol. 23, no. 2, pp. 83–93, 1999.

[39] L. Tang and L. Nilsson, "Rapid determination of the 317 chloride diffusivity in concrete by applying an electric field," *ACI Materials Journal*, vol. 89, no. 1, pp. 49–53, 1992.

[40] Z. Yu and G. Ye, "New perspective of service life prediction of fly ash concrete," *Construction and Building Materials*, vol. 48, pp. 764–771, 2013.

[41] E. J. Garboczi and D. P. Bentz, "Computer simulation of the diffusivity of cement-based materials," *Journal of Materials Science*, vol. 27, no. 8, pp. 2083–2092, 1992.

[42] S. Kerisit and C. X. Liu, "Molecular simulations of water and ion diffusion in nanosized mineral fractures," *Environmental Science and Technology*, vol. 43, no. 3, pp. 777–782, 2009.

Hindawi Publishing Corporation
Advances in Materials Science and Engineering
Volume 2016, Article ID 3025213, 14 pages
http://dx.doi.org/10.1155/2016/3025213

Research Article

Experimental Study on Hygrothermal Deformation of External Thermal Insulation Cladding Systems with Glazed Hollow Bead

Houren Xiong,[1,2] Jinming Xu,[1] Yuanzhen Liu,[3] and Shimeng Wang[3]

[1]*Department of Civil Engineering, Shanghai University, Shanghai 200444, China*
[2]*Building Energy Efficiency Technology Laboratory, Jiaxing University, Jiaxing 314001, China*
[3]*College of Architecture and Civil Engineering, Taiyuan University of Technology, Taiyuan 030024, China*

Correspondence should be addressed to Houren Xiong; 104072005@163.com

Received 30 July 2016; Accepted 16 October 2016

Academic Editor: Doo-Yeol Yoo

This research analyzes the thermal and strain behavior of external thermal insulation cladding systems (ETICS) with Glazed Hollow Beads (GHB) thermal insulation mortar under hygrothermal cycles weather test in order to measure its durability under extreme weather (i.e., sunlight and rain). Thermometers and strain gauges are placed into different wall layers to gather thermal and strain data and another instrument measures the crack dimensions after every 4 cycles. The results showed that the finishing coat shrank at early stage (elastic deformation) and then the finishing coat tends to expand and become damaged at later stage (plastic deformation). The deformation of insulation layer is similar to that of the finishing coat but its variation amplitude is smaller. Deformation of substrate expanded with heat and contracted with cold due to the small temperature variation. The length and width of cracks on the finishing coat grew as the experiment progressed but with a decreasing growth rate and the cracks stopped growing around 70 cycles.

1. Introduction

Due to the rapid economic development, there has been a constant increase in the building energy consumption in China. According to the relevant statistics, the building energy consumption accounts for about 30% of the total energy consumption of the society at large [1]. As for a building, according to the statistics, the external walls of a building, or the barriers between the internal and the external parts, roughly account for 45% of the total building external area. The energy dissipated through the walls from the structure enclosure accounts for more than 60% of the energy loss of the entire building [2]. Accordingly, the most effective way of reducing the energy dissipation through the walls is to improve the thermal insulation of its external walls.

Many approaches have been made referred to the thermal insulation systems for the peripheral structures of buildings. Dozens of thermal insulation systems for the external walls of buildings were developed [2–4]. Specifically, by using an insulating layer made of porous inorganic materials, the external thermal insulation composite systems with Glazed Hollow Bead thermal insulation mortar (ETICS GHB) are characterized by the high thermal insulation and fireproof performances. The ETICS GHB have been widely applied in China and many researchers investigated this system in the preparation and molding [5–7], thermal insulation property and shrinkage deformation [8–10], mechanical property [11, 12], and antifrost property [13]. However, only the functional analyses were focused on the GHB mortar or concrete and single material was concerned in most approaches. Little was taken accounted for the ETICS GHB, a system made of laminated composite materials, from their hygrothermal properties [10], especially from durability in a hygrothermal environment.

In practice, due to the heat blocking action of the insulating layer, heat is usually stored in the finishing coat of the ETICS. For instance, in the summer, the temperature of the ETICS finishing coat may reach 70°C. On the other hand, if a rainstorm occurs after several sunny days, the surface temperature may suddenly drop to 50°C [14]. This

temperature change caused by sunshine and rain will reduce the strength and the thermal insulation effect of the materials in the ETICS. The temperature change may also cause hygrothermal deformation of the materials and thereafter result in the damage in the structure (such as cracking of the insulating layer, separation of the insulating layer from the base, and falloff of the finishing coat). These damage affect the normal service of ETICS [15–17]. For this reason, a high temperature-rain simulation test on ETICS, in the current study, was conducted in order to determine the hygrothermal deformation and hygrothermal mechanical properties of the finishing coat material. The test may provide vital scientific and engineering information both in evaluating the reliability and service life of the ETICS and in formulating guidelines for a safe ETICS design.

Many approaches have been made on the hygrothermal deformation of ETICS, Zirkelbach et al. [18] conducted a five-year hygrothermal coupling analysis on the mineral wool ETICS in three European countries with various climatic conditions. He compared the temperature and humidity data from southern Portugal and northern Finland with those measured in central Germany. Zhang et al. [19] used a finite difference method to analyze the temperature stresses in the internal and external thermal insulation walls. Collina and Lignola [20] combined stress-strain to analyze the influence of various stresses (such as shear stress and thermal stress) on the durability of ETICS. Balocco et al. [21] used the finite element software ANSYS to conduct a thermal fatigue study on ETICS. Passa et al. [22] conducted the thermal strain test on various structural layers of EPS thermal insulation systems in oven heating and analyzed the influence of external temperature on the deformation of various structural layers. Yiu et al. [23] used a simple equipment to conduct the hygrothermal cycle test on the small-scale wall test specimens pasted with strain gauges in order to obtain the deformation curves of the concrete, rendering, and tiles. Griciute and Bliudzius [24] conducted the contrast tests in the indoor and natural ageing on ETICS made of three finishing coat materials (i.e., acrylic, silicone, and silicate). They analyzed the change features in the microstructures, ingredients, and water contents of these materials. Daniotti et al. [25] used six cameras to monitor the finishing coat of the ETICS in the accelerated ageing test and recorded the degradation failure phenomena at different deformation stages.

However, the degradation features of various structural layers in the ETICS GHB under hygrothermal cycle are of great importance; few of the existing studies, as we know, focused on these features. In this study, referring to the test method as described in the European standard ETAG 004 [26], a high temperature-rain periodic test was conducted on large-scale ETICS GHB. The temperature sensors and strain gauges were embedded in various structural layers to measure the temperature and strain of various structural layers under hygrothermal cycles. The changes in temperature and strain in various structural layers of the ETICS GHB were also examined. The degradation characteristics of the finishing coat with the number of cycles were thereafter quantitatively investigated.

Table 1: Properties of GHB.

Properties	Values
Particle size (mm)	0.5–1.5
Cylindrical compress strength (kPa)	≥150
Bulk density (kg/m^3)	80–130
Thermal conductivity (W/(m K))	0.032–0.045
Surface vitrified close cell content (%)	≥95
Volatile water absorption (%)	20–50
Volume floating rate (%)	≥98

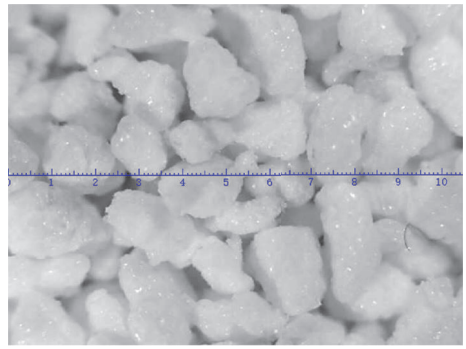

Figure 1: Glazed Hollow Bead dimension (mm).

2. Materials and Experimental Procedure

2.1. Glazed Hollow Bead. Glazed Hollow Beads were produced by Henan Xinyang Yongxin Perlite Plant (China). The GHB particle sizes dimensions are shown in Figure 1. The properties of GHB particles are shown in Table 1.

2.2. Preparation of Rig for Test. The substrate of the rig was prepared in accordance with the dimensions in [26], which is 3.0 m (width) × 2.0 m (height) concrete wall with 0.6 mm (height) × 0.4 m (width) aluminum alloy window (see Figure 2). The structure of the rig from inside to outside is formed by substrate, bonding layer, insulation layer, reinforced base coat, and finishing coat (see Figure 3). The thermal parameters of the rig wall are detailed in Table 2.

The preparation procedure was described as follows. The substrate base was first cleaned and moisturized. The adhesion agent was then brushed. After drying the adhesion agent for at least 24 h, two layers of the GHB thermal insulation mortar were applied. The second layer was applied after setting the initial conditions of the system and completing the first layer. After curing the insulating layer in three days, two layers of the anticrack mortar were applied on and pressed in the alkali-resistant glass fiber mesh between the first and second layers which were set. Then, the anticrack layer was cured for three days and the flexible putty was applied twice after being cured for at least one day. The external wall waterproof priming coat was sprayed and the top layer was finished. Furthermore, the system was cured at laboratory for 28 days. After completing the curing stage, the weathering test was conducted. To monitor the distribution of the temperature at different positions and structural layers along the horizontal

Table 2: Tested walls: layers and their thermal characteristics.

Structure layer	Materials	Thickness (mm)	Conductivity (W/(m K))	Density (kg/m^3)	Specific heat (J/(kg K))	Sketch of structure
Substrate (Sub)	Concrete wall	150	1.740	2500	862	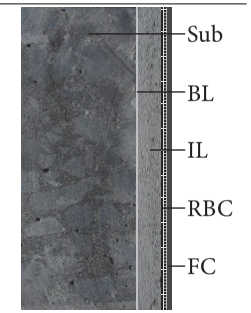
Bonding layer (BL)	Adhesion agent	1	0.760	1500	1050	
Insulation layer (IL)	GHB thermal insulation mortar	30	0.068	325	1170	
Reinforced base coat (RBC)	Anticrack mortar Glass fiber mesh	4	0.750	1937	780	
Finishing coat (FC)	Putty + prime coat + top coat with acrylic binder	3	0.58	1420	1000	

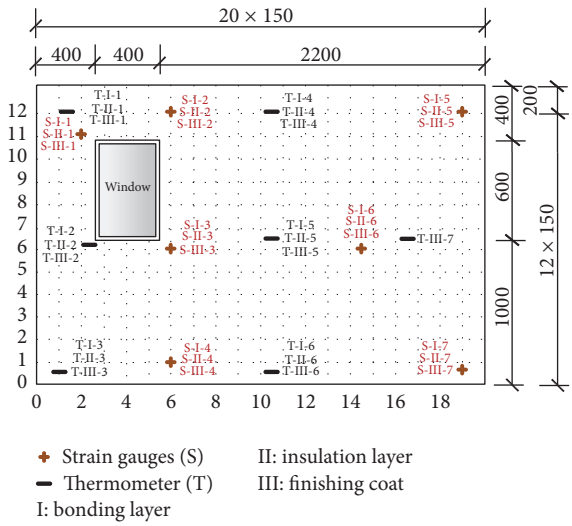

Figure 2: Schematic graph of measuring points (mm).

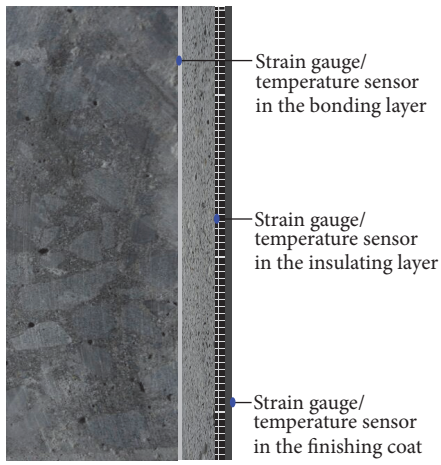

Figure 3: Strain gauges and temperature sensors profiles in the vertical section.

and vertical directions of the test wall surface, the strain gauges and temperature sensors in preparing ETICS GHB should be installed at the same positions as the concrete base, the insulating layer (outer surface), and the finishing coat. Seven strain gauges and six temperature sensors were installed in each layer (see Figures 2–4).

2.3. Test Apparatus. (1) The weathering test chamber can simulate the effect of hot and rainy summer weather with evaporators and fans on the ceiling and spraying system set up by the two sides of the chamber near the testing rigs (see Figure 5). Altogether the test chamber can reproduce the damage to ETICS in a few weeks that occur over many years outdoors, where the range of simulated temperature is from −25°C to 100°C and the range of simulated rainwater temperature is 10°C to 20°C with the precision of ±1.0°C.

(2) INV2312N wireless bus static strain test system: the system is characterized by high sampling rate and high stability with a temperature drift less than 1 $\mu\varepsilon$/°C, a time drift less than 3 $\mu\varepsilon$/4 h, and the measurement precision of ±0.3% FS ± 2 $\mu\varepsilon$.

(3) KON-FK (N) crack width detector: the detector may automatically and quickly record the width of a crack with a precision of 0.01 mm.

(4) GM eight-channel temperature acquisition system: in connecting to the DS18B20 waterproof copper sensor probe, the system may simultaneously record temperature signals at 32 points within the temperature from −55°C to 125°C and the resolution of 0.0625°C.

(5) Scanning electron microscopy (SEM) micrographs of the top coat and GHB mortar were obtained, respectively, using the types of SU-1510 and JSM-6700 (Hitachi, Japan) at various cycles.

(6) KFG/KFW-5-120-D16-11L1M2S strain gauge: the biaxial overlapping configuration was used in the strain gauge in substrate combining with polyimide resin. The strain temperature drift in this arrangement may show by itself without connecting to a compensating plate. It is noted that the KFG series strain gauges were mainly laid out in the internal structures of the ETICS to make high waterproof and moisture-resistant performance. The series of strain gauges in KFW were mainly laid on the outdoor surface of the ETICS, even in the underwater or rainy environments. Table 3 shows the performance indexes of the strain gauges.

2.4. Artificial Weathering Tests. The cured ETICS GHB test specimens were placed inside the large-scale weathering test chamber. The strain gauges and temperature sensors should be properly connected Figure 6 shows the assembled test specimens. During a hygrothermal cycle test, the temperature range of hygrothermal cycle was set from 15°C to 70°C, and the number of cycles was set at 80 with each cycle lasting for 6 h. The heating process consists of raising the air temperature to 70°C in approximately 60 minutes and then maintaining the temperature at 70 (±5)°C for 120 minutes. The rain process consists of spraying water continuously for 60 minutes and then resting for 120 minutes. Both strain and temperature were recorded at an interval of 10 min. A shutdown surface observation of the test wall was carried out at an interval of once in every four cycles to monitor the effect exerted by the thermal fatigue damage (i.e., crack, detachment, and swell). In order to quantitatively compare the surface damage results of the test specimen after different number of cycles, the surface of the test specimen was subdivided by a grid spacing of 15 cm (i.e., 20 grids in the horizontal direction and 13 grids in the vertical direction), as shown in Figure 2.

3. Results and Analysis

3.1. Temperature Field. To analyze the effect of temperature changes on various structural layers, it is necessary to determine the temperature features in various layers in the weathering test chamber. Taking 80 cycles in the hygrothermal conditions as an example, the data recorded at the fifth cycle were selected to examine the local change features in temperature at each point. Figure 7(a) shows the temperature changing curves at the measuring points T-I/II/III-4, T-I/II/III-5, and T-I/II/III-6 on the wall surface in

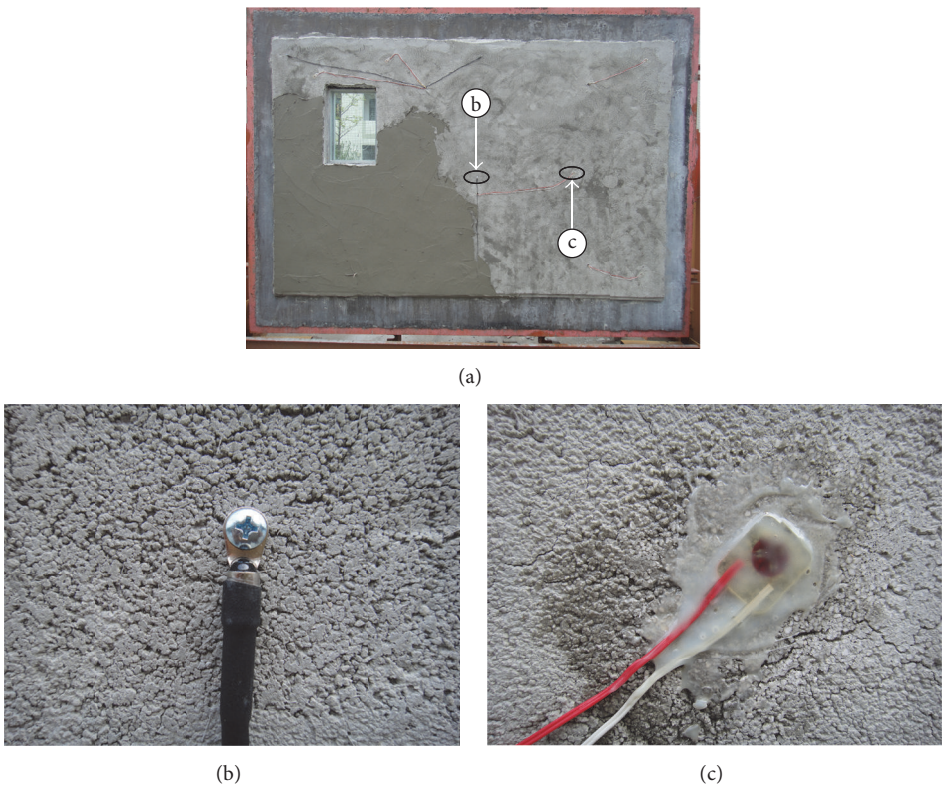

(a)

(b) (c)

Figure 4: (a) The rig wall during construction phase and instrumented with temperature sensors and strain gauges between GHB mortar and reinforced base coat. (b) Temperature sensor. (c) Strain gauge.

Table 3: Performance indexes of KFG/KFW.

Series	Self-compensating temperature range/°C	Self-compensating expansion coefficient/10^{-6}/°C	Strain limit/%	Fatigue life/number of times
KFG	10–100	11.0	5.0	1.2×10^7
KFW	0–80	10.8	2.8	3.0×10^4

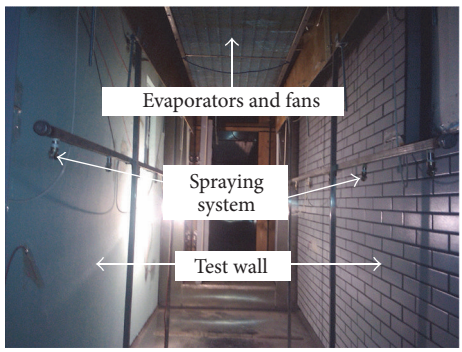

Figure 5: The weathering test chamber.

the vertical direction. Figure 7(b) shows the related curves at the measuring points T-I/II/III-2, T-I/II/III-5, and T-III-7 on the wall surface in the horizontal direction. Figure 8 shows the variations in temperature at the measuring points T-I/II/III-1, T-I/II/III-2, T-I/II/III-5, and T-I/II/III-6 along the wall thickness direction.

(1) As shown in Figure 7, the temperature changing trend at different measuring points on the surfaces of the finishing coat and the insulating layer are similar and have a shape of a rectangular wave. However, the changing trend on the surface of the bonding layer has a shape of a triangular wave. The results imply that the GHB insulating material has an excellent thermal insulation effect in reducing the temperature transferred from the external temperature on the substrate wall; the temperature change rate of the bonding layer would slow down during the rising phase and raining phases and improve the indoor thermal comfort.

(2) As shown in Figure 7(a), the test chamber caused a progressively top-down decline in the temperature of the finishing coat, insulating layer, and bonding layer along the vertical direction of the wall surface. In this case, the largest temperature differences are among the upper and lower parts (i.e., 30°C for the finishing coat, 26°C for the insulating layer, and 12°C for the bonding layer). These temperature differences

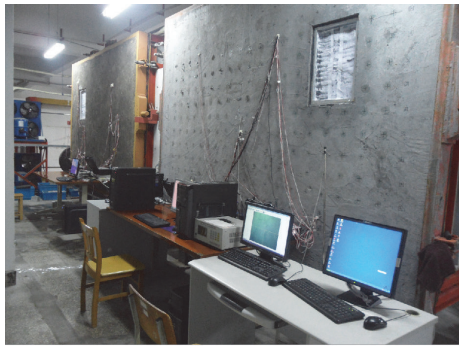

Figure 6: Data acquisition system of temperature and strain.

resulted in the deformation on the wall surface along the vertical direction and of the cracks along the horizontal direction. Figure 7(b) displays the temperature difference between the bonding layers and insulating layer is only about 1°C along the horizontal direction of the wall surface. Furthermore, the fluctuations at the measuring point T-III-7 of the finishing coat are more significant than those at the other points in the middle part, indicating that there is an unbalance in the local temperature in the test chamber.

(3) As shown in Figure 8, the maximum temperature differences between the upper points T-I-1 and T-III-1, the middle points T-I-2 and T-III-2 near the window, the middle points T-I-5 and T-III-5 near the center, and the lower points T-I-6 and T-III-6 were 30.9°C at 60 min, 22°C at 120 min, 22°C at 120 min, and 17.3°C at 180 min, respectively. These results indicate that the surface temperatures at various points were affected by the local positions along the wall thickness direction. However, the differences in the temperatures from the top to lower parts are smaller with the largest one happening later.

3.2. Strain Field. In the test, the data recorded by the strain gauges are the total strain in each structural layer of the wall. The data in a total of 80 hygrothermal cycles were analyzed here. For the purpose of comparison, the measured temperatures near each measuring point, the strain-time-temperature relationship curves of the finishing coat, insulating layer, and bonding layer at different positions were depicted in Figures 9, 10, and 11.

(1) As shown in Figure 9, for each period at the temperature rising and maintaining phases, the strain of the finishing coat changes synchronously with the temperature in the external layer. This indicates that the material of the finishing coat tended to expand with heat and to contract with cold surroundings at these two phases. At the raining phase, the temperature and strain of the finishing coat drop abruptly with a slight lag in the later curve (see Figures 9(b), 9(d), and 9(f)). At the resting phase, the temperature of the finishing coat continues to fall at a slower rate. On the other hand, the strain would increase followed by an initial decrease as the temperature reaches that at the rising phase in the next period. These results are consistent with those obtained by Yiu et al. [23]. Therefore, the increase in strain during the resting phase may be caused by the hygroscopic expansion of the finishing coat material. For the entire cycle process, the maximum vertical and horizontal strains at the upper point S-III-1 and the lower point S-III-4 on the surface of the finishing coat are 9469 $\mu\varepsilon$ and 1752 $\mu\varepsilon$ at $N = 80$, 1379 $\mu\varepsilon$ at $N = 78$, and 682 $\mu\varepsilon$ at $N = 5$, respectively (N stands for the hygrothermal cycle). However, the vertical and horizontal strains at the middle point S-III-6 rapidly drop to failure at $N = 60$ and at $N = 70$, respectively. These results indicate that the thermal deformation of the wall surface caused by the temperature difference in the vertical direction is two to four times of the deformation in the horizontal direction; in the finishing coat of the large-scale ETICS, the temperature gradient generated by the heat blocking action of the insulating layer results in an inconsistent overall hygrothermal deformation in different directions. These deformation gradients would accelerate the cracking of the finishing coat material and thereby shorten the durability of the material, as verified in Figures 15 and 16.

The finishing coat shrinks at early stage and expands after a number of cycles. The reason is that the micropores on the surface of the finishing coat are gradually blocked by the carbonized crystals at early time while the macropores may be generated between the crystals regions under the cycle load [24]. Figure 12 shows the scans electronic microscopy of the top parts of the finishing coat, respectively, before and after the test. The macropore structures appeared between the crystals in Figure 12(b). These pores resulted from the water-loss and shrinkage of the finishing coat. In the late stage of the 20th cycle, there is insignificant change in the structural porosity of the finishing coating material. As a consequence, the expansion with heat and the contraction with cold occurred in most positions, especially as in the maintaining phases. At this stage, an irreversible temperature-dependent creep deformation in the finishing coating material might be generated and accumulated with the cyclic temperature fluctuations. The continuous expansion would cause the coating material to split.

(2) Figures 9 and 10 show the results of the strains on the surfaces of the finishing coat and insulating layer. The change trends in these two figures are basically similar to each other, implying that the strain in the insulating layer may effectively illustrate the deformation of the insulating layer. However, the measured strain in the insulating layer is much smaller than that in the finishing coat due to the less influences of the external temperature and humidity on the GHB material of the insulating layer. From Figures 9 and 10, it can be also seen that most of the drying-shrinkage deformation occurred in the early stage and some of the thermally expansion deformation occurred at the later stage. During the hygrothermal cycle, the maximum/minimum vertical and horizontal strains were 495/−962 $\mu\varepsilon$ and 1072/−188 $\mu\varepsilon$, respectively. As shown in Figure 11, the strain in the bonding layer decreases abruptly due to the protection effect of the insulating material. None of the deformation exceeds the elastic limit in the concrete substrate regions. Hence, the safety is guaranteed for the internal concrete enclosure structure; the service life of the concrete might be lengthened. The maximum/minimum

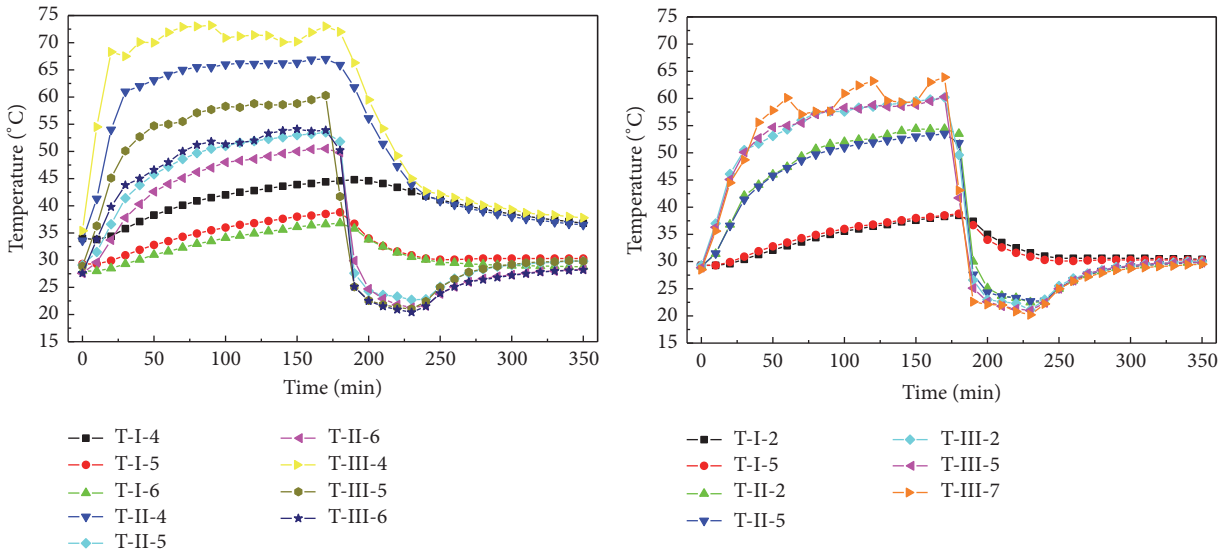

(a) Along the vertical direction of wall surface

(b) Along the horizontal direction of wall surface

Figure 7: Temperature changing curves at various measuring points.

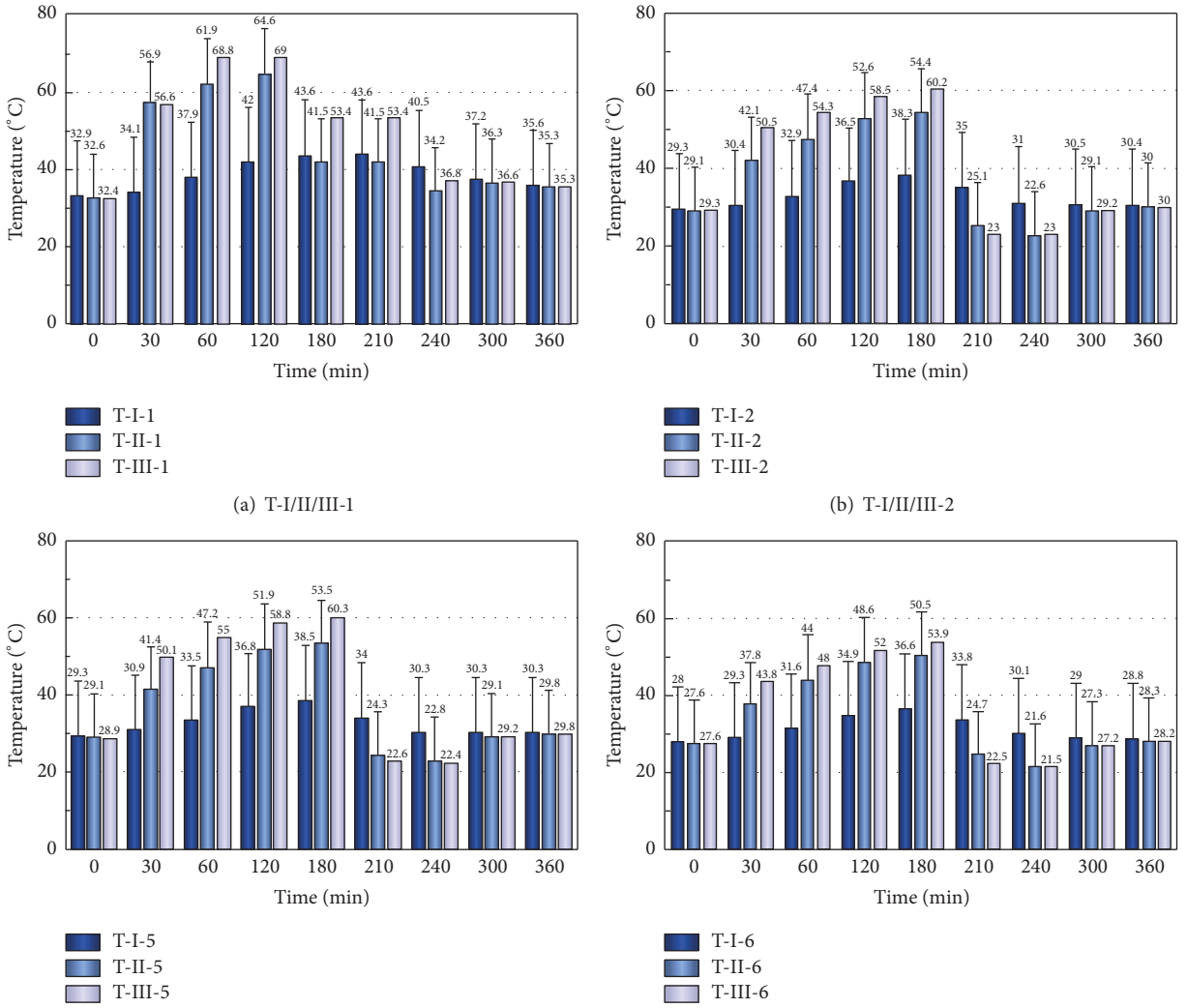

(a) T-I/II/III-1

(b) T-I/II/III-2

(c) T-I/II/III-5

(d) T-I/II/III-6

Figure 8: Temperatures at various instants for different measuring points along the direction of wall thickness.

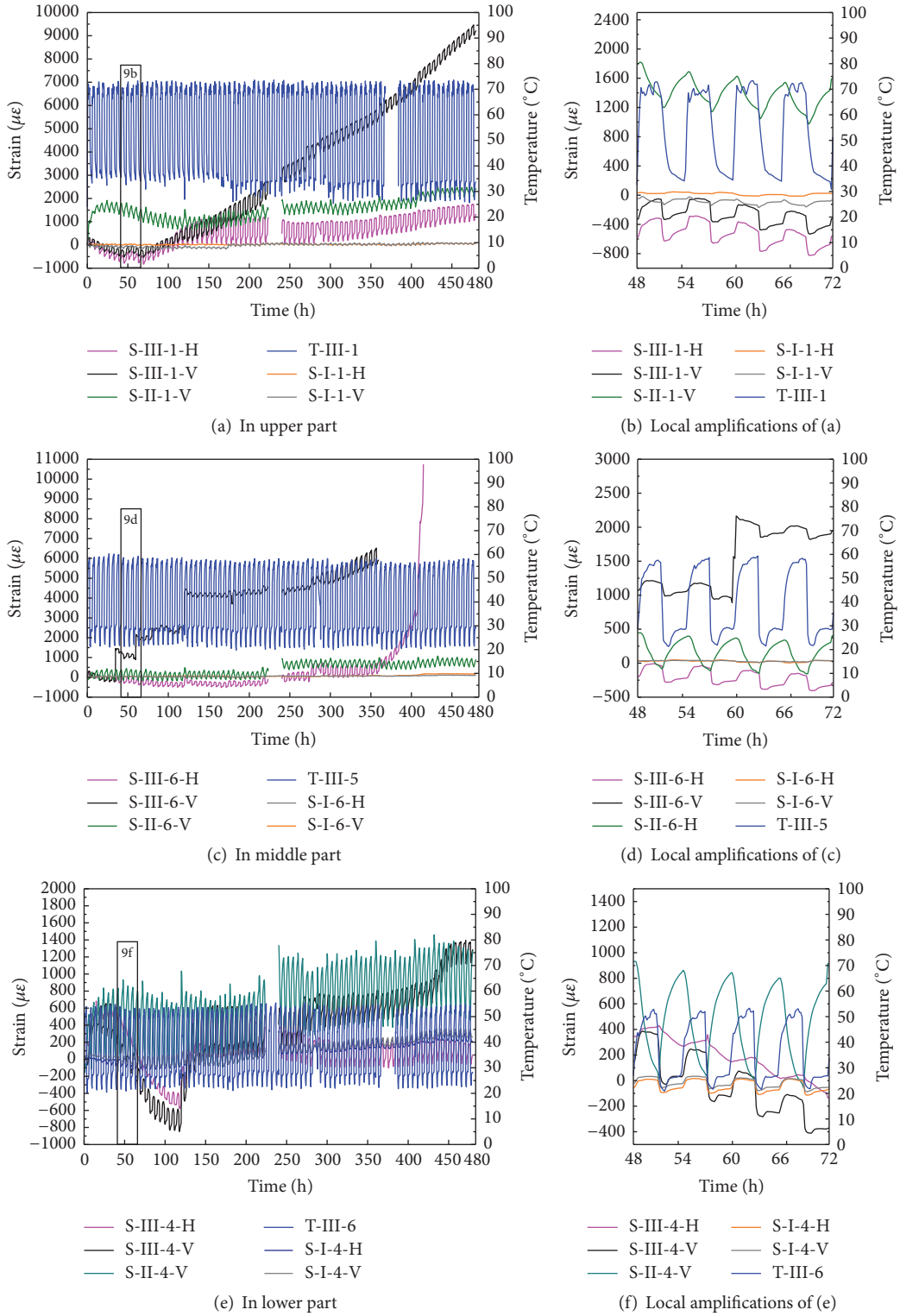

Figure 9: Strain-time-temperature relationship of three surfaces.

vertical and horizontal strains on the surface of the bonding layer are 359/−181 $\mu\varepsilon$ and 330/−120 $\mu\varepsilon$, respectively.

The different thermal deformation modes demonstrate that the hygrothermal resistance property of the bonding layer is better than that of the insulating layer. The improvement in hygrothermal resistance of the bonding layer can be explained by the influence of GHB particles. From Figure 13, it can be seen that the microstructure of GHB mortar did

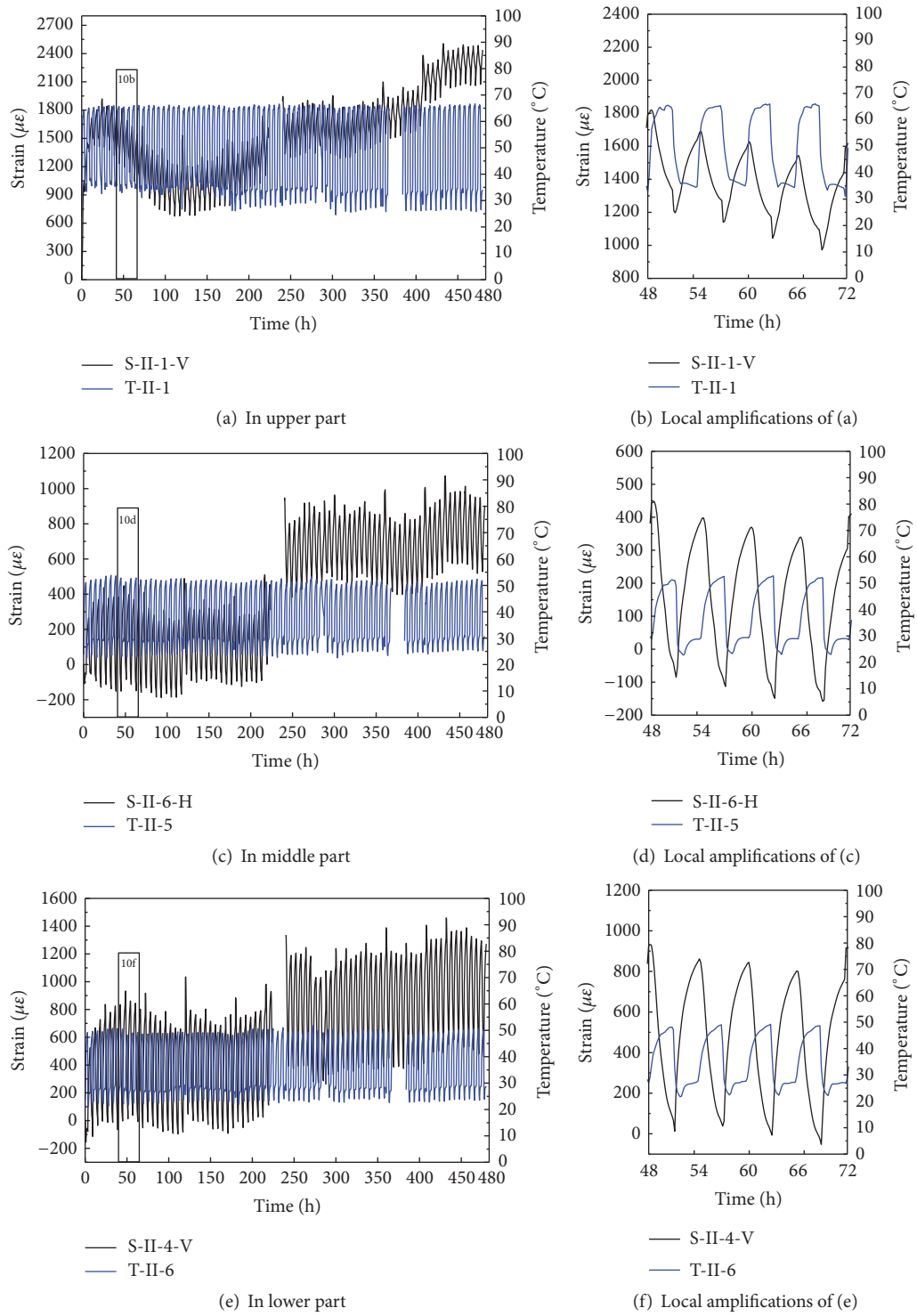

Figure 10: Strain-time-temperature relationship of insulating layer.

not change obviously under various hygrothermal cycles, the internal honeycomb pores were relatively smooth, and no significant deterioration was observed. Hence, GHB can improve hygrothermal behavior of the GHB mortar in reducing thermal deformation of the concrete substrate surface.

(3) The strain-time relationship changing curve may be divided into three stages (see Figure 14). Before the 20th hygrothermal cycle, the strain of each structural layer decreases with the increase of N, that is, implying the shrinkage deformation occurs (see Figure 15). The most, second to

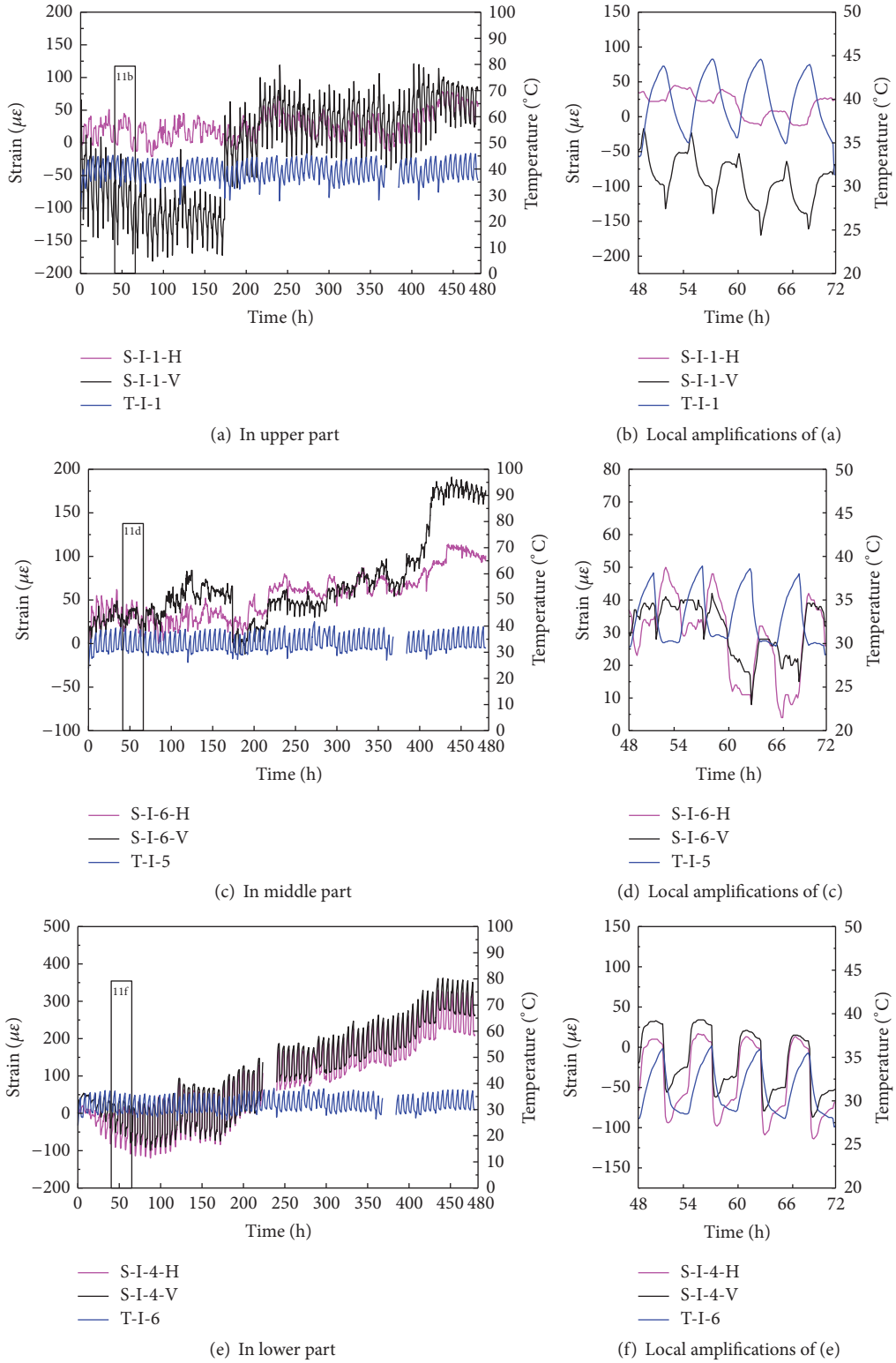

Figure 11: Strain-time-temperature relationship of bonding layer.

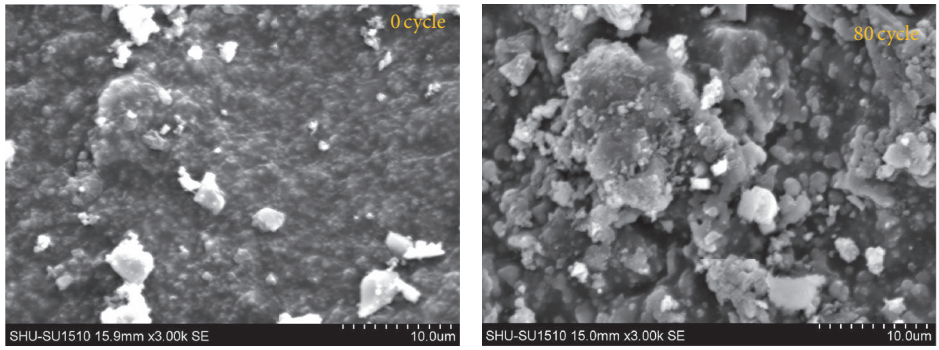

Figure 12: SEM graphs of top finish on the finishing coat.

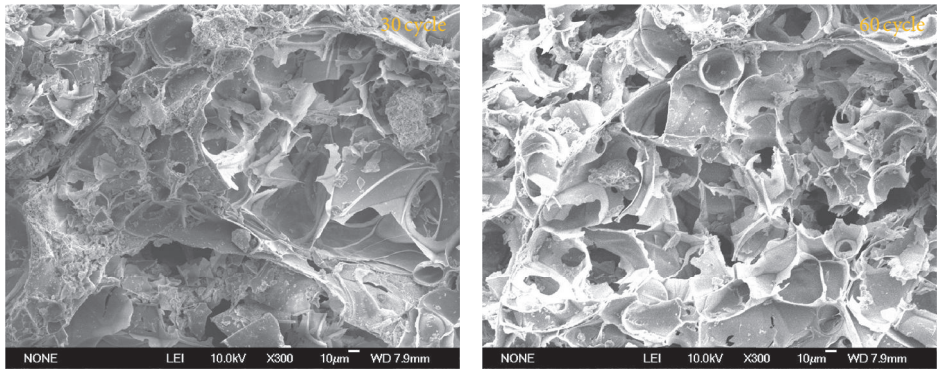

Figure 13: SEM graphs of GBH mortar on insulating layer.

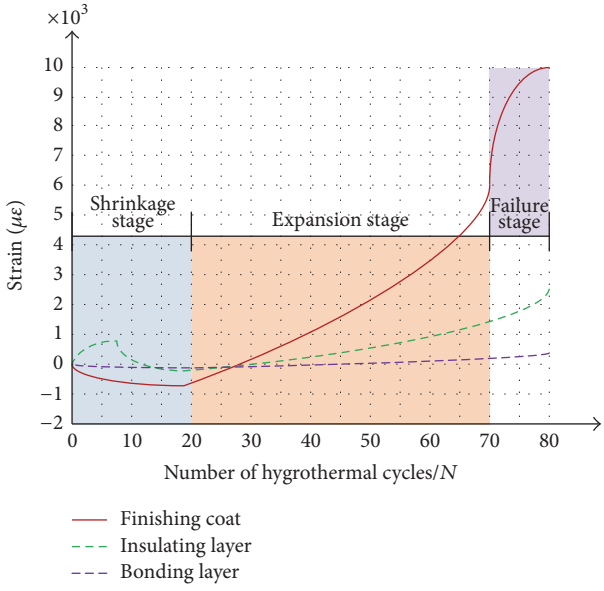

Figure 14: Accumulating process of fatigue damage.

most, and less significant shrinkage are located in the finishing coat, insulating layers, and bonding layers, respectively. On the whole, the deformations in the materials may be regarded at the elastic stage. At $N = 70$, the changing trends in the strains of various structural layers are not similar. The horizontal strains in the finishing coat and the total strains in the insulating and bonding layers increase continuously with a relative slowly rate until the end of the test. Conversely, the vertical strains in the finishing coat increase, implying that the expansion deformation generated (see Figure 16). The tensile strain only recovers partially, especially the vertical strain of the finishing coat behaviors of the plastic deformation mode. These changing trends are consistent with those of change features in the temperature shown in Figure 7. During the last ten cycles, there is an abrupt change in the vertical strain in the finishing coat. To be specific, the changes in the strains are not significant at the upper position (Figure 9(a)) and at the lower position (Figure 9(e)) on finishing coat surface; while the strain gauge placed at middle position (see Figure 9(c)) damages, the deformation enters the failure mode.

3.3. Surface Crack. Figures 15 and 16 show the sketches of the cracks recorded by the crack width detector at $N = 20$ and $N = 80$. In these two instants, the cracks and swells on the finishing coat appeared as lines and circles. In all procedure of the test, the cracks, swells, and other degradation always occurred on the finishing coat. The rules relations between the length, width, and distribution of the cracks on the finishing coat and the number of cycles are relatively obvious. The degradation characteristics of the finishing coat from the perspectives of crack length and width will be examined as follows.

(1) On the surface of the finishing coat (see Figure 15), most of the cracks are in the horizontal direction,

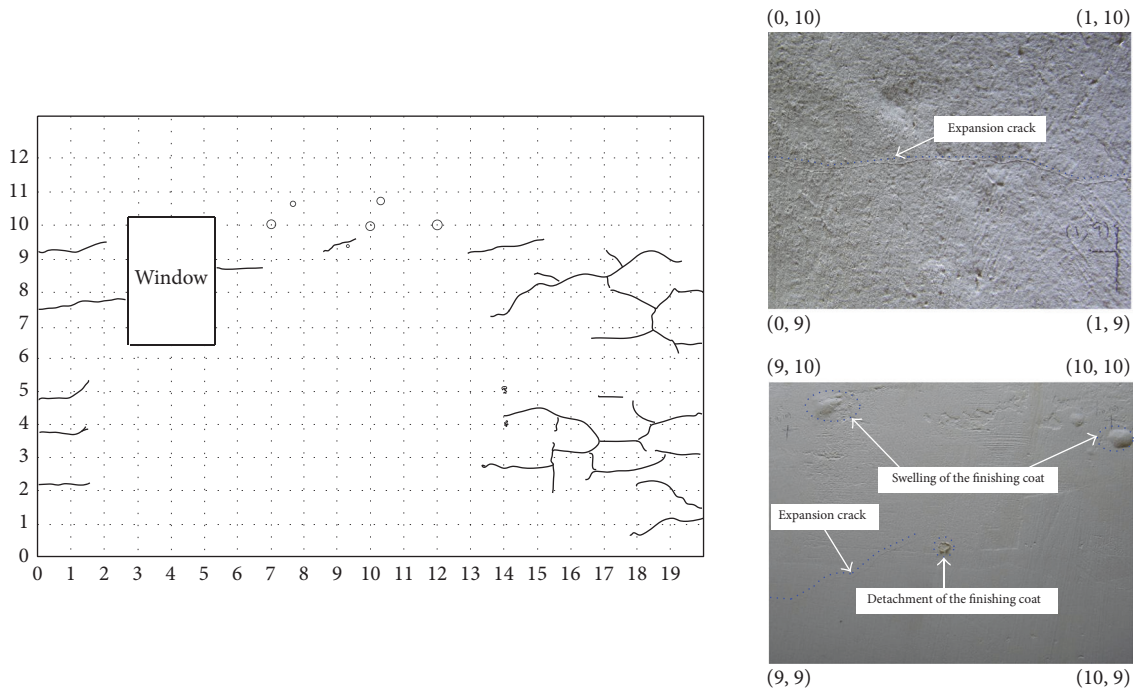

Figure 15: Crack propagations on the finishing coat, the 20 cycles.

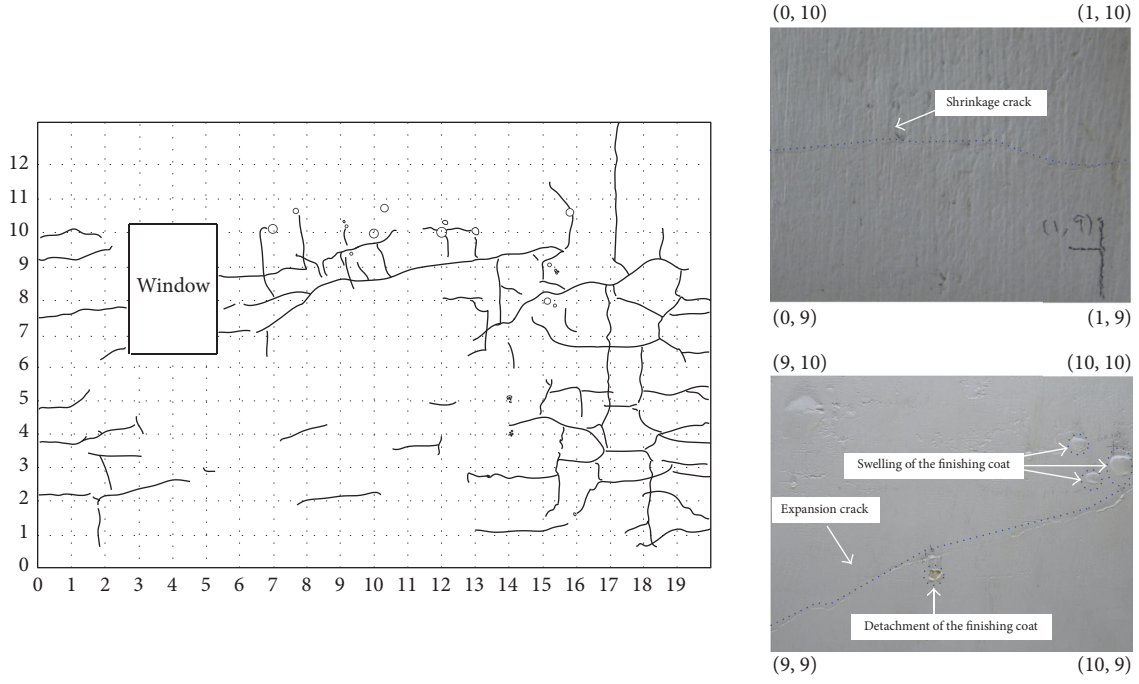

Figure 16: Crack propagations on the finishing coat, the 80 cycles.

the second to most of the cracks are vertical ones, and very few of the oblique cracks appeared. The reason is that the temperatures on the surface of the finishing coat in the vertical direction changed more intensely than those in other directions (see Figures 7 and 8). So, the newly generated temperature stress made it easier for cracks to emerge. As a result, under the repeated actions of the hygrothermal load, most of the cracks formed along the horizontal direction and developed relatively quickly. These cracks may converge to some extent. To be specific, the horizontal and vertical cracks converged regionally, while the oblique cracks distributed locally. The cracks on the finishing coat only initially existed on the surface

Table 4: Number, length, and increase magnitude of cracks.

Number of cycles/N	Number	Total length/m	Increase magnitude/%		Max. width/mm
			Number	Total length	
12	28	8.51	—	—	0.07
20	45	12.13	61	43	0.09
40	64	18.22	42	50	0.10
60	80	22.05	25	21	0.12
72	89	24.18	11	10	0.16
80	92	24.68	3	2	0.17

of the coating material but subsequently extended to the inside of the material. However, they did not penetrate the finishing coat.

(2) As shown in Table 4, the number, the length, and width of the cracks on the surface of the finishing coat gradually increase with the increase in the number of cycles. Specifically, the most significant increase is the number of cracks, followed by the total length of cracks. The increase in the width of cracks is not significant. All of these three parameters decrease with the increasing in N. In particular, for $N > 20$, the cracks on the surface of the finishing coat developed rapidly, also being verified by the strains in Figure 9(c). For $N = 72$, only a few new cracks formed and stably propagated. Therefore, after 72 hygrothermal cycles, the degradation of the ETICS is not significant, suggesting that setting the number of hygrothermal cycles at 80 in ETAG 004 [26] is appropriate.

4. Conclusions

In this study, the temperature and strain in three various structural layers (i.e., finishing coat, insulating layer, and the bonding layer) of the ETICS GHB under the hygrothermal cycles were investigated. Based on the test results, the following conclusions were obtained:

(1) Due to the differences in the thermophysical properties, the relations between temperature distributions on the surface and inside the chamber are different for three structural layers. These differences contributed to the internal stresses in the structural layers. The temperature difference between different positions on the same plane of the finishing coat and the insulating layer is 20°C. On the other hand, for the bonding layer, the difference is only around 5°C. The local temperature difference existing on the surface of the finishing coat may cause the surface crack openning on the finishing coat. The temperature of the bonding layer is not excessively high because of the thermal insulation action of the insulating layer.

(2) Most of the thermal deformation on the surface of three layers is moisture expansion and drying-shrinkage one and thermal expansion one, respectively, at the early stage and at the later stage. The surface strain of the finishing coat shows three stages of deformation with the increasing of N: for $N < 20$, the shrinking elastic deformation occurs; for $20 < N < 70$, the expansion-type elastoplastic deformation occurs; for $N > 0$, the plastic failure deformation occurs. The change trends of the surface strains in the insulating and bonding layers with the increase of N are similar, except that magnitude in the insulating layer is smaller. Due to the surface strain of the bonding layer, the elastic deformation occurs.

(3) The cracks on the surface of the finishing coat mostly converged into horizontal ones, followed by vertical cracks, and, lastly, locally formed a few of oblique cracks. With increasing N, the most significant increase is the number of cracks on the finishing coat and then the length of the cracks. The width of the cracks increased is gradually. However, the increase rate of these parameters (i.e., number, length, and width) decreases with the increase in N. The cracks of the finishing coat are the generation, expansion, and saturation modes, respectively, for $N < 20$, $20 < N < 70$, and $N > 70$.

(4) GHB mortar with internal honeycomb pores and smooth closed surface has good water retention capacity and stable structure. Hence, the special pore structure can reduce the thermal conductivity of GHB mortar, prevent the moisture migration extension of concrete substrate, and accordingly alleviate the hygrothermal behavior of the bonding layer.

Competing Interests

The authors declare that they have no competing interests.

Acknowledgments

This work was financially supported by the National Natural Science Foundation of China (no. 41472254 and no. 51308371), Jiaxing University School-Class Key Topics of Funded Projects (no. 70115020), Jiaxing Science and Technology Project (no. 2016AY13009), and The "Twelfth Five-Year" Key Disciplines in the Universities of Zhejiang Province, Discipline of Building Energy Efficiency Technology (Department of Education of Zhejiang Province Office Document [2012] no. 80).

References

[1] Q.-P. Pu, B.-Z. Li, and W. Yu, "Energy consumption forecast model of urban residential buildings in Chongqing," *Journal of Central South University (Science and Technology)*, vol. 43, no. 4, pp. 1551–1556, 2012.

[2] T.-S. Gu, L.-Y. Xie, and G. Chen, "Building energy conservation and wall thermal insulation," *Engineering Mechanics*, vol. 23, no. 2, pp. 167–184, 2006.

[3] I. Mandilaras, I. Atsonios, G. Zannis, and M. Founti, "Thermal performance of a building envelope incorporating ETICS with vacuum insulation panels and EPS," *Energy and Buildings*, vol. 85, pp. 654–665, 2014.

[4] F. E. Boafo, Z. Chen, C. Li, B. Li, and T. Xu, "Structure of vacuum insulation panel in building system," *Energy and Buildings*, vol. 85, pp. 644–653, 2014.

[5] L. Zhao, W. Wang, Z. Li, and Y. F. Chen, "Microstructure and pore fractal dimensions of recycled thermal insulation concrete," *Materials Testing*, vol. 57, no. 4, pp. 349–359, 2015.

[6] X. Li and G. Li, "Effect of latex powder and glass fiber on the performance of glazed hollow bead thermal insulation materials," *Journal of Building Materials*, vol. 17, no. 2, pp. 314–319, 2014.

[7] J. Zhu and G. Li, "Performance of thermal insulation materials of polypropylene fiber reinforced vitrified small ball," *Journal of Building Materials*, vol. 18, no. 4, pp. 658–703, 2015.

[8] J.-Q. Gong and C.-T. Zhang, "Study on the thermal conductivity model of hollow beads insulating mortar," *Journal of Hunan University Natural Sciences*, vol. 41, no. 6, pp. 99–105, 2014.

[9] S. Fan and P. Wang, "Effect of air entraining agents on the long-term drying shrinkage of glazed hollow beads thermal insulation mortar," *Journal of Building Materials*, vol. 19, no. 1, pp. 1–7, 2016.

[10] P. Ren, X.-H. Li, and Q.-L. Meng, "Thermal and moisture performance of insulation glazed hollow bead motar," *Journal of Civil Architectural & Environmental Engineering*, vol. 32, no. 4, pp. 71–75, 2010.

[11] Q.-T. Yu, P. Pan, and Y.-K. Su, "Experimental study on seismic behavior of light-gauge steel wall filled with glazed hollow bead mortar," *Engineering Mechanics*, vol. 32, no. 3, pp. 151–157, 2015.

[12] W. Wang, L. Zhao, Y. Liu, and Z. Li, "Mechanical properties and stress-strain relationship in axial compression for concrete with added glazed hollow beads and construction waste," *Construction and Building Materials*, vol. 71, no. 11, pp. 425–434, 2014.

[13] Y. Liu, Y. F. Chen, W. Wang, and Z. Li, "Bond performance of thermal insulation concrete under freeze-thaw cycles," *Construction and Building Materials*, vol. 104, no. 2, pp. 116–125, 2016.

[14] H. Shen, H. Tan, and A. Tzempelikos, "The effect of reflective coatings on building surface temperatures, indoor environment and energy consumption—an experimental study," *Energy and Buildings*, vol. 43, no. 2-3, pp. 573–580, 2011.

[15] S. Ximenes, J. de Brito, P. L. Gaspar, and A. Silva, "Modelling the degradation and service life of ETICS in external walls," *Materials and Structures*, vol. 48, no. 7, pp. 2235–2249, 2015.

[16] B. Amaro, D. Saraiva, J. De Brito, and I. Flores-Colen, "Inspection and diagnosis system of ETICS on walls," *Construction and Building Materials*, vol. 47, pp. 1257–1267, 2013.

[17] B. Daniotti, F. R. Cecconi, R. Paolini, R. Galliano, J. Ferrer, and L. Battaglia, "Durability evaluation of ETICS: analysis of failures case studies and heat and moisture transfer simulations to assess the frequency of critical events," in *Proceedings of the 4th Portuguese Conference on Mortars and ETICS*, Coimbra, Portugal, 2012, http://www.apfac.pt/congresso2012/comunicacoes/Paper%20104_2012.pdf.

[18] D. Zirkelbach, A. Holm, and H. M. Künzel, "Influence of temperature and relative humidity on the durability of mineral wool in ETICS," in *Proceedings of the 10DBMC International Conference on Durability of Building Materials and Components*, Lyon, France, April 2005.

[19] J. Zhang, Y. Gao, and Z. Huang, "Comparative studies on the temperature stresses in external walls with different thermal insulation models," *Journal of Harbin Engineering University*, vol. 32, no. 7, pp. 895–905, 2011.

[20] A. Collina and G. P. Lignola, "The External Thermal Insulation Composite System (ETICS) more than comfort and energy saving," in *Proceedings of the 3rd Portuguese Congress on Construction Mortars*, Lisbon, Portugal, 2010 (Portuguese).

[21] C. Balocco, G. Grazzini, and A. Cavalera, "Transient analysis of an external building cladding," *Energy and Buildings*, vol. 40, no. 7, pp. 1273–1277, 2008.

[22] D. S. Passa, A. B. Sotiropoulou, Z. G. Pandermarakis, and G. D. Mitsopoulos, "Thermal and drying cyclic loading for cement based mortars and expanded polystyrene foam layers," *Applied Mechanics and Materials*, vol. 204–208, pp. 3648–3651, 2012.

[23] C. Y. Yiu, D. C. W. Ho, and S. M. Lo, "Weathering effects on external wall tiling systems," *Construction and Building Materials*, vol. 21, no. 3, pp. 594–600, 2007.

[24] G. Griciute and R. Bliudzius, "Study on the microstructure and water absorption changes of exterior thin-layer polymer renders during natural and artificial ageing," *Materials Science*, vol. 21, no. 1, pp. 149–154, 2015.

[25] B. Daniotti, R. Paolini, and F. R. Cecconi, "Effects of ageing and moisture on thermal performance of ETICS cladding," in *Durability of Building Materials and Components*, vol. 3 of *Building Pathology and Rehabilitation*, pp. 127–171, Springer, Berlin, Germany, 2013.

[26] ETAG 004, Guideline for European technical approval of External thermal insulation composite systems with rendering, European Organisation for Technical Approvals, March 2000.

Hindawi Publishing Corporation
Advances in Materials Science and Engineering
Volume 2016, Article ID 1638419, 7 pages
http://dx.doi.org/10.1155/2016/1638419

Research Article

Mechanical Properties of High Volume Fly Ash Concrete Reinforced with Hybrid Fibers

Rooban Chakravarthy, Srikanth Venkatesan, and Indubhushan Patnaikuni

School of Engineering, RMIT University, Melbourne, VIC, Australia

Correspondence should be addressed to Srikanth Venkatesan; srikanth.venkatesan@rmit.edu.au

Received 19 June 2016; Revised 10 October 2016; Accepted 9 November 2016

Academic Editor: Kazunori Fujikake

Fly ash substitution to cement is a well-recognized approach to reduce CO_2 emissions. Although fly ash concrete is prone to brittle behavior, researchers have shown that addition of fibers could reduce brittle behavior. Previous research efforts seem to have utlised a single type of fiber or two types of fibers. In this research, three types of fibers, steel, polypropylene, and basalt as 0%, 0.50%, 0.75%, and 1% by volume of concrete, were mixed in varying proportions with concrete specimens substituted with 50% fly ash (class F). All specimens were tested for compressive strength, indirect tensile strength, and flexural strength over a period of 3 to 56 days of curing. Test results showed that significant improvement in mechanical properties could be obtained by a particular hybrid fiber reinforcement combination (1% steel fiber, 0.75% polypropylene fiber, and 0.75% basalt fiber). The strength values were observed to exceed previous research results. Workability of concrete was affected when the fiber combination exceeded 3%. Thus a limiting value for adding fibers and the combination to achieve maximum strengths have been identified in this research.

1. Background

Fly ash is generally an industrial waste obtained from burning coal. Fly ash substitution to cement is a well-recognized approach to reduce CO_2 emissions. Malhotra [1] observed significant improvement in strength and durability with the substitution of high volume class F fly ash in ordinary Portland cement (OPC). Concrete in general and fly ash concrete in particular with 50% or more high volume replacements can experience brittle behavior. Under these circumstances, researchers have trialed the addition of fiber reinforcements to concrete. Thomas [2] observed that the addition of fibers led to improved stiffness of concrete or holding the matrix together after crack initiation or a combination of both mechanisms. Fiber reinforced cement composites were also observed to gain much higher strength for increasing strain rates in comparison to normal concrete [3, 4]. Reference [5] observed that the function of fibers as secondary reinforcement in concrete inhibited crack initiation and propagation and improved the mechanical properties of concrete such as compressive strength, tensile strength, flexural strength, impact resistance, and toughness. In the case of Hannant [6], the addition of fibers provided better performance for the concrete while the addition of fly ash provided better workability and strength gain. The above references provide evidence to support the combinations of fly ash concrete with fiber reinforcements to enhance the mechanical properties. Some of these works specific to different types of fibers are noted below.

In the literature, three types of fibers that were added to fly ash concrete are widely discussed: steel, polypropylene, and basalt. With the addition of steel fibers concrete toughness was observed to be proportional to fiber content in both static and dynamic loading conditions as shown by Zollo [7] and Yet et al. [8]. Further, improvements in strain rates leading to enhanced strength were also noted. Steel fiber was observed to provide better bond strength and enhanced pullout resistance [9]. The equivalent bond strength of straight steel fibers, which are commonly used in ultrahigh performance fiber reinforced concrete, was doubled by optimizing the ultrahigh performance concrete matrix through composition and particle size distribution. This led to typical pullout load slip hardening behavior that is desirable for high tensile strength, high energy absorbing, and strain hardening of

concrete [9]. Therefore it can be seen that the addition of steel fibers has the ability to bond well with concrete and can provide better pullout resistance.

Addition of polypropylene fiber was found to improve the durability of concrete composites containing fly ash and silica fume but showed adverse effect on the workability of concrete. In addition, water permeability, dry shrinkage strain, and the depth of carbonation of concrete decreased gradually with the increase of fiber volume fraction [11]. However Yao et al. [12] observed that at constant volume fraction (0.5%) of hybrid fibers, the addition of polypropylene fibers to carbon and steel fibers provided varied results. Notwithstanding these limitations, as a member of polymer fibers, polypropylene fiber captivated the most recognition among researchers because of its enhanced shrinkage cracking resistance, low cost, and its excellent toughness in the concrete [13–16, 19]. Polypropylene fibers were observed to improve the failure impact resistance of concrete with little statistical influence on the compressive or flexural strength of concrete. Flexural toughness and impact resistance showed an increase in the presence of polypropylene fibers in the concrete [14, 17]. A large number of polypropylene fibers distributed uniformly in the concrete composite resulted in decreased bleeding and segregation of the fresh concrete mixture due to the formation of grid like structures [18].

The addition of basalt fiber was observed to improve the deformation and energy absorption properties without notable enhancement in dynamic compressive strength [19]. Addition of basalt fibers up to 2% of concrete volume together with mineral admixtures improved the compressive strength and the improvement in strains corresponded to maximum compressive strength [20]. The basalt fiber significantly improved the tensile strength, flexural strength, and toughness index, whereas the compressive strength showed no obvious increase [21]. The degradation of basalt fiber in concrete changed into small parts different from their original form [22], thus strengthening the mix overall. Steel fibers were observed as a better strengthening material in high volume fly ash concrete but the addition of basalt fiber in combination resulted in decreased compressive strength. However the fracture energy and flexural strength improved with the addition of basalt fiber. As the basalt fiber content increased, concrete showed higher ultimate loads, larger deflections before failure that resulted in higher fracture energy values [23].

From the above review, it can be noted that steel fiber (high modulus fiber) is stronger and stiffer which improves the concrete strength, while polypropylene fiber (low modulus fiber) has the capacity to strengthen brittle cementitious materials and is more flexible and has the property to retain heat for a prolonged time which leads to improved toughness and strain capacity in the postcracking section and retard early cracks. Basalt fiber which is high in oxidation resistance and radiation resistance, fracture energy, and abrasion resistance leads to increase in the flexural strength.

In summary, various researchers have used steel, polypropylene, and basalt fibers mostly as individual additions and rarely as combinations to improve the properties of concrete. Therefore, it is logical to postulate that the combination of fibers may provide reasonable improvements overall and negate some of the disadvantages noted in the literature. This postulation requires an experimental investigation. Further sections of this paper present the experimental program and test results arising from the combination of fibers (steel, polypropylene, and basalt) in hybrid form added to high volume fly ash concrete.

2. Experimental Program

2.1. Materials. Following materials were used in the experimental program: cement, Type I Portland Cement with specific gravity = 3.14; fine aggregate, river sand that passed through 4.75 mm sieve; and coarse aggregate, granite stone that passed through 12.5 mm IS sieve and retained on 10 mm sieve. Fly ash procured from the Tarong Power Plant was used and it was tested in the concrete laboratory at RMIT University and the results are presented in Appendix (Table 2). The steel fiber of length 40 mm and diameter 0.3 mm, polypropylene fiber of length 15 mm with diameter 100 μm, and basalt fiber of length 12 mm with diameter 20 μm were used in this experimental investigation. The water reducing admixture, naphthalene formaldehyde sulfonate (Sikament), was used in all mixing in the experimental work. Lime powder was used to improve the presence of alkali in fly ash. Normal tap water was used for mixing the concrete throughout the experimental work. It was ensured that all of these materials complied with respective material standards or properties.

2.2. Specimen Mix Details. Control specimen is 50% cement and 50% class F fly ash with no fibers. Although the percentage of fly ash mix is dependent on a number of factors, there is sufficient agreement in the literature that brittle behavior is dominant once the fly ash percentage crosses 50%. The authors have used 50%-50% mix in our previous endeavors [24]. Variations of steel fiber are 0.5% and 1%, polypropylene at 0.5% and 0.75%, and basalt at 0.5%, 0.75%, and 1% consistent with the literature noted in the previous section. Although these combinations are selected based on previous research studies a proper combination of basalt fibers does not seem to exist. As the basalt fiber dissolves into the mix, it was decided to include only three ranges into the mixing regime. These mix details are presented in Table 1.

Cylindrical specimens were cast with dimensions of 100 mm diameter × 200 mm length for compressive strength test, cylindrical specimens with dimensions of 150 mm diameter × 300 mm length for indirect tensile strength test, and beam specimens with dimensions of 350 mm × 100 mm × 100 mm for flexural strength test. The numbers of specimens used for this research are

(i) compressive strength tests, 270 cylinders;

(ii) indirect tensile strength tests, 54 cylinders;

(iii) flexure strength tests, 54 beams.

Methodology for concrete mixing involved the following:

(1) Aggregates and sand were washed with water and completely dried. Then both were placed in the concrete mixer and dry mixed for 2 minutes.

Table 1: Specimen nomenclature.

Sl. number	Mix number	Fibers			Cement	Class F fly ash
		Steel fiber	Polypropylene fiber	Basalt fiber		
1	C	0%	0%	0%	50%	50%
2	S1	0.50%	0%	0%	50%	50%
3	S2	1%	0%	0%	50%	50%
4	P1	0%	0.50%	0%	50%	50%
5	P2	0%	0.75%	0%	50%	50%
6	B1	0%	0%	0.50%	50%	50%
7	B2	0%	0%	0.75%	50%	50%
8	B3	0%	0%	1%	50%	50%
9	X1	0.50%	0.50%	0.50%	50%	50%
10	X2	0.50%	0.75%	0%	50%	50%
11	X3	0.50%	0.75%	0.75%	50%	50%
12	X4	0.50%	0%	1%	50%	50%
13	Y1	1%	0.50%	0.50%	50%	50%
14	Y2	1%	0.75%	0%	50%	50%
15	Y3	1%	0.75%	0.75%	50%	50%
16	Y4	1%	0%	0.75%	50%	50%
17	Y5	1%	0%	1%	50%	50%
18	Y6	1%	1%	1%	50%	50%

Table 2: Chemical composition of fly ash.

Characteristics	Tarong fly ash	ASTM class F fly ash
SiO_2	65.9	The sum of SiO_2 + Al_2O_3 + Fe_2O_3 (min 70%)
Al_2O_3	28.89	
Fe_2O_3	0.38	
TiO_2	1.97	
MnO	0	
MgO	0.15	
CaO	0.06	
Na_2O	0.05	
K_2O	0.26	
P_2O_5	0.08	
SO_3	0.03	Max, 5%
LOI	1.24	Max, 6%

(2) Cement, fly ash, and lime powder (5%) were added in the mixer with aggregates and sand and dry mixed for 2 minutes.

(3) Then fibers (steel fiber, polypropylene fiber, and basalt fiber) were added one after another and dry mixed for 1 minute. Then normal water (85%) is added and mixed for approximately 2 minutes.

(4) Remaining mixing water (15%) and plasticizer were added to the mixer and mixed for 3 minutes. Then the mixed concrete was cast into the specimen moulds and vibrated simultaneously in the vibrator for 1 minute to remove any air remaining entrapped mainly to avoid voids. Each specimen was allowed to stand for 24 hours in concrete laboratory before demolding.

2.3. Tests and Methods

2.3.1. Compressive Strength Test (AS 1012.9). The compressive strength test was carried out in accordance with Australian Standard [25] using MTS machine with a loading capacity of 1000 kN and a loading rate of 20 ± 2 MPa/minute. Three cylindrical specimens (100 mm diameter × 200 mm length) were tested for compressive strength at the age of 3 days, 7 days, 14 days, 28 days, and 56 days after casting. The average results of the three cylindrical specimens are reported in this paper.

2.3.2. Indirect Tensile Strength (AS 1012.10). The Indirect tensile strength test was carried out in accordance with Australian Standard [26] using MTS machine with a loading capacity of 1000 kN and a loading rate of 1 ± 0.1 MPa/minute provided with indirect tensile strength test equipment (for details of testing arrangement refer to [26]). Three cylindrical specimens (150 mm diameter × 300 mm length) were tested for flexural strength at the age of 28 days after casting. The average results of the three cylindrical specimens are reported.

The indirect tensile strength (T) of the specimen was calculated using

$$T = \frac{2000P}{\pi LD}, \quad (1)$$

where T is indirect tensile strength (MPa), P is maximum applied force indicated by the testing machine, L is length (mm), and D is diameter (mm).

2.3.3. Flexural Strength Test: Four-Point Bending Test (AS 1012.11). The modulus of rupture development of concrete test was carried out in accordance with Australian Standard [27] using hydraulic MTS testing machine having a loading capacity of 1000 kN (for details of testing arrangement refer to [26]). Three beam specimens were tested for flexural strength until the maximum load is reached after 28 days of casting. The average results of the three beam specimens are reported.

The modulus of rupture (f_{cf}) of the specimen was calculated using

$$f_{cf} = \frac{PL\,(1000)}{BD^2}, \tag{2}$$

where f_{cf} is modulus of rupture (MPa), P is maximum applied force indicated by testing machine (kN), L is span length (mm), B is average width of specimen at the section of failure (mm), and D is average depth of specimen at the section of failure (mm).

The modulus of rupture (f_{cf}) is used to find the tensile strength of the concrete. The correlation between the modulus of concrete rupture and its tensile strength (f_{ct}) based on Australian Standard [28] Article 3.1.1.3 (a) as follows:

$$f_{ct} = 0.6 f_{cf}, \tag{3}$$

where f_{ct} is the uniaxial tensile strength (MPa) and f_{cf} is the modulus of rupture in accordance with AS 1012.11 (MPa).

3. Results and Discussion

3.1. Compressive Strength. As can be seen from Figures 1 and 2, an increase in compressive strength between the control mix and hybrid mixes is clearly evident. In particular it can be seen that at 7 days (Figure 1) some of the mixes appear to have low strengths more than X3, Y3, and Y5 while at around 28 days the strength values seem to stabilize owing to curing of concrete. An average increase of 30% in compressive strength of fiber specimens over control concrete is observed at 28 days with a peak value of 75% increase for specimen Y3 (1% steel, 0.75% polypropylene, and 0.75% basalt). At 56 days no significant differences in strengths were observed to 28-day strengths, suggesting that 28-day comparisons are reliable for further discussion.

As Y3 mix is observed to have the greatest strength from Figure 2, a comparison of Y3 mix and control mix with results of OPC obtained by Çolak [10] is presented in Figure 3. This comparison clearly shows that the control mix has lower strength values than the OPC which might be due to the presence of fly ash while the Y3 mix has increased compressive strength more than both the OPC and the control mix. We also note there are other mixes such as Y5 that have greater strength than OPC. In general, it can be noted that fiber mix concrete can ensure higher compressive strength than normal OPC.

3.2. Indirect Tensile Strength. Figure 4 presents the comparison of indirect tensile strength test results of all mixes at 3 days, 7 days, 14 days, 28 days, and 56 days. There is a random strength increase throughout the duration of observation.

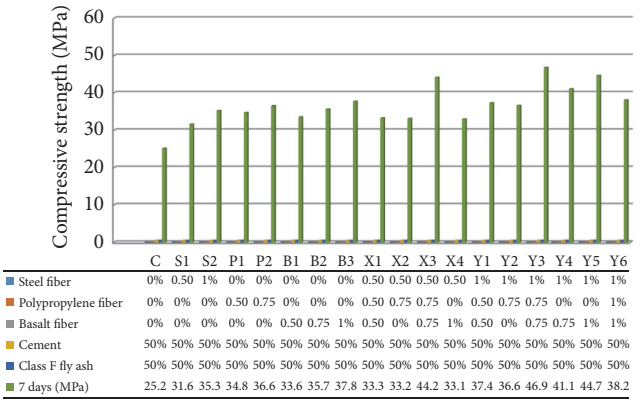

	C	S1	S2	P1	P2	B1	B2	B3	X1	X2	X3	X4	Y1	Y2	Y3	Y4	Y5	Y6
Steel fiber	0%	0.50	1%	0%	0%	0%	0%	0%	0.50	0.50	0.50	0.50	1%	1%	1%	1%	1%	1%
Polypropylene fiber	0%	0%	0%	0.50	0.75	0%	0%	0%	0.50	0.75	0.75	0%	0.50	0.75	0.75	0%	0%	1%
Basalt fiber	0%	0%	0%	0%	0%	0.50	0.75	1%	0.50	0%	0.75	1%	0.50	0%	0.75	0.75	1%	1%
Cement	50%	50%	50%	50%	50%	50%	50%	50%	50%	50%	50%	50%	50%	50%	50%	50%	50%	50%
Class F fly ash	50%	50%	50%	50%	50%	50%	50%	50%	50%	50%	50%	50%	50%	50%	50%	50%	50%	50%
7 days (MPa)	25.2	31.6	35.3	34.8	36.6	33.6	35.7	37.8	33.3	33.2	44.2	33.1	37.4	36.6	46.9	41.1	44.7	38.2

Figure 1: Comparison of compressive strength between control concrete (50% cement, 50% fly ash, and no fibers) and hybrid fiber mixes at 7 days.

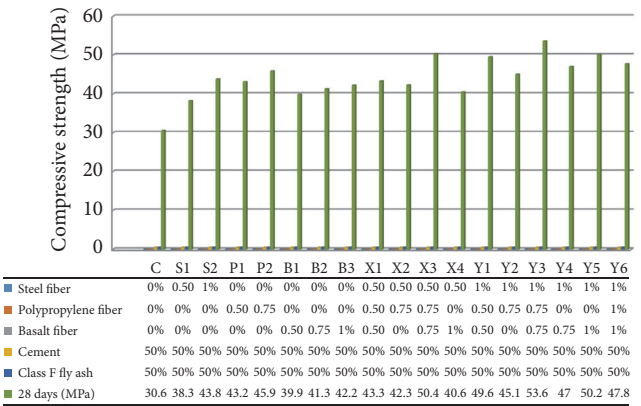

	C	S1	S2	P1	P2	B1	B2	B3	X1	X2	X3	X4	Y1	Y2	Y3	Y4	Y5	Y6
Steel fiber	0%	0.50	1%	0%	0%	0%	0%	0%	0.50	0.50	0.50	0.50	1%	1%	1%	1%	1%	1%
Polypropylene fiber	0%	0%	0%	0.50	0.75	0%	0%	0%	0.50	0.75	0.75	0%	0.50	0.75	0.75	0%	0%	1%
Basalt fiber	0%	0%	0%	0%	0%	0.50	0.75	1%	0.50	0%	0.75	1%	0.50	0%	0.75	0.75	1%	1%
Cement	50%	50%	50%	50%	50%	50%	50%	50%	50%	50%	50%	50%	50%	50%	50%	50%	50%	50%
Class F fly ash	50%	50%	50%	50%	50%	50%	50%	50%	50%	50%	50%	50%	50%	50%	50%	50%	50%	50%
28 days (MPa)	30.6	38.3	43.8	43.2	45.9	39.9	41.3	42.2	43.3	42.3	50.4	40.6	49.6	45.1	53.6	47	50.2	47.8

Figure 2: Comparison of compressive strength between control concrete (50% cement, 50% fly ash, and no fibers) and hybrid fiber mixes at 28 days.

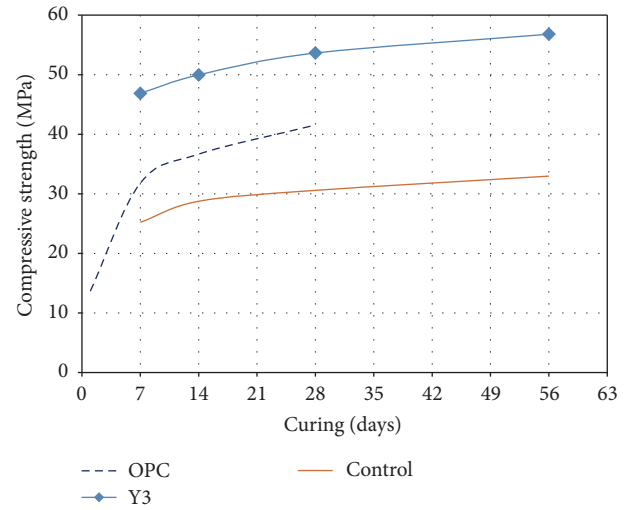

Figure 3: Comparison of compressive strength for hybrid fiber mix Y3 and control mix with compressive strength of OPC from Çolak [10].

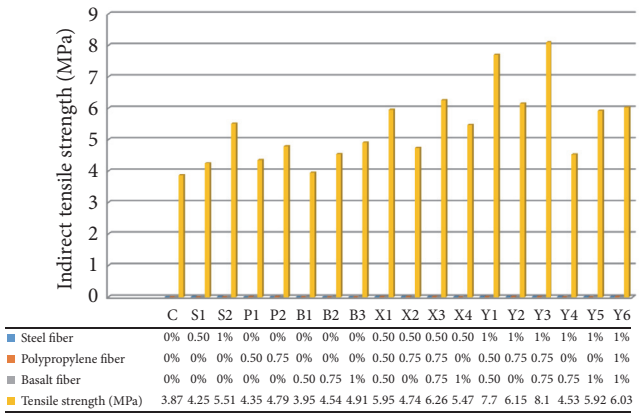

Figure 4: Comparison of indirect tensile strength for hybrid fibers at 28 days.

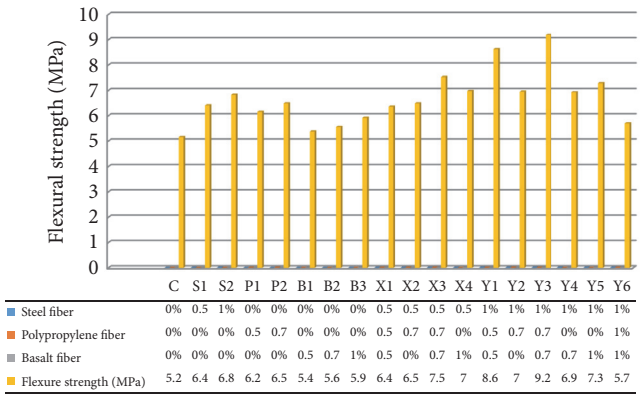

Figure 5: Comparison of flexural strength for hybrid fiber mixes at 28 days.

Comparing indirect tensile strength test results, Y1 (1% steel fiber, 0.5% polypropylene fiber, and 0.5% basalt fiber) and Y3 (1% steel fiber, 0.75% polypropylene fiber, and 0.75% basalt fiber) in hybrid form give higher tensile strength when compared to control concrete and individual fibers.

3.3. Flexural Strength from Four-Point Bending Tests. Figure 5 presents the comparison of flexural strength test results at 3 days, 7 days, 14 days, 28 days, and 56 days. Slight increase in strengths can be observed throughout the duration of observation. Comparing flexural strength test results, Y1 (1% steel fiber, 0.5% polypropylene fiber, and 0.5% basalt fiber) and Y3 (1% steel fiber, 0.75% polypropylene fiber, and 0.75% basalt fiber) in hybrid form give maximum flexural strength when compared to control concrete, individual fiber reinforced high volume fly ash concrete, and other hybrid mix.

Clearly the above figures have shown that the mix Y3 has significantly higher values across the testing regime. Brief investigations of the contribution of different mix proportions to the three strengths were analysed using strength values obtained at 28 days. First, the contribution of individual fibers is presented in Figure 6. It is interesting to

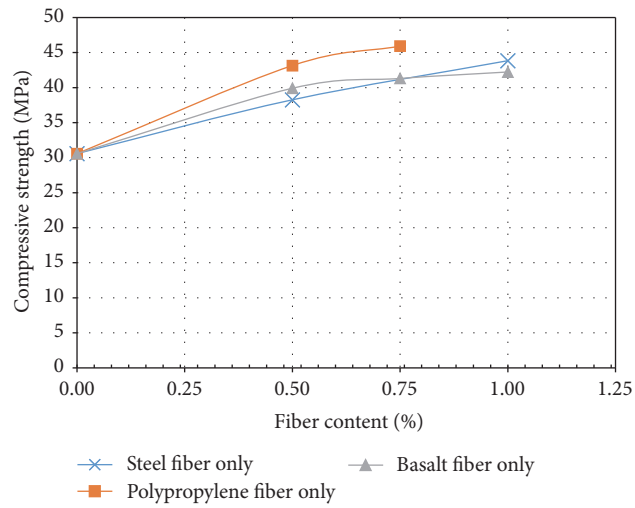

Figure 6: Comparison of compressive strengths in individual fiber mix.

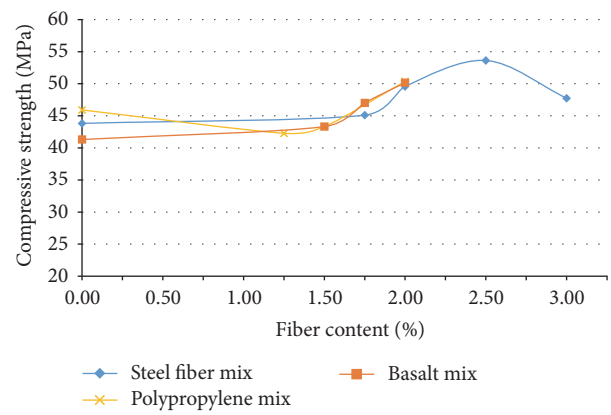

Figure 7: Comparison of compressive strengths with fiber mix at different proportions.

note that polypropylene fiber provides higher initial strengths although it starts to flatten out around 0.75%. A similar but low level of strength is observed for basalt fiber. However the trend line for steel is linear up to 1%. This observation suggests that an increase in steel fiber may be desirable although the use of basalt and polypropylene fibers beyond 0.75% may not be necessary. This observation from Figure 6 is quite interesting as the results show a higher strength value for the Y3 mix (i.e., 1% steel, 0.75% polypropylene, and 0.75% basalt). We also observed the workability of concrete to be affected when the combined percentage exceeded 3%.

A comparison of compressive strengths with hybrid combination is presented in Figure 7. It can be seen that hybrid combinations up to 1.75% lead to similar strengths but the noticeable jump is observed only at Y3 combination (a total of 2.5% with 1% steel and polypropylene and basalt at 0.75%) and when all the three mixed at 3% the values drop down significantly.

Figure 8: Specimens cast and ready for testing.

(a) (b)

Figure 9: Crack patterns at ultimate failure load: control specimen (a) and specimen (Y3) (b). Reduced cracks in Y3 specimen.

4. Concluding Remarks

This paper has shown that three fibers (steel, polypropylene, and basalt) can be added in a hybrid combination to achieve compressive strengths higher than the normal OPC. In particular, a hybrid combination of 1% steel, 0.75% polypropylene, and 0.75% basalt provided the highest strength results in terms of common mechanical properties. The paper has also shown that significant increase in flexural strength and tensile strengths can be observed simultaneously leading to the suggestion that some of the negative effects of individual fiber additions can be avoided using the hybrid fiber combination. A limiting combination of 3% overall has also been determined based on the workability of concrete. Further work may include the analysis of specimens in terms of matrix formulations, cracking behavior, and concrete toughness.

Appendix

See Table 2. For photos of specimens see Figures 8 and 9.

Competing Interests

The authors declare that there is no conflict of interests regarding the publication of the paper.

References

[1] V. M. Malhotra, "Durability of concrete incorporating high-volume of low-calcium (ASTM Class F) fly ash," *Cement and Concrete Composites*, vol. 12, no. 4, pp. 271–277, 1990.

[2] J. A. G. Thomas, "Fibre composites as construction materials," *Composites*, vol. 3, no. 2, pp. 62–64, 1972.

[3] A. E. Naaman and V. S. Gopalaratnam, "Impact properties of steel fibre reinforced concrete in bending," *International Journal of Cement Composites and Lightweight Concrete*, vol. 5, no. 4, pp. 225–233, 1983.

[4] M. Maalej, S. T. Quek, and J. Zhang, "Behavior of hybrid-fiber engineered cementitious composites subjected to dynamic tensile loading and projectile impact," *Journal of Materials in Civil Engineering*, vol. 17, no. 2, pp. 143–152, 2005.

[5] X. Luo, W. Sun, and S. Y. N. Chan, "Characteristics of high-performance steel fiber-reinforced concrete subject to high velocity impact," *Cement and Concrete Research*, vol. 30, no. 6, pp. 907–914, 2000.

[6] D. J. Hannant, "Durability of polypropylene fibers in Portland cement-based composites: eighteen years of data," *Cement and Concrete Research*, vol. 28, no. 12, pp. 1809–1817, 1998.

[7] R. F. Zollo, "Fiber-reinforced concrete: an overview after 30 years of development," *Cement and Concrete Composites*, vol. 19, no. 2, pp. 107–122, 1997.

[8] T. C. Yet, R. Hamid, and M. Kasmuri, "Dynamic stress-strain behaviour of steel fiber reinforced high-performance concrete

with fly ash," *Advances in Civil Engineering*, vol. 2012, Article ID 907431, 6 pages, 2012.

[9] P. Zhang and Q.-F. Li, "Effect of polypropylene fiber on durability of concrete composite containing fly ash and silica fume," *Composites Part B: Engineering*, vol. 45, no. 1, pp. 1587–1594, 2013.

[10] A. Çolak, "A new model for the estimation of compressive strength of Portland cement concrete," *Cement and Concrete Research*, vol. 36, no. 7, pp. 1409–1413, 2006.

[11] C. X. Qian and P. Stroeven, "Development of hybrid polypropylene-steel fibre-reinforced concrete," *Cement and Concrete Research*, vol. 30, no. 1, pp. 63–69, 2000.

[12] W. Yao, J. Li, and K. Wu, "Mechanical properties of hybrid fiber-reinforced concrete at low fiber volume fraction," *Cement and Concrete Research*, vol. 33, no. 1, pp. 27–30, 2003.

[13] N. Banthia and R. Gupta, "Influence of polypropylene fiber geometry on plastic shrinkage cracking in concrete," *Cement and Concrete Research*, vol. 36, no. 7, pp. 1263–1267, 2006.

[14] A. M. Alhozaimy, P. Soroushian, and F. Mirza, "Mechanical properties of polypropylene fiber reinforced concrete and the effects of pozzolanic materials," *Cement & Concrete Composites*, vol. 18, no. 2, pp. 85–92, 1996.

[15] H. A. Toutanji, "Properties of polypropylene fiber reinforced silica fume expansive-cement concrete," *Construction and Building Materials*, vol. 13, no. 4, pp. 171–177, 1999.

[16] K. Komloš, B. Babál, and T. Nürnbergerová, "Hybrid fibre-reinforced concrete under repeated loading," *Nuclear Engineering and Design*, vol. 156, no. 1–2, pp. 195–200, 1995.

[17] R. Bagherzadeh, A.-H. Sadeghi, and M. Latifi, "Utilizing polypropylene fibers to improve physical and mechanical properties of concrete," *Textile Research Journal*, vol. 82, no. 1, pp. 88–96, 2012.

[18] O. Kayali, "Effect of high volume fly ash on mechanical properties of fiber reinforced concrete," *Materials and Structures*, vol. 37, no. 269, pp. 318–327, 2004.

[19] W. M. Li and J. Y. Xu, "Mechanical properties of basalt fiber reinforced geopolymeric concrete under impact loading," *Materials Science and Engineering A*, vol. 505, no. 1-2, pp. 178–186, 2009.

[20] T. Ayub, N. Shafiq, and F. M. Nuruddin, "Mechanical properties of high-performance concrete reinforced with basalt fibers," *Procedia Engineering*, vol. 77, pp. 131–139, 2014.

[21] C. H. Jiang, K. Fan, F. Wu, and D. Chen, "Experimental study on the mechanical properties and microstructure of chopped basalt fibre reinforced concrete," *Materials & Design*, vol. 58, pp. 187–193, 2014.

[22] N. Kabay, "Abrasion resistance and fracture energy of concretes with basalt fiber," *Construction and Building Materials*, vol. 50, pp. 95–101, 2014.

[23] J. Sim, C. Park, and D. Y. Moon, "Characteristics of basalt fiber as a strengthening material for concrete structures," *Composites Part B: Engineering*, vol. 36, no. 6-7, pp. 504–512, 2005.

[24] M. Solikin, S. Setunge, and I. Patnaikuni, "Experimental design analysis of ultra fine flyash, lime water, and basalt fiber in mix proportion of high volume flyash concrete," in *Proceedings of the 3rd CUTSE International Conference*, Sarawak, Malaysia, November 2013.

[25] AS 1012.9, *Method 9: Determination of the Compressive Strength of Concrete Specimens*, Australian Standard Comittee, Strathfield, Australia, 1999.

[26] AS 1012.10, *Methods of Testing Concrete. Method 10: Determination of Indirect Tensile Strength of Conrete Cylinders ("Brazil" or Splitting Test)*, Australian Standard Association, Sydney, Australia, 2000.

[27] AS 1012.11, *Method 11: Determination of the Modulus of Rupture*, Australian Standard Committee, Strathfield, Australia, 2000.

[28] AS 3600, *Concrete Structures*, Standards Australia, Sydney, Australia, 2009.

Hindawi Publishing Corporation
Advances in Materials Science and Engineering
Volume 2016, Article ID 9838213, 9 pages
http://dx.doi.org/10.1155/2016/9838213

Research Article

Predicting Pumpability and Shootability of Crushed Aggregate Wet-Mix Shotcrete Based on Rheological Properties

Kyong-Ku Yun,[1] Pangil Choi,[2] and Jung Heum Yeon[3]

[1]*Department of Civil Engineering, Kangwon National University, Chuncheon 24341, Republic of Korea*
[2]*Department of Civil and Environmental Engineering, Texas Tech University, Lubbock, TX 79409, USA*
[3]*Department of Civil and Environmental Engineering, Gachon University, Seongnam 13120, Republic of Korea*

Correspondence should be addressed to Jung Heum Yeon; jyeon@gachon.ac.kr

Received 4 October 2016; Accepted 17 October 2016

Academic Editor: Doo-Yeol Yoo

This study aims to estimate the pumpability and shootability of wet-mix shotcrete (WMS) made with crushed aggregates and various admixtures such as silica fume, fly ash, ground granulated blast furnace slag (GGBFS), metakaolin, and steel fiber based on rheological properties. The IBB rheometer was employed as an apparatus to measure the rheological properties of freshly mixed shotcrete such as flow resistance and torque viscosity. Results have shown that the use of silica fume and metakaolin led to satisfactory pumpability, whereas mixtures with fly ash and steel fiber failed to meet the pumping criteria at normal pump pressure. The build-up thickness, an indicator to represent shotcrete shootability, was predicted to vary between 68 and 218 mm, demonstrating that the use of admixtures resulted in a wide spectrum of shootability. In particular, the use of metakaolin was found to substantially increase the predicted build-up thickness only with a small replacement. The findings of this study are expected to be used as an easy-to-use guideline for estimating pumpability and shootability of WMS when no compliance testing data is available.

1. Introduction

Pumpability and shootability are important functional parameters considered in the design procedure for wet-mix shotcrete (WMS) mixtures [1]. Even if mechanical and durability performance requirements are met, shotcrete may not perform per the design intent without proper pumpability and shootability. Commonly, pumpability of WMS has been quantified via pump pressure and power requirement measurements [2–6]. Because such methods offer visual examinations of the pumpability in real time, relatively accurate and reliable data can be obtained. However, since the measured pump pressure and power requirement are subjected to large variations depending on the pumping equipment used, new compliance testing to assess actual pumpability is necessary whenever there is a change in equipment or process for a given project. This step often involves inefficient, time-consuming, and labor-intensive tasks as the compliance testing needs to be conducted under actual field conditions.

One feasible approach to address this limitation is to indirectly estimate the pumpability through rheological properties of fresh materials, namely, yield stress and plastic viscosity of the Bingham model (or equivalent). Several studies have been conducted to estimate the pumpability of normal- and high-performance shotcrete/concrete based on the rheology and other flow characteristics. Browne and Bamforth [5] attempted to predict the pumpability of fresh concrete based on slump and pressure bleed tests. Beaupre [1] correlated the rheological parameters (i.e., flow resistance and torque viscosity) of WMS to pumpability through piston pressure measurements. Burns [7] characterized WMS pumped through small-diameter hoses by identifying the relationship among rheology, tribology, and pump pressure based on a solid scientific approach. McAskill [8] proposed technical tips to prevent pumping problems during wet-mix process. Seo [9] carried out an experimental study to evaluate the pumpability and fluidity of concrete on the basis of rheological properties. Kwon et al. [10] quantified the pumping characteristics of high-strength concrete by means of

a continuous pumping system. Yun et al. [11] assessed the rheological properties of WMS with various mineral and chemical admixtures and correlated them to pumpability by measuring piston pump pressure.

Even though many theoretical and practical research attempts to quantify the pumpability of WMS have been made based on prevailing theories of rheology, research studies on shootability predictions have been relatively limited. This is because the shootability is generally subjected to a number of construction uncertainties (such as workmanship of a nozzle operator and field conditions including climates as well as equipment/method used), which made the research approach towards shootability estimation quite challenging [11]. Moreover, most previous studies have been limited to assessing the pumpability and shootability of mixtures with natural aggregate sources such as river gravel. In recognition of the issues, this paper contributes to providing a simple empirical methodology to predict the pumpability and shootability of WMS containing crushed aggregate obtained from tunnel excavation and different type and dosage of admixtures based on rheological measurements, along with performance criteria given in previous research [1]. In addition, dosage ranges for each admixture that provide proper pumpability and shootability were provided to serve as an implementation guideline for WMS. The findings from this study would provide an advanced understanding of fresh WMS behavior, as well as an easy-to-use prediction scheme for pumpability and shootability of WMS.

2. Experimental

2.1. Materials. A commercially available Type I portland cement complying with KS L 5201 was employed. The specific gravity and fineness of the portland cement used were 3.15 and 3,289 cm^2/g, respectively. The chemical compositions were as follows: 20.8% SiO_2, 6.3% Al_2O_3, 61.2% CaO, 3.3% MgO, 2.3% SO_3, and 0.61% loss-on-ignition (LOI).

Crushed granite obtained from the surrounding rock of tunnel walls was used as coarse aggregate after being sieved and washed. The coarse aggregate used had a maximum aggregate size of 10 mm, a specific gravity of 2.65, and a fineness modulus of 5.70. As fine aggregate, washed crushed sand with a specific gravity of 2.62 and a fineness modulus of 2.77 was employed. The coarse and fine aggregates used in this study conformed to the gradation specifications of ASTM C33.

A Type I fly ash as per the classification of the Korean Industrial Standards (KS) was used. The chemical properties of the fly ash used were 41.5% SiO_2, 16.8% C, 22.9% Al_2O_3, 4.91% CaO, and 1.84% Fe_2O_3, all of which met the requirements of KS L 5405. The density of the fly ash used was 2.25 g/cm^3, which complied with the specified lower limit of 1.95 g/cm^3.

Silica fume with a density of 3.0–3.5 g/cm^3, a specific surface area of 200,470 cm^2/g, a 0–45 μm particle size portion of 98.0% (by weight), and a moisture content of 1.15% was employed. The chemical compositions of the silica fume used were as follows: 90.4% SiO_2, 2.0% CaO, 3.0% Fe_2O_3, 1.5% Al_2O_3, and 2.72% LOI.

Ground granulated blast furnace slag (GGBFS) with a density of 2.90 g/cm^3, a specific surface area of 4,306 cm^2/g, an activity index at 91 days of 117, and a flow of 102% was used. The chemical properties of the GGBFS used were as follows: 5.61% MgO, 1.0% SO_3, 0.43% LOI, and 0.007% chloride ion.

Metakaolin with a specific gravity of 2.63 and a specific area of 12,000 cm^2/g was adopted as a mineral admixture. The chemical compositions of the metakaolin used were 56% SiO_2, 37% Al_2O_3, 2.4% Fe_2O_3, 0.2% CaO, 0.3% MgO, 0.8% K_2O, and 0.2% Na_2O.

A bundle-type steel fiber with a density of 7.80 g/cm^3, a tensile strength of 1,195.5 MPa, and an aspect ratio of 60 (ϕ0.5 × 30 mm) was used as a reinforcing additive.

2.2. Mixture Proportions. 22 mixtures with a constant water-to-cementitious material ratio (w/cm) of 0.41 and a fine aggregate-to-total aggregate fraction (S/a) of 0.71 were prepared while varying replacement/addition levels as seen in Table 1. The mixture proportions were chosen based on a survey of previous research [1]. Except for the silica fume mixtures, a 9.1% silica fume replacement was consistently used to ensure suitable levels of pumpability and shootability, slump (220 mm), air contents before and after shooting (17 and 5%, resp.), and 28-day compressive strength (48 MPa). Dosages of sulfonate silica-based air-entraining agent and polycarboxylate-based superplasticizer were 0.044 and 4.84 kg/m^3, respectively, which were kept constant among the mixtures.

2.3. Methods

2.3.1. Rheometer Test. The IBB rheometer, of which the original and revisited designs were devised at The University of British Columbia and IBB Rheology Inc., respectively, was employed to monitor the rheological properties of freshly mixed shotcrete (see Figure 1). The apparatus is proven to accurately measure the rheological properties of fresh mixtures with inclusions of coarse aggregate [1, 11]. The testing procedure was as follows:

(1) Calibrate the torque resolution (±0.5 N·m) and set the built-in strain gage to a null position.

(2) Pour freshly mixed shotcrete into a 21-liter mixing bowl up to a level of 200 mm.

(3) Lift the mixing bowl until the H-shaped impeller is fully buried in the mixture.

(4) Begin operation with the lowest rotational speed, and gradually increase the speed as required.

During the operation, the torque applied to the rotary impeller as it stirs the mixture with a specified revolving speed was continuously measured by means of a load cell. The testing was conducted under a constant temperature condition of 23°C so as to eliminate the unexpected effect of temperature. Figure 2 presents an example of the obtained data, which was fitted by the following form of equation:

$$T = G + HN \quad (1)$$

Table 1: Mixture proportions of WMS.

Admixture	Replacement[1] (%)	Weight per unit volume (kg/m^3)							
		SF	FA	GGBFS	MK	C	W	F/A	C/A
SF	0	0	—	—	—	440	180	1159	480
	5	22	—	—	—	418	180	1153	478
	9.1	40	—	—	—	400	180	1149	476
	15	66	—	—	—	374	180	1142	473
FA	0	40	0	—	—	400	180	1149	476
	10	40	44	—	—	356	180	1137	471
	20	40	88	—	—	312	180	1125	466
	30	40	132	—	—	268	180	1113	461
GGBFS	0	40	—	0	—	400	180	1149	476
	10	40	—	44	—	356	180	1146	475
	20	40	—	88	—	312	180	1144	474
	30	40	—	132	—	268	180	1142	473
	40	40	—	176	—	224	180	1140	472
MK	0	40	—	—	0	400	180	1149	476
	5	40	—	—	22	378	180	1146	475
	10	40	—	—	44	356	180	1144	474
	15	40	—	—	66	334	180	1141	473
Steel fiber	0[2]	40	—	—	—	400	180	1149	476
	30[2]	40	—	—	—	400	180	1149	476
	40[2]	40	—	—	—	400	180	1149	476
	50[2]	40	—	—	—	400	180	1149	476
	60[2]	40	—	—	—	400	180	1149	476

Notes. SF = silica fume; FA = fly ash; GGBFS = ground granulated blast furnace slag; MK = metakaolin; C = cement; W = water; F/A = fine aggregate; and C/A = coarse aggregate.
[1]% by weight of total cementitious material content.
[2]A given weight per unit volume (kg/m^3) of steel fibers was added to mixtures.

in which T is the torque exerted on the rotary impeller (N·m); G is the flow resistance (N·m); H is the torque viscosity (N·m·s); and N is the angular speed of the rotary impeller (rev/s); in other words, the slope of the result plot denotes the torque viscosity, while the y-intercept denotes the flow resistance.

The torque viscosity and flow resistance have comparable physical meanings to yield stress and plastic viscosity, respectively, by definition of the Bingham model as follows [12]:

$$\tau_0 = 136G, \qquad \mu = 15.2H, \tag{2}$$

where τ_0 is the yield stress (Pa); G is the flow resistance (N·m); μ is the plastic viscosity (Pa·s); and H is the torque viscosity (N·m·s).

2.3.2. Pumpability Predictions. The pumpability of WMS was estimated based on previously published data by Beaupre [1]. Beaupre correlated the pumpability of various shotcrete mixtures (total 42 mixtures) with and without steel fibers subjected to different levels of pump pressure to their rheological parameters and then determined borderline values for flow resistance and torque viscosity, as shown in Figure 3. If a given mixture had flow resistance and torque viscosity smaller than the suggested borderline values (flow resistance $G = 4.3$ N·m and torque viscosity $H = 2.9$ N·m·s) at the same time, the mixture was considered "pumpable," whereas it was considered "nonpumpable" if either or both were greater than the borderline values.

2.3.3. Shootability Predictions. The shootability of WMS is often characterized by a build-up thickness. In this study, flow resistance was chosen as an indicator to predict the build-up thickness of WMS because the build-up thickness had a fairly proportional relationship to flow resistance (see Figure 4(a)), whereas it exhibited a quite random relationship with torque viscosity, particularly within the torque viscosity range of 0-1 N·m·s, as shown in Figure 4(b).

Two different relationships presented in former studies—one based on the two-point test [13] and the other based on the zero-speed measurement [1]—were used to construct a single equation that describes the relationship between the build-up thickness and flow resistance. As noted in Figure 4(a), the regression equation encompassing the two data sets yielded a high level of coefficient of determination of over 0.85, which would be reliably used to predict the build-up thickness once the flow resistance is determined via laboratory experiments.

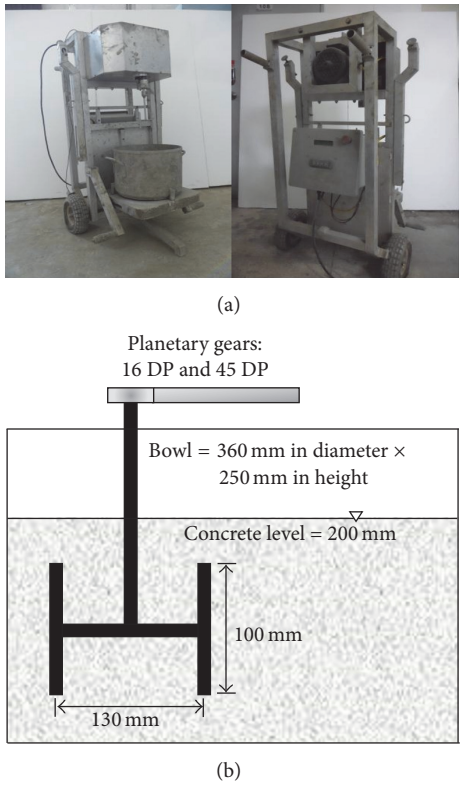

FIGURE 1: IBB rheometer: (a) front and rear view and (b) schematic diagram.

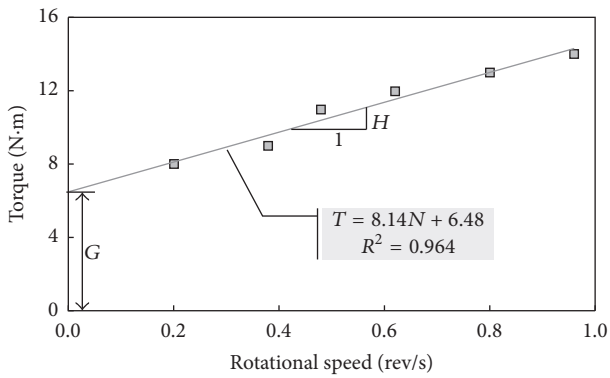

FIGURE 2: Typical data obtained from the IBB rheometer.

3. Results and Discussion

3.1. Rheological Behavior

3.1.1. Results. The results of rheometer tests for various silica fume mixtures are shown in Figure 5. The results indicate that increasing the silica fume replacement from 0 to 15% gradually increased the y-intercept of the regression line, thereby increasing the flow resistance. On the other hand, the silica fume replacement led to a general reduction in torque viscosity, but this reduction effect was pronounced only when

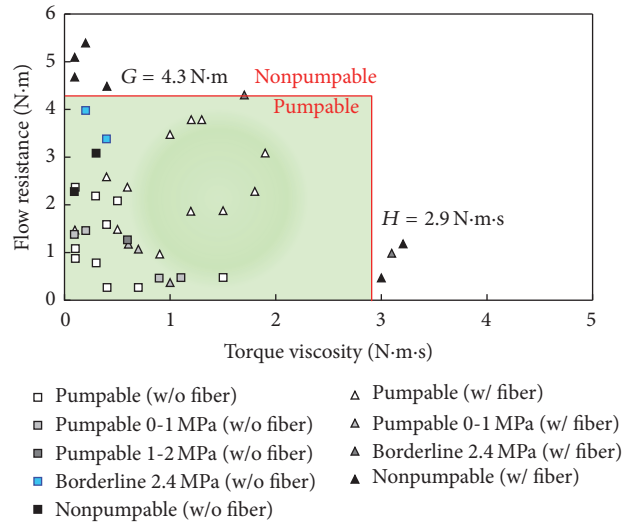

FIGURE 3: Rheological properties for different mixtures and their borderline values [1].

a 5% silica fume replacement was used, which was different from the findings of previous studies [1, 14].

Figure 6 shows the applied torque and angular speed relationships for mixtures containing fly ash with a 9.1% silica fume replacement. Note that the slope of the regression line significantly increased upon fly ash replacements, thereby increasing the torque viscosity. The rate of slope increase tended to decrease with increased fly ash replacement. Also, the use of fly ash led to a general increase in flow resistance by raising the y-intercept of the regression line. No evident difference in flow resistance was found between 20 and 30% mixtures.

The experimental data and their regression lines for GGBFS mixtures are presented in Figure 7. It is evident from the results that the GGBFS replacements lowered the flow resistance by shifting the regression line downwards along the y-axis, which may reduce the build-up thickness. In particular, a substantial reduction in flow resistance was detected when a 10% GGBFS replacement was used, even though it was quite difficult to discern evident discrepancies across the 20, 30, and 40% mixtures. There were no clear differences in the slope of the regression line among the GGBFS mixtures.

Figure 8 shows how the applied torque was varied to obtain prescribed impeller angular speeds for metakaolin mixtures with 9.1% silica fume. Note that no noticeable changes in flow resistance and torque viscosity were observed when 5% metakaolin was used compared with nonmetakaolin mixture. However, the flow resistance dramatically increased upon more than 10% metakaolin replacements, thereby increasing the predicted build-up thickness. A significant increase in torque viscosity was obtained when 15% metakaolin was used. This behavior is most likely attributed to the large specific surface area of the metakaolin used and eventual microfiller effect (i.e., dense packing of the cement matrix) [15].

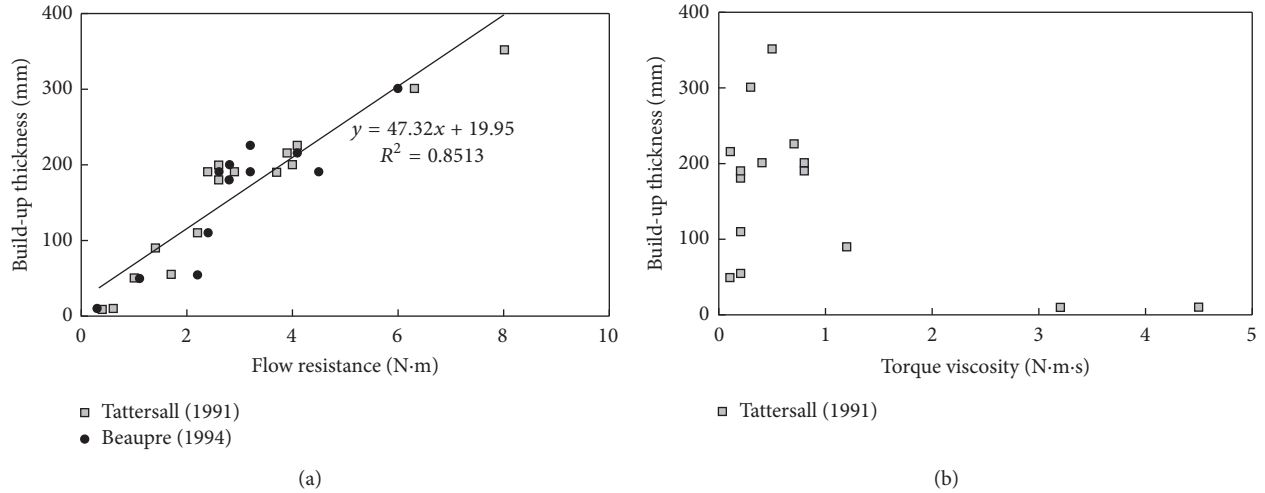

Figure 4: Relationships between rheological parameters and build-up thickness: (a) flow resistance versus build-up thickness; (b) torque viscosity versus build-up thickness [1].

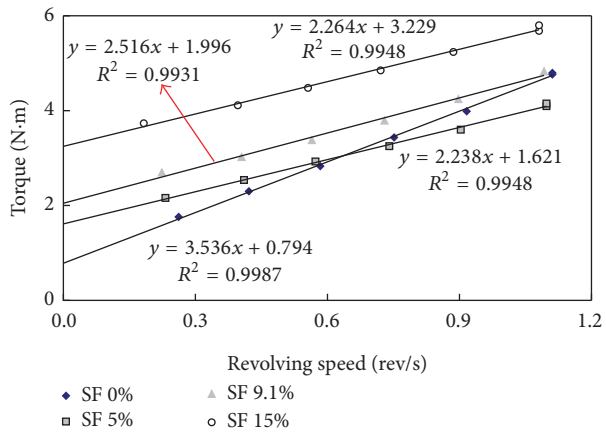

Figure 5: Exerted torque versus rotational speed relationship for silica fume mixtures.

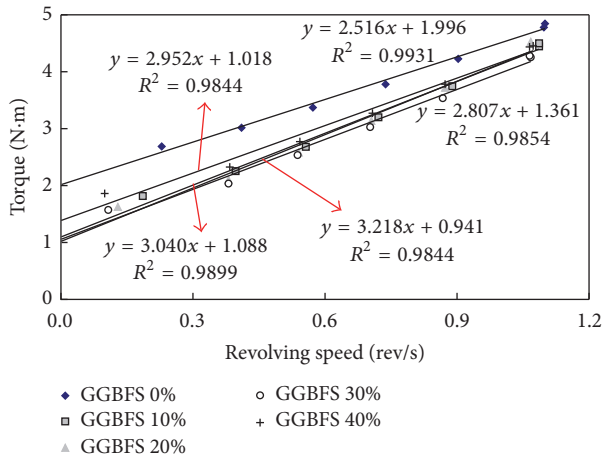

Figure 7: Exerted torque versus rotational speed relationship for GGBFS mixtures with 9.1% silica fume.

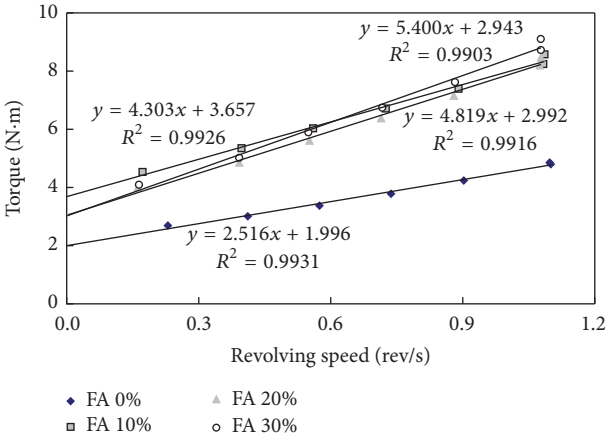

Figure 6: Exerted torque versus rotational speed relationship for fly ash mixtures with 9.1% silica fume.

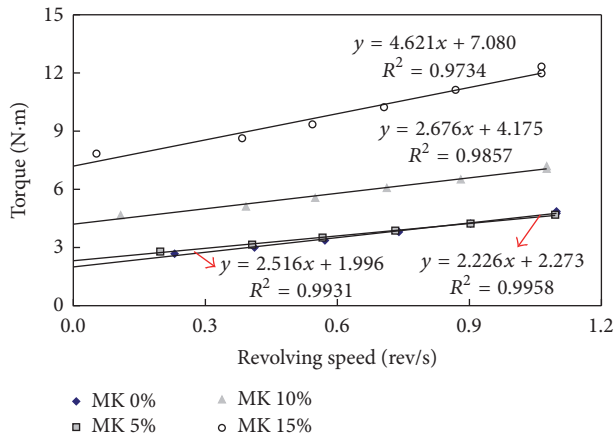

Figure 8: Exerted torque versus rotational speed relationship for metakaolin mixtures with 9.1% silica fume.

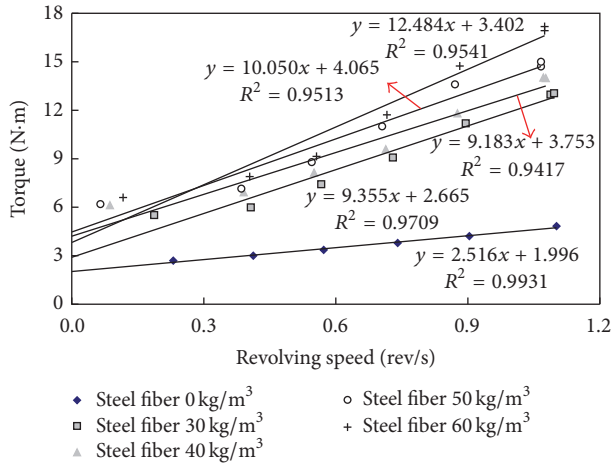

Figure 9: Exerted torque versus rotational speed relationship steel fiber mixtures with 9.1% silica.

The rheometer test results for steel fiber mixtures with a 9.1% silica fume replacement are given in Figure 9. As the results show, the regression lines for steel fiber mixtures were all above the regression line for non-steel fiber reinforced mixture, indicating that the steel fiber additions increased the flow resistance of WMS even though the trend was not consistent. Also noted is that the use of steel fibers resulted in regression lines with a greater slope, thereby reducing the pumpability of WMS. The pumpability reduction effect (or the torque viscosity-increasing effect) tended to become more pronounced when a high dosage (>50 kg/m^3) of steel fibers was used, which is quite unfavorable for WMS applications.

3.1.2. Discussion. Figures 10(a) and 10(b) illustrate the variations in flow resistance and torque viscosity depending on the admixture type and replacement level, drawn based on Figures 5–9. It is remarkable that the use of silica fume led to an overall decrease in torque viscosity, while increasing the flow resistance almost in proportion to the replacement level. This behavior would play a beneficial role in both pumpability and shootability, especially when applied to a project where strict build-up thickness control is required; for example, a silica fume replacement should be minimized when multiple-layer spraying is allowed, while it should be increased as required when single-layer spraying is needed. The fly ash replacement was found to worsen the pumpability of WMS by markedly increasing the torque viscosity, while improving the shootability. The use of GGBFS had a negligible effect on the pumpability by maintaining a similar level of torque viscosity, while reducing the shootability. Metakaolin was predicted to have the most significant effect on the shootability increase particularly when more than 10% replacement was used, although a substantial increase in torque viscosity occurred upon 15% replacement. Accordingly, a maximum of 10% replacement is recommended to exploit the benefits of metakaolin in shootability, without adversely affecting the pumpability. Steel fiber additions were likely to cause severe pumping problems as the torque viscosity of steel fiber mixtures was 3.6 to 5 times as high as that of controlled mixture. Thus, caution should be taken when steel fibers are selected as a reinforcing additive for WMS.

3.2. Pumpability Predictions Based on Rheological Properties. Figure 11 graphically summarizes the results of pumpability prediction for each WMS mixture, in which the area surrounded by the red dotted lines is the "pumpable" zone identified by the previous study [1]. The zoom-in view around the "pumpable" zone is also given in the top right corner of the plot. The results have shown that three silica fume mixtures (i.e., 5, 9.1, and 15% mixtures) fell within the "pumpable" zone, meeting the suggested threshold values for rheological parameters (which enables WMS to be pumped at normal pump pressure) while non-silica fume mixture failed to meet the criteria. This was obtained most probably because an adequate amount of spherical silica fume particles incorporated promoted the ball-bearing effect and prevented the drainage of lubricating water from the cement paste matrix, lowering the torque viscosity of the mixtures [16]. Also noted is that the flow resistance increment between 5 and 15% mixtures was about twice that between 5 and 9.1% mixtures, while maintaining a similar level of torque viscosity. This implies that, as previously mentioned, the use of silica fume is quite effective in increasing the build-up thickness, even without the use of accelerator.

Furthermore, the results of pumpability prediction for fly ash mixtures are presented in Figure 11. It can be seen that the pumpable condition was achieved only when no fly ash was used, while all mixtures with fly replacements (i.e., 10, 20, and 30%) fell on the "nonpumpable" zone. To make the fly ash mixtures pumpable by reducing the torque viscosity, an air-entraining agent (AEA) may be used [17], but the use of AEA was found to rather decrease the pumpability and air content because part of the AEA was adsorbed by unburned carbon in fly ash. To obtain the required pumpability, thus, a greater dosage of AEA is recommended in consideration of the AEA losses due to adsorption, as well as the fineness of the fly ash used.

When GGBFS was used, two mixtures (i.e., 0 and 40%) successfully obtained the pumpable condition, while other mixtures failed to meet the pumping requirements. However, it appears that the GGBFS itself had a nonsignificant effect on the pumpability because the variations in torque viscosity and flow resistance per the replacement level were quite small compared with other mixture groups. This, in turn, implies that the high fineness of the GGBFS used (4,310 cm^2/g) had a minimal effect on the rheological properties of WMS.

The results given in Figure 11 also show how the use of metakaolin affected the pumpability of WMS. It should be noted that the 5% metakaolin mixture rather had smaller torque viscosity and greater flow resistance compared to non-metakaolin mixture. The metakaolin mixtures were found to satisfy the pumpable criteria until the replacement level increased up to 10%, which demonstrates that metakaolin can be a good alternative or complement to silica fume. However, because more than 10% metakaolin replacement may degrade the pumpability by providing a substantial

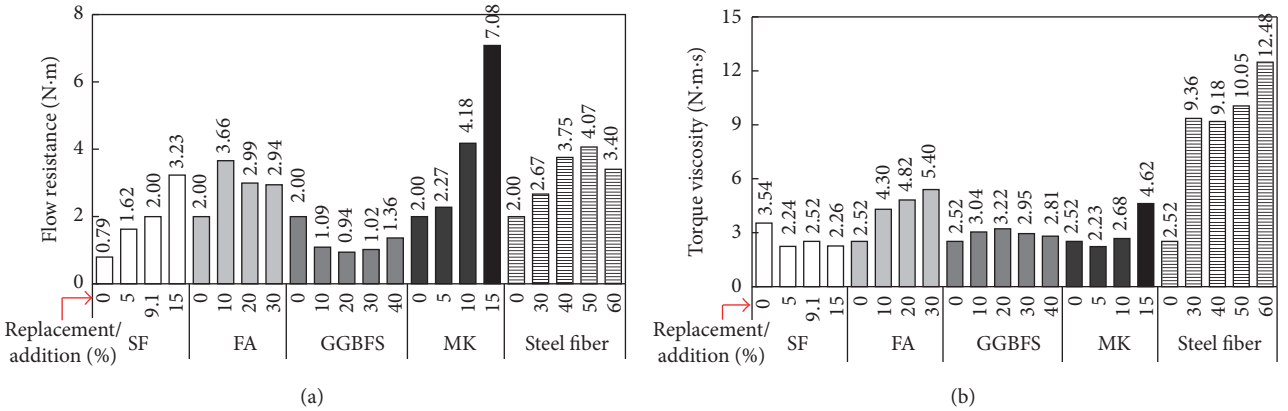

Figure 10: Variations in rheological properties for various WMS mixtures: (a) variations in flow resistance and (b) variations in torque viscosity.

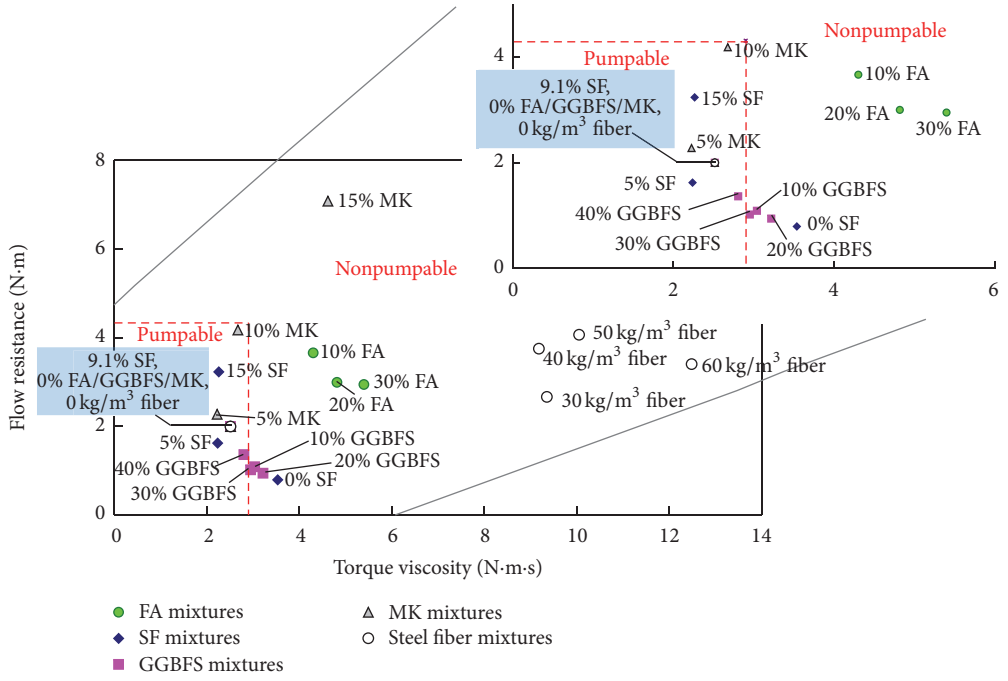

Figure 11: Pumpability predictions for various WMS mixtures.

increase in both torque viscosity and flow resistance, no more than 10% replacement is recommended when metakaolin is chosen as a mineral admixture for WMS.

All mixtures with steel fibers were found to fall on the "nonpumpable" zone. This is because the steel fiber additions enormously increased the torque viscosity as high as 9.18–12.48 N·m·s—about 3.17–4.3 times greater than the border line value for torque viscosity—while keeping a similar level of initial slump (i.e., 215–230 mm). Accordingly, when steel fibers are to be used for a shotcrete project, compliance testing may need to be conducted prior to field practice to check the actual pumpability.

Table 2 provides the recommended replacement/addition ranges for each mixture group determined based on the rheometer test results and data from the previous study [1]. While some of silica fume, GGBFS, and metakaolin mixtures

Table 2: Recommended replacement/addition ranges for each admixture.

Mixture group	Pumpable (%)	Nonpumpable (%)
Silica fume only	5–15	<5
Fly ash	—	All
GGBFS	30–40	<30
9.1% silica fume		
Metakaolin	0–10	>10
Steel fiber	—	All

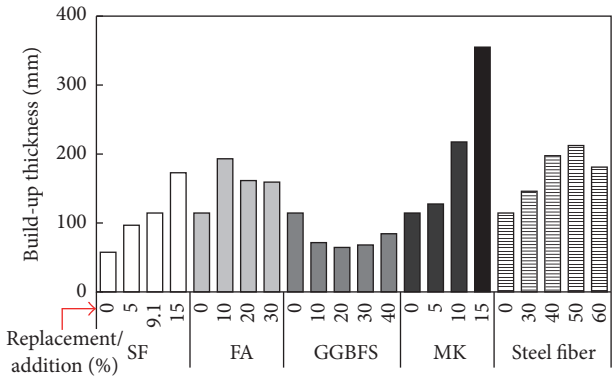

Figure 12: Shootability (build-up thickness) predictions for various WMS mixtures.

met the pumpable criteria, fly ash and steel fiber mixtures were all unpumpable for entire replacement/addition ranges. In particular, silica fume and metakaolin mixtures tended to meet the requirements only with relatively small replacement levels, which implies that silica fume and metakaolin may be used in WMS with good expected pumping performance. To implement those materials in actual shotcrete projects, additional research is needed to better understand how silica fume and metakaolin affect other material properties such as mechanical properties and durability.

3.3. Shootability Predictions Based on Flow Resistance. The build-up thickness of various WMS mixtures, as a measure of shootability, was predicted using the regression equation derived in Figure 4(a) and measured flow resistance, and the results are presented in Figure 12. The predicted build-up thickness for silica fume mixtures tended to increase as the silica fume replacement increased because the use of silica fume led to an increase in flow resistance. The shootability of 9.1% mixture was found to be worse than expected, because there was only a small increment in build-up thickness between 5 and 9.1% mixtures, compared with that between 0 and 5%. Also found is that the rate of build-up thickness increase substantially increased when the silica fume replacement exceeded 10%, which implies that modifications to mixture proportions may be needed for the control of build-up thickness when more than 10% silica fume replacement is expected.

The maximum build-up thickness for fly ash mixtures was obtained when 10% fly ash was used. The build-up thickness then decreased as the fly ash replacement increased above 10%. The inconsistent trend of build-up thickness changes according to the replacement level may be due to the effect of different air contents among the mixtures—the air contents for 0, 10, 20, and 30% fly ash mixtures were 18, 15, 11, and 10%, respectively. A further investigation needs to be conducted to clearly identify the sole influence of flow resistance on the build-up thickness.

The build-up thickness of GGBFS mixtures was predicted as 65–114 mm, which was relatively smaller than that of other mixtures. This is most likely because, as previously described, GGBFS gave rise to the ball-bearing effect, thereby increasing the workability of mixtures. Given the relatively smaller build-up thicknesses and little effect of GGBFS replacement level on the build-up thickness, it appears that GGBFS is not a suitable admixture for shootability improvements.

Table 3: Predicted build-up thickness ranges for WMS mixtures meeting pumping requirements.

Mixture group	Pumpable range (%)	Predicted build-up thickness (mm)
Silica fume only	5–15	97–173
Fly ash	—	—
GGBFS	30–40	68–84
9.1% silica fume		
Metakaolin	0–10	114–218
Steel fiber	—	—
Overall range	5–15	68–218

Metakaolin mixtures led to an overall increase in predicted build-up thickness with an increased metakaolin replacement. Specifically, a substantial increase in build-up thickness was observed when the replacement level became greater than 5%. This implies that caution should be taken to control the build-up thickness when proportioning shotcrete mixtures with more than 5% metakaolin, while up to 5% metakaolin can be used without essential modifications to mixture proportions.

The predicted build-up thickness for steel fiber mixtures was found to increase until the addition level reached up to 50 kg/m^3, whereas a noticeable reduction was observed at a higher addition level beyond 50 kg/m^3. Even though the build-up thicknesses predicted were overall sufficient for the use in actual practice, however, steel fiber may not be a suitable additive given the poor pumpability of WMS, as previously discussed.

Table 3 summarizes the ranges of predicted build-up thickness for each mixture group meeting the pumpability requirements. The results show that the predicted build-up thickness of 97–173 mm was achieved with silica fume replacements only. Metakaolin with 9.1% silica fume enabled the build-up thickness to vary in a broad range between 114 and 218 mm, whereas GGBFS with 9.1% silica fume resulted in only small variations in build-up thickness between 68 and 84 mm. In particular, a 10% metakaolin replacement provided a build-up thickness of up to 218 mm, which could be suitably used for massive construction. Build-up thickness predictions for fly ash and steel fibers mixtures could not be made since they did not comply with the pumping criteria at all. Based on the findings, metakaolin, when combined with silica fume, appears to be a promising admixture that effectively enhances both pumpability and shootability even with a small replacement level (i.e., less than 10%).

4. Conclusions and Recommendations

In this paper, the pumpability and shootability of wet-mix shotcrete (WMS) with crushed aggregates and various

admixtures were estimated based on a series of rheometer tests. Optimum replacement/addition ranges for each admixture were also proposed as a guideline for actual practice, along with expected build-up thicknesses upon shooting. Based on the findings of this study, the following conclusions can be made:

(i) Silica fume had positive effects on both pumpability and shootability by decreasing torque viscosity and increasing flow resistance simultaneously.

(ii) Fly ash replacements increased the torque viscosity of WMS, which may lead to poor pumpability.

(iii) Ground granulated blasted furnace slag (GGBFS) replacements tended to reduce the shootability of WMS, while it had a nonsignificant effect on the pumpability.

(iv) Metakaolin replacements significantly increased the shootability of WMS, while keeping a similar level of pumpability across the mixtures.

(v) Adding steel fibers resulted in a substantial increase in torque viscosity, which may not be a good strategy to enhance the pumping performance.

(vi) While all fly ash and steel fiber mixtures failed to meet the pumping requirements, several silica fume, GGBFS, and metakaolin mixtures complied with the pumping criteria at normal pump pressure. In particular, silica fume and metakaolin mixtures were found to have good pumping performance.

(vii) A wide range of build-up thicknesses between 68 and 218 mm was obtained for WMS mixtures with various type and dosage of admixtures. Particularly, the use of metakaolin dramatically increased the build-up thickness only with a 10% replacement.

The results outlined in this study would be used as a simple estimate of the pumpability and shootability predictions, as far as no compliance testing is conducted for a given project. A little more conservative approach is recommended taking into account the errors that may be caused by measurements and material variability. Future research will be performed to understand how the use of those admixtures plays a role in actual pumpability and shootability.

Competing Interests

The authors declare that there is no conflict of interests regarding the publication of this paper.

Acknowledgments

This research was supported by both grant A (13RDRP-B066780) and grant B (15TLRP-B079261-02), funded by Ministry of Land, Infrastructure and Transport of Korean government, and was partly supported by Kangwon National University (Grant no. 120131837), Chuncheon, Republic of Korea.

References

[1] D. Beaupre, *Rheology of high performance shotcrete [Ph.D. thesis]*, University of British Columbia, Vancouver, Canada, 1994.

[2] O. Dawson, "Pumping concrete—friction between concrete and pipeline," *Magazine of Concrete Research*, vol. 1, pp. 135–140, 1945.

[3] A. N. Ede, "The resistance of concrete pumped through pipelines," *Magazine of Concrete Research*, vol. 9, no. 27, pp. 129–140, 1957.

[4] J. E. Gary, "Laboratory procedure for comparing pumpability of concrete mixtures," *Proceedings of ASTM*, vol. 62, pp. 964–971, 1962.

[5] R. D. Browne and P. B. Bamforth, "Test to establish concrete pumpability," *ACI Journal*, vol. 74, pp. 193–203, 1977.

[6] G. M. Idorn, "Rheology in fresh concrete," in *Proceedings of the Materials Research Society Symposium*, Boston, Mass, USA, November 1982.

[7] D. Burns, *Characterization of wet-mix shotcrete for small line pumping [M.S. thesis]*, University of Laval, Quebec City, Canada, 2008.

[8] N. McAskill, "Overcoming pumping problems," *American Shotcrete Association Magazine*, vol. 2, no. 4, pp. 22–23, 2000.

[9] I. Seo, *Study on the evaluation of pumpability and fluidity of concrete using rheological parameters [M.S. thesis]*, Hanyang University, Ansan, South Korea, 2010.

[10] D.-H. Kwon, H.-S. Lee, J.-Y. Jeon, W.-T. Jeong, H.-K. Jo, and H.-R. Kim, "Evaluation of pumping characteristics of high strength concrete using continuous pumping system," *Journal of the Korea Institute of Building Construction*, vol. 11, no. 4, pp. 387–395, 2011.

[11] K.-K. Yun, P. Choi, and J. H. Yeon, "Correlating rheological properties to the pumpability and shootability of wet-mix shotcrete mixtures," *Construction and Building Materials*, vol. 98, pp. 884–891, 2015.

[12] G. H. Tattersall and P. F. G. Banfill, *The Rheology of Fresh Concrete*, Chapman & Hall, London, UK, 1983.

[13] G. H. Tattersall, *Workability and Quality Control of Concrete*, Chapman & Hall, London, UK, 1991.

[14] J. Wolsiefer and D. R. Morgan, "Silica fume in shotcrete," *Concrete International*, vol. 15, no. 4, pp. 34–39, 1993.

[15] P. Dinakar, P. K. Sahoo, and G. Sriram, "Effect of metakaolin content on the properties of high strength concrete," *International Journal of Concrete Structures and Materials*, vol. 7, no. 3, pp. 215–223, 2013.

[16] E. Sakai, Y. Kakinuma, K. Yamamoto, and M. Daimon, "Relation between the shape of silica fume and the fluidity of cement paste at low water to powder ratio," *Journal of Advanced Concrete Technology*, vol. 7, no. 1, pp. 13–20, 2009.

[17] K.-K. Yun, S.-Y. Choi, and J. H. Yeon, "Effects of admixtures on the rheological properties of high-performance wet-mix shotcrete mixtures," *Construction and Building Materials*, vol. 78, pp. 194–202, 2015.

Hindawi Publishing Corporation
Advances in Materials Science and Engineering
Volume 2016, Article ID 7261816, 10 pages
http://dx.doi.org/10.1155/2016/7261816

Research Article

Effect of Concrete Age and Creep on the Behavior of Concrete-Filled Steel Tube Columns

HaiYang Wang,[1,2] XiaoXiong Zha,[2] and Wei Feng[2]

[1]*School of Environment and Energy, Peking University Shenzhen Graduate School, Shenzhen 518055, China*
[2]*School of Civil and Environment Engineering, Harbin Institute of Technology Shenzhen Graduate School, Shenzhen 518055, China*

Correspondence should be addressed to XiaoXiong Zha; zhahero@126.com

Received 4 July 2016; Accepted 19 September 2016

Academic Editor: Doo-Yeol Yoo

The influence of concrete age and creep on the ultimate axial loading capacity of concrete-filled steel tube (CFST) columns is experimentally and numerically investigated. After validation of numerical models, a parametric study is conducted and the results are used to formulate empirical formulas for predicting the ultimate axial load-bearing capacity of the columns. Formulas are also proposed for predicting both the composite creep and aging coefficients of the CFST columns, which consider the confinement action of steel tubes on concrete. Then, the proposed formulas are validated independently by comparing their predictions with existing test results performed by other researchers. The comparisons show that the empirical formulas have the potential to be used in the practical design of CFST columns.

1. Introduction

Concrete-filled steel tube (CFST) columns have been extensively used in civil engineering structures over the past few decades. Extensive experimental and theoretical investigations on CFST components have been conducted and are well documented in the literature. The experimental work includes tests reported by O'Shea and Bridge [1] and Giakoumelis and Lam [2], who conducted research on the bearing capacity of short CFST columns. Zhong [3] and Zha [4] also reported their works on short and long CFST columns. Han et al. [5] and Wang [6] also studied property of the CFST under long-time load, while these results cannot be implemented conveniently considering the new code (GB50936-2014). Although significant work has been conducted on the properties of matured CFST columns, less emphasis has been placed on the influence of concrete age. Tan and Qi [7] have worked systematically by testing the effect of creep on columns under axially applied eccentric compressive load. Terry et al. [8] and Luo et al. [9] tested the creep of CFST columns and plain concrete in order to investigate the influence of steel tube reinforcement. Ichinose et al. [10] also reported a series of similar tests to obtain creep coefficients. Naguib and Mirmiran [11] and Liu et al. [12] developed an algorithm for the time-dependent behavior of CFST using the rate of flow method and the double power law functions for the creep of concrete. Shrestha and Chen [13] worked on the aging and creep coefficients of confined concrete, but the effect of steel tube was excluded in their formulas.

This study investigates the effect of concrete age and creep by experimental test and FEM modeling. Then, empirical formulas are proposed by treating a CFST column as a structural component made of a single material through homogenization.

2. Simulation and Methods

After pouring concrete into the steel tube, the elastic modulus of concrete increases with age. At the early stage, the steel tube is subjected to higher values of load than that specified by the design code. Thus, the ultimate bearing capacity of the CFST column is lower than the designed value. In this section, laboratory tests and FEM model are used to obtain the time-dependent load-bearing capacity. An empirical formula is established to provide a simple form of calculation for estimating the age-related ultimate load-bearing capacity.

Table 1: Geometrical and mechanical properties of the specimens.

D (mm)	T (mm)	L (mm)	f_y (MPa)	f_{ck} (MPa)	E_s (MPa)
219	4.5	766	345	40.7	2.06e5

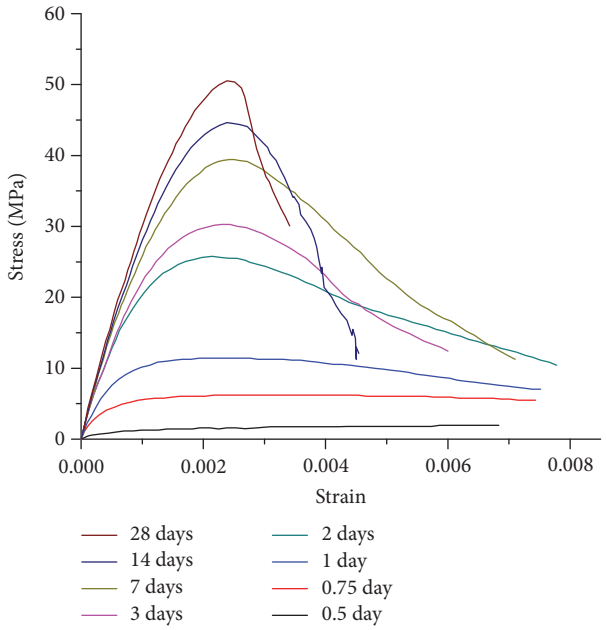

Figure 1: Stress strain relations of concrete at different ages.

2.1. FEM Modeling of CFST Columns. The numerical model is implemented in ABAQUS eight-node quadrilateral in-plane continuum shell elements which are used for the steel tube whereas the concrete is modeled employing eight-node linear brick element. The bilinear material model is adopted for the steel, with tangent modulus being 5% of the elastic modulus of 2.06e5 MPa. The material model used for the concrete is the damaged plasticity model, and hardening of concrete at different ages follows the curves proposed by Yi et al. [14], as shown in Figure 1. Other mechanical and geometrical parameters of the column are given in Table 1. FE meshes of both concrete and steel are shown in Figure 2. The contact between the steel tube and concrete is assumed to be perfect; here the nodes on the interface between solid and shell elements are tied.

Different meshing schemes are tested in order to assess the convergence of the FEM model, and the details are listed in Table 2, where N_Ring, N_Radius, and N_Axial are, respectively, the numbers of elements in the circumferential, radial, and axial directions. E_Section and E_Total are the total number of elements on a cross section and of the whole column, respectively. N_3 d and N_28 d are the ultimate axial loads of the column at ages of 3 days and 28 days.

Figure 3 shows terms of load against relative displacement of the different meshing FE model for concrete at the age 3 of and 28 days. With the increase in the number of elements, from M1 to M6, Table 2 shows the convergence of the ultimate load. When the elements number is more than that of M4, the difference between the different meshing schemes is nonsignificant. Therefore, meshing scheme M4 will be used in the following numerical simulations.

Laboratory tests have been conducted (see Figure 4) on the column specified in Table 1 in order to verify the FEM model. Load-bearing capacity tests are conducted at ages equal to 3, 7, 14, 21, 28, and 49 days.

The experimental test results of the time-dependent elastic modulus at different ages are shown in Table 3, and the load-bearing capacity of the CFST column is shown in Figure 5 as a function of the considered ages. Comparison between experimental and numerical results shows that the FE model can clearly predict the age-dependent load-bearing capacity.

2.2. Empirical Formula of the Age-Related Load-Bearing Capacity. Parametric studies on a variety of CFST columns presented in Table 4 are conducted to derive an empirical formula for the load-bearing capacity of the CFST columns, whose numerical results are presented in Table 5.

Supposing that the age-strength relationship of concrete in the steel tube has the same form as when it is unconfined, according to ACI-209 [15], the following equation can be established:

$$\frac{N_{\mathrm{ut}} - N_k}{N_{u28} - N_k} = \frac{t}{a + bt}, \tag{1}$$

where the two unknown constants in the equation can be estimated by fitting FE results presented in Table 5. Then, $a = 1.243$ and $b = 0.977$ are obtained with the maximum error of 3.4%. Therefore, the ultimate load-bearing capacity of the CFST column is obtained as follows:

$$N_{\mathrm{ut}} = N_k + \frac{(N_{u28} - N_k)\, t}{1.243 + 0.977t}. \tag{2}$$

The previously presented equation is validated through its application on the specimen defined in Table 1, and a comparison between experimental and numerical results is shown in Figure 6. F(exp) and F(FEM) are obtained applying (2) to the experimental and numerical results, respectively, shown in Figure 5. The predicted ultimate loading capacities obtained from the formula are consistent with those obtained from the experimental tests and FE modeling.

3. Influence of Creep on CFST Columns

In this section, a composite creep coefficient of CFST columns is proposed, in order to consider steel confinement, and the factor of the effective aging coefficient is obtained by regression on the FEM results.

3.1. Creep Coefficient of the CFST Column. Yi et al. [14] proposed the age-adjusted effective modulus method, also known as BT theory, which represents an effective method to analyze the long-term effect of concrete creep. An aging coefficient was introduced in order to consider the effect of

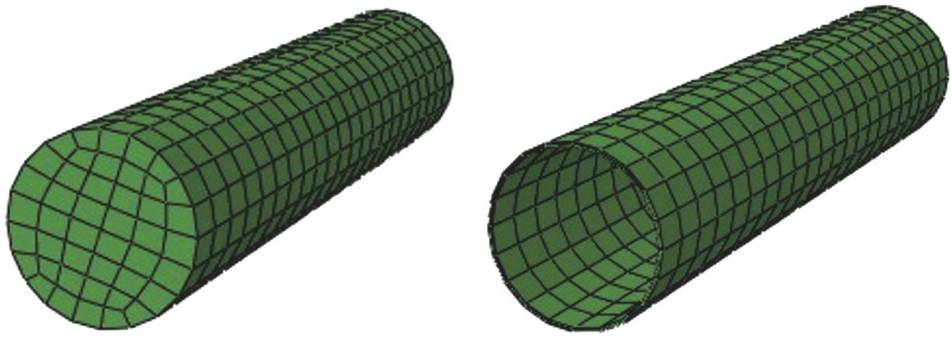

(a) (b)

Figure 2: Finite element mesh of (a) concrete and (b) steel tube.

Table 2: Meshes parameter and results.

Model	N_Ring	N_Radius	N_Axial	E_Section	E_Total	N_3 d (kN)	N_28 d (kN)
M1	12	2,3	18	56	1120	2240	2868
M2	12	3,4	18	68	1224	2256	2904
M3	16	3,4	18	96	1728	2285	2942
M4	20	3,4	18	104	1872	**2358**	**2965**
M5	24	3,4	18	132	2376	2372	2972
M6	28	3,4	18	160	2880	2377	2979

concrete aging on the ultimate creep, and the integral equation for creep was transformed into an algebraic equation by employing the integral mean value theorem.

When stress varies with time, the corresponding total strain at time t can be expressed as follows:

$$\varepsilon_c^c(t) = \frac{\sigma_{c1}^0(\tau_0)}{E_c(\tau_0)}\left[1+\varphi(t,\tau_0)\right] + \frac{1}{E_c(\tau_0)}\int_{\tau_0}^{t}\frac{d\sigma_{c1}(\tau)}{d\tau}\left[1+\varphi(t,\tau)\right]d\tau, \tag{3}$$

where $\varepsilon_c^c(t)$ is the strain of concrete when creep is with no steel confinement at age t days, $\sigma_{c1}^0(\tau_0)$ is the stress of the concrete at τ_0 days, $E_c(\tau_0)$ is the elastic modulus of concrete at τ_0 days, and $\varphi(t,\tau_0)$ is the creep coefficient at t when loaded at τ_0 days.

Applying the integral mean value theorem on formula (3) leads to

$$\varepsilon_c^c(t) = \frac{\sigma_{c1}^0(\tau_0)}{E_c(\tau_0)}\left[1+\varphi(t,\tau_0)\right] + \frac{\sigma_{c1}(t)-\sigma_{c1}^0(\tau_0)}{E_\varphi}. \tag{4}$$

Consider

$$E_\varphi = \frac{E_c(\tau_0)}{1+\rho\varphi(t,\tau_0)}, \tag{5}$$

where $\sigma_{c1}(t)$ is the stress of concrete at age of t days. E_φ is the age-adjusted effective modulus. ρ is the aging coefficient of concrete that is calculated as follows:

$$\rho = \frac{E_c(\tau_0)}{1-e^{-\varphi(t,\tau_0)}} - \frac{1}{\varphi(t,\tau_0)}. \tag{6}$$

The following calculation is based on the assumption of plane section and superposition principle of creep regardless of the toroidal shrinkage and strain. The axial strains of concrete and steel tube at age of τ_0 are denoted as ε_{c1}^0 and ε_{s1}^0, respectively, whereas σ_{c1}^0 and σ_{s1}^0 represent the related stresses. The creep of concrete with no steel confinement is $\varepsilon_c^c = \varepsilon_c^0\varphi(t,\tau_0)$ at the age of t. As a result of the effect of the steel tube confinement, the concrete creep is reduced to ε_{c1}^c, as shown in Figure 7.

It is clear that the strain increment of the steel tube is the actual concrete creep. Hence,

$$\begin{aligned}\varepsilon_{sc1}^c &= \varepsilon_{s1}^c,\\ \varepsilon_{s1}^c &= \varepsilon_c^c - \varepsilon_{c1}^c,\\ \varepsilon_{s1}^0 &= \varepsilon_{c1}^0,\end{aligned} \tag{7}$$

where ε_{sc1}^c is the axial creep strain of the CFST column, ε_{s1}^c is the axial strain of steel tube due to concrete creep, ε_c^c is the creep strain of the concrete with no steel confinement, ε_{c1}^c is the reduced strain of the concrete considering the steel tube confinement, ε_{s1}^0 is the strain of the steel tube when loaded at τ_0 days, and ε_{c1}^0 is the strain of the concrete when loaded at τ_0 days.

The total strain of CFST, or concrete in the steel tube, is derived as follows:

$$\varepsilon(t) = \varepsilon_{c1}^0 + \varepsilon_c^c - \varepsilon_{c1}^c. \tag{8}$$

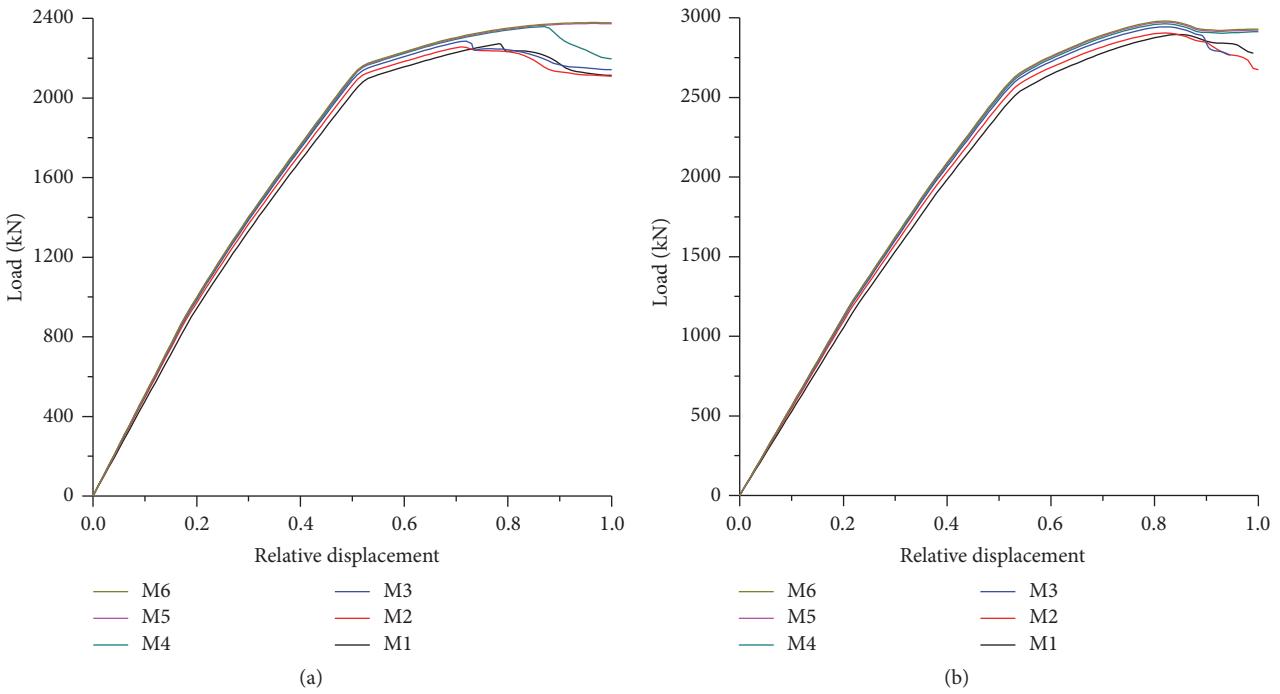

Figure 3: The load curve for different meshes at the (a) age of 3 days and (b) age of 28 days.

From (3), it becomes

$$\begin{aligned}\varepsilon(t) &= \frac{\sigma_{c1}^{0}}{E_c(\tau_0)}\left[1+\varphi(t,\tau_0)\right] \\ &\quad + \frac{1}{E_c(\tau_0)}\int_{\tau_0}^{t}\frac{d\sigma_{c1}(\tau)}{d\tau}\left[1+\varphi(t,\tau)\right]d\tau, \\ \varepsilon_{c1}^{0} &= \frac{\sigma_{c1}^{0}}{E_c(\tau_0)}, \\ \varepsilon_{c}^{c} &= \frac{\sigma_{c1}^{0}}{E_c(\tau_0)}\varphi(t,\tau_0).\end{aligned} \tag{9}$$

From (8) and (9), it is obtained that

$$\varepsilon_{c1}^{c} = -\frac{1}{E_c(\tau_0)}\int_{\tau_0}^{t}\frac{d\sigma_{c1}(\tau)}{d\tau}\left[1+\varphi(t,\tau)\right]d\tau \tag{10}$$

and by considering (4) and (5)

$$\begin{aligned}\varepsilon_{c1}^{c} &= -\frac{\left[1+\rho\varphi(t,\tau_0)\right]\left[\sigma_{c1}(t)-\sigma_{c1}^{0}\right]}{E_c(\tau_0)} \\ &= -\frac{\left[1+\rho\varphi(t,\tau_0)\right]\sigma_{c1}^{c}}{E_c(\tau_0)},\end{aligned} \tag{11}$$

where σ_{c1}^{c} is the stress change of the concrete due to creep. In spite of extensive microcracks that will be induced in the core as reported by previous researchers and splitting cracks that can occur at 30% to 40% stress [16–18], the cracks could close if they are subject to an outer sustained compression load at an early age. The confining stress would delay the formation of splitting cracks and restrict the widening of splitting cracks [19, 20], and the confinement effect appears based on the splitting cracks formation [21]. There will be no or little splitting cracks in the core concrete under the maximum sustained load after seven stages at an early age that is 40% bearing capacity of the specimens in the experiment and this had been contained naturally in the total creep. Therefore, the effect of splitting cracks on the creep was not considered separately here.

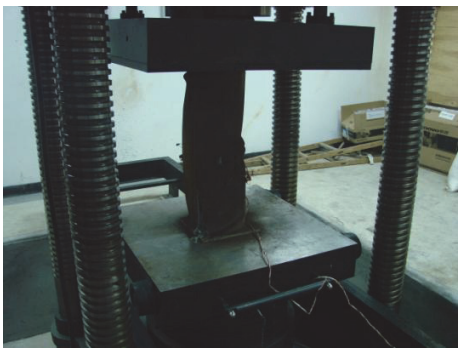

Figure 4: Load-bearing capacity test of the CFST column.

Table 3: Elastic modulus of the concrete at different age.

Age (days)	3	7	14	21	28
E_c (MPa)	30680	32319	34053	35101	35905

Table 4: Axially compressed short columns.

Number	$D \times T \times L$ (mm)	f_y (MPa)	f_{ck} (MPa)	α	ξ
1	$1000 \times 12 \times 3000$	345	40.7	0.050	0.422
2	$1000 \times 18 \times 3000$	345	40.7	0.076	0.645
3	$1000 \times 24 \times 3000$	345	40.7	0.103	0.876
4	$1000 \times 30 \times 3000$	345	40.7	0.132	1.117
5	$1000 \times 36 \times 3000$	345	40.7	0.161	1.366

α is the area ratio of the steel with respect to that of concrete ($\alpha = A_s/A_c$), whereas ξ is the hoop effect coefficient ($\xi = A_s f_y / A_c f_{ck}$).

The equilibrium force condition in the axial direction satisfies the following equations:

$$\sigma_{c1}^{c} A_c + \sigma_{s1}^{c} A_s = 0,$$
$$\sigma_{c1}^{c} = -\frac{A_s \sigma_{s1}^{c}}{A_c} = -\alpha \sigma_{s1}^{c}, \tag{12}$$

where σ_{s1}^{c} is the stress change of steel tube due to creep.

Not considering the creep of the steel tube and taking steel as elastic modulus value a constant give

$$\varepsilon_{s1}^{c} = \frac{\sigma_{s1}^{c}}{E_s} = -\frac{\sigma_{c1}^{c}}{\alpha E_s} \tag{13}$$

and (11) becomes

$$\frac{\sigma_{c1}^{0}}{E_c(\tau_0)} \varphi(t, \tau_0) + \frac{[1 + \rho\varphi(t, \tau_0)]\, \sigma_{c1}^{c}}{E_c(\tau_0)} = -\frac{\sigma_{c1}^{c}}{\alpha E_s}; \tag{14}$$

letting $n = E_s/E_c(\tau_0)$ in (14), the change in stresses on concrete and steel tube because of the concrete creep is expressed as follows:

$$\sigma_{c1}^{c} = -\frac{\alpha n \sigma_{c1}^{0} \varphi(t, \tau_0)}{1 + \alpha n [1 + \rho(t, \tau_0) \varphi(t, \tau_0)]}, \tag{15a}$$

$$\sigma_{s1}^{c} = \frac{n \sigma_{c1}^{0} \varphi(t, \tau_0)}{1 + \alpha n [1 + \rho(t, \tau_0) \varphi(t, \tau_0)]}. \tag{15b}$$

Consider the following equations:

$$\sigma_{s1}^{c} = \varepsilon_{s1}^{c} E_s = \varepsilon_{sc1}^{c} E_s,$$
$$\sigma_{c1}^{0} = E_c(\tau_0)\, \varepsilon_{sc1}^{0} = \frac{E_s \varepsilon_{sc1}^{0}}{n}. \tag{16}$$

Equations (16) are introduced into (15a) and (15b) to obtain the total creep strain ε_{sc1}^{c} of the CFST column, as follows:

$$\varepsilon_{sc1}^{c} = \frac{\varepsilon_{sc1}^{0} \varphi(t, \tau_0)}{1 + \alpha n [1 + \rho(t, \tau_0) \varphi(t, \tau_0)]}. \tag{17}$$

Here the creep prediction function $\varphi(t, \tau_0)$ employed the equation from ACI-209 [15]. Then, the composite creep

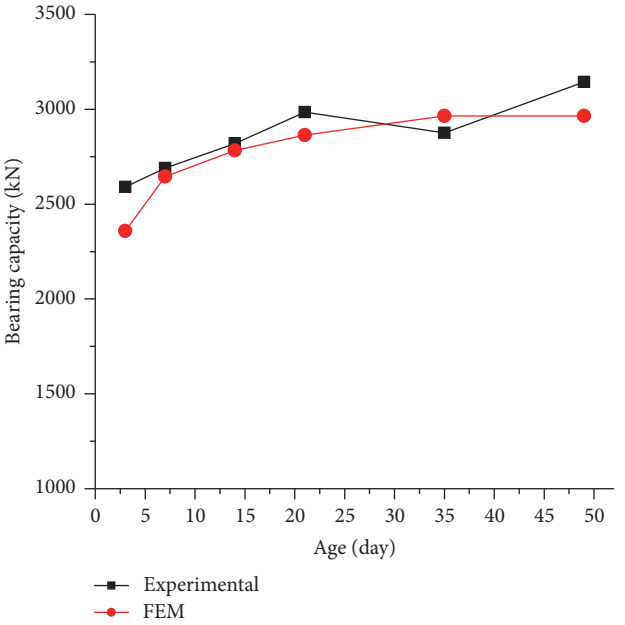

Figure 5: Load-bearing capacity of the CFST column at different ages.

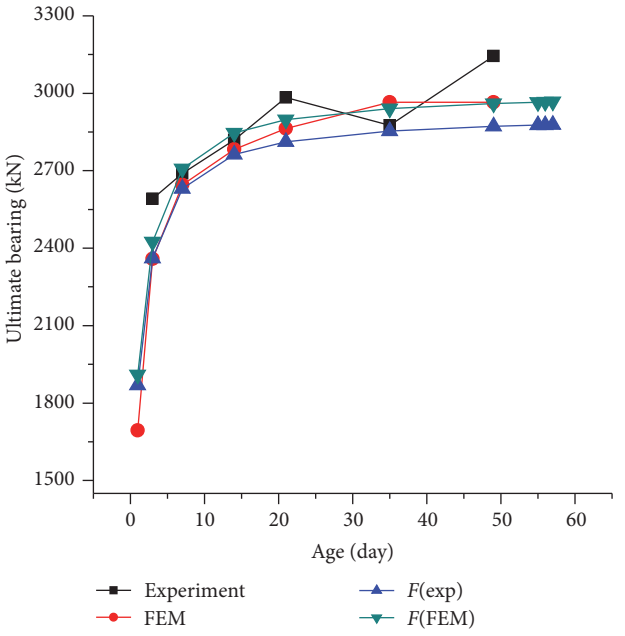

Figure 6: Comparison with the experimental and numerical results.

coefficient of the CFST, $\varphi_{sc}(t, \tau_0) = \varepsilon_{sc1}^{c}/\varepsilon_{sc}^{0}$, is obtained as follows:

$$\varphi_{sc}(t, \tau_0) = \frac{\varphi(t, \tau_0)}{1 + \alpha n [1 + \rho_{sc}(t, \tau_0) \varphi(t, \tau_0)]}, \tag{18a}$$

$$\varphi(t, \tau_0) = \frac{(t - \tau_0)^{0.6}}{10 + (t - \tau_0)^{0.6}} \varphi_{cu}, \tag{18b}$$

$$\varphi_{cu} = 2.35 \gamma_{la} \gamma_h \gamma_\psi \gamma_s \gamma_\lambda \gamma_a, \tag{18c}$$

Table 5: Ultimate load-bearing capacity of the axially compressed columns.

	N_k (kN)	N_{ut} ($\times 10^3$ kN)					$(N_{ut} - N_k)/(N_{u28} - N_k)$			
Concrete age (day)	0	1	3	7	14	28	1	3	7	14
Number 1	13.070	30.876	43.497	49.731	52.161	54.934	0.425	0.727	0.876	0.934
Number 2	19.235	38.841	51.250	57.432	59.979	63.839	0.440	0.718	0.856	0.913
Number 3	25.238	45.828	58.000	64.098	66.483	70.591	0.454	0.722	0.857	0.909
Number 4	31.084	52.171	64.129	70.131	72.343	76.533	0.464	0.727	0.859	0.908
Number 5	36.770	58.070	69.795	75.706	77.777	81.960	0.471	0.731	0.862	0.907

$N_k = A_s f_y$; N_{u28} is the load-bearing capacity when the concrete age is equal to 28 days.

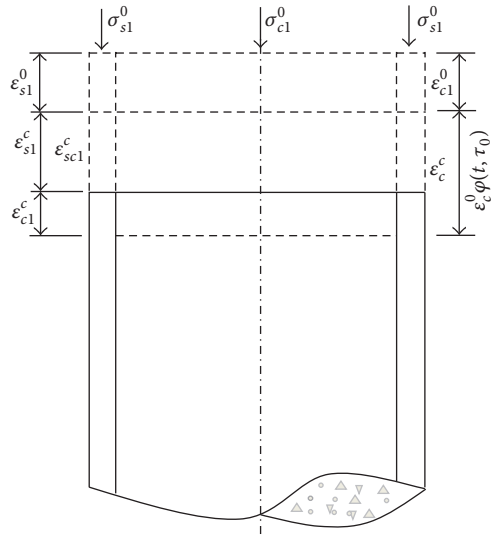

Figure 7: Creep strain of CFST member under axial compression.

Figure 8: Experimental testing devices.

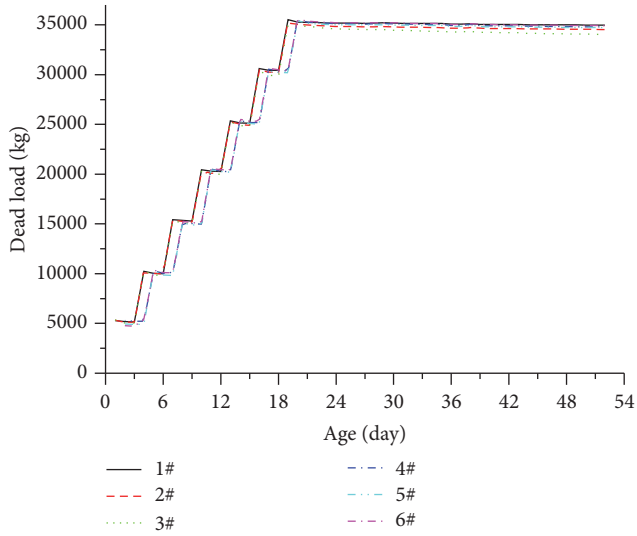

Figure 9: The dead load applied at related time.

where φ_{cu} is the ultimate creep of concrete; γ_{la} is the influence coefficient of loading age; γ_h is influence coefficient of average thickness or the ratio of volume and area of the component; γ_ψ is influence coefficient of the fine aggregate content; γ_s is influence coefficient of the concrete slump; γ_λ is influence coefficient of the ambient humidity; γ_a is influence coefficient of the air content.

In this study, $\rho_{sc}(t, \tau_0)$ represents the aging coefficient that introduce the effect of not only concrete age but also the steel tube confinement when the CFST column is considered as a single homogeneous material, which is distinguished by $\rho(t, \tau_0)$, the aging coefficient of concrete.

Experimental test and FEM creep analysis of the CFST column are conducted in order to determine the aging coefficient, $\rho_{sc}(t, \tau_0)$.

3.2. Experimental Test and FEM Simulation of the Creep Model during Construction. A special loading device was designed and manufactured in order to simulate the loading process during construction, as shown in Figure 8. Six columns, divided into two groups, were tested. The three columns in the first group are filled with concrete with recycled aggregates, whereas the other three columns in the second group are filled with concrete with conventional aggregates. The volume percentage of the expansive agent is 0%, 5%, and 10% for the three columns in each group, respectively. The design details of the columns are shown in Table 6.

The ultimate bearing capacity of the columns is designed as 1,100 kN, whose 40% represents the maximum dead load of 350 kN reached at the final stage of loading. The entire loading process is divided into seven stages and the load at each stage is recorded by the force sensor, as shown in Table 7 and Figure 9. An initial load of approximately 50 kN is applied to all columns of the two groups when concrete is three days

Table 6: Geometrical and mechanical properties of tests columns.

Number	D (mm)	T (mm)	H (mm)	f_y (MPa)	f_{ck} (MPa)	Aggregate kind	Percent of expansive
1#	133	4.5	400	345	30.4	Recycled	0
2#	133	4.5	400	345	30.4	Recycled	5
3#	133	4.5	400	345	30.4	Recycled	10
4#	133	4.5	400	345	30.4	Conventional	0
5#	133	4.5	400	345	30.4	Conventional	5
6#	133	4.5	400	345	30.4	Conventional	10

Table 7: Registered load at each stage (kN).

Number	1st stage	2nd stage	3rd stage	4th stage	5th stage	6th stage	7th stage
1#	53.05	102.45	154.42	204.31	253.60	306.10	355.20
2#	53.31	103.40	153.87	203.30	252.75	305.05	354.28
3#	53.54	102.70	152.94	202.90	252.58	303.37	349.58
4#	54.48	103.40	151.44	208.40	253.92	305.79	355.70
5#	52.90	103.16	150.71	204.46	253.00	304.43	354.28
6#	49.40	103.50	152.39	205.95	255.11	306.54	355.99

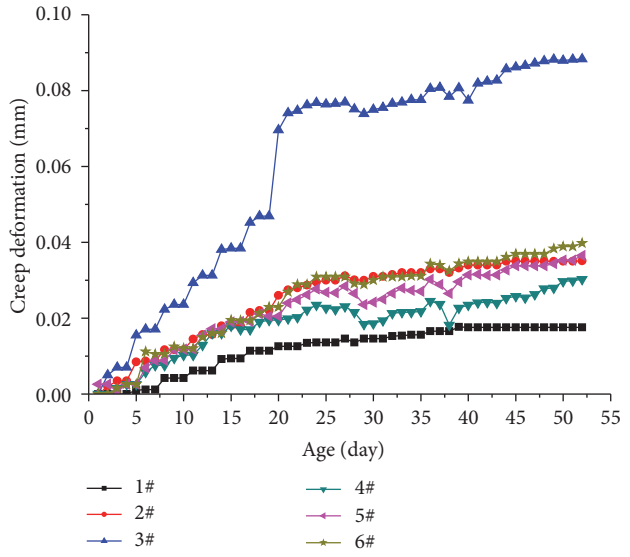

Figure 10: Longitudinal creep deformation curve obtained by FE model.

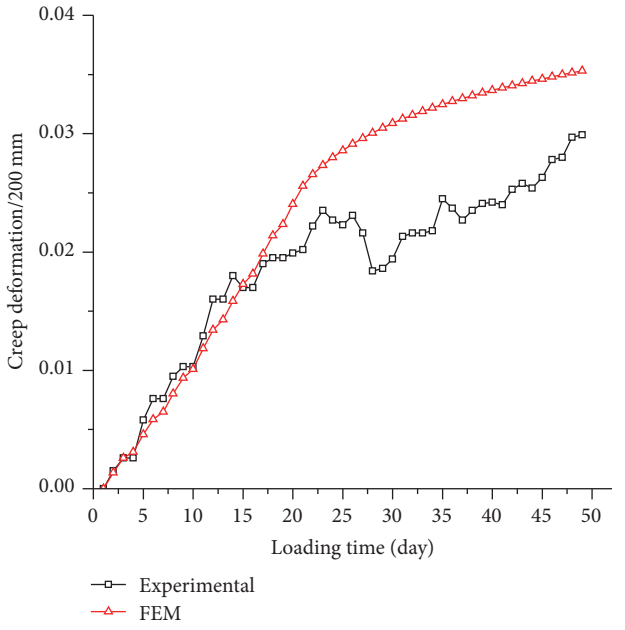

Figure 11: Experimental and numerical longitudinal creep deformation curves of specimen 4#.

old. Dead load increases by approximately 50 kN at each stage with a three-day interval, until it reaches 350 kN.

The creep deformation of the columns is measured by excluding the instantaneous displacements from the total displacement, as shown in Figure 10. Instantaneous displacements from the dead load are recorded immediately after such a load is applied, at each stage of the loading process. From Figure 10, the longitudinal deformation of the columns caused by the creep is notable and an increase in the expansion agent results in a larger creep deformation.

Column 4 is modeled by ABAQUS using a user-supplied subroutine of the creep effect. The creep model of ACI-209 [15], which considers the moist-cured condition, is adopted in the subroutine, where the progression method proposed by Gao et al. [22] is used to consider the change in concrete elastic modulus with age.

Creep deformation of column 4 obtained from the FE analysis is compared with the experimental results shown in Figure 11. In general, the FE solutions are consistent with the experimental test results.

After validating the FE analysis, the model is used to evaluate the aging coefficient $\rho_{sc}(t, \tau_0)$ of the columns specified in Table 8; here the composite creep coefficient $\varphi_{sc}(t, \tau_0)$ is obtained by ratio between creep and instantaneous displacements from the numerical result, shown in Figure 12.

Table 8: Parameters of column needed in calculation.

D (mm)	T (mm)	H (mm)	f_y (MPa)	f_{ck} (MPa)	τ_0 (day)	TL (day)	φ_{cu}
1000	12~36	4000	345	40.7	7	50	2.12

TL is the time of the load duration; φ_{cu} is the ultimate creep coefficient of concrete according to Terry et al. [8].

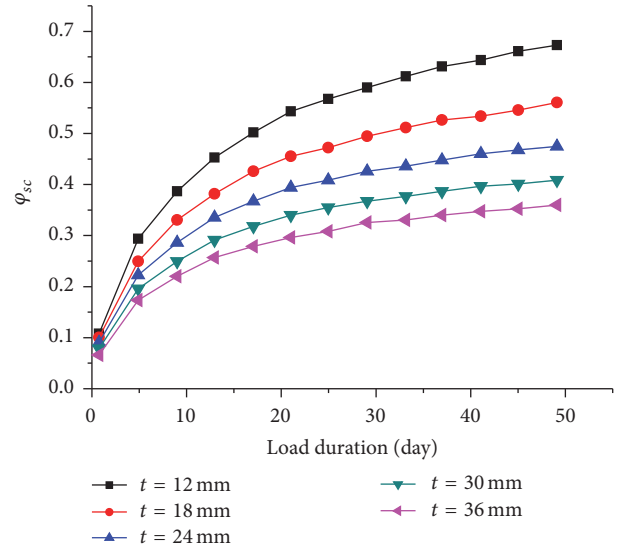

Figure 12: Composite creep coefficient.

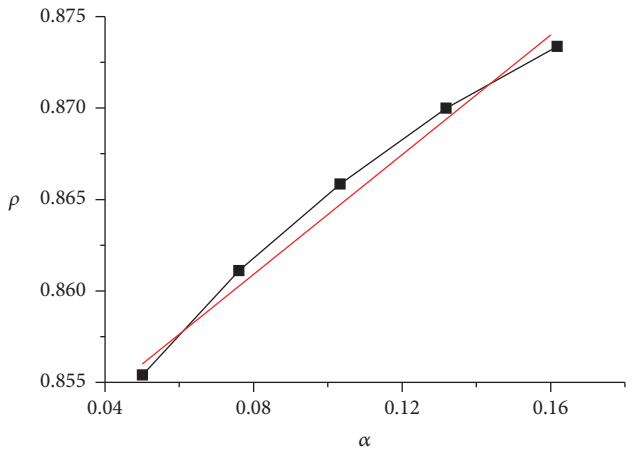

Figure 13: Aging coefficient of CFST column.

$\rho_{sc}(t, \tau_0)$ can be back calculated employing (18a), (18b), and (18c) with known $\varphi_{sc}(t, \tau_0)$ in Figure 12. Figure 13 shows the resulting aging coefficients, which are almost linear for the steel ratio α ranging from 0.05 to 0.20, representing the typical reinforcement ratio of practical designs. Thus, the aging coefficient within this range can be approximately computed as follows:

$$\rho_{sc}(t, \tau_0) = 0.848 + 0.16\alpha. \quad (19)$$

Then, the composite creep coefficient $\varphi_{sc}(t, \tau_0)$ of a CFST column can be calculated employing (18a), (18b), (18c), and (19).

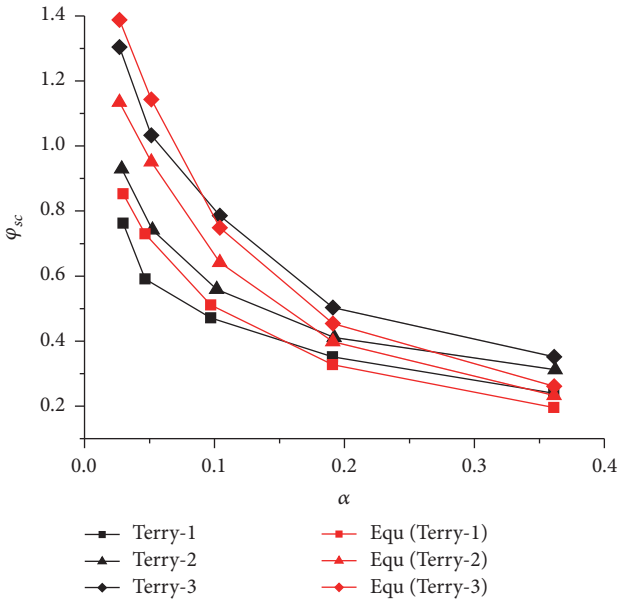

Figure 14: Composite creep coefficient compared with results of Terry et al. [8].

Predictions by (18a), (18b), and (18c) are compared with the test results from the studies of Terry et al. [8], in order to verify such equations, as shown in Figure 14, where Equ(Terry-1) is the equation result obtained by (18a), (18b), and (18c) related to the experimental test of Terry-1. A quite agreement can be seen, with some differences due to the different value adoptions of the ultimate creep of concrete and the loading duration.

4. Conclusion

In this study, the effect of concrete age and creep on the ultimate loading capacity of CFST columns had been experimentally and numerically investigated. The validated numerical models were employed in order to propose a set of empirical equations that can be used to predict the axial loading capacity of CFST columns with different concrete ages and composite creep coefficients.

According to the analysis of formula derivation and verification by experimental test and FE method, the ultimate bearing capacity considering the age of the CFST column can be calculated using (2). When treating the CFST column as a single material, both the unity creep and the aging coefficient, determined by employing (18a), (18b), (18c), and (19), respectively, can be used for long-term property analysis.

Equations in this study will be simplified to a certain degree on the design and time-dependent analysis of the CFST column. More studies considering the step upload will be conducted in the future.

Symbols

$E_c(t)$: The elastic modulus of concrete at time t
E_c^{28}: The elastic modulus of concrete at 28th day
E_s: The elastic modulus of the steel tube
E_{sc}: The elastic modulus of the CFST column
A_c: The area of the cross section of the concrete
A_s: The area of the cross section of the tube
α: Ratio between cross areas of steel and concrete
n: The ratio between the elastic modulus of the steel and the concrete at t time
N_{ut}: The ultimate bearing capacity of CFST column at t time (days)
N_k: The bearing capacity of hollow steel tube
N_r: The stability of the CFST column
N_{u28}: The ultimate bearing capacity of CFST column at 28th day
$E_c(\tau_0)$: The elastic modulus of concrete at loading age τ_0
$\varphi(t, \tau_0)$: The concrete creep coefficient
$\xi = \alpha f_y / f_{ck}$: The hoop effect coefficient
D: The outer diameter of the steel tube
T: The thickness of the steel tube
L: The length of the steel tube
t: The age of the concrete
e: The eccentricity of the load
λ: The slenderness of the column
$\varepsilon_c^c(t)$: The total strain of concrete when creep is with no steel confinement at age t days
$\sigma_{c1}^0(\tau_0)$: The initial stress of the concrete when loaded at τ_0 days
$E_c(\tau_0)$: The elastic modulus of concrete at τ_0 days
$\varphi(t, \tau_0)$: The creep coefficient at t when loaded at τ_0
$\sigma_{c1}(t)$: The stress of concrete at age t days
ρ: The aging coefficient of concrete
E_φ: The age-adjusted effective modulus
ε_{sc1}^c: The axial creep strain of the CFST column
ε_{s1}^c: The axial strain of steel tube due to concrete creep
ε_c^c: The creep strain of the concrete with no steel confinement
ε_{c1}^c: The reduced strain of the concrete due to the effect of the steel tube confinement
ε_{sc1}^0: The initial strain of CFST when loading
ε_{s1}^0: The initial strain of the steel tube when loaded
ε_{c1}^0: The initial strain of the concrete when loaded
σ_{c1}^c: The stress change of concrete due to creep
σ_{s1}^c: The stress change of steel tube due to creep
$\varphi_{sc}(t, \tau_0)$: The unity creep coefficient of CFST
$\rho_{sc}(t, \tau_0)$: The aging coefficient of CFST.

Competing Interests

The authors declare that they have no competing interests.

References

[1] M. D. O'Shea and R. Q. Bridge, "Design of circular thin-walled concrete filled steel tubes," *Journal of Structural Engineering*, vol. 126, no. 11, pp. 1295–1303, 2000.

[2] G. Giakoumelis and D. Lam, "Axial capacity of circular concrete-filled tube columns," *Journal of Constructional Steel Research*, vol. 60, no. 7, pp. 1049–1068, 2004.

[3] S. T. Zhong, *The Concrete-Filled Steel Tubular Structures*, Tsinghua University Press, 3rd edition, 2005 (Chinese).

[4] X. X. Zha, *Hollow and Solid Concrete-Filled Steel Tube Columns Structure*, Science Press, 2011 (Chinese).

[5] L.-H. Han, W. Li, and R. Bjorhovde, "Developments and advanced applications of concrete-filled steel tubular (CFST) structures: members," *Journal of Constructional Steel Research*, vol. 100, pp. 211–228, 2014.

[6] Y. F. Wang, *Creep of the Concrete-Filled Steel Tubular Structures*, Science Press, 2006.

[7] S. J. Tan and J. L. Qi, "Experimental investigation of the effect on strenth of concrete filled steel tubular compressive members under long-time load," *Journal of Harbin Engineering University*, no. 2, pp. 10–24, 1987 (Chinese).

[8] P. J. Terry, M. A. Bradford, and R. I. Gilbert, "Creep and shrinkage in concrete filled steel tubes," in *Proceedings of the 6th International Symposium in Tubular Structures Melbourne*, pp. 293–298, Melbourne, Australia, 1994.

[9] K. Luo, Y.-L. Pi, W. Gao, M. A. Bradford, and D. Hui, "Investigation into long-term behaviour and stability of concrete-filled steel tubular arches," *Journal of Constructional Steel Research*, vol. 104, pp. 127–136, 2015.

[10] L. H. Ichinose, E. Watanabe, and H. Nakai, "An experimental study on creep of concrete filled steel pipes," *Journal of Constructional Steel Research*, vol. 57, no. 4, pp. 453–466, 2001.

[11] W. Naguib and A. Mirmiran, "Creep modeling for concrete-filled steel tubes," *Journal of Constructional Steel Research*, vol. 59, no. 11, pp. 1327–1344, 2003.

[12] H. Liu, Y. Wang, M. He, Y. Shi, and H. Waisman, "Strength and ductility performance of concrete-filled steel tubular columns after long-term service loading," *Engineering Structures*, vol. 100, pp. 308–325, 2015.

[13] K. M. Shrestha and B. C. Chen, "Aging coefficient, creep coefficient and extrapolating aging coefficient from short term test for sealed concrete," *Journal Wuhan University of Technology, Materials Science Edition*, vol. 26, no. 1, pp. 154–159, 2011.

[14] S.-T. Yi, J.-K. Kim, and T.-K. Oh, "Effect of strength and age on the stress-strain curves of concrete specimens," *Cement and Concrete Research*, vol. 33, no. 8, pp. 1235–1244, 2003.

[15] ACI, "Prediction of creep, shrinkage, and temperature effects in concrete structures," ACI 209, ACI Special Publication, 1992.

[16] P. Shokouhi, A. Zoëga, and H. Wiggenhauser, "Nondestructive investigation of stress-induced damage in concrete," *Advances in Civil Engineering*, vol. 2010, Article ID 740189, 9 pages, 2010.

[17] J. Newman, "Strength and failure of concrete under short-term, cyclic and sustained loading," in *Advanced Concrete Technology—Concrete Properties*, J. Newman and B. S. Choo, Eds., Elsevier, 2003.

[18] G. T. Liu, H. Gao, and F. Q. Chen, "Microstudy on creep of concrete at early age under biaxial compression," *Cement and Concrete Research*, vol. 32, no. 12, pp. 1865–1870, 2002.

[19] M. M. Attard and S. Setunge, "Stress-strain relationship of confined and unconfined concrete," *ACI Materials Journal*, vol. 93, no. 5, pp. 432–442, 1996.

[20] I. Imran and S. J. Pantazopoulou, "Experimental study of plain concrete under triaxial stress," *ACI Materials Journal*, vol. 93, no. 6, pp. 589–601, 1996.

[21] A. Kwan, C. Dong, and J. Ho, "Axial and lateral stress–strain model for concrete-filled steel tubes," *Journal of Constructional Steel Research*, vol. 122, pp. 421–433, 2016.

[22] Z. G. Gao, D. G. Huang, and G. F. Zhao, "A method for creep stess analysis of concrete structures," *China Civil Engineering Journal*, vol. 34, no. 4, pp. 10–14, 2001 (Chinese).

Hindawi Publishing Corporation
Advances in Materials Science and Engineering
Volume 2016, Article ID 5283706, 8 pages
http://dx.doi.org/10.1155/2016/5283706

Research Article

Influence of Nano-SiO_2 on the Consistency, Setting Time, Early-Age Strength, and Shrinkage of Composite Cement Pastes

Yu Chen, Yi-fan Deng, and Meng-qiang Li

School of Traffic and Transportation Engineering, Changsha University of Science & Technology, Changsha 410004, China

Correspondence should be addressed to Yu Chen; just4ujust43@163.com

Received 28 April 2016; Revised 17 June 2016; Accepted 26 June 2016

Academic Editor: Doo-Yeol Yoo

The study outlined the raw materials and mix proportions to prepare composite cement pastes with the addition of silica-based micro- and nanoparticles. The effects of amorphous nano-SiO_2 on the early-age properties, including the consistency, setting time, early-age strength, and chemical and autogenous shrinkages, were investigated. Under the condition of the same dosage of superplasticizer used, the consistency of cement paste with nano-SiO_2 is higher than that with silica fume. Significant reductions of the initial and final setting times are observed especially for nano-SiO_2 addition groups, and the time difference between the initial and final setting times goes up with the increasing proportions of nano-SiO_2. The addition of nano-SiO_2 is more helpful to the improvement of early-age strengths of the paste with or without fly ash admixed than silica fume additive for the same mass proportion. Both the chemical and autogenous shrinkages of cement paste develop with the increasing amount of micro- or nanolevel silica particles; however, nano-SiO_2 plays a more active role than silica fume in inspiring early-age shrinkage. The physical and chemical mechanisms of nano-SiO_2 in cement paste are also discussed.

1. Introduction

Silica fume, as the most widely used supplemental cementitious materials (SCMs) in cement-based materials, has been successfully studied and applied for more than 80 years. Silica fume (SF for short), consisting essentially of silica in noncrystalline form with a high specific surface, exhibits great pozzolanic activity and thus has been commonly adopted to manufacture HPC. In recent years, nanotechnology has attracted considerable scientific interest due to the new potential uses of particles in nanometer (10^{-9} m) scale, such as the application of nano-SiO_2 (NS) to manufacture Ultra-HPC [1, 2] or high-volume fly ash concrete [3] or the addition of nano-TiO_2 photocatalysis into cementitious materials to minimize air pollution in urbanized areas [4] and to produce self-cleaning concrete [5].

It was reported that dramatically improved properties could be obtained with NS added to cement-based materials if compared to the conventional grain-size materials of the same chemical composition [6–8]. Based on mini spread-flow test, Quercia et al. [9] found that water demand of cement paste decreased when amorphous NS was added. However, Lin et al.'s research [10] indicated that the amount of water needed at standard consistency increased as more NS was added; and obvious increasing values of the torque, yield stress, and plastic viscosity in mortar samples prepared with the use of 0~3% NS and 0.5 water/binder weight ratio were measured [11]. Therefore, the influence of NS particles on the water demand and consistency of cement paste still needed more testing and verification.

Zhang and Islam [12] reported that, in comparison to the reference concrete with 50% fly ash, the incorporation of 2% NS by mass of cementitious materials, respectively, reduced the initial and final setting times by 90 and 100 min and raised 3 d and 7 d compressive strengths by 30% and 25%. It was also demonstrated that the NS was more valuable in enhancing strength than SF [13, 14], and the results of SEM examinations [15, 16] showed that NS reacted with calcium hydroxide (CH) and increased the amount of calcium silicate hydrate (C-S-H) produced, leading to a compact microstructure. Not only did NS particles behave as a filler to improve microstructure, but also they behaved as an activator to promote pozzolanic

Table 1: Chemical compositions and properties of cementitious materials.

Items	OPC	FA	SF	NS
SiO_2 (%)	23.4	59.5	98.0	99.9
Al_2O_3 (%)	5.1	28.1		
CaO (%)	60.3	1.6		
MgO (%)	1.5	0.4		
Fe_2O_3 (%)	4.4	5.7		
SO_3 (%)	2.5	0.3		
LOI (%)	2.6	2.1	1.1	0.1
Specific gravity (g/cm^3)	3.17	2.73		
Avg. particle size	16 μm	12 μm	0.1 μm	30 ± 10 nm

reaction, resulting in the consequently improving mechanical properties of hardened mixtures [17–19]. Though there were some confirmed conclusions about the effects of NS on both setting time and early-age strength of cement paste, a comparative analysis of the addition of silica-based micro- and nanoparticles at the same additive levels seemed valuable. Besides, it should be noted that though the volume stability (especially at early ages) of cement-based materials with the nanoscale additives is of much significance for the application in civil engineering structures, very limited research has been conducted.

The presented study outlined the raw materials and mix proportions to prepare composite cement pastes with the addition of silica-based micro- and nanoparticles. And by comparative analysis, the effects of NS on the early-age properties, including the consistency, setting time, early-age strength, and chemical and autogenous shrinkages as the main focuses, were investigated in detail.

2. Experiment Program

2.1. Materials and Properties. Cementitious materials used were ordinary Portland cement (OPC), fly ash (FA), silica fume (SF), and amorphous nano-SiO_2 (NS) particles, with the details listed in Table 1. The SiO_2 content of SF reached 98.0%, while NS had 99.9%. Scanning electron micrograph (SEM) photographs of both SF and NS were shown in Figure 1. In order to promote the NS or SF particles homogeneously dispersing in all mixes, a polycarboxylic superplasticizer (SP) with relative density of 1.09 was incorporated. The content of SP was adjusted for each mix to ensure that no segregation and bleeding would occur.

2.2. Mix Proportions and Tests. Referring to Table 2, cement pastes with different silica addition for test were prepared. Based on pretests, the ratio of water to the total cementitious materials in mass for all mixes was determined as a typical value of 0.36 for moderate paste consistency in general, in order that the properties of composite cement pastes could be investigated on the condition of the same water-to-cementitious materials ratio. First, the designed dosage of SP was diluted in a proper amount of water; then, SF or NS powder was added to the produced liquid for 5 min ultrasonic mixing using ultrasonic mixer with 90 W power input; at last, all other cementitious materials were blended to make homogenous mixtures. The mixing consisted of a sequence of mixing that involved a total of 2 min at a paddle speed of both 62 rpm (revolution) and 140 rpm (rotation), a 15 s stop, and another total of 2 min at a speed of both 125 rpm (revolution) and 285 rpm (rotation).

Table 2: Mix proportions of composite cement pastes (unit: wt%).

Serial number	OPC	FA	SF	NS	SP
0#	100				0.3
A1	98.0		2.0		0.3
A2	96.0		4.0		0.4
A3	94.0		6.0		0.5
B1	98.0			2.0	0.4
B2	96.0			4.0	0.9
B3	94.0			6.0	1.2
C1	70	30			0.2
C2	66.0	30	4.0		0.3
C3	66.0	30		4.0	0.6

The following experiments were carried out:

(1) Test of consistency and setting time of cement pastes: the consistency and setting time of fresh pastes were tested according to GB 1346-2011 [20]. The consistency was ascertained by putting the paste in a mold consisting of a steel ring (40 mm in height) on a sheet of glass and by determining the penetration depth of a plunger applied to the top surface of the paste specimen. The initial and final setting time were determined using the needle of the Vicat apparatus.

(2) Test of strength: compressive strength tests were carried out on 40 mm cube specimens and bending strength tests used 40 × 40 × 160 mm beam specimens, which were demolded 20 h after casting, cured in 23 ± 0.5°C water, and then dried 4 h prior to testing for every mix at 1, 3, and 7 days. Each specimen was tested for at the given ages by a hydraulic press with 100 kN capacity and 0.5 MPa/s loading speed.

(3) Test of chemical and autogenous shrinkages: chemical shrinkage of cement pastes was measured basically according to ASTM C1608-2012 [21]. However, the glass bottles for chemical shrinkage measurement might crack due to the inconsistent deformation of the samples and the bottles, leading to the interruption of testing. So the modified ASTM C1608 method was recommended. As illustrated in Figure 2, an open ultrathin elastic cap was adopted to be filled with the paste mixtures to avoid its direct contact with the internal wall of the glass bottle. The chemical shrinkage values of the paste at the ages of 90 min, 3 h, 6 h, 12 h, 24 h, 48 h, 3 d, 7 d, and 14 d were recorded. Autogenous shrinkage of cement pastes was surveyed in strict accordance with ASTM C1698-2014 [22].

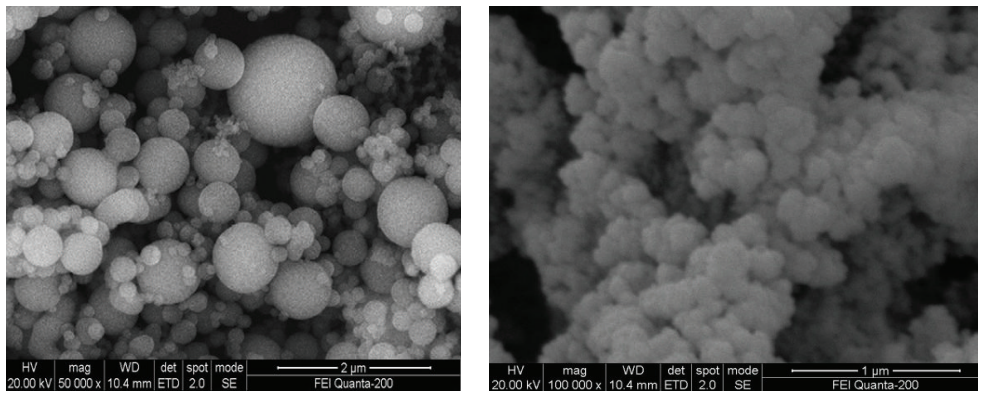

(a) (b)

Figure 1: SEM photographs of SF (a) and NS (b).

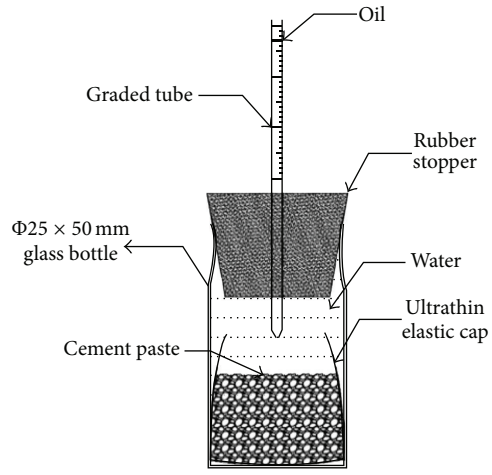

Figure 2: Sketch map of improved experimental apparatus for ASTM C1608 1#, A2, B2, and C1 samples at the age of 3 d.

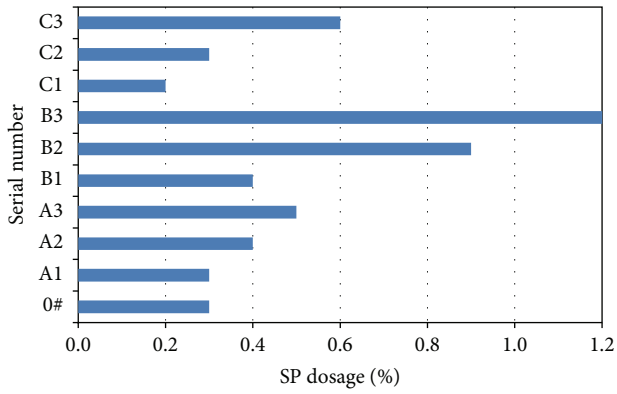

Figure 3: SP needed for all mixes for standard consistency.

The time for length measurement of corrugated pipe samples was individual at 30 min, 1 h, 3 h, 12 h, 1 d, 3 d, 7 d, and 14 d after the final setting of the paste.

(4) For each mixture, 5 samples were measured for all the above properties, and the average value was recorded and analyzed. But any measured value which exceeded the average by 15% was deleted; and if there were more than 2 invalid pieces of data, this mixture must be reprepared and retested. All test data listed in the paper and illustrated in the figures were the effective average value.

3. Results and Discussions

3.1. Consistency and Setting Time. In the present study, the dosage of SP added was accurately adjusted to produce each mix until the standard consistency of cement paste was obtained. Test results were illustrated in Figure 3. Compared to the control group 1#, with the increasing of the mass percentages of SF or NS, the needed SP obviously rises, but the increments for NS addition groups are more dramatic than those for SF added. For instance, on the basis of 4.0% amorphous silica addition, the SP dosage for A2 is 0.4%, while that for B2 is 0.9%. In particular, when the NS amount reaches 6.0%, B3 mixture needs an amazing 1.2% of SP to achieve the standard consistence. When 30% FA in mass percentage is blended into cement paste, a similar conclusion can be made.

The increase of paste consistency is due to the improvement of water adsorption by fresh mixture, since very high specific surface areas in the paste are created by NS. The effectiveness of SP in adjusting the flow behavior (after mechanical mixing) in pastes with distinct concentrations of NS is very important for the control of the following impact of nanoparticles. Moreover, the rheological behavior of nanoparticle dispersed in a suspension depends not only on the particle diameter but also on an adequate relation between solid fractions and the optimum molecular weight of dispersant [11]. At high dosages of SP, the long chains of polycarboxylic superplasticizer are forced by mutual repulsion out into the solution where they interact with other particles, and consequently, the plastic viscosity values increase [23].

The setting times of all mixes were provided in Table 3. Significant reductions of the initial and final setting times

Table 3: Setting time and early-age compressive strength of cement pastes.

Serial number	Setting time			Compressive strength (MPa)		
	Initial	Final	Time difference	1 d	3 d	7 d
0#	8 hr 15 min	9 hr 20 min	1 hr 5 min	12.3	27.1	34.0
A1	8 hr 10 min	9 hr 10 min	1 hr	13.0	28.4	36.7
A2	6 hr 50 min	8 hr 5 min	1 h 15 min	14.5	31.3	40.1
A3	6 hr 35 min	7 hr 55 min	1 h 20 min	15.2	35.4	45.0
B1	5 hr 50 min	7 hr 20 min	1 h 30 min	15.3	36.0	45.4
B2	5 hr 25 min	7 hr 15 min	1 hr 50 min	16.7	38.2	47.2
B3	4 hr 50 min	6 hr 45 min	1 hr 55 min	16.0	39.4	47.5
C1	9 hr 10 min	10 hr 20 min	1 hr 10 min	6.7	14.5	28.4
C2	7 hr 40 min	9 hr	1 hr 20 min	10.8	28.7	38.6
C3	6 hr 15 min	7 hr 45 min	1 hr 30 min	14.0	32.5	41.7

were observed for both SF and NS addition groups by contrast with group 1#. The incorporation of 2.0%, 4.0%, and 6.0% SF reduces the initial and final setting times of cement pastes by 5, 85, and 100 min and 10, 75, and 85 min, respectively; and the corresponding reduction values for NS additives are 145, 170, and 208 min and 120, 125, and 155 min. The effects of NS are remarkably surprising, even though FA is also admixed to produce composite cement paste. Besides, the time difference between the initial and final setting times goes up with the increasing proportions of SF or NS in cement paste, while there are by far wider time gaps for NS groups than SF ones at the same mass content.

Test data indicate that the time shortened is mainly a result of the shortening of the initial setting, which is caused by the reduction in the hibernation period of hydration. With NS added to the paste, the increase in surface energy of the mixes speeds up the rate of the hydration reaction. Therefore, the C-S-H gel and $Ca(OH)_2$ are generated at a faster speed, and an early initial setting time is achieved. The reduction in setting time becomes noticeable when the increased amount of NS is admixed [10].

3.2. Early-Age Strength. Figure 4 shows the compressive strength development of all specimens at the ages of 1 d, 3 d, and 7 d. As can be seen, the early-age compressive strength developed in pastes containing SF or NS particles in every case is apparently higher than that of the reference group 1#. The strengths of A1, A2, and A3 specimens with the addition of 2.0%, 4.0%, and 6.0% SF improve obviously, but the strengthening effects are far inferior to those of NS. In general, it is noticed that the compressive strengths of the specimens, especially before the age of 7 d, sharply drop as a large amount of FA is added, which is mainly due to the immature pozzolanic reaction in the paste and the preventive growth of C-S-H gel caused by the blended SCMs. As demonstrated in Figure 4, the addition of NS is more helpful to the improvement of early-age compressive strength of the paste with FA admixed than SF additives on the condition of the same mass proportion. The compressive strength of C2 with 4.0% SF rises by 61.2%, 98.0%, and

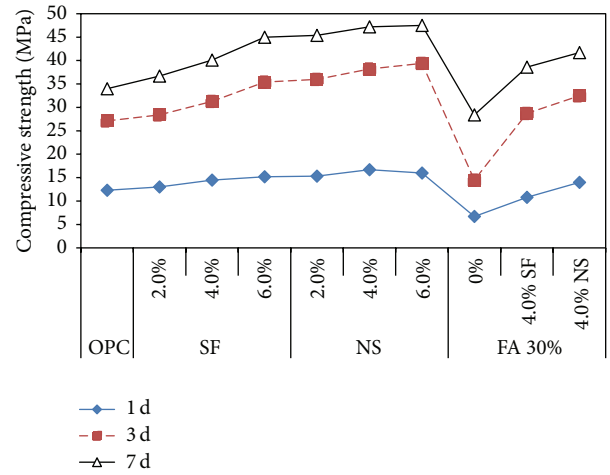

Figure 4: Early-age compressive strength of composite cement pastes.

35.9% at 1 d, 3 d, and 7 d, respectively, compared to that of the reference group C1, while the corresponding increments of C2 with the same amount of NS are 109.0%, 124.1%, and 46.8%.

Table 4 provided the compressive and bending strengths, as well as the ratios of bending to compressive strength of cement stone at the prescribed age of 7 d. As for SF and NS additives concerned, their effects on the bending strength are quite similar to those on the compressive strength, while from the data of ratios of bending to compressive strength at the same age, 3 fundamental principles can be deduced: (1) both SF and NS particles are helpful to increase the early-age strength, but it seems that bending strength increments are more significant by comparison; (2) with the increasing amount of SF or NS, the development of bending strength is clearly superior to that of compressive strength; and (3) on the condition of the same 4.0% of SF and NS admixed (i.e., C1, C2, and C3), the addition of FA appears very estimable to further improve the bending strength along with SF or NS.

Both NS and SF are highly reactive silica, but the average primary particle size of the former is about 10 times smaller

Table 4: Strength and ratio of bending to compressive strength of hardened cement paste at 7 d.

Serial number	Compressive strength① (MPa)	Bending strength② (MPa)	Ratio of bending to compressive strength ② ÷ ①
0#	34.0	3.6	0.106
A1	36.7	3.9	0.106
A2	40.1	4.4	0.110
A3	45.0	5.1	0.113
B1	45.4	5.3	0.117
B2	47.2	5.6	0.119
B3	47.5	5.7	0.120
C1	28.4	3.3	0.116
C2	38.6	4.8	0.124
C3	41.7	5.1	0.122

than that of the latter, referred to in Figure 1. The mechanisms by which SF modifies cement paste, mortar, and concrete were summarized in ACI Committee 234 report [24]. As the particle sizes of the NS are much smaller than those of the SF, the physical and chemical effects of the former are likely more substantial than the latter, which are discussed in the later section.

3.3. Chemical and Autogenous Shrinkages. With SF or NS additives in paste, the early-age shrinkage of cement paste undoubtedly gets more complicated. Figures 5 and 6 provide test results of the chemical shrinkage of all mixes listed in Table 2. The following conclusions can be drawn:

(1) Vigorous hydration of cementitious materials in turn results in significant growth of the chemical shrinkage in all pastes with time passing. Until the age of 14 d, as an example, 1#, A2, B2, C1, C2, and C3 are measured at 0.0411, 0.0478, 0.0678, 0.0287, 0.0433, and 0.0611 mL/g of chemical shrinkage individually, based on the absolute volume method according to modified ASTM C1608.

(2) Compared to pure cement paste (1#), both SF and NS promote the chemical shrinkage of all cement pastes during the time period under study, except that A1 with only 2.0% SF addition indicates almost similar development of the chemical shrinkage, because of its very low admixing amount. In general, the chemical shrinkage of cement paste goes up with the increasing amount of micro- or nanolevel silica particles; however, it is evident that NS plays a more active role than SF in inspiring early-age shrinkage. Based on the control group 1#, the chemical shrinkage of A3 with 6.0% SF admixed, for instance, increases by 83.9%, 48.0%, and 45.7% at the age of 6 h, 48 d, and 7 d separately, while the values recorded for B3 with the same amount of NS reflect the corresponding increments of 148.4%, 83.2%, and 73.7%.

(3) The line, the closest one to cross axis in Figure 5, illustrates the growth of chemical shrinkage of C1, whose cement is replaced by 30% of FA in mass percentage. As can be seen, the amorphous spherical FA particles, uniformly dispensing into the cement matrix, are very helpful to reduce its chemical shrinkage at early ages. Nevertheless, the influences of SF and NS on the chemical shrinkage of composite cement paste with admixture of FA are quite similar to those on pure cement paste.

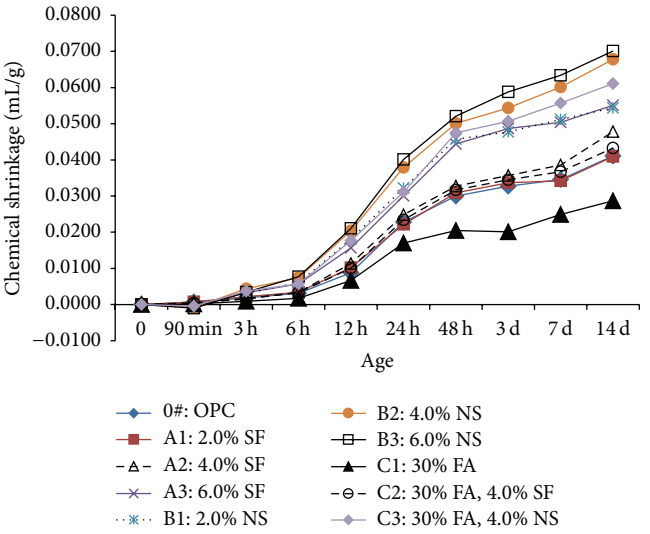

Figure 5: Chemical shrinkage of composite cement pastes at early ages.

Self-desiccation driving the development of autogenous shrinkage has been used extensively across literature [25, 26]. In reality, a volume change commences immediately after the cementitious materials and water come in contact during mixing. Therefore, less pozzolanic activity of FA is beneficial to control the autogenous shrinkage of cement paste, but both SF and NS, due to their very high potential and ability of hydration, have the opposite effects, which are clearly demonstrated in Figure 7.

Three different incorporation percentages, 2.0%, 4.0%, and 6.0%, are all taken into consideration, and the addition of SF in cement paste leads to 15.8%, 33.0%, and 31.7% of the average increasing percentages of autogenous shrinkage, separately at 3 d, 7 d, and 14 d in contrast with the control group 1#. In addition, the corresponding average values

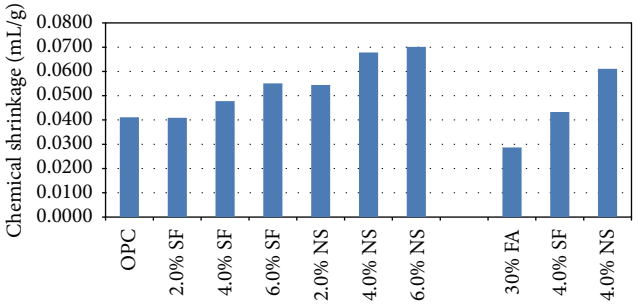

Figure 6: Chemical shrinkage of composite cement pastes at 14 d.

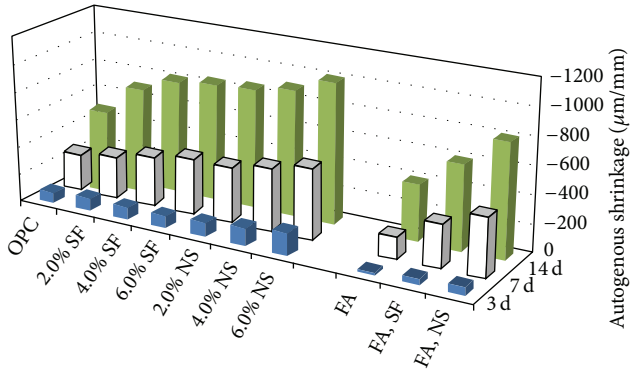

Figure 7: Autogenous shrinkage of composite cement pastes at early ages.

change to 68.8%, 70.5%, and 54.1% at the same ages, as NS is admixed. Though FA additive limits the autogenous shrinkage of cement paste before 14 d, seen from C1 group, the compound adding of NS (C3) still endows 57.9% and 35.9% of the autogenous shrinkage increments at 7 d and 14 d, if compared to the pure paste (1#).

Early-age shrinkage of cementitious matrices is the result of several complex physicochemical phenomena. Those phenomena are related to the hydration reactions between cementitious materials and water and to the progressive hardening of the mineral skeleton. It is generally considered that when cement hydrates, chemical shrinkage occurs, because the hydration products occupy less space than the original reactants, and that at mature ages, in autogenous conditions, the autodesiccation of the material, that is, the progressive desaturation of its porosity, generates compressive forces high enough to cause volume changes called autogenous shrinkage. These forces are particularly intense in cement-based matrices with low water-to-cementitious materials ratio.

As an example, Figure 8 reveals that different additives result in the diverse hydration products and microstructures at 3 d, leading to different early-age shrinkages. The addition of SF consumes the bulky crystal $Ca(OH)_2$ produced by cement (seen from Figure 8(a)) and promotes the hydration of composite paste, generating a large amount of C-S-H and short needle AFt (shown in Figure 8(b)). More complex hydration products and denser microstructure bring the higher chemical and autogenous shrinkages. Moreover, Figure 8(c) is the SEM photograph intensified by 5000 times of the sample B2 with the admixture of 4.0% NS. By comparison with Figure 8(b), the hydration products are smaller, are more uniformly distributed, and have more homogenous and compact microstructure. Besides, the incorporation of a certain amount of FA also consumes $Ca(OH)_2$ but limits the hydration and shrinkage of paste because as indicated in Figure 8(d), quite a number of unhydrated FA particles fill and support the microstructure to keep its volume stable to a certain extent.

In summary, the effects of NS on the early-age properties of cement paste can be explained as follows: from the chemical point of view, the extremely fine particles of amorphous NS not only have high surface energy (atoms in the surface have a high activity, which leads the atoms to react on outer ones easily) but also greatly develop the very early-age hydration by providing high amount of nucleation sites for precipitation of cement hydration products. From physical perspective, in addition to the nucleation effect, NS may act as reactive filler to reduce bleeding and increase packing density of solid materials by occupying space between cement and FA particles. Besides, the small amount of aggregating NS is not a weak zone, so the strength of cement paste increases with the increasing content of NS even when the small amount of NS is not well dispersed. Consequently, the pozzolanic activity of NS at early ages is higher than that of SF. The microstructure of the mixture containing NS reveals a dense, compact formation of hydration products and a reduced number of $Ca(OH)_2$ crystals [15, 16].

4. Conclusions

(1) The needed SP to produce cement pastes with SF or NS added rises, and its dosages for NS addition groups are more than those for SF added. Under the condition of the same dosage of SP used, the consistency of cement paste with NS is higher than that with SF.

(2) There are significant reductions of the setting times for SF or NS addition groups by contrast of pure cement. But the effects of NS are remarkably surprising, even though FA is also admixed. The time difference between the initial and final setting times goes up with the increasing proportions of NS in cement paste.

(3) The early-age compressive strength develops in pastes containing SF or NS particles, and the improvement of bending strength seems more evident. But the strengthening effects of SF are inferior to those of NS, and the addition of FA appears estimable to further improve the bending strength along with SF or NS.

(4) Both chemical and autogenous shrinkages of cement paste develop with the increasing amount of SF or NS; however, NS plays a more active role than SF in inspiring early-age shrinkage. The extra admixture of FA in cement paste shows the similar principals.

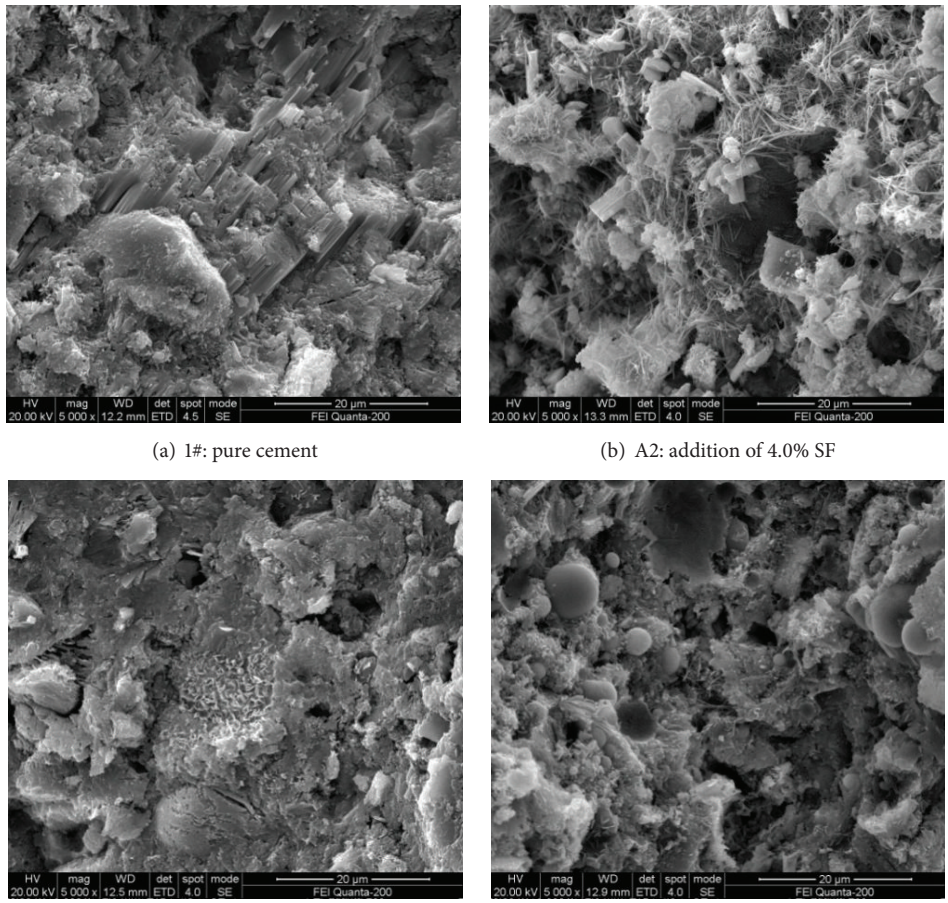

(a) 1#: pure cement

(b) A2: addition of 4.0% SF

(c) B2: addition of 4.0% NS

(d) C1: addition of 30% FA

Figure 8: SEM photographs of 1#, A2, B2, and C1 samples at the age of 3 d.

(5) The above phenomena resulting from the NS additive can be explained as follows: since the particle sizes of NS are much smaller than those of SF, the physical and chemical effects of the former are likely more substantial than the latter. Extremely fine particles of the NS, with high surface energy and high activity, accelerate cement and FA hydration by providing high amount of nucleation sites for precipitation of cement hydration products. Besides, NS may act as superfine filler to manufacture more homogeneous and denser microstructure of cement stone.

Competing Interests

The authors declare that they have no competing interests.

Acknowledgments

The present study is supported by the National Natural Science Foundation of China (Grant no. 51302020) and Project supported by Ministry of Transport of China (Grant no. 2015 319 825 180). All experiments are carried out in Key Laboratory of Ministry of Transportation for Road Materials and Structures in Changsha University of Science and Technology.

References

[1] M. Rebentrost and G. Wight, "Experience and applications on ultra-high performance concrete in Asia," in *Proceedings of the 2nd International Symposium on Ultra High Performance Concrete*, E. Fehling, Ed., pp. 19–30, Kassel, Germany, March 2008.

[2] K. K. Walsh and E. P. Steinberg, "Moment redistribution capacity in ultra-high performance concrete," in *Proceedings of Hipermat 3rd International Symposium on UHPC and Nanotechnology for High Performance Construction Materials*, M. Schmidt, E. Fehling, C. Glotzbach, S. Fröhlich, and S. Piotrowski, Eds., pp. 639–646, Kassel University Press, Kassel, Germany, March 2012.

[3] G. Li, "Properties of high-volume fly ash concrete incorporating nano-SiO_2," *Cement and Concrete Research*, vol. 34, no. 6, pp. 1043–1049, 2004.

[4] J. Chen, S.-C. Kou, and C.-S. Poon, "Photocatalytic cement-based materials: comparison of nitrogen oxides and toluene removal potentials and evaluation of self-cleaning performance," *Building and Environment*, vol. 46, no. 9, pp. 1827–1833, 2011.

[5] A. Maury-Ramirez, K. Demeestere, and N. De Belie, "Photocatalytic activity of titanium dioxide nanoparticle coatings applied on autoclaved aerated concrete: effect of weathering on coating physical characteristics and gaseous toluene removal," *Journal of Hazardous Materials*, vol. 211-212, pp. 218–225, 2012.

[6] J. S. Belkowitz and D. Armentrout, "An investigation of nano silica in the cement hydration process," in *Proceedings of the Concrete Sustainability Conference*, pp. 1–15, National Ready Mixed Concrete Association, 2010.

[7] L. Senff, D. Hotza, W. L. Repette, V. M. Ferreira, and J. A. Labrincha, "Mortars with nano-SiO_2 and micro-SiO_2 investigated by experimental design," *Construction and Building Materials*, vol. 24, no. 8, pp. 1432–1437, 2010.

[8] I. Flores, K. Sobolev, L. M. Torres-Martinez, E. L. Cuellar, P. L. Valdez, and E. Zarazua, "Performance of cement systems with nano-SiO_2 particles produced by using the sol-gel method," *Transportation Research Record*, vol. 2141, pp. 10–14, 2010.

[9] G. Quercia, G. Hüsken, and H. J. H. Brouwers, "Water demand of amorphous nano silica and its impact on the workability of cement paste," *Cement and Concrete Research*, vol. 42, no. 2, pp. 344–357, 2012.

[10] K. L. Lin, W. C. Chang, D. F. Lin, H. L. Luo, and M. C. Tsai, "Effects of nano-SiO_2 and different ash particle sizes on sludge ash-cement mortar," *Journal of Environmental Management*, vol. 88, no. 4, pp. 708–714, 2008.

[11] L. Senff, D. Hotza, S. Lucas, V. M. Ferreira, and J. A. Labrincha, "Effect of nano-SiO_2 and nano-TiO_2 addition on the rheological behavior and the hardened properties of cement mortars," *Materials Science and Engineering A*, vol. 532, pp. 354–361, 2012.

[12] M.-H. Zhang and J. Islam, "Use of nano-silica to reduce setting time and increase early strength of concretes with high volumes of fly ash or slag," *Construction and Building Materials*, vol. 29, pp. 573–580, 2012.

[13] M. Ltifi, A. Guefrech, P. Mounanga, and A. Khelidj, "Experimental study of the effect of addition of nano-silica on the behaviour of cement mortars," *Procedia Engineering*, vol. 10, pp. 900–905, 2011.

[14] D. F. Lin, K. L. Lin, W. C. Chang, H. L. Luo, and M. Q. Cai, "Improvements of nano-SiO_2 on sludge/fly ash mortar," *Waste Management*, vol. 28, no. 6, pp. 1081–1087, 2008.

[15] B.-W. Jo, C.-H. Kim, G.-H. Tae, and J.-B. Park, "Characteristics of cement mortar with nano-SiO_2 particles," *Construction and Building Materials*, vol. 21, no. 6, pp. 1351–1355, 2007.

[16] F. Kontoleontos, P. E. Tsakiridis, A. Marinos, V. Kaloidas, and M. Katsioti, "Influence of colloidal nanosilica on ultrafine cement hydration: physicochemical and microstructural characterization," *Construction and Building Materials*, vol. 35, pp. 347–360, 2012.

[17] H. Noorvand, A. A. A. Ali, R. Demirboga, H. Noorvand, and N. Farzadnia, "Physical and chemical characteristics of unground palm oil fuel ash cement mortars with nanosilica," *Construction and Building Materials*, vol. 48, pp. 1104–1113, 2013.

[18] P. Hou, S. Kawashima, D. Kong, D. J. Corr, J. Qian, and S. P. Shah, "Modification effects of colloidal nanoSiO_2 on cement hydration and its gel property," *Composites Part B: Engineering*, vol. 45, no. 1, pp. 440–448, 2013.

[19] M. Aly, M. S. J. Hashmi, A. G. Olabi, M. Messeiry, E. F. Abadir, and A. I. Hussain, "Effect of colloidal nano-silica on the mechanical and physical behaviour of waste-glass cement mortar," *Materials and Design*, vol. 33, no. 1, pp. 127–135, 2012.

[20] GB 1346-2011: Test methods for water requirement of normal consistency, setting time and soundness of the Portland cement (Chinese).

[21] ASTM C1608-2012: Standard test method for chemical shrinkage of hydraulic cement paste.

[22] ASTM, "Standard test method for autogenous strain of cement paste and mortar," ASTM C1698-2014, 2014.

[23] M. Hosokawa, *Nanoparticle Technology Handbook: Chemical, Petrochemical & Process*, Elsevier, New York, NY, USA, 2007.

[24] ACI 234R, "Guide for the use of silica fume in concrete," ACI Committee Report 234, American Concrete Institute, Michigan, Mich, USA, 2006.

[25] R. Polat, R. Demirboğa, and W. H. Khushefati, "Effects of nano and micro size of CaO and MgO, nano-clay and expanded perlite aggregate on the autogenous shrinkage of mortar," *Construction and Building Materials*, vol. 81, pp. 268–275, 2015.

[26] D. Snoeck, O. M. Jensen, and N. De Belie, "The influence of superabsorbent polymers on the autogenous shrinkage properties of cement pastes with supplementary cementitious materials," *Cement and Concrete Research*, vol. 74, pp. 59–67, 2015.